From optical properties to passive radiative cooling applications of cement-based materials

Jozef Janovec

2026

Supervised by
Andrés Ayuela Fernández

and co-supervised by
Jorge Sánchez Dolado

eman ta zabal zazu

Universidad del País Vasco
Euskal Herriko Unibertsitatea

Acknowledgements

In the first place, my gratitude goes to Dr. Andrés for creating a productive but at the same time unstressful working environment, for always being fair, generous and helpful. I have truly enjoyed my time here, in the Basque Country and in Spain, and I'm very grateful for this opportunity. I want to acknowledge Dr. Zelený without whom I wouldn't have been here doing what I do. I would also like to thank all former and current members of the group, namely Dr. Jorge, Raul, Mikel, Alberto, Rodrigo, Emre, and Diego. I also thank to my CFM friends Alba, Zuzanna, Adam, Matia, Ďordi, Victor, Paschalis, Kateryna, Nathaniel, and many others. I am also thankful to prof. Talat, Lyman, and Dr. Volodymyr for being such great people.

Most importantly many thanks to my parents and sisters with families, and my new family Mari Carmen, Julio, María and Asia. I have to thank especially to Ane, for all the beautiful memories and those yet to come.

List of abbreviations

ATW	atmospheric transparency window
BB	black-body
BSE	Bethe-Salpeter equation
BZ	Brillouin zone
C2S	belite, dicalcium silicate
C3A	tricalcium aluminate
C3AH	tricalcium aluminate hydrate
C3S	alite, tricalcium silicate
C4AF	tetracalcium aluminoferrite
C-S-H	calcium-silicate-hydrate
CBM	conduction band minimum
CS	wollastonite, calcium silicate
DFT	density functional theory
DFPT	density functional perturbation theory
e-h	electron-hole
fcc	face centered cubic
GGA	generalized gradient approximation
HH	Hapke-Hulst
IMSA	isotropic multiple-scattering approximation
IPA	independent particle approximation
IR	infrared
JBS	joint band structure
JDOS	joint density of states
JBS	joint band structure
JDOS	joint density of states
KS	Kohn-Sham
LDA	local density approximation
mBSE	model-BSE
MBPT	many-body perturbation theory
MSTM	multiple sphere T-matrix
NIR	near-infrared
PAW	projected augmented wave
PBE	Perdew-Burke-Ernzerhof
PC	photonic concrete
RPA	random phase approximation
SCAN	strongly constrained and appropriately normed
T11	tobermorite 11Å
T14	tobermorite 14Å
TDA	Tamm-Dancoff approximation
UV	ultraviolet
VASP	Vienna ab-initio simulation package
VBM	valence band maximum
Vis	visible
WM	Wannier-Mott
xc	exchange-correlation

Contents

Abstract 1

Abstract 3

1 Introduction 7
- 1.1 Cement and concrete . . . 7
- 1.2 Radiative cooling . . . 10
- 1.3 Dielectric function . . . 11

2 Computational methods 15
- 2.1 Density functional theory . . . 16
  - 2.1.1 Exchange-correlation functional . . . 18
  - 2.1.2 Plane-wave basis . . . 20
- 2.2 Many-body perturbation theory . . . 21
  - 2.2.1 Dyson equation . . . 22
  - 2.2.2 Excitation energies . . . 22
  - 2.2.3 GW approximation . . . 24
  - 2.2.4 Bethe-Salpeter equation . . . 27
- 2.3 Dielectric response . . . 29
  - 2.3.1 Ionic dielectric response . . . 30
- 2.4 Mie scattering . . . 31
- 2.5 MSTM . . . 33
- 2.6 Hapke model . . . 34
  - 2.6.1 Emissivity . . . 34
  - 2.6.2 Reflectance . . . 35
- 2.7 Equations for radiative cooling . . . 36

3 Crystal and electronic structure of cement and concrete phases 39
- 3.1 Computational details . . . 39
- 3.2 Simple cement-forming oxides . . . 39
- 3.3 Cement phases . . . 43
- 3.4 Hydrated concrete phases . . . 45
- 3.5 Raw materials and additives . . . 48
- 3.6 Outline . . . 51

4 Optical properties of cement and concrete **53**
4.1 Computational details . . . 53
4.2 Simple cement-forming oxides . . . 54
4.2.1 Optical spectrum - electronic contribution . . . 54
4.2.2 Optical spectrum - ionic contribution . . . 65
4.3 Cement phases . . . 67
4.4 Hydrated concrete phases . . . 70
4.5 Raw materials and additives . . . 74
4.6 Outline . . . 80

5 Radiative cooling in the bulk **81**
5.1 Computational details . . . 81
5.2 Bulk emissivity . . . 82
5.3 Net radiated powers . . . 86
5.3.1 Atmospheric losses . . . 87
5.3.2 Solar losses . . . 89
5.4 Outlook . . . 90

6 Photonic properties of cement and concrete **91**
6.1 Computational details . . . 91
6.2 Size dependent IR emissivity . . . 92
6.2.1 MSTM emissivity . . . 99
6.3 Size-dependent solar reflectance . . . 100
6.4 Radiative cooling potential . . . 105
6.5 Outlook . . . 109

Conclusions **111**

List of publications **113**

Appendices **115**

A Green's functions representation **117**

B GW formalism **121**
B.1 Second quantization in GW . . . 121
B.2 Equation of motion . . . 122
B.3 GW approximation . . . 125

C Bethe-Salpeter equation **127**

D Ionic dielectric response **129**

E GW convergence **131**

Bibliography **143**

Abstract

Cement and concrete are of immense importance to society as concrete is the most widely produced and, after water, the second most consumed material on Earth. Traditionally, research in construction materials has focused primarily on the mechanical properties of concrete. However, significant carbon footprint related to the production of cement has attracted new scientific interests that aim to reduce CO_2 emissions both during clinker production and throughout the use of concrete structures. Furthermore, novel high-tech applications of concrete have been recently proposed, such as energy storage, batteries or optically active photonics, which make this materials far more interesting. The present work explores radiative cooling as a strategy for effective thermal regulation of modern buildings and cities. Due to the large-scale production and widespread use of concrete, even modest improvements in its functional properties could have a significant positive environmental impact.

As one of the potential solutions, photonic concrete (PC) has been proposed as an innovative construction material with the potential to reduce the CO_2 footprint associated with energy usage of buildings. By incorporating photonic and radiative cooling functionalities into cement-based materials, PC represents a promising candidate for the next-generation thermal envelopes and insulation. In particular, PC has attracted growing interest for daytime radiative cooling applications. These technologies offer an energy-efficient approach to temperature regulation, with the potential to substantially reduce the demand for air-conditioning, which is an important contributor to global energy consumption. Beyond energy savings at the building scale, large-scale use of radiative cooling materials could play an important role in mitigating the urban heat island effect, a phenomenon caused by excessive heat absorption and limited night-time cooling in densely built areas.

Radiative cooling is based on a passive dissipation of heat into outer space by emitting thermal radiation through the atmospheric transparency window (ATW) in the infrared (IR) wavelength range of 8–13 µm. Most of the radiation emitted within this spectral window is not absorbed by the atmosphere and escapes directly into space, without contributing to atmospheric warming. As a result, PC could decrease its surface temperatures even under a direct solar irradiation. Thanks to reduced heat accumulation, PC could improve thermal comfort and decrease the overall contribution of surfaces covered by concrete to heat trapping in urban environments.

In order to study the radiative cooling potential of construction materials, we describe the light-matter interaction, absorption, thermal emissivity and reflectance of concrete-related materials. Our analysis ranges from the simple cement-forming oxides, raw materials and additives, through the most important cement phases, to hydrated concrete phases. Description of radiative properties requires calculation of the optical properties of cement, concrete and related phases. For this purpose, we used density functional theory (DFT) calculations, which allow for

an accurate description of materials at the atomic level. To overcome the inaccuracies of DFT, we employed the GW method and the solution of the Bethe-Salpeter equation (BSE), which accounts for the many-body electron-hole interactions necessary to obtain an accurate description of the optical spectra. This approach enables us to gain a detailed understanding of the role of individual oxides in the optical response of cementitious composites. These findings are particularly relevant for engineering of advanced composites, in which the optical functionality of each oxide can be used to tailor thermal emittance and photonic response.

In order to evaluate the size-dependent optical properties, we applied Mie theory, multiple sphere T-matrix method (MSTM) and the Hapke model to calculate scattering, albedo, emissivity, reflectance and absorbance. We analyzed selective emissivity, net radiated powers, and solar reflectance of the studied cement and concrete phases. Hydrated calcium silicates were identified as the most promising candidates for radiative cooling applications due to their low solar losses, high reflectance, and strong thermal emission. In general, many phases that naturally occur in concrete exhibit intrinsic passive cooling capability. These findings demonstrate that cement and concrete are not only construction materials but also promising platforms for radiative cooling applications and beyond.

The thesis is divided into six chapters, starting an introduction to cement-based materials, radiative cooling and dielectric properties of matter. Chapter 2 describes computational methods and methodology used in this work. The results are organized into four chapters. Chapter 3 establishes a solid foundation for calculating the optical and radiative properties of cement and concrete by determining the ground-state crystal and electronic structures. Since accurate optical spectra critically depend on reliable band gap values, we employed many-body perturbation theory (MBPT), specifically the GW method, to overcome the band gap underestimation inherent to semi-local exchange-correlation functionals. We assessed the influence of the ground-state functional by comparing the generalized gradient approximation (GGA) and meta-GGA exchange-correlation functionals. We showed that the SCAN+G_0W_0 approach provides impressive agreement with experimental data and provides reliable predictive capabilities.

In Chapter 4, we present the optical spectra of cement and concrete phases, including electronic and ionic contributions to the dielectric function. We compare results obtained within the independent-particle approximation (IPA) and the BSE framework. Special attention is devoted to excitonic features in simple cement-forming oxides, which constitute the backbone of more complex phases. Complex refractive indices in the IR region are also provided. The results presented in this chapter are essential for the discussion of the radiative cooling performance.

Chapter 5 focuses on the radiative properties in the bulk single-crystal limit. We analyze emissivity spectra and their characteristic features, as well as temperature-dependent net radiative powers, and solar radiation absorption.

In Chapter 6, we extend the discussion in Chapter 5 and provide a comprehensive analysis of the radiative cooling potential of the studied materials. We evaluate size-dependent emissivity across the IR range and reflectance in the ultraviolet (UV), visible (Vis) and near-infrared (NIR) regions. We examine the behavior of particles in both air and within a concrete-like matrix approximated by the dielectric function of tobermorite 14 Å. The radiative cooling potential is assessed through a combined analysis of size-dependent emissivity, solar reflectance, and absorption.

Resumen

El cemento y el hormigón revisten una enorme importancia para la sociedad, ya que el hormigón es el material más producido y, después del agua, el segundo más consumido del planeta. Tradicionalmente, la investigación en materiales de construcción se ha centrado principalmente en las propiedades mecánicas del hormigón. Sin embargo, la considerable huella de carbono asociada a la producción de cemento ha suscitado un nuevo interés científico destinado a reducir las emisiones de CO_2 tanto durante la producción de clinker como a lo largo de la vida útil de las estructuras de hormigón. Además, recientemente se han propuesto nuevas aplicaciones de alta tecnología del hormigón, como el almacenamiento de energía, las baterías o la fotónica ópticamente activa, lo que hace que este material resulte mucho más interesante. El presente trabajo explora el enfriamiento radiativo como estrategia para la regulación térmica eficaz de los edificios y ciudades modernos. Debido a la producción a gran escala y al uso generalizado del hormigón, incluso pequeñas mejoras en sus propiedades funcionales podrían tener un impacto ambiental positivo significativo.

Como una de las posibles soluciones, se ha propuesto el hormigón fotónico (PC) como un material de construcción innovador con el potencial de reducir la huella de CO_2 asociada al consumo energético de los edificios. Al incorporar funcionalidades de refrigeración fotónica y radiativa en materiales a base de cemento, el PC representa una opción prometedora para las envolventes térmicas y el aislamiento de próxima generación. En particular, el PC ha suscitado un interés creciente para aplicaciones de refrigeración radiativa durante el día. Estas tecnologías ofrecen un enfoque energéticamente eficiente para la regulación de la temperatura, con el potencial de reducir sustancialmente la demanda de aire acondicionado, que es un importante factor que contribuye al consumo energético global. Más allá del ahorro energético a escala de edificio, el uso a gran escala de materiales de refrigeración radiativa podría desempeñar un papel importante en la mitigación del efecto isla de calor urbano, un fenómeno causado por la absorción excesiva de calor y el enfriamiento nocturno limitado en zonas densamente urbanizadas.

El enfriamiento radiativo se basa en una disipación pasiva del calor hacia el espacio exterior mediante la emisión de radiación térmica a través de la ventana de transparencia atmosférica (ATW) en el rango de longitudes de onda infrarrojas (IR) de 8 a 13 µm. La mayor parte de la radiación emitida dentro de esta ventana espectral no es absorbida por la atmósfera y se escapa directamente al espacio, sin contribuir al calentamiento atmosférico. Como resultado, el PC podría reducir sus temperaturas superficiales incluso bajo irradiación solar directa. Gracias a la reducción de la acumulación de calor, el PC podría mejorar el confort térmico y disminuir la contribución global de las superficies cubiertas de hormigón a la retención de calor en entornos urbanos.

Con el fin de estudiar el potencial de enfriamiento radiativo de los materiales de construcción, describimos la interacción luz-materia, la absorción, la emisividad térmica y la reflectancia de los

materiales relacionados con el hormigón. Nuestro análisis abarca desde los óxidos simples que forman el cemento, las materias primas y los aditivos, pasando por las fases más importantes del cemento, hasta las fases del hormigón hidratado. La descripción de las propiedades radiativas requiere el cálculo de las propiedades ópticas del cemento, el hormigón y las fases relacionadas. Para ello, utilizamos cálculos de la teoría del funcional de la densidad (DFT), que permiten una descripción precisa de los materiales a nivel atómico. Para superar las imprecisiones de la DFT, empleamos el método GW y la solución de la ecuación de Bethe-Salpeter (BSE), que tiene en cuenta las interacciones de muchos cuerpos entre electrones y huecos necesarias para obtener una descripción precisa de los espectros ópticos. Este enfoque nos permite comprender en detalle el papel de los óxidos individuales en la respuesta óptica de los compuestos cementosos. Estos hallazgos son especialmente relevantes para la ingeniería de compuestos avanzados, en los que la funcionalidad óptica de cada óxido puede utilizarse para adaptar la emitancia térmica y la respuesta fotónica.

Con el fin de evaluar las propiedades ópticas dependientes del tamaño, aplicamos la teoría de Mie, el método de la matriz T de esferas múltiples (MSTM) y el modelo de Hapke para calcular la dispersión, el albedo, la emisividad, la reflectancia y la absorbancia. Analizamos la emisividad selectiva, las potencias radiadas netas y la reflectancia solar de las fases de cemento y hormigón estudiadas. Se identificaron los silicatos de calcio hidratados como los candidatos más prometedores para aplicaciones de enfriamiento radiativo debido a sus bajas pérdidas solares, alta reflectancia y fuerte emisión térmica. En general, muchas fases que se dan de forma natural en el hormigón presentan una capacidad intrínseca de enfriamiento pasivo. Estos hallazgos demuestran que el cemento y el hormigón no son solo materiales de construcción, sino también plataformas prometedoras para aplicaciones de enfriamiento radiativo y más allá.

La tesis se divide en seis capítulos, comenzando con una introducción a los materiales a base de cemento, el enfriamiento radiativo y las propiedades dieléctricas de la materia. El capítulo 2 describe los métodos computacionales y la metodología utilizados en este trabajo. Los resultados se organizan en cuatro capítulos. El capítulo 3 establece una base sólida para calcular las propiedades ópticas y radiativas del cemento y el hormigón mediante la determinación de las estructuras cristalinas y electrónicas en el estado fundamental. Dado que la precisión de los espectros ópticos depende fundamentalmente de valores fiables de la banda prohibida, empleamos la teoría de perturbaciones de muchos cuerpos (MBPT), concretamente el método GW, para superar la subestimación de la banda prohibida inherente a los funcionales de intercambio-correlación semilocales. Evaluamos la influencia del funcional del estado fundamental comparando los funcionales de intercambio-correlación de aproximación de gradiente generalizado (GGA) y meta-GGA. Demostramos que el enfoque SCAN+G_0W_0 ofrece una coincidencia impresionante con los datos experimentales y proporciona capacidades predictivas fiables.

En el capítulo 4, presentamos los espectros ópticos de las fases del cemento y el hormigón, incluyendo las contribuciones electrónicas e iónicas a la función dieléctrica. Comparamos los resultados obtenidos mediante la aproximación de partículas independientes (IPA) y el marco BSE. Se presta especial atención a las características excitónicas de los óxidos simples que forman el cemento, los cuales constituyen la base de fases más complejas. También se proporcionan los índices de refracción complejos en la región del infrarrojo. Los resultados presentados en este capítulo son esenciales para el análisis del rendimiento del enfriamiento radiativo.

El capítulo 5 se centra en las propiedades radiativas en el límite de monocristal macizo. Analizamos los espectros de emisividad y sus características, así como las potencias radiativas netas en función de la temperatura y la absorción de la radiación solar.

En el capítulo 6, ampliamos el análisis del capítulo 5 y ofrecemos un análisis exhaustivo del potencial de enfriamiento radiativo de los materiales estudiados. Evaluamos la emisividad dependiente del tamaño en todo el rango del infrarrojo y la reflectancia en las regiones del ultravioleta (UV), el visible (Vis) y el infrarrojo cercano (NIR). Examinamos el comportamiento de las partículas tanto en el aire como dentro de una matriz similar al hormigón, aproximada por la función dieléctrica de la tobermorita de 14 Å. El potencial de enfriamiento radiativo se evalúa mediante un análisis combinado de la emisividad dependiente del tamaño, la reflectancia solar y la absorción.

Chapter 1

Introduction

Buildings account for approximately 32% of global electricity consumption [1]. Depending on geographic location and climate conditions, a significant fraction of this energy is spent on air conditioning. Such high energy demand is closely linked to substantial CO_2 emissions associated with electricity production. Therefore, buildings represent a major source of greenhouse gas emissions and contribute significantly to global climate change. Consequently, strategies aimed at reducing energy consumption of buildings have a potential to mitigate their environmental impact and improve overall energy sustainability.

In recent years, significant efforts have been devoted to reduce the energy dependence and operating costs of buildings through the development of construction materials with novel functionalities. Among these, photonic concrete (PC) has emerged as a particularly promising solution, with the potential to provide substantial cost savings and significantly lower CO_2 emissions [2]. PC is well suited for daytime radiative cooling applications [2–5], which offers a passive way to reduce air-conditioning demand and simultaneously helps to mitigate the urban heat island effect [6]. The need for such technologies is underscored by the growing frequency and intensity of summer heatwaves, which are further amplified by heat trapping in densely built urban environments. Worldwide, these extreme events are related to tens of thousands of deaths every year [7]. Hence, innovative approaches in urban planning, building design, and construction materials development are necessary. In this context, passive cooling strategies, such as PC, represent a scalable, low-maintenance complement to existing climate adaptation measures, that suggest new solutions in both urban development and material design.

Optimization of the photonic properties of PC relies on a thorough understanding of the optical properties of cement phases and their additives. Since concrete is a heterogeneous composite consisting of multiple constituents, its macroscopic response is commonly approximated using effective medium approaches that average over the properties of the individual phases [2,8]. The key quantity governing the optical behavior and the design of PC is the complex dielectric function. We therefore study the dielectric properties of a wide range of cement and concrete related phases, as discussed in the following.

1.1 Cement and concrete

Cement is produced on a large scale to meet the growing demand for construction and infrastructure development. The most commonly used type, the ordinary Portland cement, is manu-

factured through a high-temperature reaction between limestone ($CaCO_3$) and various minerals and clays. The resulting clinker consists mainly of calcium silicates, such as alite (C3S[1]) and belite (C2S), as well as minor phases including calcium aluminate (C3A) and calcium aluminoferrite (C4AF) [9], as shown in Figure 1.1. These complex clinker phases are composed CaO, SiO_2, Al_2O_3, and Fe_2O_3. These simple oxides are also commonly used as additives in concrete.

Cement is produced in rotary kilns, where high-temperature fusion of simple oxides leads to the formation of clinker phases. The raw materials are first dehydrated and decomposed into simple oxides at temperatures around 600 °C. Solid-state reactions among these oxides initially produce belite, aluminate, and ferrite phases. Higher temperatures, above 1400 °C, are required for the reaction of CaO with belite to form alite. The final composition of cement typically contains up to 70 % of alite, approximately 20 % of belite, 5–15 % of C3A, and up to 10 % of C4AF [10]. Alite and belite crystallize in various polymorphs with different reactivities toward water. C3A crystallizes in a cubic structure and C4AF in an orthorhombic structure, but their exact crystal structures depend on stoichiometry. Based on the chemical composition of the raw materials, other oxides and impurities, such as Na and Mg, may also be present in cement phases [9, 11].

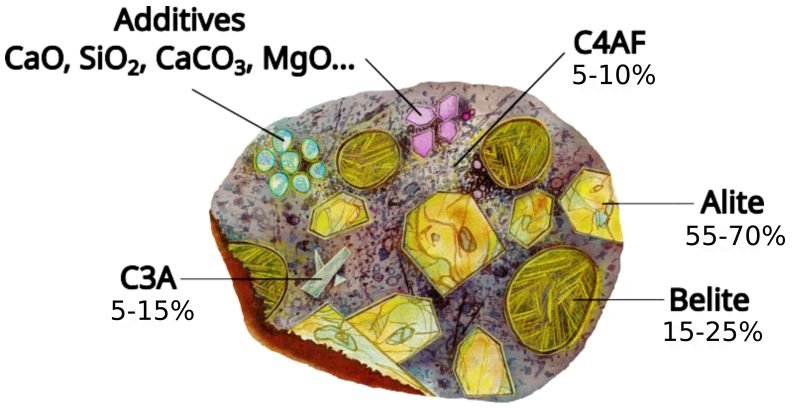

Figure 1.1: Typical composition of ordinary Portland cement. Adapted from [12].

Concrete is formed through the hydration of cement, which acts as a binder between sand, aggregates, fillers and additives. The main hydration products are calcium-silicate-hydrate gel (C-S-H) and portlandite. The C-S-H gel is structurally closely related to tobermorite, but can exhibit varying stoichiometry and may be partially or fully amorphous. The hydration of alite is primarily responsible for early strength development, as most of it reacts within the first 28 days. The hydration of belite produces the same phases as alite but proceeds at much slower rates and therefore contributes mainly to the long-term strength. C3A reacts rapidly with water, which significantly reduces the workability of fresh cement paste. The addition of sulfates, typically in the form of gypsum, leads to the formation of a protective layer on C3A grains, which delays hydration and prevents flash setting. As a result, ettringite (calcium-aluminum-sulfate-hydrate) forms on the surface of C3A particles. C4AF also hydrates relatively quickly but contributes little to the final mechanical strength and is responsible for the gray color of concrete.

The hydration of cement is an exothermic process. Upon contact with water, a rapid heat evolution occurs, mainly due to the reaction of C3A and partly due to the formation of C-S-H

[1]Following the cement and concrete notation, where C, S, A and F stand for CaO, SiO_2, Al_2O_3 and Fe_2O_3, respectively.

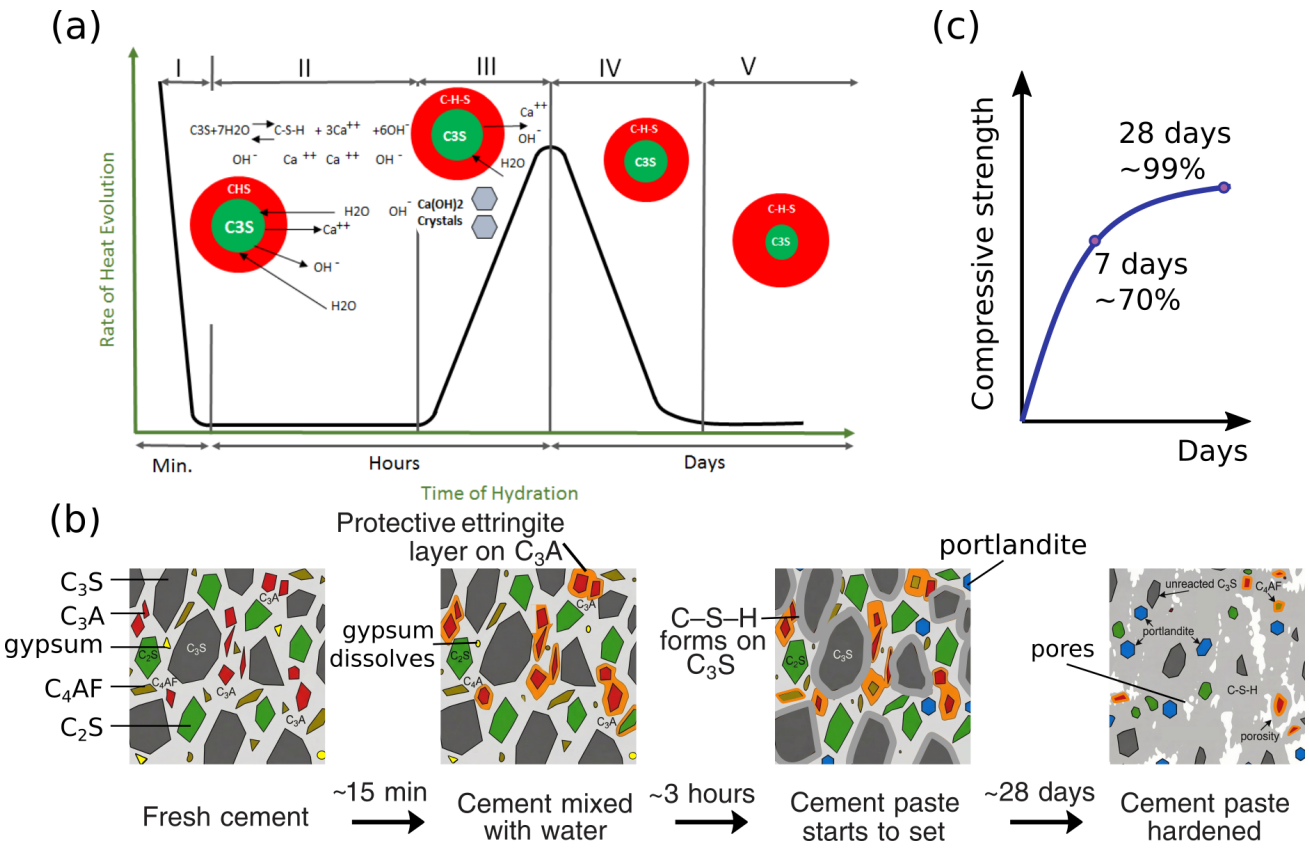

Figure 1.2: (a) Typical hydration curve of cement [13], (b) depiction of the hydration process on the micro scale [14], and (c) a sketch of the compressive strength of concrete as a function of time.

on the surface of alite (phase I in Figure 1.2a). This stage is followed by the dormant period characterized by a slow reaction rate (phase II). Subsequently, during the acceleration period (phase III), alite hydrates rapidly, which leads to the formation of C-S-H gel and portlandite. In the following deceleration phase, hydration of alite and belite continues within the growing C-S-H shells (phase IV), and finally transitions into a slow, long-term reaction stage (phase V). A depiction of the hydration process is shown in Figure 1.2b. The first panel illustrates the main cement constituents. Upon the addition of water, gypsum begins to dissolve, which slows the rapid hydration of C3A by forming a protective layer on the surface of the C3A grains, as shown in the second panel. After the crystallization of ettringite, the dormant period (phase II) begins. The third panel shows the growth of C-S-H on alite and the formation of portlandite, which corresponds to the acceleration stage, or phase III of the reaction. The final panel depicts the steady-state period, during which most of alite and belite have been transformed into C-S-H gel. The initially fast reaction of C3A reduces the workability of cement paste and must therefore be controlled by the addition of sulfates. Concrete develops most of its compressive strength within the first 28 days of curing, as shown in Figure 1.2c. However, hardening continues for years, primarily due to an ongoing hydration and the gradual polymerization and bridging of SiO_4 tetrahedra within the C-S-H structure [9, 14].

Additives are often incorporated into concrete to enhance specific properties of the final composite. In fact, nano- and micro-scale oxide additions can transform cementitious composites

into concrete-based metamaterials with exceptional photonic properties. Likewise, the pore structure plays a crucial role in determining concrete performance. The optical functionality of concrete composites is becoming increasingly relevant for applications such as radiative cooling, energy efficiency, and photonics. The incorporation of carefully selected and engineered nano-additives could enable the application of concrete within these emerging fields.

1.2 Radiative cooling

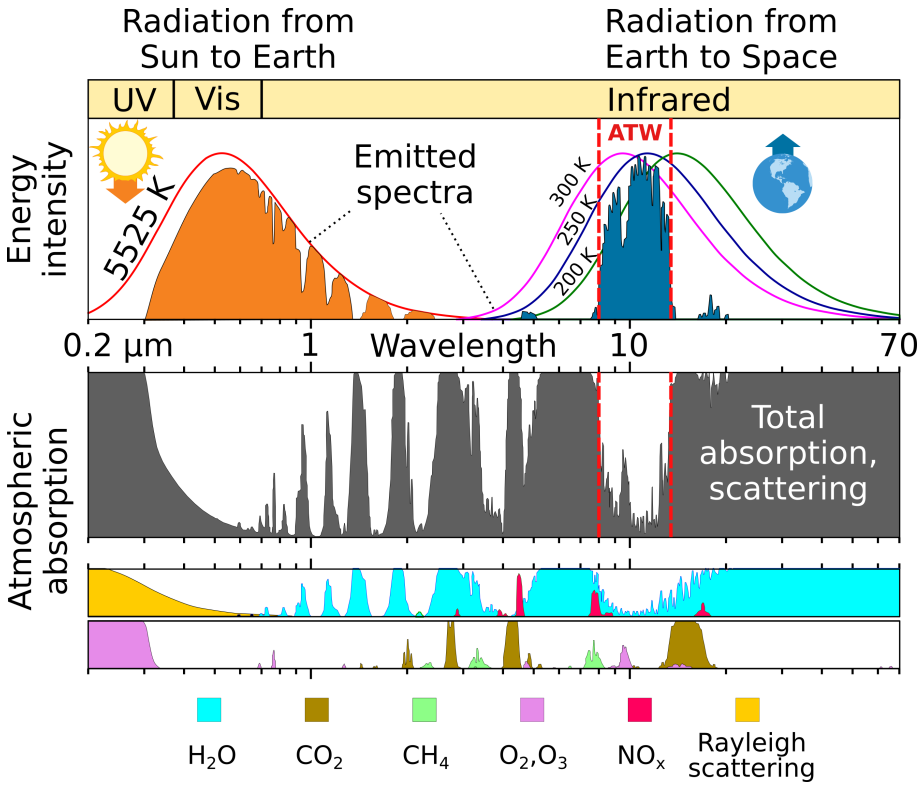

Figure 1.3: Spectra of solar irradiance and atmospheric absorption with contribution of different molecules. The dashed red lines highlight the atmospheric transparency window. Adapted from [15].

Radiative cooling is a naturally occurring phenomenon, commonly observed for example in deserts. At night, sand releases the heat accumulated during the day using radiative cooling, which leads to differences up to 40 °C between day and night. The physical principle of radiative cooling is the efficient dissipation of heat within the frequency range of the atmospheric transparency. The atmosphere is partially transparent in the IR atmospheric transparency window (ATW), which spans wavelengths from 8 to 13 µm [3–5], as shown in Figure 1.3. Materials that emit thermal radiation within this spectral range are thermally coupled to outer space rather than to the surrounding atmosphere. This enables efficient heat transfer and faster decrease in temperature that can even reach sub-ambient values. Similarly to the ATW, there is another less significant transparency window around 20 µm, which can contribute to the cooling performance. Since thermal radiation in the ATW range does not contribute to atmospheric heating, the use of PC capable of radiative cooling has the potential to reduce the contribution of concrete

to the greenhouse effect. As shown in Figure 1.3, most of the atmospheric absorbance comes form the water molecules. The radiative cooling is therefore an especially good concept for hot and dry areas with low cloud cover. The objective of the ongoing research is the development of functional solutions based on radiative cooling that allow for efficient cooling even under daytime conditions.

We propose passively cooled construction materials based on abundant and already easily accessible materials, such as cement and concrete. Optically active PC offers a scalable solution without the need for high-tech manufacturing processes. The passive radiative cooling technology takes advantage of maximizing both the thermal emission within the ATW and the solar reflectance. Recent studies have demonstrated the cooling potential of cement-based materials [2, 16–19], that support the feasibility of concrete for radiative cooling applications.

The passive radiative cooling requires selective thermal emission in the mid-infrared ATW spectral region. In order to obtain cooling performance, an object has to radiate more energy than it absorbs. The net radiative cooling power P_{Rad}, or emittance, is defined as P_{Rad}=P_{Mat}-P_{Sun}-P_{Atm}-P_{NR}, where P_{Mat} is the power radiated by material, P_{Sun} are the losses from the absorption of the solar radiation, P_{Atm} are the losses from the surrounding atmosphere and P_{NR} are the non-radiative losses from conduction and convection [3]. A detailed explanation of radiative cooling equations can be found in section 2.7. A material is capable of radiative cooling if the radiated power is greater than the sum of the absorption losses.

The efficiency of radiative cooling is primarily determined by two key parameters: high emissivity in the IR region and high reflectance across the solar spectrum, which extends from the UV to the NIR wavelengths. The selective emissivity increases P_{Mat}, while high reflectance in the solar range reduces P_{Sun}. Since both emissivity and reflectance can be related to light-matter interactions, the development and design of a new generation of PC-based green concrete critically depend on a detailed understanding of the optical properties of cement and concrete constituents.

1.3 Dielectric function

The dielectric function is a fundamental material property that defines how matter interacts with light. It serves as a measure of a material polarizability, which is the ability to form internal dipoles in response to external electric fields. While this value appears as a simple constant in static fields, its behavior becomes significantly more complex in frequency-dependent fields [20]. As the frequency of the external field varies, different physical mechanisms of relaxations and resonances contribute to the overall dielectric response, which is schematically shown in Figure 1.4.

The specific source of polarizability depends on the energy of the incident electric field. At low frequencies (high wavelengths), the field varies slowly with response similar to the static conditions. In polar or dipolar materials slowly varying fields allow for the physical rearrangement of molecular dipoles and the movement of ions. At IR frequencies, the dielectric function captures resonant processes, specifically the absorption of energy by lattice vibrations or phonons. Finally, at the sub-micron wavelengths of Vis and UV light, the displacement of electron clouds and the excitation of electrons across the bandgap act as the primary source of polarizability [20].

The frequency-dependent dielectric function has the real and imaginary parts and writes $\epsilon = \epsilon_1 + i\epsilon_2$. The real part ϵ_1 is related to the polarization response of the material and describes

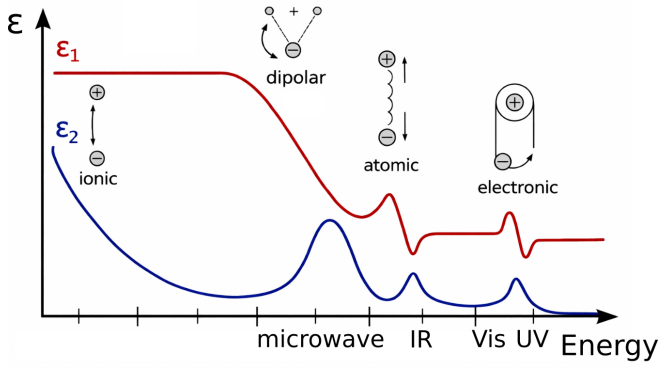

Figure 1.4: Different contributions to dielectric function as a function of wavelength. Adapted from [21].

its ability to store energy under an external electromagnetic perturbation. The imaginary part ϵ_2 accounts for energy dissipation and is responsible for absorption and losses.

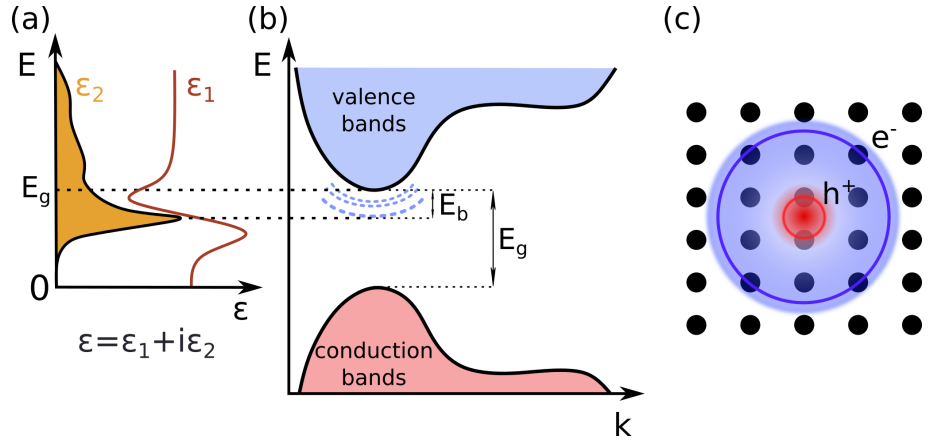

Figure 1.5: (a) Complex dielectric function with an exciton peak in the imaginary part, (b) reciprocal space representation of excitons within the band structure with excitonic energy states, the binding E_b and band gap E_g energies, and (c) exciton delocalization in real space.

In materials with a finite band gap, electrons excited by light of sufficient energy can interact with the positively charged holes left behind and form bound quasiparticles known as excitons. These excitonic states give rise to distinct features in optical absorption spectra that usually appear as sharp peaks below the band gap energy, as illustrated in Figure 1.5a. The exciton binding energy is defined as the difference between the corresponding band-to-band transition energy and the location of the exciton peak. As a result of the finite binding, excitons can introduce discrete energy levels within the band gap, as shown in Figure 1.5b. Depending on their spatial extent and the atomic orbitals involved, excitons can exhibit varying degrees of localization in real space, as shown in Figure 1.5c. On this basis, excitons are commonly classified into delocalized Wannier-Mott and charge-transfer excitons, as well as highly localized Frenkel excitons [22]. The Wannier-Mott excitons are typically formed between electrons and holes located on the same type of atoms, while the holes and electrons of charge-transfer excitons belong to different species of atoms. The Frenkel excitons are typical for molecules.

The properties of excitons are strongly influenced by symmetry, dimensionality, and interactions with the environment. Only excitons allowed by the optical selection rules can be directly excited by light. On the other hand, dark excitons can play an important role in exciton dynamics and relaxation processes. Although optical experiments primarily probe direct excitations with near-zero momentum, finite-momentum excitons can be excited with the help of phonons. The excitonic binding energy, lifetime, and radius depend on dielectric screening, temperature, and coupling to phonons or defects. The reduced screening in low-dimensional systems normally leads to a particularly strong electron-hole binding. Excitons may interact to form complex bound states such as trions or biexcitons [22].

Understanding light-matter interactions in cement and concrete through the dielectric response allows us to establish a foundation for the design of concrete-based composites with tailored optical and radiative properties. These insights have the potential to guide the development of advanced construction materials for passive energy management applications such as radiative cooling, in line with sustainable and energy-efficient construction technologies.

Chapter 2

Computational methods

The primary objective of this work is to calculate and understand the optical properties of cement and concrete phases from first principles. A reliable description of light–matter interaction in these materials requires an accurate determination of their dielectric response over a broad spectral range, extending from the ultraviolet through the visible and into the infrared. To achieve this, we used density functional theory (DFT) and the GW method, which provides improved quasiparticle energies and more accurate band gaps, as well as the Bethe-Salpeter equation (BSE) method. Excitonic contributions can significantly modify the optical spectra near the band edge, particularly in wide band gap materials, as is the case for many cement-forming oxides. By explicitly including these many-body interactions, the BSE approach yields highly accurate dielectric functions.

As an addition to the experimental investigation, which is challenging due to a large number of external parameters, we propose a theoretical study of the fundamental physical properties of cement. First principles calculations have become well-established in the field of cement and concrete research. The highly accurate predictive power of this theoretical approach have been realized in for mechanical properties [23–25], thermoelectric properties [26], description of

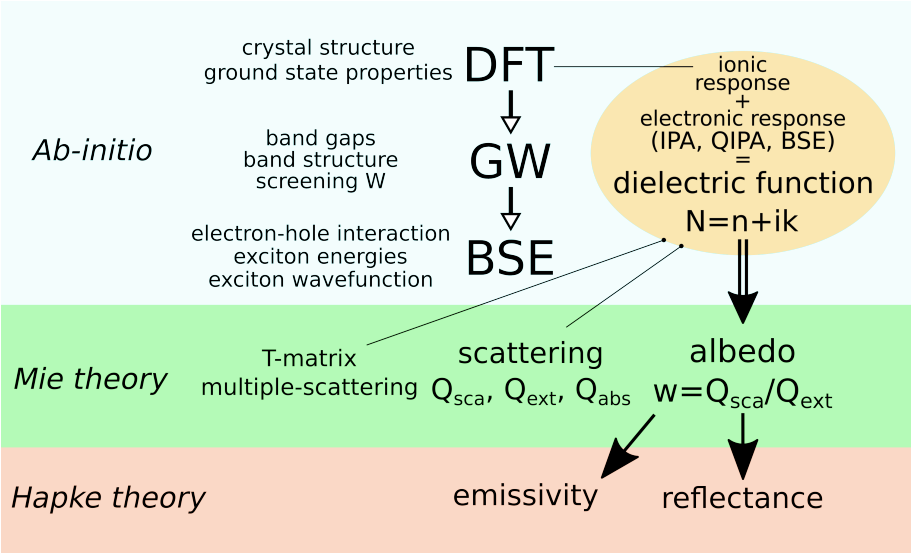

Figure 2.1: Diagram of the methods used in the thesis.

hydration [27, 28], structural analysis [29–31], and the design of cement-based nanocomposites [32–35]. First principles calculations provide a comprehensive picture of the optical properties of materials, ranging from the IR to UV–Vis frequencies.

The methods introduced in this chapter are summarized in a schematic way in Figure 2.1. The radiative cooling properties of cement and concrete related materials are evaluated based on their emissivity and reflectance, calculated using Hapke theory. The photonic properties and size depencence are available via Mie theory that requires dielectric functions as an input. Highly accurate dielectric properties are calculated using first principles calculations, at the DFT level and beyond. The combination of these methods provides a complete theoretical description of radiative cooling properties and has a practical predictive potential.

2.1 Density functional theory

Theoretical solid-state physics and chemistry aim to predict material properties using a quantum-mechanical description of materials. This allows the macroscopic observables to be described by only few fundamental inputs on the atomic scale. These inputs are the number of electrons, the nuclear charges and the ionic positions. Methods that seek to understand experimental observations directly from the many-body quantum mechanics, without empirical parameters, are therefore referred to as first principles or *ab-initio* calculations.

A quantum system is fully described by its wavefunction, from which experimentally accessible physical quantities are obtained by the action of appropriate operators. The total energy of an interacting many-body electron-nucleus system is determined by the Hamiltonian, which in its basic form consists of the kinetic energy of electrons and nuclei, as well as the electron-electron, electron-nucleus, and nucleus-nucleus interactions. The Hamiltonian may be extended to include additional effects, such as magnetism, relativistic spin-orbit coupling for heavy elements, or interactions with external fields [36].

In principle, the solution of the Schrödinger equation for a system of electrons and nuclei defined by the full interacting wavefunction yields the exact total energy of the system through the action of the Hamiltonian operator. However, the computational complexity of the problem grows rapidly with the system size and a full quantum mechanical description of all interactions is impractical for realistic materials. The first widely used simplification is the Born-Oppenheimer approximation, which neglects the motion of the nuclei due to the large mass difference between nuclei and electrons. Within this approximation, the total wavefunction is split into the electronic and ionic parts. The Schrödinger equation is then solved for the electronic part with fixed nuclear positions. The interaction between electrons and nuclei is defined by the external potential and the nucleus-nucleus interaction contributes with a constant energy term [37].

Even with the Born-Oppernheimer approximation the number of interactions that needs to be explicitly evaluated is prohibitive for the application in realistic systems. DFT provides a framework, in which the central quantity is the electronic density rather than the complicated many-body wavefunction. In DFT, the ground state density uniquely determines all ground state properties, and the exact wavefunction is not required explicitly.

The theoretical foundation of DFT is given by the two Hohenberg-Kohn theorems [38]. The first theorem states that, for a system of interacting electrons, the external potential is uniquely determined, up to an additive constant, by the ground state electron density. Consequently, there is a one-to-one correspondence between the ground state density, the external potential,

and the ground state wavefunction, which implies that the density fully determines all ground state properties. Since the Hamiltonian is defined by the external potential, the ground state density defines all ground state properties of the system.

The second Hohenberg-Kohn theorem establishes the existence of an universal energy functional of the electron density whose minimization with respect to the density leads to the ground state energy. The second theorem basically establishes the variational principle in DFT. This means that we only need an exact energy functional to determine both the ground state energy and electron density by a self-consistent cycle. Together, these theorems justify the use of the electron density as the fundamental variable in first principles calculations.

The goal of DFT is to describe the ground state of an interacting many-electron system using the electron density as the fundamental variable. In the Kohn-Sham (KS) ansatz [39], the interacting many-body problem is mapped onto an auxiliary system of fictitious non-interacting electrons that reproduces the exact ground state density of the real system. The KS electronic density is obtained as a sum of single particle densities

$$n(\mathbf{r}) \equiv \sum_{\sigma} \sum_{j}^{N} |\phi_{j,\sigma}(\mathbf{r})|^2, \tag{2.1}$$

constructed from the one-electron KS orbitals $\phi_{j,\sigma}(\mathbf{r})$, where the sum runs over all occupied states and the spin σ. The Kohn-Sham orbitals are auxiliary mathematical objects that reproduce the exact ground state density and do not, in general, have a direct physical interpretation.

The total energy can therefore be expressed as a functional of the density,

$$E[n] = T[n] + E_{\text{ext}}[n] + E_{\text{H}}[n] + E_{\text{xc}}[n]. \tag{2.2}$$

The total energy is formally evaluated as an action of the wavefunction on the Hamiltonian. The wavefunction in the KS framework is defined using the anti-symmetric Slater determinant constructed from single-particle orbitals. Therefore, the kinetic energy of the non-interacting KS electrons is given by the sum of the single-particle contributions as

$$T[n] = \sum_{\sigma} \sum_{j}^{N} \int \phi^*_{j,\sigma}(\mathbf{r}) \left(-\frac{1}{2}\nabla^2 \right) \phi_{j,\sigma}(\mathbf{r}) \mathrm{d}^3\mathbf{r}, \tag{2.3}$$

where σ represents the spin and $\phi_{j,\sigma}(\mathbf{r})$ are the single-particle wavefunctions. The integral in Equation 2.3 can be written as $\langle\phi| -\frac{1}{2}\nabla^2|\phi\rangle$ using the Dirac notation and atomic units. The remaining density-dependent terms that contribute to the total energy are the classical Hartree term

$$E_{\text{H}}[n] = \frac{1}{2} \int \int \frac{n(\mathbf{r})n(\mathbf{r}')}{|\mathbf{r} - \mathbf{r}'|} \mathrm{d}^3\mathbf{r} \mathrm{d}^3\mathbf{r}', \tag{2.4}$$

the external potential energy due to interaction of electrons and nuclei,

$$E_{\text{ext}}[n] = \int v_{\text{ext}}(\mathbf{r}) n(\mathbf{r}) \mathrm{d}^3\mathbf{r}, \tag{2.5}$$

where $v_{\text{ext}} = \sum_i \frac{-Z_i}{|\mathbf{r}-\mathbf{R}_i|}$ runs over all nuclei. Lastly, the exchange-correlation (xc) energy $\mathrm{E_{xc}}[n]$ accounts for all many-body effects beyond the classical electrostatic interaction, including exchange, correlation, and the difference between the true fully interacting and KS kinetic energies.

The variational principle in DFT determines the ground state electron density by minimizing the total energy functional with respect to the density. In the Kohn-Sham formalism, the minimization is performed indirectly, with respect to single-electron orbitals. The variational principle leads to the KS equations, a set of effective single-particle Schrödinger-like equations, written as

$$\left(-\frac{1}{2}\nabla^2 + V_{\text{eff}}(\mathbf{r})\right)\phi_j(\mathbf{r}) = \epsilon_j^{KS}\phi_j(\mathbf{r}), \tag{2.6}$$

where $V_{eff}(\mathbf{r})$ is the effective potential comprising the external, Hartree, and xc potentials. The total KS energy is given by

$$E = \sum_{j,\text{occ}} \epsilon_j^{KS} - \int v_{\text{ext}}(\mathbf{r})n(\mathbf{r})\mathrm{d}^3\mathbf{r} - E_{\text{H}}[n] + E_{\text{xc}}[n], \tag{2.7}$$

where ϵ_j^{KS} are the KS single-particle energies.

In DFT codes, the KS equations are solved self-consistently. Starting from an initial trial density, for example a superposition of atomic densities, the effective potential is constructed and the Kohn-Sham equations are solved to obtain a new set of orbitals and eigenvalues. The single particle eigenvalues and the new set of orbital coefficients are obtained from the diagonalization of the Hamiltionian. These orbitals define an updated electron density, which is then compared to the previous one. To improve convergence and ensure numerical stability, the new density is typically mixed with the previous density using a suitable mixing scheme. This procedure is repeated until self-consistency is achieved, i.e., until the input and output densities agree within the chosen convergence limit. [36].

2.1.1 Exchange-correlation functional

The choice of the exchange-correlation functional is a crucial step in every DFT calculation. All many-body effects beyond the classical electrostatic interaction, including exchange due to the Pauli exclusion principle and correlation arising from Coulomb repulsion, are contained within the xc functional. Local and semi-local functionals, such as those within the local density approximation (LDA) or generalized gradient approximation (GGA), offer high efficiency but suffer from systematic errors, for example the underestimation of electronic band gaps. More advanced functionals, including meta-GGA or hybrid functionals, can improve accuracy at the expense of increased computational cost. The quality of the xc approximations determines the predictive accuracy and the computational cost of the calculation.

LDA is the simplest approximation to the xc energy, which is based on the assumption that the electron density varies slowly in space [39]. In LDA, the xc energy at each point is approximated by that of a homogeneous electron gas with the same local density,

$$E_{\text{xc}}^{\text{LDA}}[n] = \int n(\mathbf{r})\epsilon_{\text{xc}}(n(\mathbf{r}))\mathrm{d}^3\mathbf{r}, \tag{2.8}$$

where $\epsilon_{xc}(\mathbf{r})$ is xc energy per-electron of the uniform gas. The exchange contribution is known analytically, while the correlation energy is parameterized using quantum Monte Carlo simulations. Physical interpretation of the xc interaction is provided by the xc-hole picture. Around each electron, an exchange hole arises from the Pauli exclusion principle and integrates to -1 for electrons of the same spin, while a correlation hole originates from Coulomb repulsion and

redistributes the density around electrons in the way the spatial integral of the correlation hole density equals to zero. LDA adopts the xc hole of the homogeneous electron gas evaluated at the local density. It preserves the exact properties of the xc-hole and reproduces the electron-electron interaction reasonably well, since it depends only on the spherical average of the xc-hole. Errors in the exchange and correlation contributions tend to cancel, which explains the accuracy of LDA for systems with slowly varying densities, such as simple metals. However, the LDA exchange potential decays as $n(\mathbf{r})^{1/3}$ rather than the correct $-1/\mathbf{r}$ dependence, which together with self-interaction errors leads to overestimated binding energies, underestimated bond lengths and overestimated cohesive energies [36].

GGA is the semi-local extension of the LDA functional that incorporates the local density gradient ∇n [36], such as

$$E_{\mathrm{xc}}^{\mathrm{GGA}}[n] = \int n(\mathbf{r})\epsilon_x^{\mathrm{unif}} F_x(s)\, d^3\mathbf{r} + \int n(\mathbf{r})[\epsilon_c^{\mathrm{unif}} + H(n, \nabla n)] d^3\mathbf{r}. \tag{2.9}$$

Here $F_x(s)$ is the exchange enhancement factor that modifies the LDA exchange via a dimensionless density gradient $s = \frac{|\nabla n|}{(2k_F n)}$ with the local Fermi wave vector k_F, and the gradient contribution to the correlation energy $H(n, \nabla n)$. The limit $s \to 0$ recovers the LDA approximation. The density gradient corrections try to account for inhomogeneities like different orbital types or bonds. In the case of Perdew-Burke-Ernzerhof (PBE) functional, the exchange factor is defined as $F_x(s) = 1 + \kappa - \kappa^2(1 + \mu s^2)^{-1}$, where κ and μ are coeficients defined in Ref. [40]. The GGA exchange hole extends further and becomes less deep in low-gradient regions (when s is small), while gradient terms allow the hole to spread anisotropically or adjust its shape for rapid density changes, which allows for a more realistic description of bonding. As a result, GGA significantly improves bond lengths and geometries compared to LDA and achieves chemical accuracy for many molecular and solid-state properties. However, due to their semi-local nature, GGAs fail to capture long-range dispersion interactions, suffer from self-interaction and band gap errors, cannot describe strong correlation effects and fail to mimic the exact $1/\mathbf{r} \to 0$ behaviour.

The family of meta-GGA functionals represents a further development beyond the GGA that introduces an explicit dependence of the xc functional on additional local ingredients. Most commonly, these functionals include the orbital kinetic-energy density $\tau(\mathbf{r}) = \sum_j |\nabla\phi_j(\mathbf{r})|^2$ and, in some formulations, higher derivatives of the electron density [41]. By incorporating τ alongside ∇n, meta-GGAs gain access to information related to the local orbital structure, which enables a distinction between different chemical environments, such as core, valence, and bonding regions. The additional flexibility allows meta-GGAs to satisfy a larger number of exact constraints, reduce self-interaction errors, and provide a more realistic description of the xc hole, particularly in bonding regions. A general form of a meta-GGA xc functional can be written as

$$E_{\mathrm{xc}}^{\mathrm{mGGA}}[n] = \int n(\mathbf{r})\, \epsilon_{\mathrm{xc}}^{\mathrm{unif}}(n)\, F_{\mathrm{xc}}(s, \alpha)\, d^3\mathbf{r}, \tag{2.10}$$

where F_{xc} is an enhancement factor which depends on the reduced density gradient s and the dimensionless parameter $\alpha = \frac{\tau - \tau_W}{\tau_{\mathrm{unif}}}$, which measures the deviation from single-orbital behavior and is closely related to the electron localization function. Here, $\tau_W = |\nabla n|^2/(8n)$ is the von Weizsäcker kinetic-energy density, which is exact for any single-orbital system, and τ_{unif} is the kinetic-energy density of the uniform electron gas. Therefore, the difference $\tau - \tau_W$ quantifies the

excess kinetic energy arising from orbital overlap and electron delocalization, while the quantity τ_{unif} represents the fully delocalized limit. The SCAN functional was constructed to satisfy all known exact constraints applicable to meta-GGAs [42]. By using α to interpolate between the uniform-gas and rapidly varying limits, SCAN achieves improved accuracy for structural properties and typically yields larger band gaps than standard GGA functionals such as PBE.

2.1.2 Plane-wave basis

In practical implementations of DFT, a number of computational choices must be made, including the selection of basis functions, the treatment of boundary conditions, numerical discretization, and handling of core electrons. For extended crystalline systems, we commonly employ the infinite crystal approximation and the periodic boundary conditions. In this framework, the electronic wavefunctions obey Bloch theorem and are written as a product of the plane-wave factor and the lattice-periodic function,

$$\psi_{j\mathbf{k}}(\mathbf{r}) = e^{i\mathbf{k}\cdot\mathbf{r}} u_{j\mathbf{k}}(\mathbf{r}), \tag{2.11}$$

where $\mathbf{k}$ is a crystal momentum vector within the first Brillouin zone (BZ), and the periodic function $u_{j\mathbf{k}}(\mathbf{r})$ with the periodicity of the crystal lattice. The periodic functions can be expressed in plane waves, which makes it convenient to work in reciprocal space. The periodicity of the system allows for the electronic problem to be defined within the repeated primitive unit cell. Another simplification is the discretization of reciprocal space, which replaces integrals by discrete sums over a finite set of k-points. The electronic structure is therefore determined by sampling the BZ with appropriately chosen and converged k-meshes [36].

Plane-wave basis sets are highly efficient for describing regions where the wavefunctions vary smoothly. However, near atomic nuclei, the wavefunctions exhibit rapid oscillations that require a large number of plane waves. To overcome this limitation, most plane-wave DFT codes use pseudopotentials, which replace the all-electron potential in the core region with a smoother effective potential. Pseudopotentials yield pseudo-wavefunctions that are smooth near the nuclei but match the true all-electron wavefunctions outside the core region.

A more advanced approximation used in many DFT codes is the projector augmented wave (PAW) method, which combines the efficiency of pseudopotentials with explicit reconstruction of the all-electron wavefunctions [43]. Pseudo-wavefunctions are in the augmentation region replaced by a set of all-electron partial waves, so that the full wavefunction writes

$$|\phi_j\rangle = |\tilde{\phi}_j\rangle + \sum_j (|\psi_j\rangle - |\tilde{\psi}_j\rangle) \langle \tilde{p_j}|\tilde{\phi}_j\rangle \,. \tag{2.12}$$

The principle of the PAW method is shown in Figure 2.2. The full single-electron wavefunction ϕ_j is replaced by a smooth pseudo-wavefunction $|\tilde{\phi}_j\rangle$. The pseudo- and all-electron wavefunctions are identical in the interstitial region, while within the augmentation spheres the full wavefunction is reconstructed from all-electron, atom-centered partial waves ψ_j. The partial waves ψ_j are solutions of the Schrödinger equation for a reference atom and are products of radial functions and spherical harmonics. The pseudo partial waves $|\tilde{\psi}_j\rangle$ correspond to $|\tilde{\phi}_j\rangle$ inside the pseudopotential and must be subtracted from the pseudo-wavefunction. The projector functions $\tilde{p}_j$ are used to bridge the pseudofunctions to the all-electron wavefunctions, they are smooth functions that vanish outside the augmentation region [44].

Another commonly used approximation is the frozen-core approximation, in which core electrons are kept fixed and only valence electrons are treated explicitly. This approximation is justified by the strong localization of core states and the fact that chemical bonding and most macroscopic properties are governed by the valence electrons, while the core electrons mainly provide a static screening. The number of valence electrons treated explicitly can be adjusted and should be tested depending on the specific problem.

2.2 Many-body perturbation theory

The complicated many-body problem described by the Schrödinger equation can be simplified by considering the solution for a system of non-interacting particles with the external potential added as a perturbation. This is the philosophy of the many-body perturbation theory (MBPT) methods. In practice, the reference solution is often given by DFT, and electron-electron interactions beyond the mean-field level are incorporated through perturbative corrections.

The primary goal of MBPT is to describe excited-state phenomena, such as quasiparticle energies and optical excitations, which are not fully captured by ground state DFT. In contrast to wavefunction-based approaches, MBPT is formulated in terms of Green's functions. The central quantity is the one-particle Green's function, which contains information about the electronic structure and excitation spectrum of the system. Physically, the Green's function can be interpreted as propagation an electron added to (or removed from) the ground state ψ_0 between two points in space and time. For this reason, Green's functions are often referred to as propagators. They provide direct access to quantities such as quasiparticle energies, lifetimes, and spectral functions. Furthermore, higher-order Green's functions allow for the treatment of electron-hole (e-h) interactions, which lead to the description of excitonic effects within the Bethe-Salpeter equation framework. A more detailed formal discussion of Green's functions and their role in MBPT is provided in Appendix A.

Finally, it is usually assumed that the external perturbation, such as an electromagnetic field, is weak and treated using linear response theory. The Green's functions and response functions are therefore defined for the unperturbed system, with the external potential introduced as a perturbation to calculate observable quantities, such as absorption spectra.

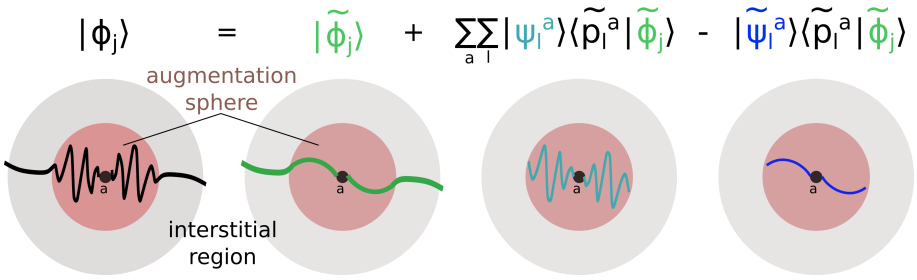

Figure 2.2: Illustration of the PAW wavefunction for an atom a, decomposed into the augmentation and interstitial regions.

2.2.1 Dyson equation

Changes in the wavefunction caused by an external perturbing potential can be described using the Lippmann-Schwinger equation [45]. In this representation, the Schrödinger equation can be written in the integral form in terms of the free-particle Green's function and the scattering potential as

$$\Psi(\mathbf{r},t) = \psi_0(\mathbf{r},t) + \int_{-\infty}^{t}\int G_0(\mathbf{r},t;\mathbf{r}',t')V(\mathbf{r}',t')\Psi(\mathbf{r}',t')\,d^3\mathbf{r}'dt'. \tag{2.13}$$

Iterative substitution of the full wavefunction Ψ on the right hand side of Equation 2.13 generates a perturbative expansion known as the Born series, which describes the propagation of a particle undergoing successive scattering events due to the potential V. By repeated substitution of Ψ one obtains a geometric series, which can be rewritten as

$$G = G_0 + G_0VG, \tag{2.14}$$

which is the famous Dyson equation for Green's function [46]. In interacting systems, the full response can be expressed in terms of the non-interacting Green's function G_0 via the Dyson equation. In interacting many-body systems, the potential V is replaced by the self-energy operator Σ, which accounts for exchange and correlation effects beyond the noninteracting approximation.

2.2.2 Excitation energies

The non-interacting Green's function G_0 describes the propagation of a free particle. In order to describe realistic excitations, we have to explicitly introduce particle addition and removal. A convenient way of introducing the change in the particle count is available in second quantization, which is widely used for many-body problems. It provides a systematic way to describe systems of many identical particles and automatically enforces quantum statistics and particle indistinguishability. In many-body systems, the number of particles may be large or even variable, and explicitly antisymmetrizing or symmetrizing wavefunctions in first quantization quickly becomes impractical. Second quantization shifts the focus from many-particle wavefunctions to operators that create and annihilate particles in single-particle states, which naturally fulfill the Pauli exclusion principle. This formalism makes it straightforward to describe particle addition and removal, whose propagation through the interacting system accounts for collective excited states and all many-body processes [45–47].

The action of the creation operator $c^\dagger$ on the vacuum state $|0\rangle$ creates a particle in an eigenstate $||j\rangle$, $c_j^\dagger|0\rangle = |j\rangle$, and the annihilation operator c removes a particle, $c_j|j\rangle = |0\rangle$. In the position representation, field operators can be defined as expansions over a complete set of single-particle wavefunctions ϕ_j, as

$$\hat{\psi}^\dagger(\mathbf{r}) = \sum_j \phi_j(\mathbf{r})c_j^\dagger, \tag{2.15}$$

$$\hat{\psi}(\mathbf{r}) = \sum_j \phi_j(\mathbf{r})c_j. \tag{2.16}$$

The field operators represent addition or removal of a particle at position $\mathbf{r}$ from whatever single-particle state j weighted by their amplitudes at that position. The field operators are the sums

of all possible ways to add or remove a particle to the system at position $\mathbf{r}$ through any of the basis states ϕ_j.

The Green's function formalism can be naturally expressed in terms of field operators. To describe propagation in time, one introduces the time-ordering operator, which ensures that operators are ordered according to their time arguments [48]. The time-ordered one-particle Green's function is defined as the expectation value of a time-ordered product of field operators in the many-body ground state, as

$$iG(\mathbf{r},t,\mathbf{r}',t') = \langle\Psi_0^N|T[\hat{\psi}(\mathbf{r},t)\hat{\psi}^\dagger(\mathbf{r}',t)]|\Psi_0^N\rangle \tag{2.17}$$

$$= \theta(t-t')\,\langle\Psi_0^N|\hat{\psi}(\mathbf{r},t)\hat{\psi}^\dagger(\mathbf{r}',t)|\Psi_0^N\rangle - \theta(t'-t)\,\langle\Psi_0^N|\psi^\dagger(\mathbf{r},t)\hat{\psi}(\mathbf{r}',t)|\Psi_0^N\rangle\,, \tag{2.18}$$

where Ψ_0^N is the exact ground state wavefunction of a system of N-electrons, and T is the time-ordering operator. The first part of the one-body time-ordered Greens function in Equation 2.18, also called the retarded Green's function, is defined for $t > t'$ and describes the propagation of an electron from $\mathbf{r}'$ to $\mathbf{r}$, that was created at time t' and annihilated at time t. It gives a probability of finding an electron at $(\mathbf{r},t)$ if an electron was created at $(\mathbf{r}',t')$. Similarly, when $t < t'$, the second part in Equation 2.18, also called the advanced Green's function, can be interpreted as the propagator of a hole. In the presence of an external potential, single-particle Green's functions describe the propagation of particles and holes that interact with the environment via a series of scattering processes defined by the Dyson equation Equation 2.14. Green's functions therefore provide a direct access to the excited-state properties that are not directly available in ground state theories such as DFT.

In order to gain an explicit dependence on the excitation energies, one introduces complete sets of many-body eigenstates of the systems with N+1 and N–1 particles. By inserting the closure relation $\sum_j |\Psi_j\rangle\langle\Psi_j| = 1$ into Equation 2.18 and Fourier transforming from the time domain to the energy domain, we obtain the Lehmann representation of the Green's function

$$G(\mathbf{r},\mathbf{r}',\omega) = \sum_j \frac{d_j^{N+1}(\mathbf{r})d_j^{*N+1}(\mathbf{r}')}{\omega - E_j^{N+1} + i\eta} + \sum_j \frac{d_j^{N-1}(\mathbf{r})d_j^{*N-1}(\mathbf{r}')}{\omega - E_j^{N-1} - i\eta}, \tag{2.19}$$

defined using the Dyson orbitals d, which describe overlap of the N and $N \pm 1$ electron states as $d_j^{N-1}(\mathbf{r}) = \langle\Psi_j^{N-1}|\hat{\psi}(\mathbf{r})|\Psi_0^N\rangle$ and $d_j^{N+1}(\mathbf{r}) = \langle\Psi_j^N|\hat{\psi}(\mathbf{r})|\Psi_0^{N+1}\rangle$. Dyson orbitals are effective one-electron wavefunctions associated with the addition or removal of an electron and include all correlation and relaxation effects of the many-body states. The Lehmann representation provides a direct link between the poles of the Green's function and the many-body excitation energies $E_j^{N+1} = \epsilon_j^{N+1} - \epsilon_0^N$ and $E_j^{N-1} = \epsilon_0^N - \epsilon_j^{N-1}$, where ϵ_0 is the the total energy of the ground state and $\epsilon_j^{N\pm1}$ is the total energy of the j-th excited state. The Lehmann representation establishes a direct connection between the Green's function and measurable excitation spectra, such as those observed in photoemission and inverse photoemission experiments [47, 48]. The Lehmann representation is exact for interacting many-body systems and forms the foundation of many-body perturbation theory methods such as the GW approximation.

The reformulation of the many-body problem in terms of Green's functions requires solving the corresponding equation of motion [45, 48, 49]. However, the equation of motion of single Green's function leads to a higher order, two-body Green's function, the time variation of which leads to a three-body problem and so on. This property is called hierarchy of Green's function, which makes the differential problem impossible to solve exactly.

The perturbation theory can be used to truncate the hierarchy of G by introducing a fictitious external potential U. The functional derivative of a single particle Green's function with respect to U, using the notation $(\mathbf{r}, t) = 1$, $(\mathbf{r}', t') = 2$ etc., results in

$$\frac{\partial G(1,2)}{\partial U(3)} = -G(1,3;2,3^+) + G(1,2)G(3,3^+), \tag{2.20}$$

where 3^+ represents infinitesimally larger time. The potential U is a mathematical tool to remove the two-body term and is set to zero after the calculation. As shown in Appendix B, the solution of the equation of motion of the one-particle Green's function leads to the expression

$$\left[i\frac{\partial}{\partial t} - \hat{h_0}(\mathbf{r}) - V_H(1)\right] G(1,2) - \int \Sigma(1,3)G(3,2)d3 = \delta(1,2), \tag{2.21}$$

with the non-interacting Hamiltonian h_0, composed of the kinetic energy and the external potential. The exchange-correlation interactions beyond the Hartree term are described by the non-local and frequency dependent self-energy operator Σ. The Equation 2.21 is a self-contained equation that can be expressed in terms of the Dyson equation $G = G_0 + G_0\Sigma G$.

By rewriting Equation 2.21, the self-energy [50] can be expressed as

$$\Sigma(1,2) = i\int W(3,1^+)G(1,4)\Gamma(4,2;3)d3d4, \tag{2.22}$$

where Γ is the three body operator called irreducible vertex function that contains complex functional derivative of the self-energy with respect to the Green's function, and W is the screened Coulomb interaction. Here W is screened via the dielectric function

$$\begin{aligned} W(1,2) &= \int \epsilon^{-1}(1,3)v_c(3,2)d3 = v_c(1,2) + \int v_c(1,3)\chi(3,4)v_c(4,2)d3d4 \\ &= v_c(1,2) + \int v_c(1,3)P(3,4)W(4,2)d3d4, \end{aligned} \tag{2.23}$$

where W and ϵ^{-1} are time (or frequency) dependent quantities. These relations can be in the matrix representation written as $\epsilon^{-1} = 1 + v_c\chi = (1 - v_cP)^{-1}$ and $\chi = P + Pv_c\chi$, where $v_c(1,2) = \delta(t_1 - t_2)\frac{1}{|\mathbf{r}_1 - \mathbf{r}_2|}$ is the Coulomb interaction, χ is the reducible polarizability and P in the irreducible polarizability. The irreducible polarizability is defined as the variation of the density due to the total potential.

The equations are in principle exact if the interacting Green's function and the vertex function are known. However, in practice the solution of the many-body problem has to be approximated. A commonly used approximation is the GW method, which was employed in this thesis as well.

2.2.3 GW approximation

The equations for G, W, Γ, P and Σ defined in the previous section form a self-consistent set known as Hedin equations [51], which are graphically represented as a pentagram, as shown in Figure 2.3. The self-energy and the vertex function contain functional derivatives of the Green's function and are difficult to be evaluated. One of the most widely used simplification is the GW method, in which the self-energy is approximated as $\Sigma = iGW$, by setting the vertex function to one.

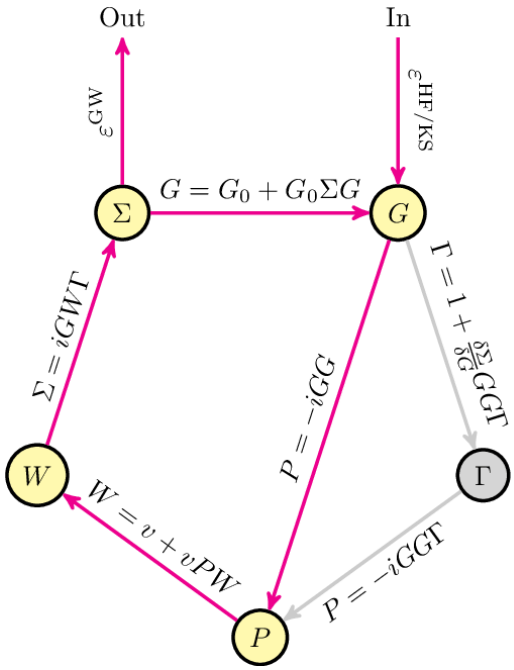

Figure 2.3: Hedin's pentagram and the GW approximation [53].

In practical GW calculations, one typically begins with a non-interacting Green's function G_0, constructed from the eigenvalues and eigenfunctions obtained within a mean-field ground state framework, such as Kohn-Sham DFT. In the frequency domain, the non-interacting Green's function can be expressed as a sum over all occupied and unoccupied single-particle states, such as

$$G_0(\mathbf{r_1}, \mathbf{r_2}, \omega) = \sum_j \frac{\phi_j^{KS*}(\mathbf{r_1})\phi_j^{KS}(\mathbf{r_2})}{\omega - \epsilon_j \pm i\eta}, \tag{2.24}$$

with poles at the KS eigenvalues ϵ_j. The Lehmann representation of the non-interacting Green's functions can be expressed using DFT or other ground state orbitals instead of the Dyson orbitals. Similarly, the polarizability within the random phase approximation (RPA) can be written in terms of G_0. The free-particle irreducible polarizability becomes $P_0 = -iG_0G_0 = \chi_0$. Following Equation 2.23, the screened Coulomb interaction W becomes $W_0 = v_c + v_c\chi_0 v_c = v_c + v_c P_0 W_0$, and the self-energy is written as $\Sigma = iG_0W_0$.

The self-energy contains exchange and correlation parts. The exchange part corresponds to the Hartree-Fock exchange and can be written as $\Sigma_x = iG_0v_c$. The correlation part arises from the dynamical screening and is associated with the difference between the screened and bare interactions, which writes $\Sigma_c = iG_0(W - v_c)$. Physically, the exchange term represents first-order exchange processes, while the correlation term accounts for higher-order screening processes and contains both bubble and ladder diagrams summed by the Dyson equation. By replacing Σ_{xc} with Σ_x we obtain the Hartree-Fock approximation, while by replacing the self-energy with the local exchange-correlation potential we obtain the definition of DFT. Therefore, the GW approximation can be viewed as a dynamically screened generalization of the Hartree-Fock theory [52].

As shown in Figure 2.3, the GW self-consistency can stop after performing a single circle, which is called a single-shot G_0W_0 method. After this first cycle, G, W or both can be updated

to continue the calculation, which leads to self-consistent GW solution.

The screened interaction W describes the bare Coulomb interaction modified by the response of the electronic system. When an electron or a hole is added to the system, the surrounding charge density rearranges, which reduces their interaction with the surrounding charges. The screened interaction is weaker than the bare Coulomb potential. The screened particles, or so called quasiparticles, mimic the excitations in interacting many-body systems, where added or removed electrons induce local changes of density.

Quasiparticle energies are obtained by solving an effective eigenvalue problem in which the xc potential is replaced by the non-local, energy-dependent self-energy. The quasiparticle equation can be formulated based on Equation 2.21 and the Lehmann representation as

$$\hat{h}^{KS}(\mathbf{r})\phi_j(\mathbf{r}) + \int \Sigma(\mathbf{r},\mathbf{r},\omega{=}\epsilon_j)\phi_j(\mathbf{r}')d^3\mathbf{r} = \epsilon_j\phi_j(\mathbf{r}), \tag{2.25}$$

where $\hat{h}^{KS}$ is the KS Hamiltonian. The self-energy is evaluated at energies that are at the same time solution of the eigenvalue problem in Equation 2.25. After multiplying by $\langle\phi(\mathbf{r})|$ and integrating, this non-linear equation leads to the expression for the GW quasiparticle energy, which is defined as

$$\omega = \epsilon_j^{KS} + \langle\phi_j(\mathbf{r})|\Sigma(\mathbf{r},\mathbf{r}',\omega) - V_{xc}^{KS}(\mathbf{r})|\phi_j(\mathbf{r})\rangle\,, \tag{2.26}$$

where V_{xc}^{KS} is the DFT xc potential. The non-linear quasiparticle equation Equation 2.26 has multiple solutions due to the frequency dependence of the self-energy. The physically relevant quasiparticle corresponds to the solution with the largest spectral weight, while additional solutions correspond to satellite features associated with plasmon excitations and other many-body effects. There are various methods to determine which solution corresponds to the quasiparticle energy. Perhaps the simplest method is the linearization via a first order Taylor expansion of the self-energy around the KS eigenvalues. This method assumes a small difference between the KS and quasiparticle energies and evaluates only a single root of the quasiparticle equation. The GW energies can be expressed as

$$\epsilon_j^{GW} = \epsilon_j^{KS} + Z_j\mathrm{Re}\left[\langle\phi_j(\mathbf{r})|\Sigma(\mathbf{r},\mathbf{r}',\epsilon_j^{KS}) - V_{xc}^{KS}(\mathbf{r})|\phi_j(\mathbf{r})\rangle\right], \tag{2.27}$$

where Z_j is the renormalization factor. More details can be found in Appendix B. The GW corrected KS eigenenergies from Equation 2.27 open the bandgap and modify the DFT band structure.

In practice, Green's functions are not stored explicitly but the polarizability is calculated directly from the KS energies and orbitals in reciprocal space and energy domain, as

$$\chi_0^{\mathbf{G},\mathbf{G}'}(\mathbf{q},\omega) = \frac{2}{\Omega_{BZ}}\sum_{c}^{unocc}\sum_{v}^{occ}\sum_{\mathbf{k}} f_{v\mathbf{k}+\mathbf{q}}(1-f_{c\mathbf{k}})\frac{\langle\phi_{c\mathbf{k}}|e^{i\mathbf{G}\mathbf{r}}|\phi_{v\mathbf{k}+q}\rangle\,\langle\phi_{v\mathbf{k}+\mathbf{q}}|e^{i\mathbf{G}'\mathbf{r}'}|\phi_{c\mathbf{k}}\rangle}{\epsilon_{v\mathbf{k}+\mathbf{q}} - \epsilon_{c\mathbf{k}} + \omega \pm i\eta}, \tag{2.28}$$

which allows to calculate the screened coulomb interaction ($W = v_c\epsilon^{-1} = v_c(1-\chi_0 v_c)^{-1}$). A convolution of W with G_0 gives the self-energy that is used to obtain the quasiparticle energies.

The calculation of the irreducible polarizability is often the bottle neck of the GW calculation as it sums over all occupied and unoccupied states. The large number of unoccupied (conduction) bands is necessary, which makes the GW calculations difficult to solve. Therefore, the self-energy is evaluated for a smaller subset of bands near the the band gap. The parameters that must be carefully tested for convergence include the energy cutoff, which determines the number of

G-vectors and the size of the dielectric matrix, the number of the electronic bands in the self-energy summation, the number of k-points and the number of frequency points used to compute the screening. An example of a convergence test for calcite is shown in Figure 2.4.

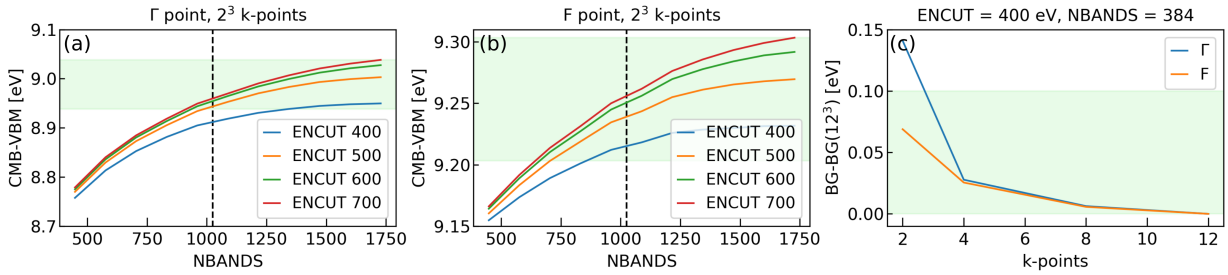

Figure 2.4: Convergence test of the GW bandgap energy of calcite as a function of the (a–b) number of empty bands at the Γ and F points, and (c) the k-point sampling [54].

Overall, the GW method is primarily used to correct mean-field band structures and obtain more accurate quasiparticle energies, particularly band gaps. The Green's functions naturally describe charged excitations, where the number of electrons is not conserved. This makes the GW method directly comparable to photoemission and inverse photoemission experiments. In this framework, the self-energy is generally complex and frequency dependent, where the real part shifts the quasiparticle energies and the imaginary part determines the finite lifetimes, while the screened interaction W is both time (or frequency) dependent and non-local [52].

2.2.4 Bethe-Salpeter equation

The GW method describes the charged excitations of a many-body system in terms of the propagation of a single added or removed electron (or hole), as represented by the one-particle Green's function. However, neutral excitations that conserve number of electrons require description of correlated electrons and holes. These processes are described by the two-particle Green's function, which can be obtained as the functional derivative of the one-particle Green's function with respect to an external perturbation, as shown in Equation 2.20. Detailed information about the BSE formalism can be found in Appendix C.

The BSE kernel is commonly separated into two contributions. One arises from the Hartree term and describes the bare Coulomb interaction, while the exchange-correlation part yields another due to the screened interaction W. Using the GW solution to define the self-energy, the four point Hartree xc kernel leads to an effective e-h interaction of the form $\Xi = v_c - W$. Hence, the two-particle BSE correlation function can be written as

$$\begin{aligned} &L(1,2,3,4) = \\ &L_0(1,2,3,4) + L_0(1,2,5,6)[v_c(5,7)\delta(5,6)\delta(7,8) - W(5,6)\delta(5,7)\delta(6,8)]L(7,8,3,4), \end{aligned} \tag{2.29}$$

or in the typical Dyson equation-like form $L = L_0 + L_0 \Xi L$ for short. Here v_c describes the repulsive e-h interaction, which corresponds to the exchange term. The term containing the screened interaction W provides an attractive direct interaction responsible for exciton formation.

In practice, L_0 is typically approximated using the non-interacting Green's functions, i.e. $L_0 = -iG_0G_0$. BSE calculations often start from the GW solution in order to use a corrected band structure and to open the band gap by replacing the KS energies with the quasiparticle

eigenvalues in Equation 2.24. Furthermore, the screened interaction W is considered in the static approximation evaluated at $\omega = 0$, which simplifies the BSE kernel.

Since the full four-coordinates equation for L is difficult to solve, the problem is projected onto a basis of single-particle transitions between valence and conduction states, which defines the so-called transition space. In this basis, the Bethe-Salpeter equation becomes an effective eigenvalue problem

$$H_{exc}X_\lambda = E_\lambda X_\lambda \tag{2.30}$$

where E_λ and X_λ are excitonic eigenvalues and eigenfunctions. This equation can be written in the matrix notation as

$$\begin{pmatrix} A & B \\ B^* & A^* \end{pmatrix} \begin{pmatrix} X_\lambda \\ Y_\lambda \end{pmatrix} = E_\lambda \begin{pmatrix} 1 & 0 \\ 0 & -1 \end{pmatrix} \begin{pmatrix} X_\lambda \\ Y_\lambda \end{pmatrix}. \tag{2.31}$$

The kernel matrix elements are in practice expressed in the single-electron basis. The matrices A describe the resonant and anti-resonant transitions between the occupied and unoccupied states. They define creation and annihilation of interacting electron-hole pairs or excitons. The matrices B describe coupling between exciting resonant and deexciting anti-resonant terms. The matrices A contain dominant terms and are related to absorption processes, therefore the B matrices are neglected within the Tamm-Dancoff approximation (TDA), which is usually a good approximation for extended systems. The use of TDA and real quasiparticle energies ensures that the Hamiltonian becomes a Hermitian operator and the eigenvalue equation is simplified to

$$AX_\lambda = E_\lambda X_\lambda. \tag{2.32}$$

As a consequence, intrinsic exciton lifetime effects are neglected. These effects originate from the imaginary part of the quasiparticle self-energy and from dynamical screening, which are not included in the standard static BSE framework.

BSE calculations require a ground state solution to obtain orbitals and single-particle energies. A GW calculation is then performed to obtain the quasiparticle corrections and the screened Coulomb interaction, from which the BSE excitonic matrix equation can be built. Diagonalization of the excitonic Hamiltonian leads to the exciton energies and wavefunctions, which can be used to compute optical spectra. The excitonic wavefunction can be written in the basis of KS orbitals as

$$\Psi(\mathbf{r}_e, \mathbf{r}_h) = \sum_{cv\mathbf{k}} X_\lambda^{cv\mathbf{k}} \psi_{c\mathbf{k}}(\mathbf{r}_e)\psi^*_{v\mathbf{k}}(\mathbf{r}_h), \tag{2.33}$$

where r_e and r_h are the electron and hole coordinates and $X_\lambda^{cv\mathbf{k}}$ are the exciton amplitudes.

The convergence parameters important for BSE calculations are the number of occupied and unoccupied bands, the maximum excitation energy, and the k-points sampling. An example of the BSE spectrum convergence for calcite is shown in Figure 2.5. The sensitivity to the number of bands included in the calculation is strongly system-dependent. In the case of well-behaved excitons that are localized around a single k-point and involve a small number of valence and conduction bands, the convergence of the exciton peaks is typically fast. The case of calcite is different since excitons are delocalized over the first BZ and various bands are involved in the excitations. The number of the bands determines up to which energy a reliable spectrum is obtained, therefore a large number of bands must be included. Furthermore, the exciton binding energy is sensitive to the k-mesh density and converges rather slowly, hence highly accurate binding energies require very dense k-meshes.

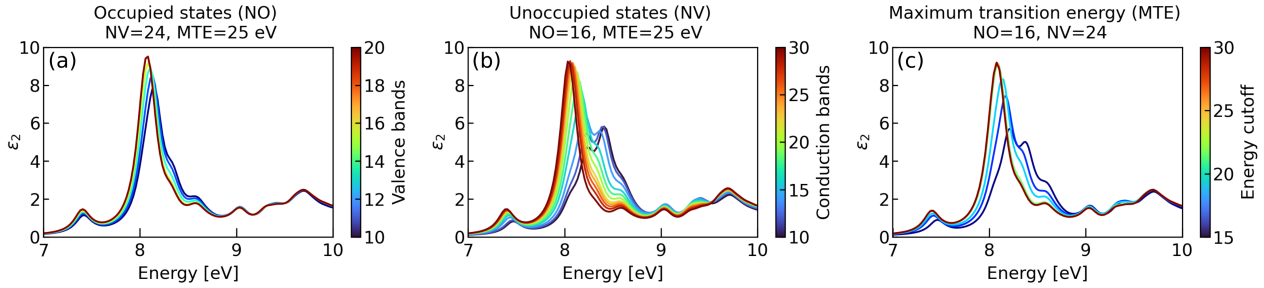

Figure 2.5: Convergence test of BSE spectra for calcite optical spectrum [54], with respect to (a) number of occupied states, (b) number of virtual states, and (c) the maximum transition energy.

2.3 Dielectric response

We describe the optical properties of materials, such as the refractive index, absorbance, reflectance, and optical conductivity, in terms of the complex dielectric function $\epsilon(\omega)$. Within linear response, the dielectric function is a material property that relates the electric displacement field to the electric field, $D(\omega) = \epsilon(\omega)E(\omega)$ [55]. The macroscopic dielectric function can also be defined as the way in which the system responds to an applied external potential $v_{tot} = \epsilon^{-1}v_{ext}$, where the total potential is given by the sum of the external and induced potentials, $v_{tot} = v_{ext} + v_{ind}$. We are interested in the response to an external probe and therefore define response functions that relate the induced change in the density to the external field. The reducible polarizability χ and the irreducible polarizability P are defined as

$$\delta n = \chi v_{ext} \tag{2.34}$$

$$\delta n = P v_{tot}, \tag{2.35}$$

where n is the electron density. The dielectric function is a macroscopic quantity, but on the scale of the unit cell, the external field introduces local rearrangements of charge, also known as local-field effects.

First principles calculations allow for the calculation of the microscopic dielectric function via the non-interacting reducible susceptibility, given by

$$\chi^0_{\mathbf{G}\mathbf{G}'}(\mathbf{q},\omega) = \sum_{i,j}(f_i - f_j)\frac{\langle\phi_j|e^{i(\mathbf{q}+\mathbf{G})\mathbf{r}}|\phi_i\rangle\,\langle\phi_i|e^{i(\mathbf{q}+\mathbf{G}')\mathbf{r}}|\phi_j\rangle}{\epsilon_i - \epsilon_j - \omega - i\eta}, \tag{2.36}$$

where f are occupation functions. This expression is known as the Adler-Wiser formula [56,57], and describes how an external perturbation at one point in space induces a density response at another point.

Within the independent-particle approximation (IPA), local-field effects are completely ignored by identifying the macroscopic dielectric function with the head of the dielectric matrix, i.e. $\mathbf{G} = \mathbf{G}' = 0$ [58]. The imaginary part of the macroscopic IPA dielectric function becomes

$$\epsilon_2^{M,IPA} = 2\frac{4\pi}{\Omega_{BZ}}\lim_{q\to 0}\frac{1}{\mathbf{q}^2}\sum_{c,v,\mathbf{k}}\mathrm{Im}\left(\frac{|\,\langle\phi_{c,\mathbf{k}+\mathbf{q}}|e^{i\mathbf{q}\mathbf{r}}|\phi_{v,\mathbf{k}}\rangle\,|^2}{\epsilon_{c\mathbf{k}+\mathbf{q}} - \epsilon_{v\mathbf{k}} - \omega - i\eta}\right), \tag{2.37}$$

which is basically the Fermi golden rule for absorption.

At the level of the random-phase approximation (RPA), local-field effects arise from changes in the Hartree potential induced by an external perturbation. The RPA dielectric function can be expressed via the Dyson equation by approximating the interacting irreducible polarizability with χ^0. The RPA microscopic dielectric function in reciprocal space is defined as

$$\epsilon^{-1}_{\mathbf{GG'}}(\mathbf{q},\omega) = \delta_{\mathbf{GG'}} + v_{\mathbf{GG'}}(\mathbf{q})\chi^0_{\mathbf{GG'}}(\mathbf{q},\omega), \tag{2.38}$$

and the macroscopic dielectric function is obtained from the head of the inverse matrix,

$$\epsilon^{M,RPA}(\mathbf{q},\omega) = \lim_{q\to 0} \frac{1}{\epsilon^{-1}_{00}(\mathbf{q},\omega)}. \tag{2.39}$$

The difference between the IPA and RPA expressions arises because, in the case of RPA, the macroscopic dielectric function corresponds to the $\mathbf{G} = \mathbf{G'} = 0$ element of the inverse microscopic dielectric matrix. This element depends on all matrix elements of the dielectric matrix and therefore cannot be obtained by simply inverting the head of the dielectric matrix, as is done in the IPA approximation.

The dielectric function calculated using the BSE solution has the following form

$$\epsilon_2^{M,BSE}(\omega) = 2\lim_{q\to 0} v_c(\mathbf{q}) \sum_{\lambda} \mathrm{Im} \left| \frac{\sum_{c,v,\mathbf{k}} \langle \phi_{v,\mathbf{k}-\mathbf{q}} | e^{-i\mathbf{qr}} | \phi_{c,\mathbf{k}} \rangle \, X_\lambda^{cv\mathbf{k}}}{E_\lambda - \omega - i\eta} \right|^2 . \tag{2.40}$$

This expression includes electron-hole interactions and excitonic effects [59]. The sum in the numerator of Equation 2.40 defines the oscillator strength of an exciton λ and describes the probability of optical transitions. The BSE eigenstates redistribute spectral weight toward lower energies, which typically produces a red shift of the optical spectrum. The BSE optical spectrum includes local-field effects through the electron-hole exchange interaction, which mixes transitions with different microscopic spatial character. The screened interaction W, which is usually computed within the RPA as a part of the GW calculation.

2.3.1 Ionic dielectric response

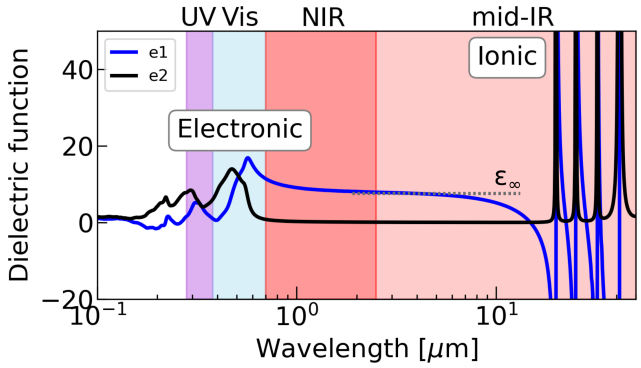

Figure 2.6: Full dielectric function of α-Fe_2O_3 with ionic and electronic contributions. The UV, Vis, NIR and mid-infrared (mid-IR) ranges are highlighted.

The ionic contribution to the dielectric response dominates in the IR spectrum range and is related to the lattice polarizability and absorbance. In order to obtain the optical spectrum we

need to calculate the phonon vibrational energies and eigendisplacements [60]. The equation of motion for an atom i writes $F_i = M_i a_i$, where F is the force, M_i is the atomic mass and a_i is the acceleration. According to the Hellmann-Feynman theorem, the force is defined as the negative partial derivative of the total energy with respect to the atomic displacement. The energy of a system with atomic positions slightly displaced from equilibrium can be expressed as a Taylor expansion around the ground state configuration. The truncation of the series at the quadratic term leads to the harmonic approximation of the lattice vibration spectrum. The phonon modes then define the absorption energies in the IR range and the location of the dielectric function peaks.

In practice the phonon modes can be calculated using the finite differences method [61], or density-functional-perturbation theory (DFPT) [60]. In the finite differences method, atoms are displaced along each Cartesian direction at least twice and the ground state is recomputed for every displacement. The calculated energies and displacements are then used to calculate forces and the dynamical matrix. On the other hand, instead of displacing atoms explicitly, DFPT calculates the first-order change in the electron density and potential due to infinitesimal atomic displacements. Further information about the derivation of the ionic dielectric function can be found in Appendix D.

Various optical functions can be obtained from the dielectric function, for example the complex refractive index N=n+ik, reflecrance R and absorption coefficient α are given by

$$n(\omega) = \left[\frac{\sqrt{\epsilon_1^2 + \epsilon_2^2} + \epsilon_1}{2}\right]^{\frac{1}{2}}, \tag{2.41}$$

$$k(\omega) = \left[\frac{\sqrt{\epsilon_1^2 + \epsilon_2^2} - \epsilon_1}{2}\right]^{\frac{1}{2}}, \tag{2.42}$$

$$R(\omega) = \frac{(n-1)^2 + k^2}{(n+1)^2 + k^2}, \tag{2.43}$$

$$\alpha = \frac{4\pi k}{\lambda}. \tag{2.44}$$

The full dielectric function is obtained by the addition the electronic and ionic contributions, as shown in Figure 2.6 for α-Fe_2O_3. It is obvious that the electronic polarization is responsible for the absorption if the UV-Vis regions and above. The electronic dielectric constant ϵ_∞ is defined as the asymptote of the plateau between the electronic and ionic ranges. The lattice polarization is active in the IR spectral range. By establishing an accurate theoretical description of the optical response, this work provides the foundation for engineering cement and concrete phases with tailored photonic and thermal-radiative functionalities.

2.4 Mie scattering

Concrete-based photonic materials can be produced by incorporating nanoparticle additives. In order to investigate this option, we study the size-dependent interaction with light, which can be studied using classical Mie theory [2,62]. Mie theory is a rigorous electromagnetic solution of Maxwell's equations that describes the reflection, refraction, diffraction, and absorption of light by individual spherical particles embedded in a homogeneous medium. It is often used as a first

approach to describe the scattering, absorption and extinction of light. Mie theory has been shown as an accurate method for description of optical properties of oxide nanoparticles [2].

To bridge the computed dielectric functions with measurable optical variables, we employed Mie theory [2, 62, 63] that accounts for light-matter interactions at the particle level. The Mie coefficients a_n and b_n for the spherical particles are defined as

$$a_n(\lambda) = \frac{N_p^2[\rho_m j_n(\rho_m)]' j_n(\rho_p) - N_m^2[\rho_p j_n(\rho_p)]' j_n(\rho_m)}{N_p^2[\rho_m h_n(\rho_m)]' j_n(\rho_p) - N_m^2[\rho_p j_n(\rho_p)]' h_n(\rho_m)}, \tag{2.45}$$

$$b_n(\lambda) = \frac{[\rho_m j_n(\rho_m)]' j_n(\rho_p) - [\rho_p j_n(\rho_p)]' j_n(\rho_m)}{[\rho_m h_n(\rho_m)]' j_n(\rho_p) - [\rho_p j_n(\rho_p)]' h_n(\rho_m)}, \tag{2.46}$$

where N_p and N_m are the complex refractive indices of the particle and medium, that enter into the size parameters $\rho_p = 2\pi r N_p/\lambda$ and $\rho_m = 2\pi r N_m/\lambda$, with the sphere radius r and the wavelength of the scattered light λ. The coefficients are defined in terms of spherical Bessel functions j_n and spherical Hankel functions h_n of the first kind and order n, where the apostrophe denotes the first derivative with respect to the argument. The Mie scattering efficiency is given by

$$Q_{sca} = \frac{2}{\rho_m^2} \sum_{n=1}^{o} (2n+1)(|a_n|^2 + |b_n|^2), \tag{2.47}$$

and the extinction efficiency by

$$Q_{ext} = \frac{2}{\rho_m^2} \sum_{n=1}^{o} (2n+1)\mathrm{Re}(a_n + b_n), \tag{2.48}$$

where o is the order of the Mie sum. The extinction coefficient is defined as the sum of scattering and absorption $Q_{ext} = Q_{sca} + Q_{abs}$.

The angular dependence of scattered intensity is defined by the Mie phase function, which is a function of the polar scattering angle θ and the azimuthal scattering angle ϕ as

$$p(\theta, \phi) = \frac{|S_1|^2 + |S_2|^2}{2}, \tag{2.49}$$

and is normalized as

$$\frac{1}{4\pi} \int_0^{2\pi} \int_0^{\pi} p(\theta, \phi) \sin(\theta) \mathrm{d}\theta \mathrm{d}\phi = 1. \tag{2.50}$$

The amplitude functions are defined as

$$S_1(\cos\theta) = \sum_{n=1}^{o} \frac{2n+1}{n(n+1)} [a_n \pi_n(\cos\theta) + b_n \tau_n(\cos\theta)], \tag{2.51}$$

$$S_2(\cos\theta) = \sum_{n=1}^{o} \frac{2n+1}{n(n+1)} [a_n \tau_n(\cos\theta) + b_n \pi_n(\cos\theta)]. \tag{2.52}$$

The angular functions satisfy the recurrence relations

$$\pi_n(\cos\theta) = \frac{2n-1}{n-1} \cos(\theta) \pi_{n-1} - \frac{n}{n-1} \pi_{n-2}, \tag{2.53}$$

$$\tau_n(\cos\theta) = n \cos(\theta) \pi_n - (n+1) \pi_{n-1}, \tag{2.54}$$

with $\pi_0 = 0$ and $\pi_1 = 1$.

Mie theory can be extended for spherical particles embedded in an absorbing medium [64]. The corresponding coefficients are written as

$$c_n = \frac{N_p[\rho_m j_n(\rho_m)]'\rho_m h_n(\rho_m) - N_p[\rho_m h_n(\rho_m)]'\rho_m j_n(\rho_m)}{N_p[\rho_p j_n(\rho_p)]'\rho_m h_n(\rho_m) - N_m[\rho_m h_n(\rho_m)]'\rho_p j_n(\rho_p)}, \tag{2.55}$$

$$d_n = \frac{N_p[\rho_m h_n(\rho_m)]'\rho_m j_n(\rho_m) - N_p[\rho_m j_n(\rho_m)]'\rho_m h_n(\rho_m)}{N_p[\rho_m h_n(\rho_m)]'\rho_p j_n(\rho_p) - N_m[\rho_p j_n(\rho_p)]'\rho_m h_n(\rho_m)}, \tag{2.56}$$

where subscripts m and p denote the medium and particle, respectively. The scattering, absorption, and extinction efficiencies in an absorbing medium are then expressed as

$$Q^m_{sca} = \frac{2\eta k_m}{r n_m[1 + (\eta - 1)e^{\eta}]} \sum_{n=1}^{o} (2n + 1)\mathrm{Im}(B_n) \tag{2.57}$$

$$Q^m_{abs} = \frac{2\eta k_m}{r n_m[1 + (\eta - 1)e^{\eta}]} \sum_{n=1}^{o} (2n + 1)\mathrm{Im}(A_n) \tag{2.58}$$

$$Q^m_{ext} = \frac{2\eta k_m}{r n_m[1 + (\eta - 1)e^{\eta}]} \sum_{n=1}^{o} (2n + 1)\mathrm{Im}(A_n + B_n) \tag{2.59}$$

where $\eta = 4\pi r k_m/\lambda$ and $N_m = n_m + ik_m$ is the complex refractive index of the medium. The coefficients A_n and B_n are

$$A_n = \frac{|c_n|^2 \rho_p j_n(\rho_p)[\rho_p j_n(\rho_p)]'^* - |d_n|^2 \rho_p j^*_n(\rho_p)[\rho_p j_n(\rho_p)]'}{2\pi n_p \lambda^{-1}}, \tag{2.60}$$

$$B_n = \frac{|a_n|^2 \rho_m h^*_n(\rho_m)[\rho_m h_n(\rho_m)]' - |b_n|^2 \rho_m h_n(\rho_m)[\rho_m h_n(\rho_m)]'^*}{2\pi n_m \lambda^{-1}}, \tag{2.61}$$

and asterisk denotes the complex conjugate. This formulation generalizes standard Mie theory and reduces to the usual expressions when the refractive index of the medium is real.

2.5 MSTM

Mie theory provides a solution to Maxwell's equations in the single-particle limit and describes the scattering of dispersed particles. In order to compare Mie and multiple-scattering effects, we used the multiple sphere T-matrix (MSTM) method, which allows for the calculation of electromagnetic scattering of aggregates composed of spherical particles [65, 66].

The T-matrix method is a rigorous electromagnetic scattering approach based on the expansion of the incident and scattered fields in vector spherical wave functions. The scattering response of a particle is described by the transition matrix, which relates the expansion coefficients of the incident field to those of the scattered field. The T-matrix depends only on the particle geometry, composition, medium and wavelength, which allows efficient evaluation of scattering properties for different incident-field configurations. The method is particularly well suited for particles with sizes comparable to the wavelength and can be extended to treat aggregates of multiple particles by accounting for multiple-scattering interactions between them.

The T-matrix method is rigorous in the sense that the results are exact up to the truncation of the vector spherical wave-function expansions [65, 66].

In the MSTM approach, each sphere contributes its own scattering response, while electromagnetic coupling between spheres is included through a self-consistent solution of the scattered fields. Translation matrices connect the vector spherical wave functions centered on different spheres, so multiple scattering appears through the repeated coupling of fields between all spheres in the cluster. This formulation enables accurate calculations of near- and far-field optical properties of particle aggregates, including extinction, absorption, and scattering cross sections [65, 66].

2.6 Hapke model

The reflectance and emissivity of powders can be approximated using the Hapke multiple-scattering model [67–70]. The Hapke model relates the optical properties of a particulate medium to its directional reflectance and emissivity and provides an approximate solution to the radiative transfer equation in a semi-infinite medium. The formulation incorporates multiple-scattering effects through approximate analytical functions, such as Chandrasekhar H-function. The single-scattering contribution is treated explicitly, while the multiple-scattering effects are approximated through analytical solutions of the radiative transfer equation based on Chandrasekhar's H-function, which can be interpreted as a two-stream approximation in the isotropic-scattering limit. In this approximation the light propagation directions are separated into upward and downward contributions and the total reflectance is expressed as the sum of diffuse radiation reflected at different depths.

Within the isotropic multiple-scattering approximation (IMSA), the angular dependence of multiple scattering is neglected even when the actual particle scattering is anisotropic. IMSA formulation is based on several assumptions. Diffraction effects arising from closely packed particles are neglected, and scattering is assumed to be isotropic, which is often a reasonable approximation for small, irregular, and randomly oriented particles. Moreover, the single-scattering albedo is determined from the ratio of scattering to extinction efficiencies, which is valid when particle sizes are sufficiently large compared to the wavelength. The Hapke model defines the single-scattering albedo as a function of the complex refractive index and geometric scattering processes, which includes contributions from external reflection and internal scattering processes derived from Fresnel reflection coefficients. In addition, the Hapke single-scattering albedo depends on the volume scattering coefficient, which is an empirical parameter [67, 70, 71].

2.6.1 Emissivity

Because of the limitations of Hapke model, we employ the Hapke-Mie approach, in which the single-particle albedo w and asymmetry factor g are obtained from Mie theory. Since diffraction effects intrinsic to Mie theory are not physically meaningful for closely packed particles, a correction in the form of diffraction subtraction has to be applied [71, 72]. The corrected albedo is then written as

$$w = 2w_{Mie} - 1 = 2\frac{Q_{sca}}{Q_{ext}} - 1, \tag{2.62}$$

where Q_{sca} and Q_{ext} are the Mie scattering and extinction efficiencies. The asymmetry parameter is defined as

$$g = \frac{1}{2}\int_0^{\pi} p(\theta)\sin(\theta)\cos(\theta)\mathrm{d}\theta, \tag{2.63}$$

where $p(\theta)$ is the Mie phase function defined in Equation 2.49 [70]. The Hapke-Mie approach eliminates the need for free parameters and allows the emissivity and reflectance to be modelled using only the material constants n, k and the particle diameter.

The IMSA hemispherical emissivity e_h of a semi-infinite particulate material [68, 70] can be written as

$$e_h = \frac{2\gamma}{\xi + \gamma}, \tag{2.64}$$

with $\gamma = \sqrt{1-w}$ and $\xi = \sqrt{1-gw}$, where w is the single particle albedo and g is the asymmetry parameter. This is a simplified expression for isotropic emissivity modified by the asymmetry parameter to approximately account for anisotropic scattering in realistic particulate emitters, which is valid for optically thick, rough, or particulate surfaces, where multiple scattering and randomization of light directions result in nearly isotropic emission. Our tests showed that the integration of the angle-dependent emissivity yields comparable results to the analytical expression in Equation 2.64.

2.6.2 Reflectance

The simplest expression for Hapke reflectance assumes isotropic scattering $p(\theta) = 1$, which corresponds to an idealized isotropic-scattering approximation. The single-particle reflectance is given by

$$r_1(i, e, s) = \frac{w\mu_i}{4\pi(\mu_i + \mu_e)} p(s), \tag{2.65}$$

where i is the incidence angle, e is the reflected angle, and μ_i and μ_e are their respective cosines. The phase angle s can be expressed as $\cos(s) = \cos(i)\cos(e) + \sin(i)\sin(e)\cos(\phi)$. In the case of normal incidence ($i = 0$) considered here, the phase angle s is equal to the angle e.

Multiple-scattering effects are described by the Ambartsumian-Chandrasekhar H-function [73]. The Hapke approximation to the H-function [67, 69] writes

$$H(\mu) \approx \left[1 - w\mu\left(r_0 + \frac{1-2r_0\mu}{2}\ln\frac{1+\mu}{\mu}\right)\right]^{-1}, \tag{2.66}$$

with the diffuse reflectance r_0 defined as

$$r_0 = \frac{1-\gamma}{1+\gamma}. \tag{2.67}$$

The H-function describes the average scattering of multiple isotropically scattering particles in a semi-infinite particulate slab [70]. The anisotropic Hapke multiple-scattering reflectance has the form

$$r(i, e, s) = \frac{w\mu_i}{4\pi(\mu_i + \mu_e)}[p(s) + H(\mu_e)H(\mu_i) - 1]. \tag{2.68}$$

The hemispherical reflectance is obtained by integrating the Hapke multiple-scattering reflectance as

$$r_h = \frac{1}{\cos(i)}\int_0^{2\pi}\int_0^{\pi/2} r(e, \phi)\cos(e)\sin(e)\mathrm{d}e\mathrm{d}\phi. \tag{2.69}$$

Mie theory predicts a strong forward-scattering lobe, especially for larger non-absorbing particles. This forward lobe is dominated by diffraction and near-forward transmission contributions and most light continues in the same direction. However, Hapke model assumes isotropic diffusion reflectance of light, and a strong forward-scattering overestimates multiple-scattering effects and total reflectance. Within the multiple-scattering approximation, the effect of strong forward scattering can be reduced by using the modified van de Hulst transport albedo w_{tr} [62], defined as

$$w_{tr} = \frac{(1-g)w}{1-gw}. \tag{2.70}$$

The Hapke-Hulst (HH) hemispherical reflectance [62, 74–76] has the analytical form

$$r_{HH}(\mu_i) = \frac{(1-s^2)(1+2\mu_i)}{2(1+2\mu_i s)}\left[1 + \frac{(1-s)\ln(1+2s)}{2s(2\mu_i s-1)} + \frac{\mu_i s(2\mu_i-1)[\ln\mu_i - \ln(1+\mu_i)]}{2\mu_i s-1}\right], \tag{2.71}$$

where s is the similarity parameter, given by $s = \sqrt{1-w_{tr}}$.

In the context of radiative cooling, the goal is to identify materials with high emissivity in the ATW and high reflectance in the solar spectral range. Therefore, the combination of Mie and Hapke models provides a practical framework for designing photonic materials and coatings based on particle size distributions.

2.7 Equations for radiative cooling

The power radiated by a material is given by an integral over a hemisphere of the product of the black body radiation $U_{BB}(T,\lambda)$ and the directional emissivity $e_{Mat}(\theta,\lambda)$

$$P_{Mat} = 2\pi \int_0^{\pi/2}\int_0^{\infty} \sin(\theta)\cos(\theta) U_{BB}(T_{Mat},\lambda) e_{Mat}(\theta,\lambda)\mathrm{d}\theta\mathrm{d}\lambda. \tag{2.72}$$

The atmospheric radiance absorbed by the material is given by

$$P_{Atm} = 2\pi \int_0^{\pi/2}\int_0^{\infty} \sin(\theta)\cos(\theta) U_{BB}(T_{Atm},\lambda) e_{Mat}(\theta,\lambda) e_{Atm}(\theta,\lambda)\mathrm{d}\theta\mathrm{d}\lambda, \tag{2.73}$$

where θ is the angle of radiation, $e_{Atm}(\theta,\lambda)$ is the atmospheric emissivity, defined as $e_{Atm}(\theta,\lambda) = 1 - t(\lambda)^{1/\cos\theta}$, with the atmospheric transmittance in the zenith direction $t(\lambda)$. The black body radiation is by Planck's law defined as

$$U_{BB}(T,\lambda) = \frac{2hc^2}{\lambda^5}\frac{1}{e^{hc/\lambda k_B T}-1}, \tag{2.74}$$

where λ is the light wavelength, T is the temperature, h is the Planck constant, c is the speed of light and k_B is Boltzmann constant [3].

When solar absorption and non-radiative heat exchange are neglected, the net radiative power P_{Rad} corresponds to the theoretical upper bound of the cooling power. Similarly to Equation 2.73, the solar losses are equal to the product of the solar irradiation and the material emissivity, written as

$$P_{Sol} = 2\pi \int_0^{\pi/2}\int_0^{\infty} \sin(\theta)\cos(\theta) I_{Sun}(\lambda) e_{Mat}(\theta,\lambda)\mathrm{d}\theta\mathrm{d}\lambda, \tag{2.75}$$

with the solar irradiance I_{Sun}. Non-radiative losses are proportional to the heat conduction constant h_c and the temperature difference between the material and the surrounding as

$$P_{NR} = h_c(T_{Atm} - T_{Mat}). \tag{2.76}$$

The coefficient of non-radiative losses h_c depends on the weather conditions, especially the speed of wind, and typically equals to 5–20 $\frac{\mathrm{W}}{\mathrm{m^2K}}$.

The absorption of light propagating through matter is described by Beer-Lambert law, defined as

$$I(d) = I_0 e^{-\alpha d}, \tag{2.77}$$

where $I(d)$ is the intensity of light in depth d, I_0 is the initial intensity and α is the absorption coefficient. In the case of single-particle absorbance the parameter d is the diameter and the absorption can be expressed as

$$A_1(d, \lambda) = 1 - R_1(\lambda) - \left((1 - R_1(\lambda)^2) \frac{e^{-\alpha d}}{(1 - e^{-\alpha d} R_1(\lambda))} \right). \tag{2.78}$$

Here $R(\lambda)$ is the single-particle reflectance. This expression assumes internal reflectance.

The relations discussed in this chapter are sufficient to describe the radiative cooling properties of the studied materials in a consistent manner. The combination of first principles calculations, radiative transfer and radiative cooling equations provides a robust and predictive framework for the analysis and design of radiative cooling materials. This combined approach enables the connection between microscopic electronic structure and macroscopic optical and thermal response without the need for empirical material parameters.

Chapter 3

Crystal and electronic structure of cement and concrete phases

In this chapter, we report on the results of structural relaxation and electronic band structures, as well as the GW-corrected fundamental electronic band gaps, for various groups of materials. We compare different exchange-correlation functionals for the ground state calculations of cement and concrete related materials. Firstly, we describe simple cement-forming oxides, followed by typical clinker and cement phases, then hydrated concrete phases, and finally raw minerals, clays, and additives.

3.1 Computational details

For the purposes of this chapter, we employed DFT using a plane-wave basis set in combination with the projector augmented wave (PAW) method [43], as implemented in Vienna *Ab-initio* Simulation Package (VASP) [77,78]. The exchange-correlation potential was approximated using GGA, following the Perdew-Burke-Ernzerhof (PBE) parametrization [40], and the meta-GGA SCAN functional [42]. The first Brillouin zone was sampled using Γ-centered k-meshes, in particular a $6\times6\times6$ mesh for CaO, calcite, TiO_2 and $Ca(OH)_2$, a $2\times2\times2$ mesh for tobermorite 14Å, C3AH, C3A, jennite and ettringite, a $3\times3\times3$ mesh for tobermorite 11Å and C4AF, and a $4\times4\times4$ mesh for the remaining structures. Single-shot G_0W_0 calculations [79] were performed using 500 eV cutoff and 100 frequency points in combination with 400 bands for CaO, 680 bands for α-SiO_2, 528 bands for α-Al_2O_3, 512 bands for α-Fe_2O_3, 1024 bands for calcite, 704 bands for aragonite, 640 bands for C4AF and 512 bands for the remaining structures. With the exception of simple oxides and $CaCO_3$, the GW band gaps were extrapolated to the infinite number of empty bands.

3.2 Simple cement-forming oxides

Most of the cement and concrete phases are composed of the simple oxides, mainly CaO and SiO_2, and to a lesser extent, Al_2O_3 and Fe_2O_3. We analyze these four simple oxides in order to determine the most convenient computational methodology for the purposes of the thesis. This involves testing the performance of GGA and SCAN meta-GGA exchange-correlation functionals in the calculation of the crystal and electronic structures of cement-related materials. We use

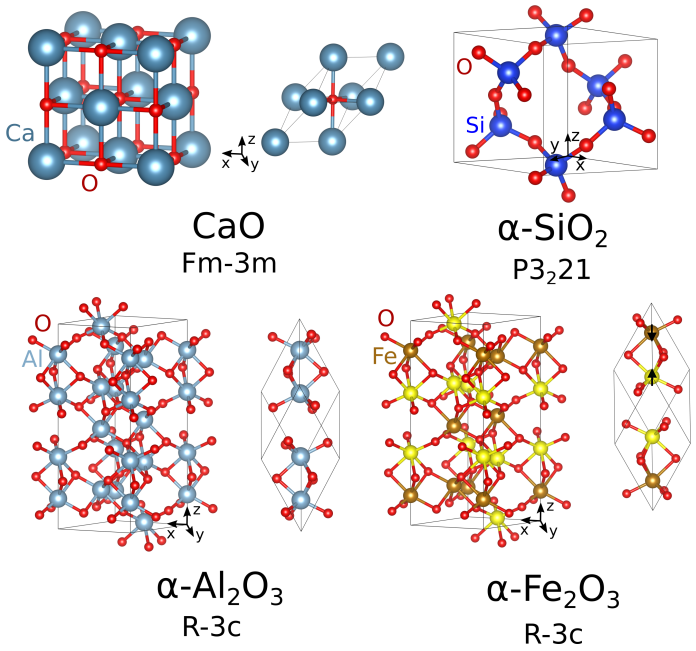

Figure 3.1: Crystal structures of CaO, α-SiO_2, α-Al_2O_3 and α-Fe_2O_3 simple cement-forming oxides. Both conventional and primitive computational cells are shown. The spin polarization of Fe atoms is distinguished by the color.

both functionals as ground state staring points for the G_0W_0 calculations, which are compared with available theoretical and experimental reports.

The crystal structures of CaO ($Fm\bar{3}m$), α-SiO_2 ($P3_221$), α-Al_2O_3 and antiferromagnetic α-Fe_2O_3 (both $R\bar{3}c$), are shown in Figure 3.1. The corresponding lattice constants and volumes, relaxed within the GGA and SCAN frameworks, can be found in Table 3.1. The lattice parameters obtained using the SCAN method are smaller than those predicted by the GGA method and are closer to the experimental values. For CaO and α-Al_2O_3, the GGA calculations predict unit cell volumes that are 1.5% and 3.4% larger than the experimental ones [80, 81], whereas the SCAN functional predicts volumes that are 0.6% and 1.3% smaller, respectively. On the other hand, both the GGA and SCAN methods overestimate the room temperature volume of α-SiO_2 [82] by 8% and 4.2%, respectively [83]. In the case of α-Fe_2O_3, both functionals predict the unit cell volumes that are smaller than the experimental values [84]; however, the SCAN functional correctly predicts a smaller lattice parameter c. Note that *ab-initio* calculations do not account for the effects of temperature, and in the typical case of a positive linear thermal expansion coefficient, the relaxed lattice parameters should be slightly smaller than the experimental values measured at room temperature, in agreement with our results.

A crucial parameter in the calculation of optical properties is the accuracy of the optical band gap. Electronic band gaps calculated using different levels of approximation are compared with available experimental values in Table 3.2. Although the GGA band gaps are systematically improved by the SCAN functional, the GW method is necessary to closely reproduce the experimental values. A comparison of band structures calculated using the SCAN and SCAN+G_0W_0 methods is shown in Figure 3.2.

Calcium oxide in the rock-salt (fcc) structure has been experimentally reported to have an

Table 3.1: Relaxed lattice parameters and volumes of conventional unit cells of CaO, α-SiO_2, α-Al_2O_3 and α-Fe_2O_3 calculated using the GGA and SCAN functionals, compared with experimental data.

	GGA			SCAN			Experiment		
	a[Å]	c[Å]	V[Å^3]	a[Å]	c[Å]	V[Å^3]	a[Å]	c[Å]	V[Å^3]
CaO	4.827	4.827	112.48	4.782	4.782	109.36	4.803	4.803	110.80 [80]
SiO_2	5.045	5.532	121.94	4.986	5.466	117.70	4.912	5.4039	112.93 [82]
Al_2O_3	4.804	13.110	262.00	4.748	12.952	252.82	4.756	12.982	254.25 [81]
Fe_2O_3	5.008	13.858	301.00	4.998	13.687	296.11	5.034	13.732	301.39 [84]

indirect band gap of approximately 6.2 eV [85], as indicated by the photoconductivity threshold [86] and the absorption spectrum onset [87]. Low-temperature reflectance experiments have reported direct gaps of 7.09 eV [88] at the Γ point and 6.9–7.3 eV [88, 89] at the X point. These values are closely approximated when using the SCAN+G_0W_0 method [83]. Notably, this approach yields better results than G_0W_0 on top of the HSE03 hybrid functional [90], which is computationally more expensive. Furthermore, SCAN+G_0W_0 maintains the order of the direct band gaps, which is consistent with the experimental findings (e.g. $E_g^\Gamma > E_g^X$). On the contrary, G_0W_0 in combination with GGA or HSE03 reduces the gap at the Γ point below the one at the X point ($E_g^\Gamma < E_g^X$).

Table 3.2: Band gaps of CaO, α-SiO_2, α-Al_2O_3 and α-Fe_2O_3 calculated using GGA and SCAN with and without G_0W_0 correction, compared to literature values.

	Gap	GGA	GGA +G_0W_0	SCAN	SCAN +G_0W_0	Hybrid +G_0W_0	Experiment
CaO	Γ− X	3.66	6.02	4.20	6.32	6.47 [90]	6.20 [86]
	Γ − Γ	4.63	6.30	5.51	6.91	6.63 [90]	7.09 [88]
	X − X	4.04	6.48	4.54	6.76	6.96 [90]	6.88 [89]
SiO_2	M −Γ	5.65[a]	8.74	6.42	9.27	-	9.65 [91]
	Γ − Γ	5.99	9.14	6.78	9.69	-	-
Al_2O_3	Γ − Γ	5.89	8.66	7.15	9.54	9.95 [92]	9.57 [93]
Fe_2O_3	S_0 − L[b]	0.67	1.32	1.49	2.42	5.05 [94]	2.60 [95]
	S_0− S_0[b]	0.76	1.42	1.52	2.50	5.10 [94]	-

[a] Indirect gap between K and Γ.

[b] Valence band maximum between Γ and S_0, conduction band minimum between L and H_0.

[c] Conduction band minimum is at three-fourths of the Γ–T distance.

Quartz (α-SiO_2) exhibits an indirect band gap with an optical absorption edge of 9.65 eV, as measured by EELS at room temperature [91]. The GGA functional predicts an indirect gap between the K and Γ points, whereas all other tested methods predict a M−Γ gap; however,

the difference between the two gaps is minimal. G_0W_0 on top of the LDA functional predicts $E_g = 9.4$ eV or even $E_g = 10.1$ eV [96, 97], possibly related to the well-known underestimation of the lattice constants by LDA [98]. Our largest calculated band gap was obtained using the SCAN+G_0W_0 method, although this value still underestimates the experimental gap [83]. The smaller calculated band gap may be a consequence of the difference between the experimental and SCAN lattice parameters.

α-Al_2O_3 is a direct gap insulator with an experimental optical absorption edge at 8.8 eV [93, 99]. Cryogenic measurements extrapolated to 0 K indicate a fundamental band gap of 9.57 eV at the Γ point [93], a value that is almost exactly reproduced by our calculations using the SCAN+G_0W_0 approach [83]. Hybrid functional calculations with the GW correction result in an overestimation of the experimentally observed band gap [92], making the SCAN functional a more accurate starting point.

Hematite (α-Fe_2O_3) is a crystalline material that absorbs light in the visible spectrum, with a band gap of 2.6 eV, as measured by photoemission experiments at room temperature [95]. Previous calculations have reported an indirect band gap [94, 100]. The SCAN+G_0W_0 approach yields good agreement with the experimental data, while the calculations performed using PBE0 hybrid functional and PBE0+G_0W_0 predict overestimated gaps [94]. The partially filled d orbitals of Fe give rise to unpaired spins and antiferromagnetic coupling. The local magnetic moment of the Fe atoms equals to 3.5 μ_B and 3.9 μ_B within the atomic projection spheres, as calculated using the GGA and SCAN functional [83]. These values are comparable to the experimental range of 4.2–4.9 μ_B [84, 101].

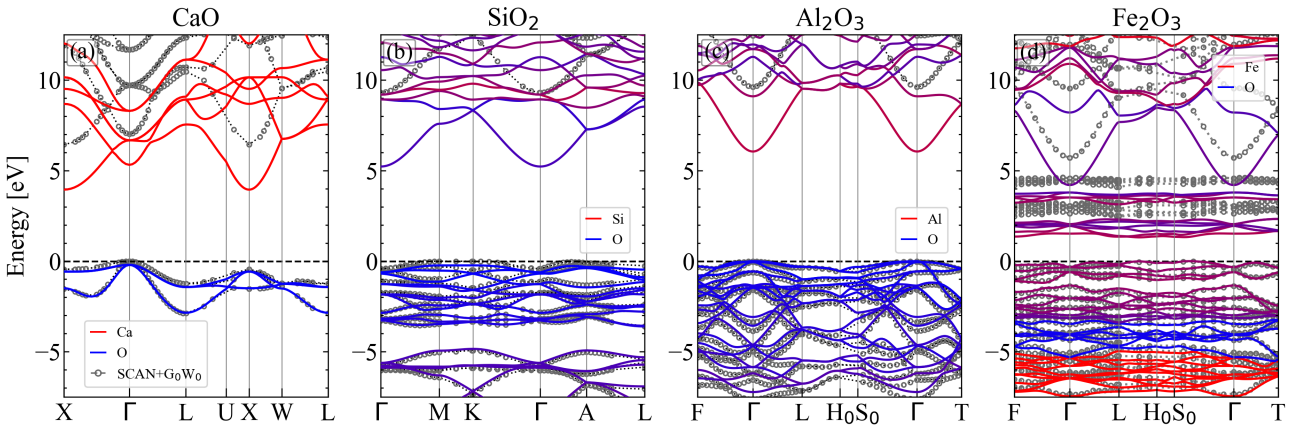

Figure 3.2: Band structures projected on atoms, calculated for (a) CaO, (b) α-SiO_2, (c) α-Al_2O_3, and (d) α-Fe_2O_3. Calculated using the SCAN functional and compared to the SCAN+G_0W_0 method. The zero energy was set to the valence band maximum in all cases.

The SCAN method produces results that are superior to those obtained using the GGA ground state, particularly with regard to structural relaxation and electronic band gaps. A comparison with the literature suggests that it performs better than some hybrid functionals as well [83]. Therefore, all results presented in the following sections use the SCAN functional for the ground state calculations.

3.3 Cement phases

The production of cement involves the fusion of raw minerals and clays, which are composed of the simple oxides described in the previous section. The most abundant phases in the resulting clinker are alite and belite, which can crystallize in various phases with different levels of water reactivity. Alite (Ca_3SiO_5 or C3S) exhibits seven crystal structures, ranging from the triclinic structure, which is the most stable at room temperature, to high-temperature rhombohedral and monoclinic phases [9,11,102]. Belite (Ca_2SiO_4 or C2S) can be found in five crystallographic structures, including hexagonal, orthorombic and monoclinic lattices [11,30]. Here, we represent the clinker phases by monoclinic alite and β-belite, which are the polymorphs with high water reactivity, a fact which is key to the cement functionality. Other less abundant clinker phases include cubic tricalcium aluminate (C3A) and orthorombic tetracalcium aluminoferrite (C4AF), also known as brownmillerite. Moreover, a common rock-forming mineral, $CaSO_4$, is usually added to the ordinary Portland cement. The stable phase at ambient conditions is the β-anhydrate [103] and its hydrated form gypsum ($CaSO_4.2H_2O$) [104]. The crystal structures of all studied phases are shown in Figure 3.3.

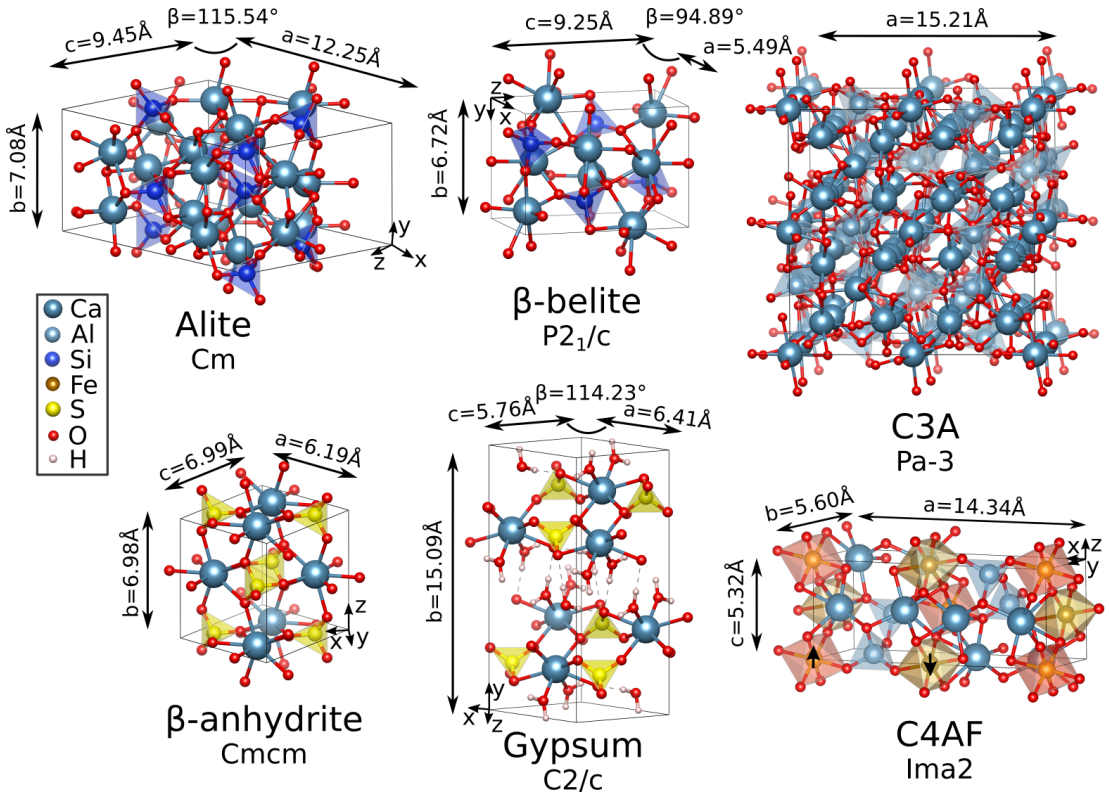

Figure 3.3: Crystal structures of monoclinic alite, β-belite and gypsum, orthorombic β-anhydrite and tetracalcium aluminoferite (C4AF), and cubic tricalcium aluminate (C3A). The Fe atoms in antiferromagnetic C4AF are distinguished according to their spin polarization direction.

The lattice parameters of the cement phases calculated using the SCAN functional are shown in Figure 3.3 and Table 3.3 [105]. The relaxed lattice parameters of monoclinic alite are consistent with the experimental values [11], with a slightly smaller monoclinic angle and a larger c lattice parameter. The relaxed crystal structure of monoclinic β-belite agrees well with the

experimental data [11]. Note that in the case of β-belite, the SCAN functional produces lower deviations from the experimental lattice constants than the GGA functional [30]. The experimental crystal structure of monoclinic gypsum is defined by the lattice parameters a = 6.28 Å, b = 15.22 Å, c = 5.68 Å and β = 114.08° [106]. While the monoclinic angle β in gypsum is consistent with the experimental value, the lattice constant a is slightly overestimated by our calculations, potentially due to the neglect of van der Waals interactions in description of the H-bonds [107]. The relaxed unit cell of orthorhombic β-anhydrate closely agrees with the experimental values [108]. In the case of β-anhydrate, the SCAN functional provides better agreement with the measured lattice parameters than the B3LYP hybrid functional [103]. The relaxed lattice parameters of the cubic C3A [11] and C4AF [109, 110] agree very well with the experimental values. The Fe atoms in brownmillerite are ordered antiferromagnetically with local magnetic moments of 4 μ_B.

Table 3.3: Lattice parameters and electronic band gaps of cement phases, to be compared with experimental data. The angles that are not listed are equal to 90°.

	SCAN				Experiment				Band gap [eV]	
	a[Å]	b[Å]	c[Å]	β[°]	a[Å]	b[Å]	c[Å]	β[°]	SCAN	G_0W_0
Alite	12.25	7.08	9.45	115.54	12.21	7.11	9.31	116.20 [11]	3.76	5.69
β-belite	5.49	6.72	9.25	94.89	5.51	6.77	9.32	94.18 [11]	4.43	7.71
Gypsum	6.41	15.09	5.76	114.23	6.28	15.22	5.68	114.08 [106]	5.52	9.51
$CaSO_4$	6.19	6.98	6.99	90	6.24	6.99	7.00	90 [107]	6.88	9.92
C3A	15.21	15.21	15.21	90	15.23	15.23	15.23	90 [11]	4.69	-
C4AF	14.34	5.60	5.32	90	14.52	5.57	5.35	90 [110]	1.49	3.24

The GW corrections are highly sensitive to various parameters and the convergence needs to be carefully checked. We performed convergence tests with respect to the number of empty bands and the energy cutoff in the GW summation, which are shown in Appendix E. Since the convergence is generally slow and the unit cell size of the cement phases makes the calculations with the fully converged setup impossible, we extrapolated the GW band gaps to an infinite number of unoccupied bands. The fundamental gaps of the cement phases calculated using the SCAN and SCAN+G_0W_0 methods are listed in Table 3.3. Moreover, the band structures are shown in Figure 3.4. Alite, β-belite, gypsum and C3A are direct band gap insulators, with the smallest band gap located at the Γ point. Contrarily, in β-anhydrite, the valence band maximum (VBM) is located at the Y (0.5, 0.5, 0) high symmetry point and the conduction band minimum (CBM) at the Γ point. The indirect band gap equals to 6.88 eV, calculated using the SCAN functional, and 9.92 eV using the SCAN+G_0W_0 method. The smallest direct G_0W_0 band gap is located at the Γ point and is equal to 10.47 eV [105]. The band gap of C4AF is located between the T (0.0, 0.0, 0.5) and R (0.0, 0.5, 0.0) points. In calcium silicates, sulfates and C3A, the band gaps separate the O-dominated valence bands from the Ca-dominated conduction bands.

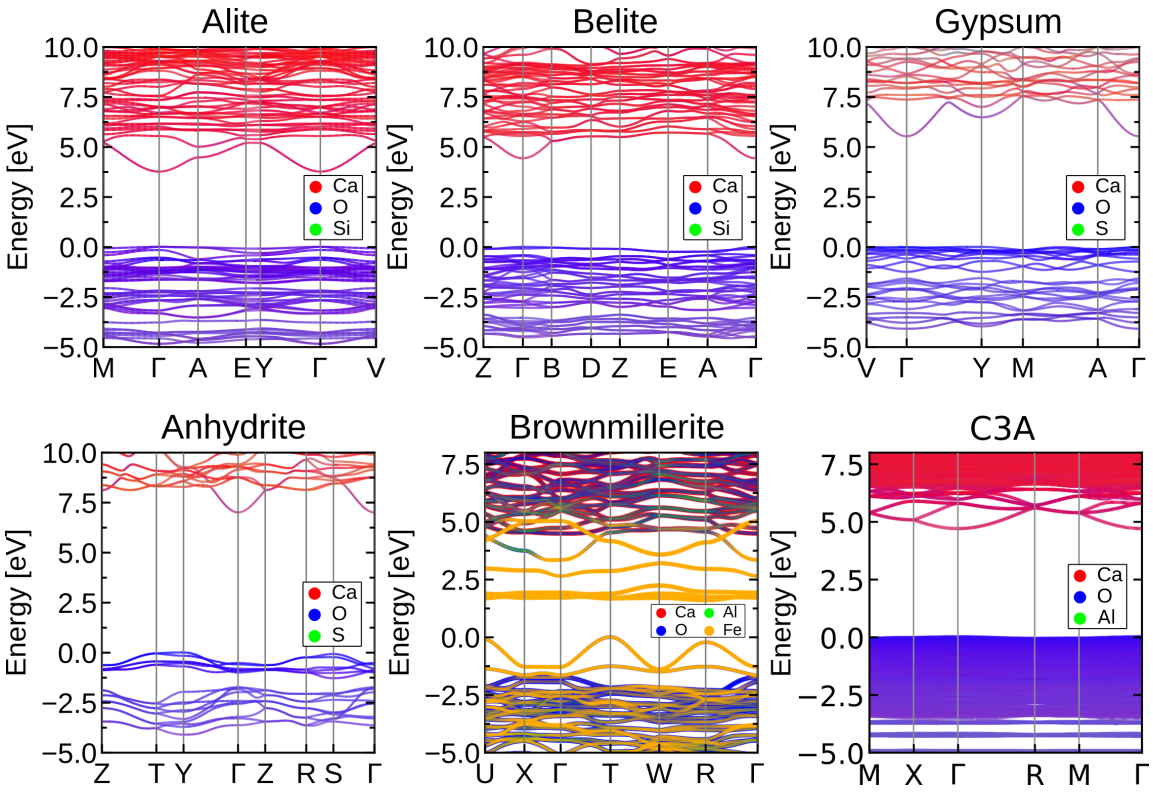

Figure 3.4: Band structures of alite, β-belite, gypsum, β-anhydrite, C4AF brownmillerite and tricalcium aluminate C3A, calculated using the SCAN functional.

Conversely, the band gap in C4AF is located between the Fe d states.

The unit cell of C3A contains 264 atoms, which makes it too large to perform the GW calculations. The GW correction calculated for its hydrate, C3AH (see Table 3.4), opens the band gap by 40 %, so we can expect the real electronic band gap of C3A to be at least 6.6 eV.

To the best of our knowledge, there is a lack of literature on the band gap measurements of cement phases. The only found experimental value is the optical band gap of alite, which is equal to 5.24 eV [105]. This value was extrapolated from the linear portion of the first electronic absorption peak obtained via reflectance measurement. The calculated band gap of alite is consistent with this value. Any deviations may be caused by the polycrystallinity of the sample, the presence of various phases or impurities. Following the results for simple oxides in the previous section, the agreement between theory and experiment for alite demonstrates the reliability of the computational methodology applied in this study and the predictive power of first principles calculations for the optical properties of cements.

3.4 Hydrated concrete phases

Concrete is obtained through the hydration of cement, which involves a series of complex chemical reactions between the clinker phases and water. Hydration produces the concrete matrix responsible for the mechanical properties required for construction purposes. During hydration, several crystalline and poorly crystalline phases precipitate and form a dense microstructure that governs strength development, durability, and long-term stability. The main binder in con-

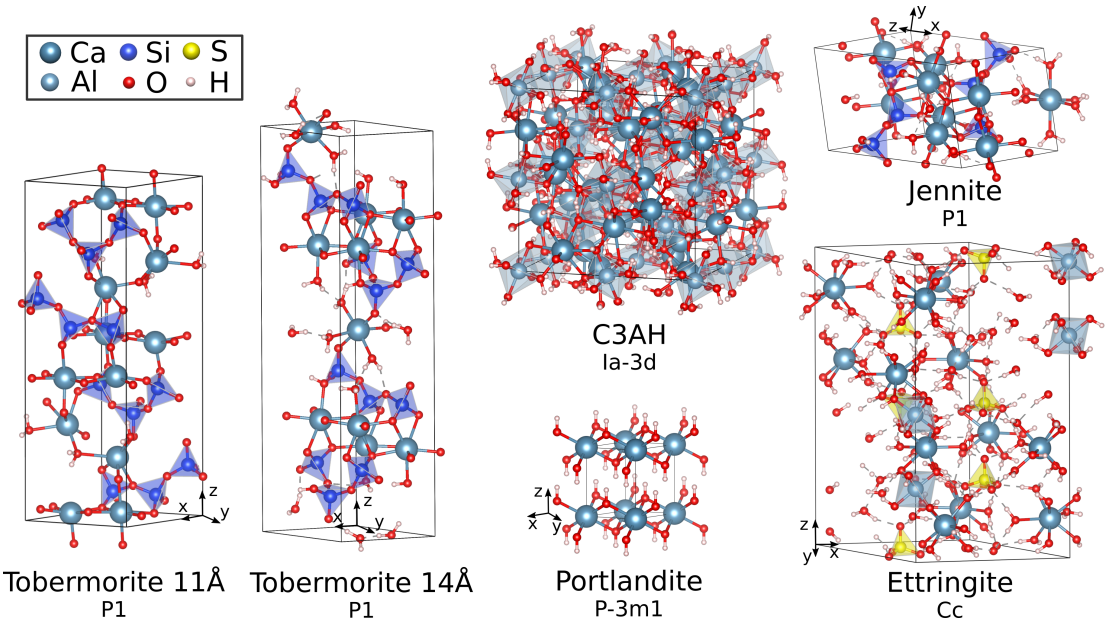

Figure 3.5: Crystal structures of hydrated concrete phases: triclinic tobermorite 14Å, tobermorite 11Å and jennite, monoclinic ettringite, hexagonal portlandite and cubic C3AH.

crete is the calcium silicate hydrate (C-S-H) gel, which gives concrete most of its strength and durability and constitutes the largest fraction of the hydrated cement paste. Although C-S-H is generally poorly crystalline, its short- and medium-range atomic order is similar to that of tobermorite crystal group, which makes it a reasonable structural analogue of C-S-H for simulations purposes. In this work, we describe the crystal structure of C-S-H using tobermorite

Table 3.4: Lattice parameters and the smallest electronic band gaps of hydrated phases, compared with experimental data.

	SCAN			Experiment			Band gap	
	a[Å]	b[Å]	c[Å]	a[Å]	b[Å]	c[Å]	SCAN	G_0W_0
	α[°]	β[°]	γ[°]	α[°]	β[°]	γ[°]	[eV]	[eV]
$Ca(OH)_2$	3.59	3.59	4.85	3.59	3.59	4.87 [111]	4.76	7.21
	90	90	120	90	90	120		
T11	6.57	7.26	23.44	6.69	7.39	22.77 [112]	4.67	7.50
	90.57	91.01	123.45	90	90	123.49		
T14	6.63	7.35	28.21	6.74	7.43	27.99 [113]	4.11	7.11
	89.29	90.62	122.82	90	90	123.25		
C3AH	12.51	12.51	12.51	12.56	12.56	12.56 [114]	4.97	6.95
	90	90	90	90	90	90		
Ettringite	10.97	10.97	21.11	11.17	11.17	21.36 [115]	4.24	-
	89.91	90.04	119.81	90	90	120		
Jennite	10.51	7.25	10.78	10.58	7.27	10.93 [116]	5.20	7.83
	101.41	97.27	109.62	101.30	96.98	109.65		

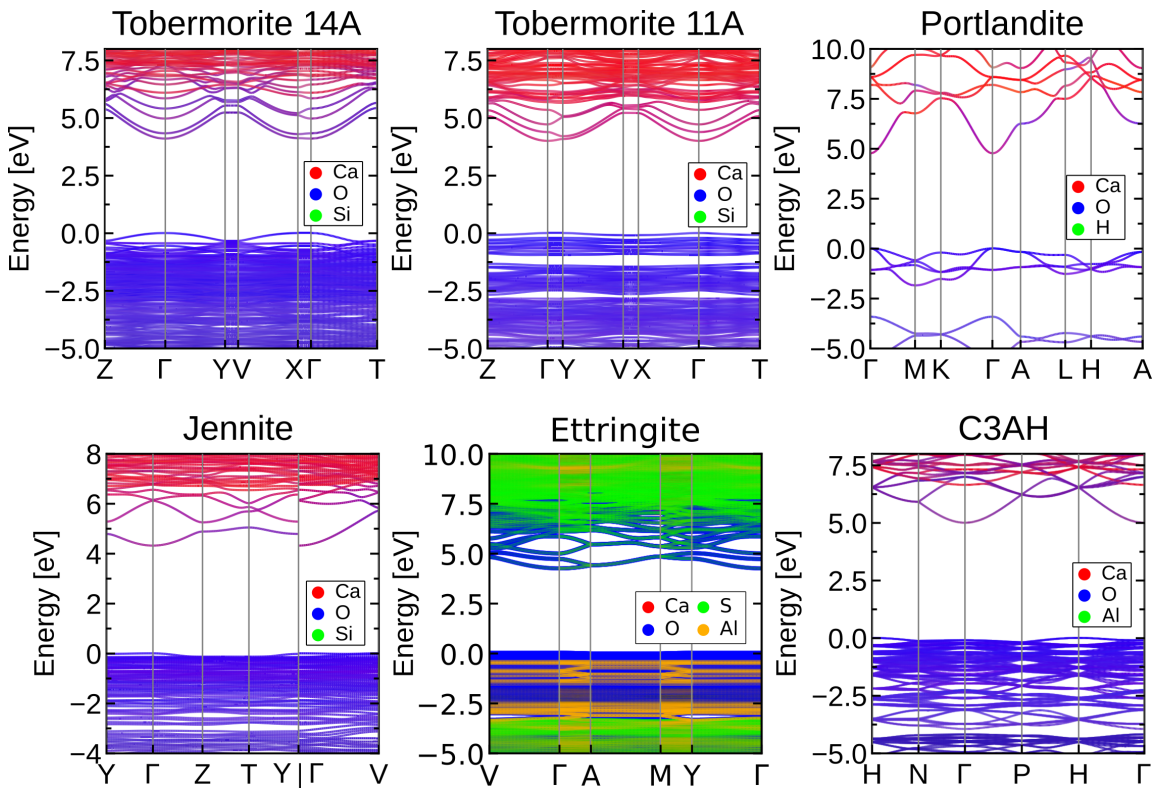

Figure 3.6: Band structures of hydrated phases tobermorite, portlandite, jennite, ettringite and C3AH.

11Å ($Ca_5Si_6O_{17}{\cdot}5H_2O$) and tobermorite 14Å ($Ca_5Si_6O_{16}(OH)_2{\cdot}7H_2O$), which differ mainly in interlayer spacing and water content. The second most abundant hydration product is $Ca(OH)_2$, commonly referred to as portlandite, which crystallizes in a layered hexagonal structure and plays an important role in maintaining the high alkalinity of the pore solution (liquid phase in pores and capillaries during hydration). Other hydrated phases typically found in concrete include jennite ($Ca_9Si_6O_{18}(OH)_6{\cdot}8H_2O$), which is another structural analogue of C-S-H at higher Ca/Si ratios, C3AH ($Ca_3Al_2O_6{\cdot}6H_2O$), a calcium aluminate hydrate that may form under specific curing conditions with low concentration of sulfates, and ettringite ($Ca_6Al_2(SO_4)_3(OH)_{12}{\cdot}30H_2O$), a needle-like phase that precipitates at early stages of hydration in presence of gypsum and strongly influences setting and expansion behaviour. The crystal structures of the concrete phases are shown in Figure 3.5.

The lattice constants calculated using the SCAN functional are in a very good agreement with experimental results, as shown in Table 3.4. Small deviations from measured values can be attributed to temperature effects, structural disorder in real samples, and the presence of defects or variable water content, which are not always fully captured in idealized computational models. The crystal structure of tobermorite is defined by linear chains of SiO_4 tetrahedra linked through bridging oxygen atoms, forming silicate chains separated by calcium ions and interlayer water molecules. These silicate chains and the associated calcium coordination polyhedra are primarily responsible for the stiffness and cohesion of the material. The relaxation of both tobermorite 11Å (T11) and tobermorite 14Å (T14) predicts triclinic structures with the angles α and β slightly deviating from the experimentally reported 90 degrees, which indicates a small distortion of the

lattice upon the full structural optimization. The structure of ettringite also differs slightly from the reported monoclinic lattice.

Like the cement phases, the hydrates are wide band-gap insulators, as shown in Table 3.4 and Figure 3.6. Their large band gaps are consistent with the predominantly ionic and covalent bonding character of calcium-oxygen and silicon-oxygen interactions and the absence of partially filled *d*-states near the Fermi level. Direct band gaps at the Γ point were found in T14, portlandite, and ettringite. The indirect band gaps in T11, C3AH, and jennite are positioned between the VBM at the Z (0, 0, 0.5), N (0, 0, 0.5), and V (0.5, 0.5, 0) points, respectively, and the CBM at the Γ point. Nevertheless, the differences between the smallest indirect and the Γ-point direct band gaps are minimal, which is a consequence of relatively flat valence band edges. The extrapolation of the G_0W_0 band gap to an infinite number of empty bands reproduces the band gaps of T11 and portlandite calculated using more demanding self-consistent GW approaches [26], which is another indication that the method chosen in this thesis is accurate. The size of the ettringite computational cell was prohibitive to calculate its GW band gap within a reasonable computational cost. The GW corrections performed for other systems studied in this thesis open the gaps by approximately 40% to 80% compared to DFT calculations. Based on these trends, we can expect the band gap of ettringite to be in the range of 6–7.7 eV.

3.5 Raw materials and additives

In this section, we describe the raw materials used in cement production, such as $CaCO_3$ and clays, represented by kaolinite and illite, which can remain in cement as intrusions. Other minerals, like TiO_2, wollastonite ($CaSiO_3$ or CS), but also $CaCO_3$, can be used as concrete additives to enhance properties of the composite.

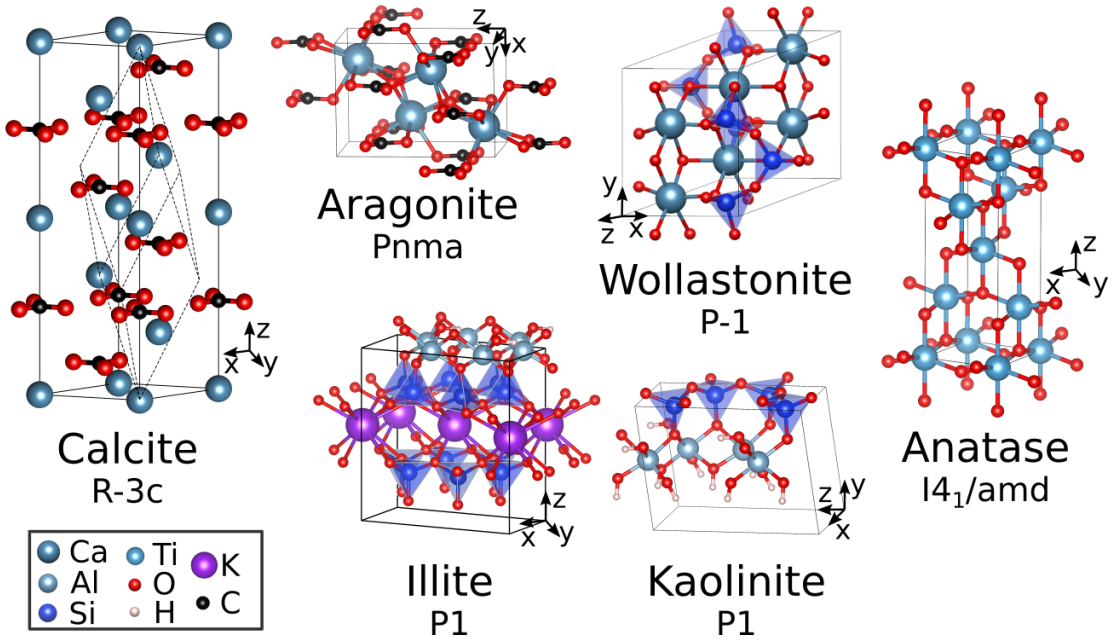

Figure 3.7: Crystal structures of calcite, aragonite, anasate, illite, kaolinite and wollastonite.

There are two main polymorphs of $CaCO_3$: hexagonal calcite ($R\bar{3}c$) and orthorombic aragonite ($Pnma$). Calcite is stable at room temperature and pressure, but the metastable aragonite

Table 3.5: Lattice parameters and electronic band gaps of calcite, aragonite, TiO_2 anatase, kaolinite, illite and CS wollastonite, to be compared with experimental data.

	SCAN			Experiment			Band gap	
	a[Å]	b[Å]	c[Å]	a[Å]	b[Å]	c[Å]	SCAN	G_0W_0
	α[°]	β[°]	γ[°]	α[°]	β[°]	γ[°]	[eV]	[eV]
Calcite	5.00	5.00	16.82	4.99	4.99	17.06 [117]	6.05	8.35
	90	90	120	90	90	120		
Aragonite	4.94	7.91	5.68	4.96	7.97	5.74 [118]	4.88	7.81
	90	90	90	90	90	90		
Anatase	3.77	3.77	9.56	3.79	3.79	9.52 [119]	2.58	3.86
	90	90	90	90	90	90		
Kaolinite	5.15	8.94	7.37	5.16	8.94	7.40 [120]	5.85	9.04
	91.72	104.96	89.741	91.70	104.86	89.82		
Illite	5.14	8.91	9.94	5.20	8.98	10.23 [121]	4.35	7.07
	91.23	98.68	90	91.70	104.86	89.82		
CS	7.15	7.39	8.02	7.07	7.32	7.93 [122]	5.51	7.95
	103.45	95.52	90.08	103.43	95.22	90.03		

also occurs naturally as a rock-forming mineral at ambient conditions. The Ca cations in calcite

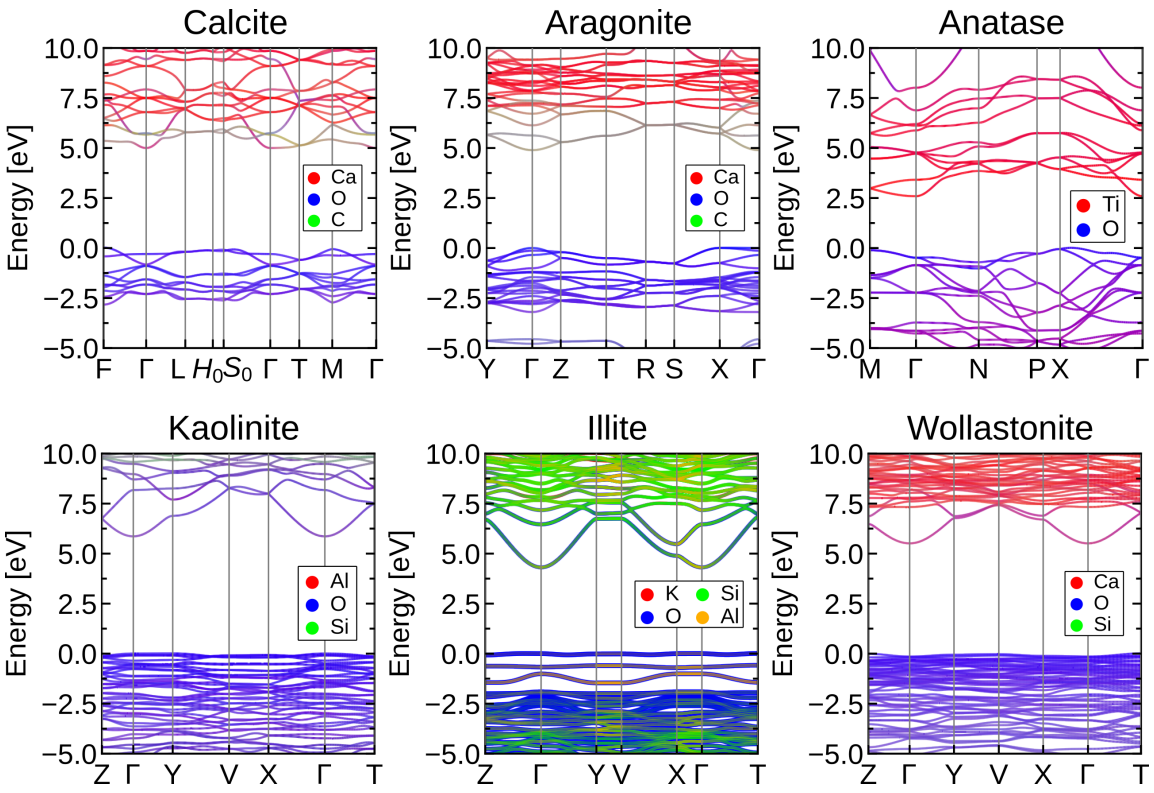

Figure 3.8: Band structures of calcite, aragonite, anasate, illite, kaolinite and CS wollastonite calculated using the SCAN functional.

occupy pseudo-cubic lattice sites at the centers of oxygen octahedra, as shown in Figure 3.7. The CO_3^{-2} groups with trigonal symmetry are located at the vertices of the oxygen octahedra and create a planar arrangement. In contrast, the Ca cations in aragonite have ninefold coordination with a nearly hexagonal symmetry and slightly aplanar CO_3^{-2} groups. For calcite, the SCAN functional predicts more precise lattice parameters than GGA [54]. The theoretical lattice parameter a, shown in Table 3.5, is larger than that measured at room temperature, which is consistent with the negative thermal expansion coefficient of calcite in the xy plane [117]. The experimental lattice constants at 0 K are equal to $a(0\text{K}) = 4.994$ Å and $c(0\text{K}) = 16.936$ Å, extrapolated from cryogenic measurements using the linear thermal expansion coefficient [117]. The bond lengths calculated using the SCAN functional equal to 1.283 Å and 2.350 Å for the C-O and Ca-O bonds, respectively, which are in qualitative agreement with the room temperature experimental values of 1.288 Å and 2.355 Å [123].

The calculated crystal structures of aragonite, anatase (the tetragonal polymorph of TiO_2) and triclinic wollastonite agree very well with the experimental values. Kaolinite ($Si_2Al_2O_5(OH)_4$) is the simplest clay mineral, composed of a stacking of Si-Al-O bi-layers, as shown in Figure 3.7. The Si and Al atoms form two quasi-hexagonal lattices placed on top of each other. Similarly, illite is formed by the stacking of Si and Al layers separated by an alkali or alkali earth metal. Note that aluminium silicate layers can even form nanotubes [124].

The calculations show a direct band gap at the Γ point in kaolinite. The remaining five structures have the CBM at the Γ point and the VBM at: the F point (0.5, 0.5, 0.0) in calcite, the X point (0.5, 0.0, 0.0) in aragonite, the X point (0.0, 0.0, 0.5) in anatase, the Y point (0.0, 0.5, 0.0) in illite and the T point (0.0, -0.5, 0.5) in CS, as shown in Figure 3.8. The calculated band gaps are summarized in Table 3.5. Anatase has the smallest indirect band gap, equal to 3.86 eV, while its smallest direct gap is located at the Γ point, equal to 4.36 eV. The largest band gaps were found in kaolinite and calcite.

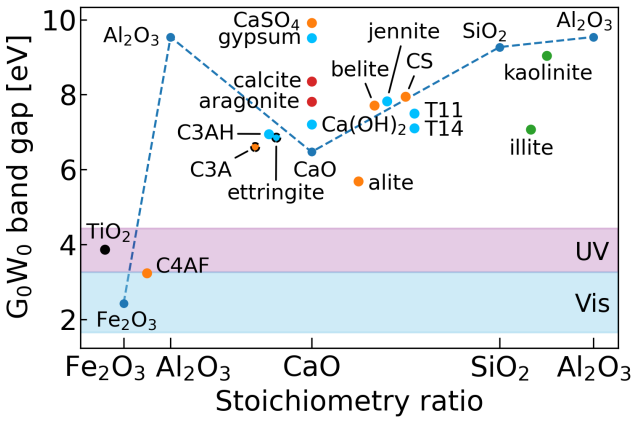

Figure 3.9: Band gaps of cement and concrete phases as a function of the concentration of the simple oxides CaO, α-SiO_2, α-Al_2O_3 and α-Fe_2O_3. The band gaps of simple oxides are shown by blue dots. The clinker phases are shown as orange, hydrated phases as light blue and clays as green circles.

The G_0W_0 band gap energies of all studied phases are summarized in Figure 3.9. In this figure, each compound is placed along the horizontal axis according to the stoichiometric ratio of the two principal simple oxides from which it is composed. As a result, calcium silicates are

located between CaO and SiO_2, calcium aluminates between CaO and Al_2O_3, and clay minerals between SiO_2 and Al_2O_3. This representation allows the band gap values to be compared not only across individual phases but also in relation to their chemical composition and parent oxides. In the case of C3A and ettringite, approximate band gaps were estimated by applying scaling factors to the SCAN values. Specifically, the band gaps of C3A and ettringite were obtained by increasing the SCAN gaps by 40% and 60%, respectively, based on the explicitly calculated GW correction for C3AH in the case of C3A, and on the corrections obtained for gypsum and anhydrite in the case of ettringite.

A clear trend can be observed for calcium silicates, whose band gaps generally follow the CaO/SiO_2 ratio, with the exception of alite, which exhibits a smaller band gap than expected. A similar compositional dependence is observed for the clay minerals: kaolinite follows the expected behavior based on its oxide constituents, whereas illite deviates from the trend, possibly due to its more complex structure and chemical composition. Among calcium aluminates, C3AH, whose band gap was explicitly calculated at the G_0W_0 level, follows the general trend defined by the band gaps of CaO and α-Al_2O_3. This comparison shows how the band gaps of complex cement phases are largely governed by the electronic structure of their constituent oxides.

α-Fe_2O_3 and C4AF have band gaps within the visible range, which means they contribute to coloration in cementitious materials. Furthermore, TiO_2 anatase absorbs in the UV region. The band gap of alite lies close to the UV absorption edge and the presence of excitonic effects may lead to weak absorption of UV light.

3.6 Outline

In this chapter, we presented the results of the structural optimization of a wide range of crystalline phases commonly found in cement and concrete. In addition to determining their equilibrium lattice constants, we analyzed their electronic band structures and reported the fundamental band gaps obtained at different levels of theory, both with and without quasiparticle corrections. These results provide a foundation for the next chapters, where the optical properties of the cements and concrete are investigated in detail.

The relaxed structures of the studied oxides, calculated using the SCAN meta-GGA functional show consistently better agreement with available experimental lattice parameters and structural data than those obtained using the conventional GGA calculations. Accurate structural models are particularly important, since small changes in bond lengths, angles, or coordination environments can significantly influence electronic and vibrational properties.

A similar trend is observed in the calculated electronic band gaps. The values obtained using the SCAN functional are systematically larger and closer to experiment than those calculated using the GGA functional, and the inclusion of quasiparticle corrections within the SCAN+G_0W_0 framework improves the results even further. Our findings indicate that the SCAN functional provides a reliable and computationally efficient ground-state for the electronic structure calculations of cement-related materials. In contrast to hybrid functionals or the scissor operator band gap correction, the SCAN+G_0W_0 approach does not require semi-empirical parameters and retains the predictive character of first principles methods. Based on these observations, the SCAN and SCAN+G_0W_0 approaches will be employed in the following chapters to study the optical properties of cement and concrete phases in a systematic way.

Some hydrated phases, such as portlandite, gypsum, and kaolinite crystallize in layered

structures composed of Ca-O or Si-O polyhedral sheets separated by interlayer water molecules or hydroxyl groups (see Figure 3.3, Figure 3.5, and Figure 3.7). Similarly, tobermorite 14Å and jennite exhibit layered arrangements with partially connected slabs through the bridging oxygen atoms. Thanks to the unusual structure, these phases could be exfoliated and studied as 2D functional materials. Such low-dimensional materials could have unusual optical and vibrational properties, including a strongly anisotropic dielectric response, the presence of various types of Reststrahlen bands in the IR region, and the formation of excitonic states that may couple to lattice vibrations or electromagnetic fields. These characteristics make layered calcium silicate and aluminate hydrates promising candidates for exploring polaritonic phenomena and other effects typically associated with two-dimensional materials.

Overall, the results reported in this chapter establish a consistent and reliable framework for calculating the structural, electronic, and optical properties of the studied materials, which are necessary for the analyses performed in the remainder of this work.

Chapter 4

Optical properties of cement and concrete

Standard DFT is useful for determining structural and qualitative electronic properties, but does not provide satisfactory description of optical spectra, particularly near the absorption edge. In many cases, the correct spectral features, such as the position of the absorption onset, the redistribution of spectral weight, and the presence of bound excitonic states, can only be reproduced by employing higher-level many-body techniques. In this chapter, we test various methods to calculate the optical properties of cement-related materials and compare them with experiment. We obtain both electronic and ionic responses, which together provide input for the calculation of radiative properties and solar reflectance.

4.1 Computational details

The calculations described in this chapter were performed using VASP code [77,78]. The setup of G_0W_0 calculations is described in the Methods section of the Chapter 1. The BSE spectra were obtained using 8-14, 18-28, 18-16 and 16-30 valence-conduction bands for CaO, α-SiO_2, α-Al_2O_3 and α-Fe_2O_3, respectively, with a maximum transition energy of 25 eV [83]. The BSE dielectric functions were also calculated for 34-56, 43-44, 32-46, 24-40 and 25-40 valence-conduction bands, respectively for alite, β-belite, gypsum, β-anhydrite and C4AF, with maximum transition energies of 18 eV for alite, belite and C4AF, and 25 eV for gypsum and anhydrite. The BSE spectra of hydrated phases were calculated using 90-80, 30-60, 6-22, 42-80 and 30-60 valence-conduction bands for T11, T14, portlandite, C3AH and jennite, respectively, with the maximum transition energy of 15 eV for T11, T14, and jennite, 18 eV for C3AH and 25 eV for portlandite. The BSE calculations with 18-24, 20-40, 12-20, 36-55, 34-52 and 34-60 valence-conduction bands were performed for calcite, aragonite, anatase, CS, illite and kaolinite, respectively, with the highest allowed transition energy of 17 eV for CS, 20 eV for illite and kaolinite, and 25eV for calcite, aragonite and anatase.

In the case of simple cement-forming oxides, cement phases, calcite and portlandite, we also employed a two-step k-mesh averaging approach to calculate the BSE spectra [125]. In the first step, we conducted a single calculation to obtain the irreducible k-points with their weights. Then, in a second step, we performed a series of calculations on k-meshes shifted by the coordinates of the irreducible k-points from the first step. The averaged spectra were

obtained as a weighted arithmetic mean of the dielectric functions calculated on each shifted k-mesh [54, 83, 105]. The advantage of k-averaging is the reduction of spurious peaks and a smoother spectrum. To obtain averaged dielectric functions, we performed averaging over 13, 16, 34, 32, 12, 13, 24, 10, 24 and 21 dielectric spectra for α-Fe_2O_3, CaO, α-SiO_2, α-Al_2O_3, calcite, portlandite, alite, β-belite, gypsum and β-anhydrite.

An alternative way to calculate the excitonic spectra, the model-BSE (mBSE) approach [126], was used to calculate excitonic wavefunctions of silica and alumina. Here the GW quasi-particle corrections are replaced by the scissor operator to match the G_0W_0 band gap, and the effective screening W is replaced by a model dielectric response. This method reduces the computational cost by avoiding the GW step and allows for the use of denser k-meshes.

4.2 Simple cement-forming oxides

4.2.1 Optical spectrum - electronic contribution

This section discusses the optical properties of simple oxides resulting from the polarization of electrons by UV–Vis light. The imaginary part of the dielectric function, ϵ_2, of CaO, α-SiO_2, α-Al_2O_3 and α-Fe_2O_3 calculated using different levels of theory, is shown in Figure 4.1. The IPA curves, depicted as blue lines, lack experimental spectral features. Quasi-particle IPA curves calculated using the G_0W_0 method, showed by orange lines, reproduce the experimental curves at higher energies, but fail to mimic the spectral onset. The BSE results, shown as red lines, reveal a significant redistribution of the spectral weights with respect to the GW results, which gives rise to peaks around the absorption edge. This redistribution is a result of the electron-hole interaction included within the BSE calculations. All four cement-forming oxides described in Figure 4.1 display peaks in the BSE spectrum below the band gap energy. The peaks below the electronic band gap are a sign of the exciton formation. The BSE curves are in close agreement with the experimental spectra. In the following, all dielectric functions are plotted as an average over the three polarization directions, i.e, $\epsilon = (\epsilon_x + \epsilon_y + \epsilon_z)/3$.

In order to provide a detailed description of the prominent spectral features observed in the BSE spectra, we analyze the peaks with the highest oscillator strengths (defined in Equation 2.40), calculated on denser k-meshes. The spatial distribution of exciton wavefunctions is illustrated by the amplitude of the k-point resolved coupling coefficient between electrons and holes, $X_\lambda^{cv\mathbf{k}}$, which is defined in Equation 2.33. The electron-hole coupling coefficient between a positively charged hole v in the valence band and a negatively charged electron c in the conduction band are obtained from the solution of the BSE eigenvalue equation. The peaks observed in the imaginary dielectric function ϵ_2 can be related to the van Hove singularities that arise from the critical points (M_0–M_3) in the joint band structure (JBS) [130, 131]. The M_0 critical points, which correspond to minima in JBS, can potentially host bound excitons [131].

CaO

Three peaks in the experimental dielectric function of CaO were assigned to excitons [88], in Figure 4.2 denoted as A, B, and C. The faint peak B, observed at low temperatures, is a series of low-intensity peaks at the high-energy shoulder or the peak A. The BSE calculations resolved all three peaks in good agreement with the experimental curve, except for an underestimation of the intensity of the peak A, and a small blue shift of the peak B [83]. The highest valence bands

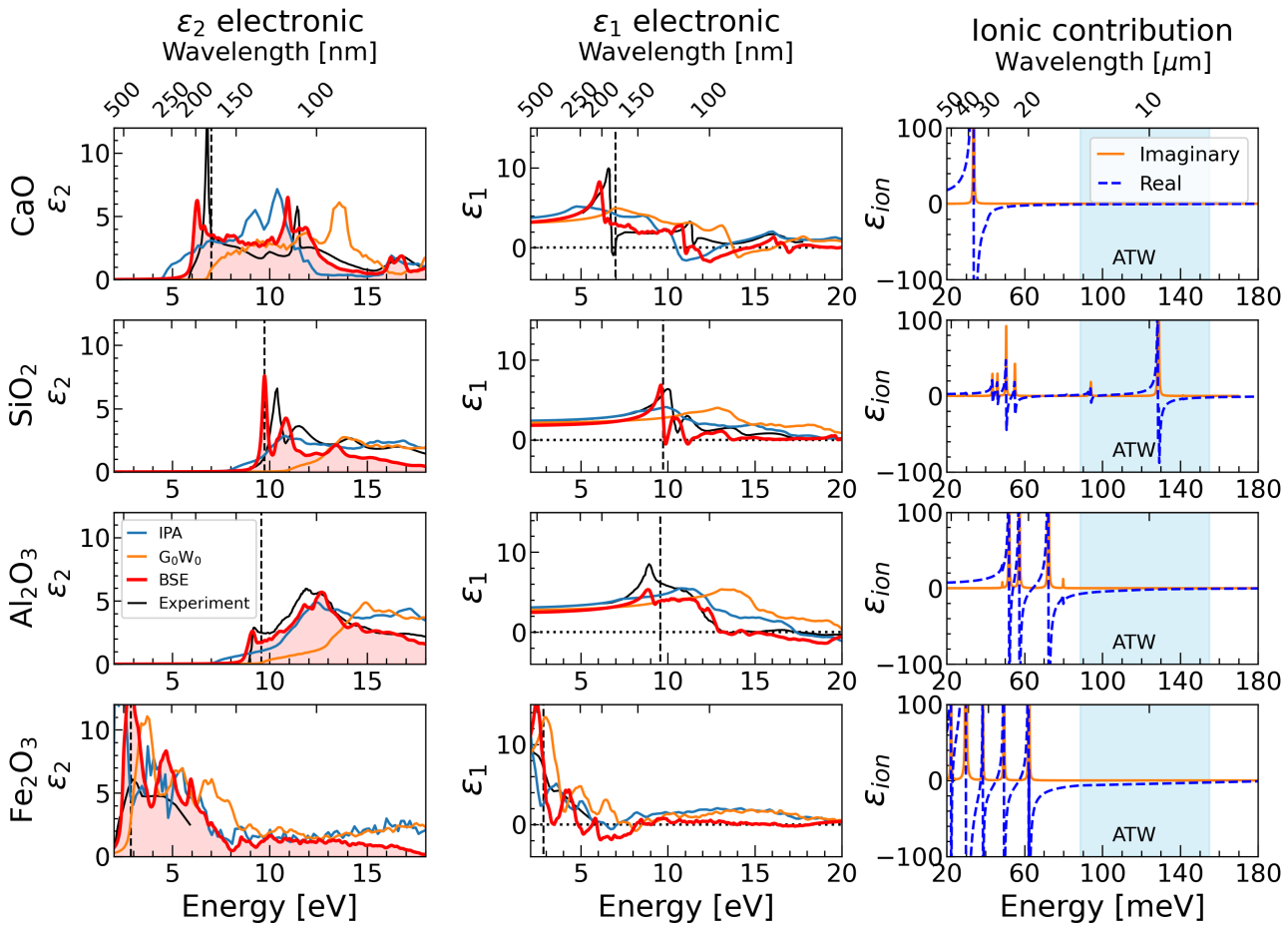

Figure 4.1: Calculated and experimental [85,88,127–129] electronic and ionic dielectric functions of CaO, α-SiO_2, α-Al_2O_3 and α-Fe_2O_3, using various levels of theory. The GW band gaps are indicated as dashed lines. Calculated dielectric functions were obtained using averaging over shifted k-meshes, as introduced in the Methods section. In the third column, the blue region corresponds to the IR atmospheric transparency window.

are composed purely of oxygen $2p$ bands, while the bottom of the conduction region is mostly made up of Ca d orbitals, which are hybridized at the Γ point with O s states (see Figure 3.2a). The holes are situated on the O atoms, while the excited electrons are mostly belong to the Ca atoms. This configuration corresponds to the formation of charge transfer excitons.

The high-intensity peak A was associated with an exciton arising from the lowest energy direct interband transition at the X point [85,88,90]. The results of our calculations, presented in Figure 4.2b, support these findings. The exciton is formed by transitions from the VBM, dominated by the O $2p$ states (e_u symmetry), to the CBM, composed of Ca d electrons (b_{2g}). The excitonic wavefunction, defined by $X_\lambda^{cv\mathbf{k}}$, is highly localized in reciprocal space, which emphasizes the need for dense k-meshes to accurately predict peak intensities. This dependence can be seen from the higher intensity of the peak A calculated on a 20^3 k-mesh comparing with a 6^3 mesh.

The peak B was identified as a Γ point exciton based on the observation of the spin-orbit splitting at low temperatures [88]. However, the hybrid functional calculations using HSE03+G_0W_0 do not align with this interpretation, as the X-point band gap was predicted to be larger than

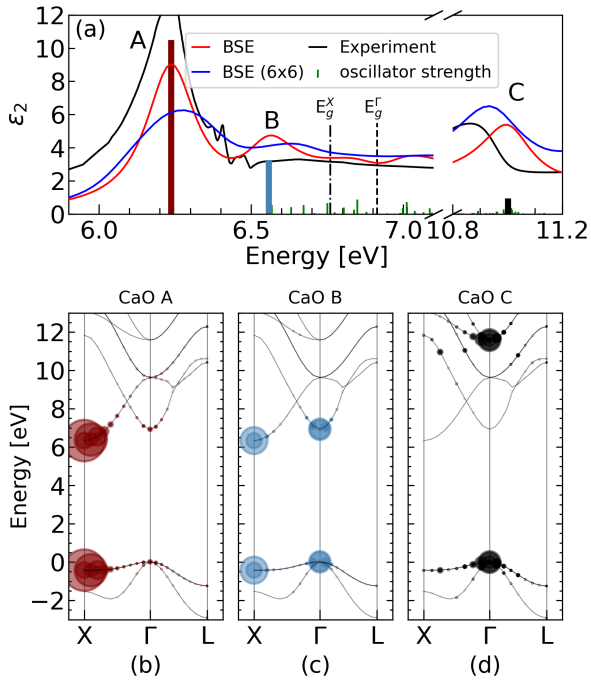

Figure 4.2: CaO spectrum calculated using G_0W_0+BSE. (a) Dielectric function calculated on a dense 20^3 k-points mesh (red line) with the corresponding oscillator strengths (green bars), compared to ϵ_2 obtained by k-mesh averaging (blue line) and the experiment (full black line) [85, 88], with the calculated band gaps (dashed and dot-dashed black lines). The experimental curve was shifted to match the excitonic peak A. (b-d) Band structures with contributions to the excitonic wavefunctions of the peaks A, B and C, given by the circle size corresponding to $X_\lambda^{cv\mathbf{k}}$ [83].

the Γ-point gap [90]. In contrast, the SCAN+G_0W_0 method produced an inverse ordering of the gaps ($E_g^\Gamma > E_g^X$) as demonstrated in Table 3.2, supporting the Γ-point origin of the exciton B. As shown in Figure 4.2c, the peak B has two principal contributions. The first contribution is localized at the X point, while the second is situated in the vicinity of the Γ point. This suggests a combination of the exciton at the Γ point with the second excitonic state of the peak A (second energy in the excitonic Rydberg-like series), with overlapping energies. The Γ exciton thus originates from transitions between the O p states at the VBM (t_{1u}) and the hybridized Ca-O s states at the CBM (a_{1g}).

The introduction of the e-h interaction gives rise to the sharp peak C at 11 eV, which suggests its many-body origin. As shown in Figure 4.2d, the excitations from the VBM to the third conduction band (e_g) at the Γ point contribute largely to the excitonic wavefunction of the peak C. However, a larger contribution originates from points outside the high-symmetry paths.

The origin of the spectral features in the imaginary part of the dielectric function can be traced back to the electronic band structure. In Figure 4.3 we plot the JBS of CaO, which were obtained by subtracting the conduction bands from the valence bands. The colors in JBS correspond to different conduction bands from which all valence bands were subtracted. The IPA and quasi-particle IPA (SCAN+G_0W_0) spectra are directly proportional to the joint density of states (JDOS) peaks in Figure 4.3c. For example, the distinct G_0W_0 peak at 14 eV corresponds to the maximum in JDOS due to transitions to the third conduction band at the X and L points,

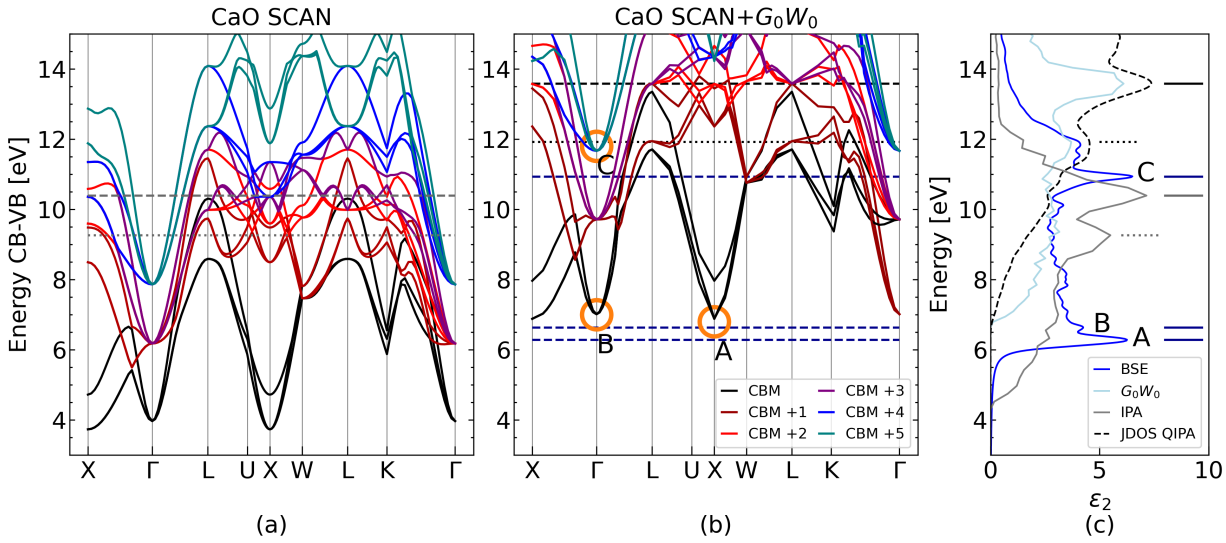

Figure 4.3: Joint band structure of CaO calculated using (a) SCAN and (b) SCAN+G_0W_0 methods, compared with the (c) k-mesh averaged (6x6) imaginary dielectric function calculated using BSE (blue line), SCAN+G_0W_0 (light blue line) and SCAN (grey line), as well as quasi-particle JDOS (dashed black line). The energy of the peaks highlighted in the panel (c) are represented by horizontal lines in the corresponding JBS diagrams in the panels (a) and (b).

whereas peak just below 12 eV coincides with a JDOS peak formed due to transitions to the fifth and sixth lowest conduction bands at the Γ point.

The excitonic peaks A, B and C shown in Figure 4.3a,b are related to M_0 type critical points, highlighted by the orange circles. The formation of the excitons A and B is related to the minima in JBS at the X and Γ points, respectively, as shown in Figure 4.3b,c. The peak C positioned at 11 eV raises some controversy since it resembles a sharp excitonic peak, yet it is located deep in the spectrum. The proposed explanation for the peak C was an exciton formed between the third-highest valence band and the conduction band minimum [88]; however, this transition could only produce a peak around 8 eV. A more plausible explanation is the Γ point excitation from the VBM to the third conduction band, deduced from the JBS [90]. In order to characterize this peak we analyze both interband transitions and the BSE excitonic wavefunction. The G_0W_0 joint density of states exhibits a peak below 12 eV, which is related to the interband transitions at the Γ point. The peak C in the BSE spectrum is formed less than 1 eV below. This exciton has a large e-h coupling contribution at the Γ point with the binding energy of 0.56 eV. However, roughly a double oscillator strength originates from outside of any high symmetry path. The JDOS in Figure 4.3c also displays a small peak at the energy of the peak C, that originates from the BZ edges. The peak C is therefore a combination of interband transitions and a Γ bound exciton between the VBM and the third lowest conduction band.

α-SiO_2

An alternative approach to the G_0W_0+BSE method is the use of a scissor operator and a model screening function within the mBSE framework [126]. This approach is characterized by favourable convergence behaviour of the exciton binding energies (E_b) with respect to k-point sampling. However, it does not incorporate the GW corrections to the electronic structure, which

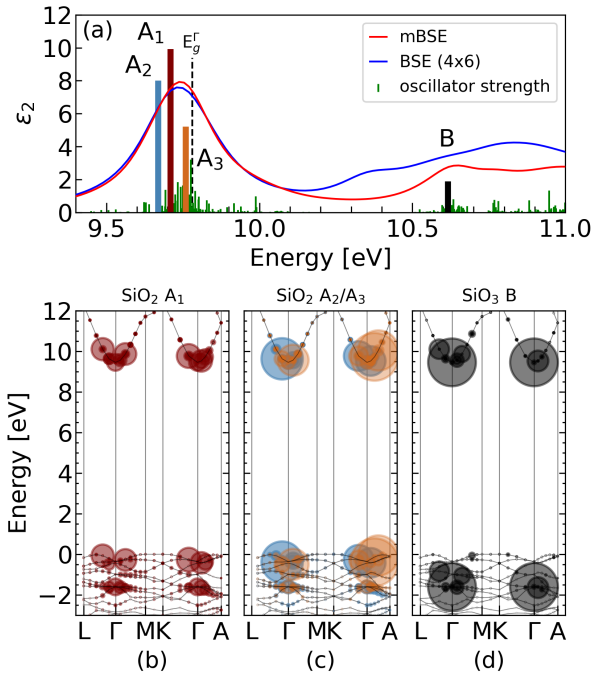

Figure 4.4: Optical spectrum of α-SiO_2. (a) Dielectric function calculated using SCAN+mBSE on dense 12^3 k-points mesh (red line), with corresponding oscillator strengths (green bars), compared to G_0W_0+BSE averaged over multiple k-meshes (blue line), with the calculated band gap (dashed black line). (b–d) Band structures with contribution to the exciton wavefunctions of the corresponding peaks.

can lead to discrepancies with experimental data. In particular, the GW corrections affect the localized *d* orbitals more than the *p* and *s* states [94]. This causes differences between the mBSE and G_0W_0+BSE spectra for materials containing Fe or Ca atoms. On the contrary, there is a notable agreement between the two methods for α-Al_2O_3 and α-SiO_2 [83].

As shown in Figure 4.1, the experimental dielectric function ϵ_2 of silica exhibits three main peaks. The lowest intensity peak positioned at 14 eV is well reproduced by the G_0W_0 method and originates from interband transitions. On the other hand, the two lower energy peaks are resolved only by the BSE method [96, 132], which manifests their excitonic origin. Figure 3.2b shows that the band gap separates the valence bands with mostly O *p* character from the mixed Si and O conduction bands. Note that the lowest conduction band consists mainly of O *s* states.

The first excitonic peak A is composed of three high intensity transitions, labeled here as A_1–A_3, and several lower intensity transitions, as shown in Figure 4.4a. The peak A is formed primarily between the upper three O *p* valence bands and the hybridized Si-O *s* conduction band minimum, as shown in Figure 4.4b and c. The peak A also contains contributions from transitions to lower-lying conduction bands at the Γ point. In comparison to CaO, the excitonic wavefunction of the peak A in α-SiO_2 is more delocalized in k-space, with contributions from multiple bands. This k-space delocalization indicates the presence of more localized excitons in real space.

The peak B is located above the fundamental band gap and corresponds to excitations from lower valence bands. Figure 4.4c assigns the peak B to the first bright Γ point exciton, which originates from transitions between the fifth-highest valence band and the CBM. Its more

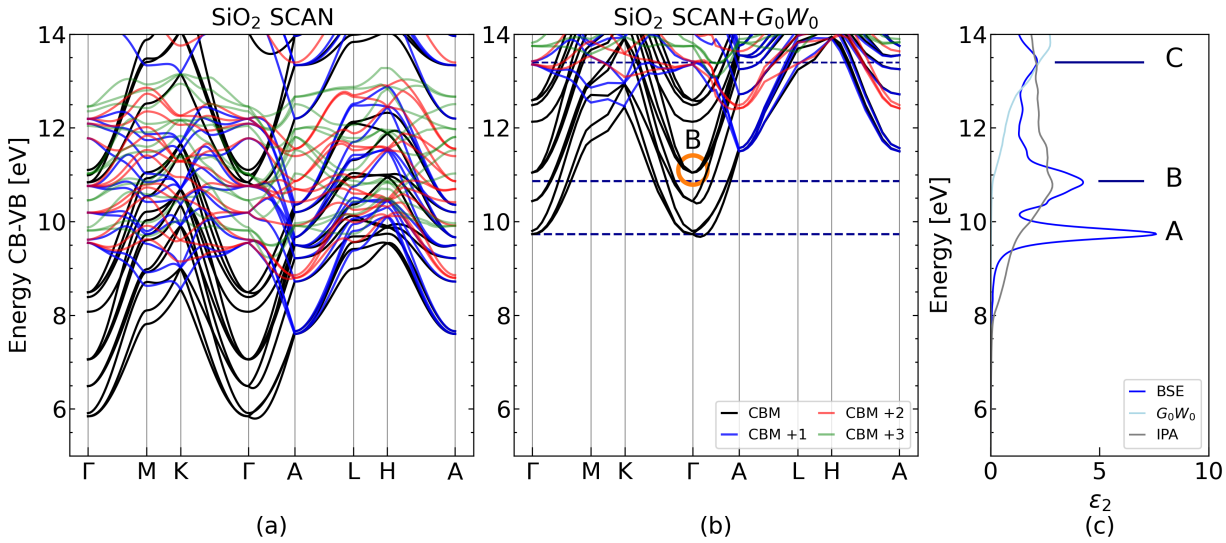

Figure 4.5: Joint band structure of α-SiO_2 calculated using the (a) SCAN and (b) SCAN+G_0W_0 methods, compared with the (c) imaginary dielectric function calculated using BSE (blue line), SCAN+G_0W_0 (light blue line) and SCAN (grey line). The energy of highlighted peaks are represented by horizontal lines in the corresponding JBS diagrams.

localized excitonic wavefunction within the first BZ indicates that the exciton B is more dispersed than the exciton A, which is consistent with the calculated hole charge density [96].

Figure 4.5 shows that the peaks A and B originate from excitations involving the lowest conduction band. The joint band structure of α-SiO_2 explains the formation of multiple transitions with high oscillator strength that contribute to the exciton peak A. The transitions from the uppermost valence bands to the CBM at the Γ point are mostly M_1 saddle points, which are unable to host an exciton [131]. On the other hand, the JBS exhibits various minima in close proximity to the Γ point, where excitons can form. This gives rise to many transitions that contribute to the peak A, especially the distinct minimum in the Γ−A direction responsible for the exciton A_3, as shown in Figure 4.4c. The excitons of the peak A also contain e-h interactions that originate from lower-lying bands at the Γ point, as shown in Figure 4.4a,b. The contribution to the coupling coefficient from the lower-lying conduction bands is roughly 30%, which implies formation of a Γ point exciton with large binding energy. The exciton A is therefore a resonance state between a strongly bound Γ point exciton and multiple interband transitions of similar energy, which explains the many high oscillator strength contributions and the high intensity of the peak. The third peak C emerges from transitions to the second and third lowest conduction bands at the Γ point, which is shown by the blue and red lines in Figure 4.5b.

The electronic band gap of α-SiO_2 has to be larger than the tabulated value of 9.65 eV [91], since the first exciton peak was experimentally found at 10.3 eV [127]. The interband transition peak C in the BSE spectrum is separated from its experimental equivalent by 0.7 eV. Given that the calculated indirect band gap is 9.27 eV (see Table 3.2), the fundamental gap can be estimated to be around 10 eV. This discrepancy arises since the experimental optical band gap is evaluated from the interpolation of the linear part of the spectral onset. In the presence of excitons, this method is strongly biased and can lead to a significant underestimation of the electronic band gap. The shift of the SCAN+G_0W_0 spectrum with respect to the experiment

may be related to the overestimation of the theoretical lattice parameters (see Table 3.1).

α-Al_2O_3

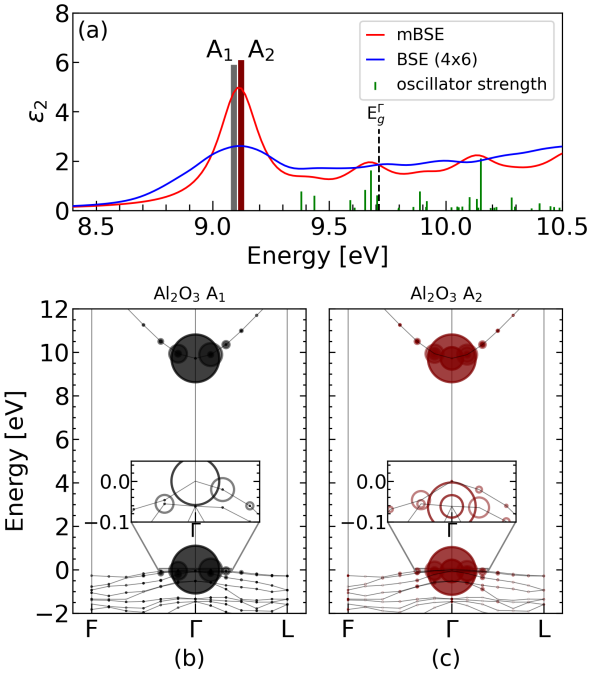

Figure 4.6: Optical spectrum of α-Al_2O_3. (a) Dielectric function calculated using SCAN+mBSE on dense 12^3 k-points mesh (red line), with corresponding oscillator strengths (green bars), compared to G_0W_0+BSE (blue line), with the calculated band gap (dashed black line). (b, c) Band structures with contribution to the excitonic wavefunctions of the corresponding peaks weighted by the $X_\lambda^{cv\mathbf{k}}$ term [83].

The experimental dielectric function of alumina shown in Figure 4.1 exhibits a small peak below 10 eV and a prominent broad peak at 13 eV, the latter of which is also present in the G_0W_0 spectrum. We label these peaks as A and B. The positions and intensities of the BSE peaks show an excellent agreement with the experimental data.

As shown in Figure 4.6a, the peak A has two strong contributions from nearly degenerate excitations, labeled A_1 at 9 eV and A_2 at 9.25 eV, which is consistent with previous reports [133, 134]. The two excitons are highly localized at the Γ point, as illustrated in Figure 4.6b–c. They originate from the splitting of the O p orbital into a single p_z uppermost valence band with a_{2u} symmetry, which gives rise to the exciton A_1, and a doubly degenerate $p_{x/y}$ band with e_u symmetry, which corresponds to the exciton A_2. The splitting is detailed in the insets of Figure 4.6b–c. The SCAN+G_0W_0 method predicts the energy difference between the two split bands to be 0.06 eV.

The BSE equivalent of the peak B is located at 12.5 eV, which is in good agreement with the experimental results [128], as shown in Figure 4.1c. The experimental peak is split into the lower and higher energy peaks, separated by 0.7 eV. The same splitting is observed in the ϵ_2 spectrum calculated using the BSE approach, but it is missing in the G_0W_0 spectrum, which

suggests the importance of the e-h interaction in the formation of the highest intensity peak of alumina.

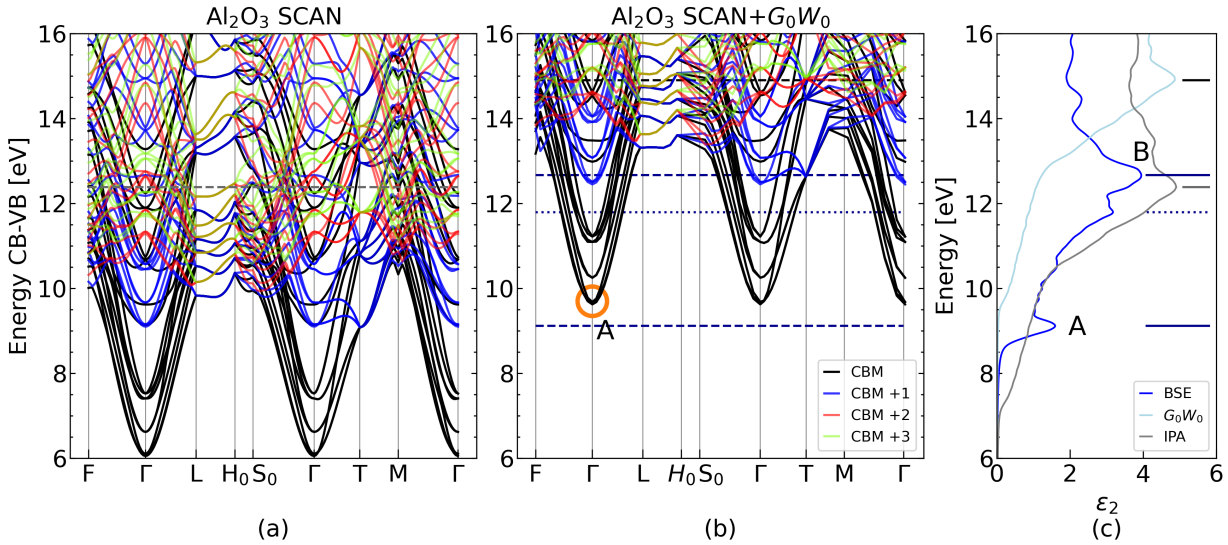

Figure 4.7: Joint band structure of α-Al_2O_3 calculated using (a) SCAN and (b) SCAN+G_0W_0 methods, compared with the (c) k-mesh averaged imaginary dielectric function calculated using BSE (blue line), SCAN+G_0W_0 (light blue line) and SCAN (grey line). The energies of highlighted peaks are represented by horizontal lines in the corresponding JBS diagrams.

The optical spectrum of α-Al_2O_3 exhibits two main features, the exciton peak A and the high intensity peak B, as shown in Figure 4.7c. The excitons that contribute to the peak A correspond to the M_0 critical points formed by transitions between the VBM and the Al-O hybridized CBM with a s character (a_{1g}). The high intensity peak B at 12.5 eV coincides with the transition energy from the VBM to the second-lowest conduction band at the Γ and T points, as shown in Figure 4.7b. Furthermore, BSE calculations reveal an additional peak on the low-energy shoulder of the peak B, right below 12 eV, which has a non-zero BSE oscillator strength. This peak, in 4.7b–c plotted using dotted lines, corresponds to a bound exciton which stems from transitions into the second lowest conduction band at the Γ point.

α-Fe_2O_3

The valence bands of hematite above -8 eV have been characterized as the flat Fe d states hybridized with the O p states [94,135], in agreement with our calculations. The GW corrections open the electronic gap and enhance the separation of bands without changing their order. The VBM exhibits a mixed character, with contributions from the Fe $d_{yz/xz}$ and d_{xy/x^2-y^2} states, as well as the in-plane O $p_{x/y}$ electrons. The lowest conduction bands are mainly formed by the Fe d states, which are split into two sets of bands, as shown in Figure 3.2. The SCAN functional predicts the separation of the two sets of d bands to be 1.59 eV, in close agreement with the GGA results [94]. The SCAN+G_0W_0 method approaches the experimental value of 1.39 eV [136] by predicting a splitting of 1.43 eV.

The dielectric function of α-Fe_2O_3 measured at room temperature [129] exhibits a prominent peak at 3 eV and a broader peak below 5 eV (Figure 4.1). These peaks originate from interband

transitions between the d bands, since they are also present in the GW spectrum. The inclusion of the e-h interaction red-shifts the G_0W_0 spectrum by 1 eV. The BSE redistribution has a weaker effect on the spectrum than in the wide band gap oxides. Nevertheless, the onset of the spectrum is raised due to the formation of excitons with low binding energies, which are insufficient to form a distinct peak. The dielectric constants of both the real and imaginary dielectric spectra are higher in α-Fe_2O_3 than in the other three simple oxides, as shown in Table 4.1.

The BSE spectrum of α-Fe_2O_3 exhibits three distinct peaks below 7 eV, as shown in Figure 4.1, including several bright excitons below the band gap energy, as shown in Figure 4.8a. The shoulder of the main peak is primarily formed by the exciton A_1, followed by the less intense exciton A_2, both of which are doubly degenerate. The Exciton A_1 is a band-edge excitation that originates from two regions of the BZ with similar contributions between the S_0–Γ and L–H_0 points. The intensity of the exciton A_2 is one-fifth that of the main peak and has minimal influence on the spectral shape. Both excitons stem from transitions between the Fe d dominated bands, which become symmetry-allowed thanks to the mixing of the valence states with the O p orbitals.

The band gap edges in α-Fe_2O_3 consist of the flat d bands. Therefore, the bands in JBS shown in Figure 4.9 are more compressed and the interband transitions responsible for the spectral features are more difficult to track. The large number of available transitions results in the spectral peaks with high intensity and multiple bright excitons. The main BSE peak, located at 2.6 eV, is related to interband transitions from the upper valence band to the three lowest

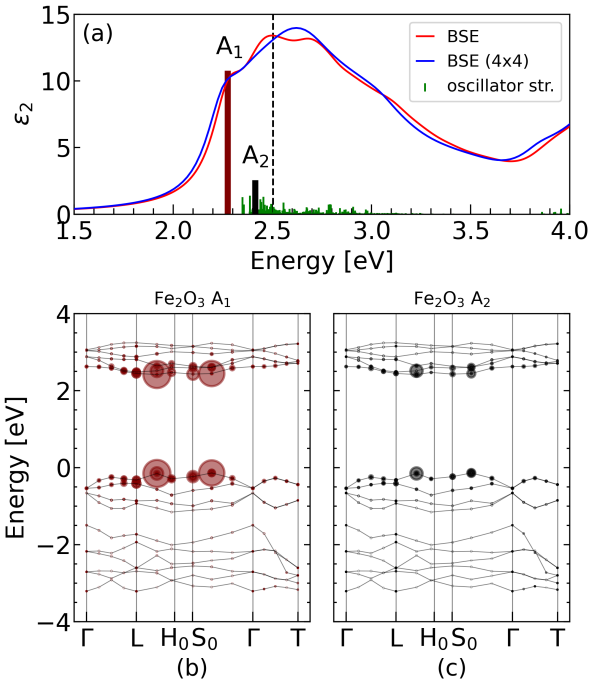

Figure 4.8: (a) Dielectric function of α-Fe_2O_3 calculated using G_0W_0+BSE calculated on a 8^3 k-mesh (red line), with corresponding oscillator strengths (green bars), compared to the BSE spectrum averaged over multiple k-meshes (blue line), and the calculated smallest direct band gap (dashed black line). (b, c) Band structure segments with contributions to the excitonic wavefunctions of corresponding excitonic peaks, given by the size of circles.

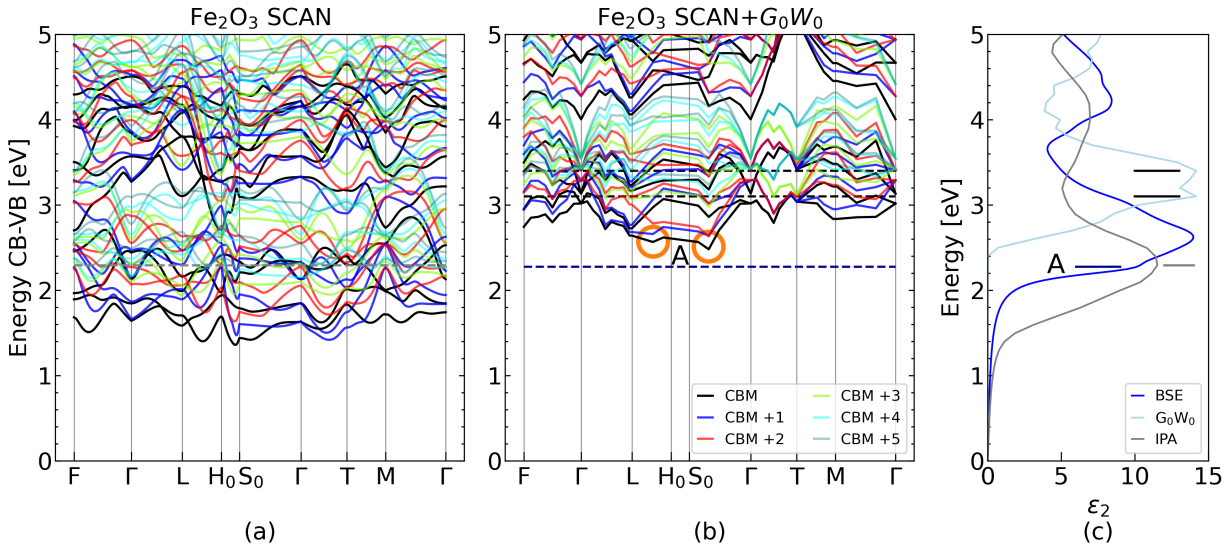

Figure 4.9: Joint band structure of α-Fe_2O_3 calculated using (a) SCAN and (b) SCAN+G_0W_0 methods, compared with (c) imaginary dielectric function calculated using BSE (blue line), SCAN+G_0W_0 (light blue line) and SCAN (grey line). Energies of the highlighted peaks are denoted by horizontal lines in the corresponding JBS diagrams.

conduction bands. The onset of the spectrum is modified by the exciton A, which is located at two JBS minima, highlighted by the orange circles in Figure 4.9b.

The delocalization of excitons in reciprocal space is larger in hematite than in CaO and α-Al_2O_3, which indicates a more localized exciton in real space in hematite. Furthermore, the contribution to the exciton wavefunction along the Γ–T path is smaller in α-Fe_2O_3 than in other directions, which suggests excitonic anisotropy. In fact, α-Fe_2O_3 shows the largest birefringence among the four cement-forming oxides, with the exciton predominantly associated with the polarization along the xy plane.

Binding energy

The position of an exciton peak is determined by the binding energy of the e-h pairs. The simple Wannier-Mott (WM) model of exciton defines the binding energy E_b as

$$E_b^n = -R\frac{\mu}{m_0\epsilon_\infty^2 n^2}, \tag{4.1}$$

with the Rydberg constant R ≈ 13.6 eV, the reduced exciton mass µ, the high-frequency electronic dielectric constant ϵ_∞, and the principal quantum number n in the exciton Rydberg-like series. The reduced effective mass μ is defined as $\mu^{-1} = m_e^{-1} + m_h^{-1}$, where m_e and m_h are the harmonic averages of the electron and hole effective masses over different directions in reciprocal space. The effective masses were obtained by means of the quadratic band approximation. The exciton radius can be approximated as

$$r_b^n = \frac{\epsilon_\infty a_0 m_0 n^2}{\mu}, \tag{4.2}$$

Table 4.1: Electronic dielectric constant ϵ_∞, ionic dielectric constant ϵ_I, effective masses of electrons m_e, light holes m_{lh} and heavy holes m_{hh}, and reduced effective masses corresponding to light μ_{lh} and heavy holes μ_{hh} of CaO, α-SiO_2, α-Al_2O_3 and α-Fe_2O_3, calculated using SCAN. The effective masses are given in units of the electron rest mass m_0.

	Dielectric constants						Effective masses					
	SCAN				SCAN+G_0W_0							
	ϵ_∞^{xy}	ϵ_∞^{z}	ϵ_I^{xy}	ϵ_I^{z}	ϵ_∞^{xy}	ϵ_∞^{z}		m_e^* [m_0]	m_{lh}^* [-m_0]	m_{hh}^* [-m_0]	μ_{lh} [m_0]	μ_{hh} [m_0]
CaO	3.53		10.00		3.26	-	Γ	0.31	0.33	1.82	0.16	0.27
							X	0.46	0.75	1.62	0.29	0.36
SiO_2	2.32	2.34	2.02	2.19	2.18	2.19	Γ	0.47	0.93	2.39	0.31	0.39
Al_2O_3	3.06	3.03	5.99	7.68	2.84	2.81	Γ	0.35	0.50	3.28	0.21	0.31
Fe_2O_3	9.89	8.38	42.66	8.77	8.16	7.06	S_0Γ	1.65	-	2.31	-	1.02
							H_0L	2.31	-	1.69	-	0.98

where a_0 is the Bohr radius ($a_0 \approx 5.29$ nm). The dielectric constants, effective masses and reduced effective masses are collected in Table 4.1. The smallest effective masses were found in CaO and α-Al_2O_3, while the largest effective masses are in α-Fe_2O_3 thanks to the flat d orbitals at the band gap edges.

The static dielectric constants calculated using the SCAN functional are listed in Table 4.1. The static electronic dielectric constant, ϵ_∞, can be obtained from the plateau of ϵ_1 at wavelengths within the electronic band gap and below the onset of phonon absorption, where only the electronic polarization contributes to the dielectric response, as shown in Figure 2.6. Cubic CaO is isotropic with electronic dielectric constant equal to $\epsilon_\infty = 3.5$. In comparison, α-SiO_2 and α-Al_2O_3 show small anisotropy, with ϵ_∞ approaching 2.3 and 3.0, respectively. The largest dielectric constant and anisotropy were found in α-Fe_2O_3. In comparison to GGA, the SCAN calculations yield lower dielectric constants.

The BSE calculations predict CaO binding energies equal to 0.52 eV, 0.35 eV, and 0.56 eV for the excitons A, B, and C, following the notation in Figure 4.2, respectively. In contrast, the WM model estimates the binding energies of the three excitons to be 0.31 eV, 0.17 eV, and 0.27 eV. The larger binding energy of the X point exciton, corresponding to the peak A, is in agreement with the WM model, mainly due to the flatter CBM. The exciton radii were calculated as 6.1 Å, 4.5 Å and 2.4 Å, respectively for excitons A, B and C.

In the case of CaO, a comparison can be made between the calculated and experimental spectra measured at low temperatures (25 K) [88]. The experimental peaks at 7.25 and 10 eV, which originate from interband transitions, align with the BSE spectrum calculated on a 20^3 k-mesh when the calculated curve is blue-shifted by 0.18 eV. If we suggest the same error in the entire band structure, this value corresponds to the G_0W_0 underestimation of the band gap. By adding this difference to the calculated GW band gap, we obtained $E_g^X = 6.94$ eV and $E_g^\Gamma = 7.09$. Similarly, the excitons in the experimental and BSE spectra agree within the shift of 0.56 and 0.42 eV for the peaks A and B, respectively. By subtracting 0.18 eV from the red-shift of these calculated exciton positions, we can estimate the binding energies for CaO. In fact this simple approach predicts $E_b^A = 0.14$ eV and $E_b^B = 0.11$ eV [83]. The BSE calculation predicts almost four times larger binding energies, which is caused mostly by the underscreening of the

e-h interaction.

The peak A in α-SiO_2 has three main contributions with binding energies of 0.34, 0.31, and 0.33 eV, in order of decreasing oscillator strength. The first bright exciton, which originates exclusively from the Γ point, is the peak B with $E_b = 0.41$ eV. The dark excitons are strongly bound, with binding energies around 1.3 eV. When the WM model was applied at the Γ point, the binding energy of the exciton B was found to be 0.78 eV, with a radius of 3.94 Å.

In the case of α-Al_2O_3, the single peak observed below the band gap energy consists of two excitons A_1 and A_2. Their binding energies, calculated using the mBSE method, are 0.52 eV and 0.55 eV, respectively. The WM model predicts that the heavy hole exciton is bound by $E_b(A_1) = 0.30$ eV and the light hole exciton by $E_b(A_2) = 0.46$ eV. The corresponding radii are 7.9 Å and 5.1 Å.

The BSE binding energy of the exciton A in α-Fe_2O_3 equals to 0.23 eV. The WM model predicts bonding energies of $E_b = 0.16$ eV and $E_b = 0.15$ eV and the exciton Bohr radii of $r_b = 5.1$ Å and $r_b = 4.9$ Å for the excitons located between the S_0–Γ and L_0–H_0 points, respectively. The flat *d* bands involved in exciton formation correspond to higher effective masses of electrons and holes; however, the large dielectric constant of α-Fe_2O_3 reduces the binding energies.

The binding energies and exciton radii obtained using the WM model are only qualitative since they depend greatly on the dielectric constant chosen. One possible approach to reduce the binding energies and achieve better agreement with experiment is to use an effective dielectric constant, which takes into account the ionic dielectric constant and lattice screening. The WM exciton radius is the largest in Al_2O_3 and CaO, whereas the most localized exciton was found in SiO_2, in agreement with the exciton wavefunction analysis in Figure 4.2–Figure 4.8. The simple WM model correctly predicts the trends of the exciton binding energies and localization, but a deep and precise insight into the mechanisms of the e-h interaction requires using the BSE approach.

4.2.2 Optical spectrum - ionic contribution

In order to study optical properties in the IR range, we calculated the ionic contribution to the dielectric response using the finite-differences method [139]. In this approach, a series of self-consistent DFT calculations is performed for multiple small, symmetry-preserving ionic displacements around the equilibrium positions. From the forces and the resulting changes in the total energy, the dynamical matrix and Born effective charges are determined, which in turn allow the calculation of phonon frequencies and the lattice contribution to the dielectric tensor. This procedure captures the coupling between lattice vibrations and the macroscopic electric field, which is responsible for infrared absorption. The ionic dielectric functions of simple cement-forming oxides are shown in Figure 4.1, where the main phonon resonances and their relative strengths can be clearly identified.

The frequency-dependent IR refractive indices and extinction coefficients are shown in Figure 4.10. These quantities are directly derived from the real and imaginary parts of the complex dielectric function, following Equation 2.41 and Equation 2.42. The extinction coefficients calculated in this study are compared with available experimental curves [129, 137, 138]. To facilitate comparison with polycrystalline or randomly oriented samples, the calculated curves were obtained from dielectric functions averaged over the three principal polarization directions. It should be noted that, with the exception of CaO, the studied simple oxides exhibit optical anisotropy, as demonstrated by the experimental curves. This anisotropy originates from the

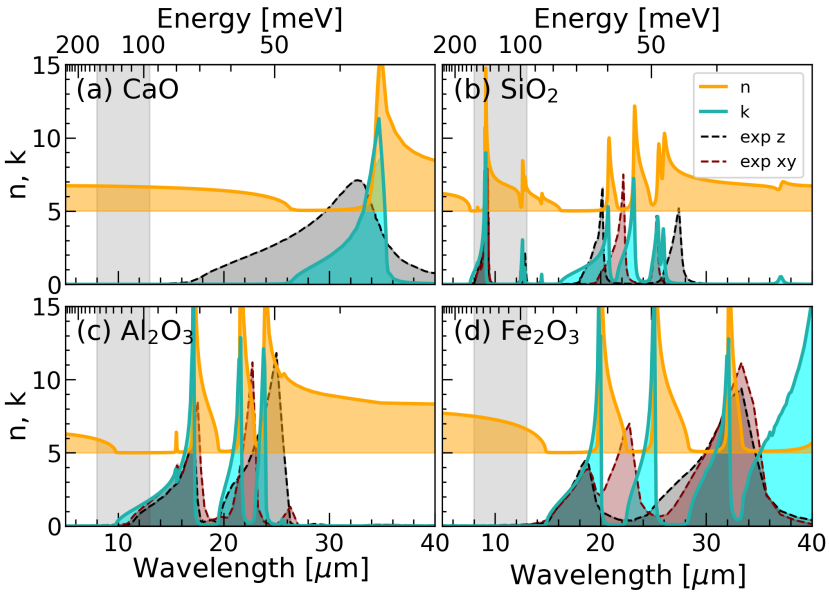

Figure 4.10: Refractive index n and extinction coefficient k in the IR spectral range for (a) CaO, (b) α-SiO_2, (c) α-Al_2O_3, and (d) α-Fe_2O_3, compared with experiments [129,137,138]. The experimental curves are separated for the extraordinary (in the xy plane) and ordinary (along the z axis) polarization rays. The refractive index n was shifted along the y axis for clarity. The atmospheric transparency window is shown by shaded area.

lower crystal symmetry and the directional character of bonding in these materials, which leads to polarization-dependent phonon modes and dielectric responses.

CaO exhibits a relatively simple IR absorption spectrum with a single dominant ϵ_1 peak, as shown in Figure 4.1. The absorption band coincides with the optical phonon branch at approximately 34 meV [140] and, as a consequence, the experimental refractive index exhibits a single pronounced peak at about 33 µm [137]. The positions of the experimental and calculated extinction coefficient peaks are in very good agreement, as shown in Figure 4.10a, whereas the intensities and widths differ somewhat due to temperature effects, anharmonic phonon broadening, and possible microstructural effects that are not captured in calculations. Apart from the IR absorption peak associated with lattice vibrations, CaO remains transparent over a wide range of IR wavelengths and absorbs only at photon energies above the electronic band gap, where interband electronic transitions become active.

In contrast, α-SiO_2 absorbs in the ATW region, highlighted by the shaded area in Figure 4.10, thanks to several pronounced k peaks around 9 and 12 µm. These absorption features are associated with Si-O stretching and bending vibrational modes, which are strongly IR-active.The simpler spectrum of α-Al_2O_3, characterized by three major peaks, agrees well with the experimental data [129] and reflects the vibrational modes of the AlO_6 octahedra. Hematite exhibits spectrum with the highest overall intensity and the largest static refractive index among the oxides considered. In general, we report good agreement with experimental data for all four oxides, particularly in the region below 20 µm, which is particularly relevant for thermal emission and radiative heat transfer applications.

The static dielectric constants of the simple cement-forming oxides are summarized in Table 4.1. The ionic contribution to the static dielectric constant is given by the large-wavelength

limit of the ionic dielectric function, which includes the full effect of lattice polarization. The isotropic ionic dielectric constant of CaO is equal to 10. On the other hand, the anisotropy of the hexagonal lattice is reflected in the ionic dielectric constants of quartz, alumina and hematite, which are equal to 2.0, 6.0 and 42.7 in the xy plane and 2.2, 7.7 and 8.8 along the z axis, respectively. The total static dielectric constant is obtained as the sum of the electronic and ionic contributions.

4.3 Cement phases

Figure 4.11 shows the electronic dielectric functions of the clinker and cement phases calculated using the SCAN functional in blue, the SCAN+G_0W_0 method in orange and the SCAN+G_0W_0+BSE method in red [105]. The electron-hole interaction included in the BSE results causes a red shift in the spectral weights, manifested as an enhanced spectral onset compared to GW spectra.

Alite exhibits a low-intensity excitonic peak below the band gap energy. This exciton forms at the Γ point between the three topmost valence bands and the CBM. The valence bands are mainly formed by O p electrons, while the CBM has s character with hybridized Ca and O orbitals, as shown in Figure 3.4. The low energy tail of ϵ_1 converges to the static electronic dielectric constant, while the negative parts of the real dielectric function are related to the formation of collective electronic excitations, called plasmons. The electronic dielectric constants of monoclinic alite are almost isotropic, equal to 3.1. The negative values of the real part of the dielectric function were found between 34 eV and 36 eV as calculated using the SCAN+G_0W_0 method [105].

Similarly to alite, the spectrum of β-belite is almost featureless below the band gap, as shown in Figure 4.11. There is a small peak within the band gap which is related to a Γ point exciton. Our BSE calculations show that excitons in both alite and β-belite are delocalized within the crystal [105]. The crystal structure of β-belite is slightly more anisotropic with electronic dielectric constants equal to 3.13 along the x and z directions, and 3.19 along the y axis. The GW calculations show that the real part of the dielectric function, ϵ_1, becomes negative at around 30 eV over a short energy range.

Among the cement phases, gypsum has the most pronounced exciton clearly separated from the rest of the spectrum, which reveals its large binding energy. This exciton originates at the Γ point [105]. The valence electrons are of the O p type, while the CBM is of the s type with hybridization of all constituent atoms, as Figure 3.4 shows. The electronic dielectric constant of 2.54 is almost isotropic. The ϵ_1 function calculated using the G_0W_0 method approaches zero at 24 eV and 34 eV, but never reaches negative values.

β-anhydrate is an indirect insulator, which explains the lack of peaks below the indirect gap in the BSE spectrum, as shown in Figure 4.11. However, spectral features appear below the lowest direct band gap, suggesting the presence of bound excitons. The excitonic wavefunction of the bright excitons is spread throughout the first BZ, suggesting low spatial extent and localized electron-hole pairs [105]. The highest valence bands consist mainly of O p states with some contribution from sulphur ions, as shown in Figure 3.4. The bottom of the conduction band is characterized primarily by the Ca-S overlap and by the hybridization of O-S s orbitals around the Γ point. The electronic dielectric constant is anisotropic, with values of 2.73 and 2.75 along the x and z directions, respectively, and 2.88 along the y axis. The plasmon peak is located at

approximately 34 eV [105].

The electronic dielectric function of C3A was calculated on the IPA level only, due to the large unit cell of C3A, shown in Figure 3.3. The cubic crystal exhibits an electronic dielectric constant of 2.6, obtained from the low-frequency limit of the real part of the dielectric function.

Similarly to Fe_2O_3 hematite, brownmillerite has a smaller band gap due to the Fe d states at the band gap edges. The BSE calculation reveals a peak below the GW band gap energy that is

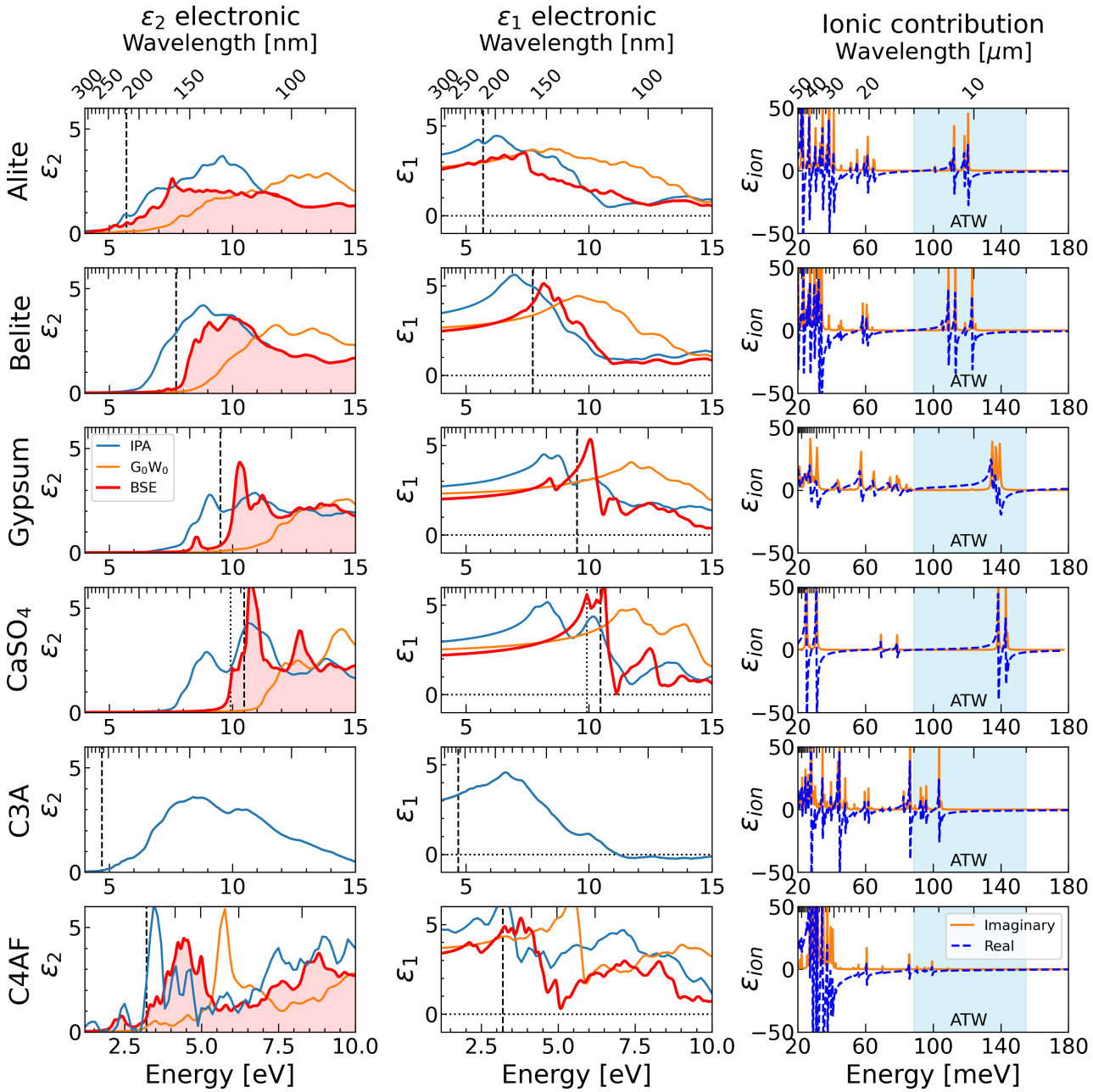

Figure 4.11: Calculated electronic and ionic dielectric functions of clinker and cement phases. The vertical dashed black lines correspond to the GW band gaps, except from the case of C3A where they represent the SCAN band gap. The blue regions in the ionic response panels show the IR atmospheric transparency window.

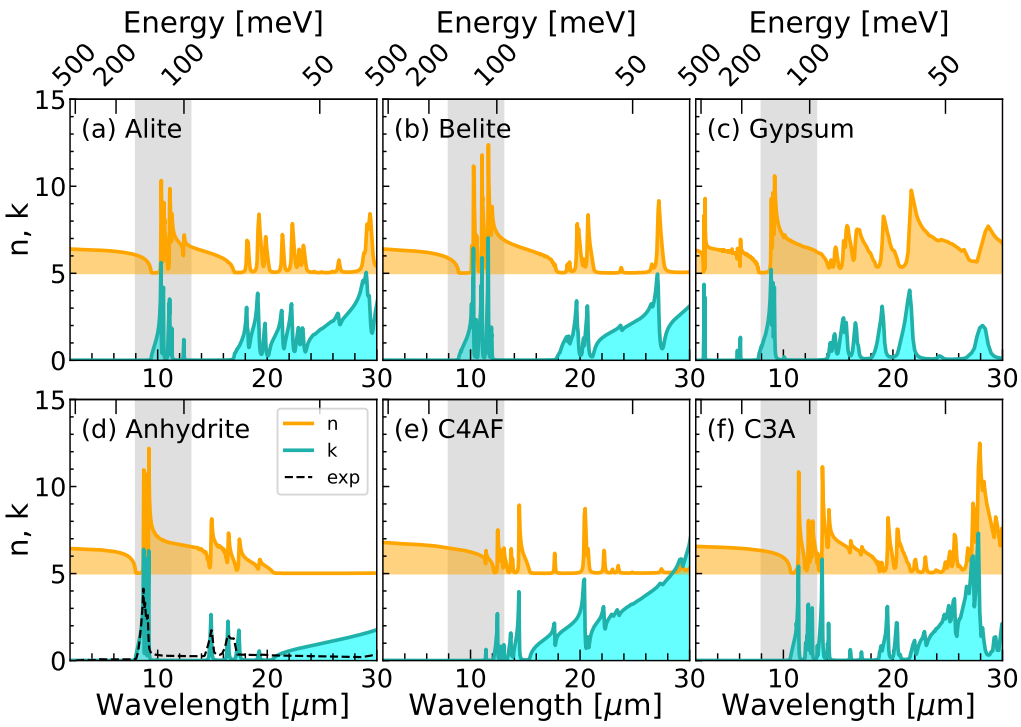

Figure 4.12: Calculated complex refractive indices of cement phases. Results for anhydrite $CaSO_4$ curve are compared with experimental data [141]. The shaded areas correspond to the ATW region.

well separated from the rest of the spectrum. This separation indicates the formation of strongly bound excitons in C4AF, which further reduces the optical absorption edge. Consequently, C4AF absorbs in the visible spectral range, which leads to a potential overheating in outdoor conditions. The static electronic dielectric constants are 4.02, 4.69 and 4.50 along the x, y and z axes, respectively.

The calculated ionic dielectric constants reveal a pronounced anisotropy in several of the clinker and sulfate phases. The optical properties of monoclinic and orthorhombic crystal structures of the calculated cement phases are anisotropic due to their lower crystal symmetry. Most of the cement oxides exhibit exciton peaks in only one polarization direction, resulting in diminished exciton peaks in the averaged spectra. Noteworthy, β-anhydrite exhibits excitons in all three directions that are slightly shifted with respect to each other, which reduces their intensity in the averaged spectrum [105]. The anisotropy in C4AF also reduces the height of the exciton peak in the averaged spectrum. In this case, the exciton is formed in the y and z directions.

The ionic response is key when evaluating the radiative cooling potential of cement phases. As Figure 4.12 shows, all cement phases exhibit absorption bands in the ATW region. The refractive index of β-ahnydrite can be compared with experimental data [141]. The measured and calculated curves overlap almost perfectly, with differences only in the intensity of the peaks, which can be attributed to finite temperature effects during measurement.

In alite, the ionic dielectric constants along the x, y, and z axes are 6.07, 6.72, and 9.72, respectively, indicating a moderately stronger lattice polarization along the z direction. β-belite exhibits a larger overall ionic contribution, with values of 11.63, 15.73, and 11.88 along

the x, y, and z axes, respectively. The particularly high value along the y axis suggests the presence of strongly IR-active phonon modes involving displacements of calcium and silicate units in that direction. Gypsum shows a markedly different behavior, with ionic dielectric constants of 7.36, 2.71, and 2.61 along the x, y, and z axes, respectively. This strong anisotropy can be attributed to its layered crystal structure and the orientation of sulfate groups and water molecules, which leads to highly directional vibrational modes. In all three monoclinic structures (alite, β-belite, and gypsum) the dielectric tensor also contains non-zero off-diagonal xz components. These terms arise because the principal axes of polarization do not coincide exactly with the crystallographic axes in monoclinic symmetry, which leads to coupling between electric fields applied along different directions. For β-anhydrite, the ionic dielectric constants are 4.71, 4.42, and 3.73 along the x, y, and z axes, respectively. These values are smaller and more isotropic than those of gypsum, which is consistent with the absence of water and the more compact arrangement of sulfate tetrahedra in the anhydrite structure. In the case of C4AF, the calculated ionic dielectric constants are 8.60, 10.53, and 8.29 along the x, y, and z axes, respectively. The relatively high values reflect the complex crystal structure and the presence of multiple cation species, which give rise to a complex spectrum of IR-active phonon modes that contribute to the dielectric response. Finally, C3A exhibits an isotropic ionic dielectric constant of 8.52 thanks to its cubic symmetry.

4.4 Hydrated concrete phases

The hydrated phases form the skeleton of concrete that provides strength and acts as a medium for additives, air pores and other constituents. The calculated dielectric constants of the hydrated phases are summarized in Figure 4.13. All the tested concrete phases have similar electronic band gaps between 7 and 8 eV, which make them transparent to solar radiation.

The BSE spectrum of tobermorite 14Å (T14) exhibits two low-intensity peaks below the band gap energy. Its electronic polarizability is almost isotropic, with a dielectric constant of 2.37. The exciton peak is predominantly present in the x and y polarization directions, i.e. in plane of the Ca-Si slabs. Overall, the inclusion of e-h interaction through the BSE formalism has only a small effect on the spectrum of T14 when compared to the IPA curve.

Similarly, tobermorite 11Å (T11) has a non-negligible dielectric function below the GW band gap, but there are no clearly defined peaks within the band gap. In T11, the exciton peaks in different polarization directions are shifted with respect to each other, which leads to a smoother averaged spectrum. The electronic dielectric constants of T11 are slightly anisotropic, equal to 2.56, 2.51 and 2.53 in the x, y and z directions, respectively. Although the e-h interaction in T11 phases is not strong enough to form distinct exciton peaks, it redistributes the spectral weights and is necessary for the accurate description of the optical spectra.

Portlandite exhibits a strong exciton peak just above 6 eV with the binding energy of 0.98 eV, in agreement with the earlier reports [142]. The exciton peak is observed in the xy plane, which corresponds to the $Ca(OH)_2$ layers. Similarly to CaO, the dielectric spectrum of portlandite has various high intensity BSE peaks at higher energies. CaO-based materials therefore have strong e-h interactions that noticeably modifies the optical spectrum in a wide range of energies. The electronic dielectric constants calculated using the SCAN functional are 2.65 in the x and y directions and 2.57 in the z direction.

Hydrated tricalcium aluminate has a low intensity excitonic peak that is clearly separated

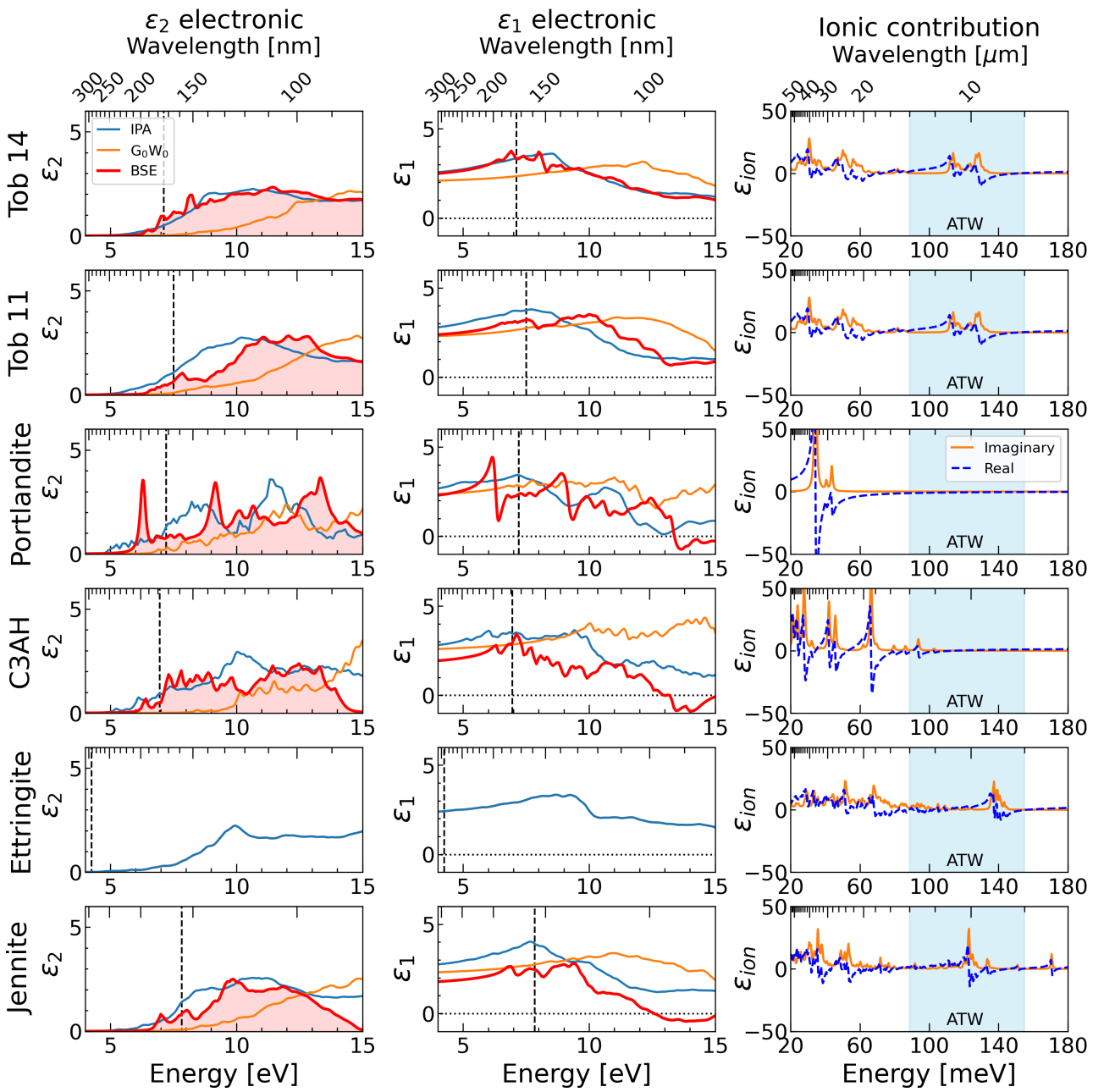

Figure 4.13: Calculated electronic and ionic dielectric functions of hydrated phases. Dashed black lines correspond to corrected GW band gaps (in the case of ettringite SCAN band gap). Blue regions show the IR atmospheric transparency window.

from the spectrum below the GW band gap energy. The strongly bound exciton is located at the Γ point. The e-h coupling also introduces various peaks just above the band gap energy. The isotropic electronic dielectric constant is equal to 2.56.

Since we did not calculate the G_0W_0+BSE spectrum of ettringite, we approximate its dielectric function by the IPA solution. A comparison with other phases helps us to evaluate the reliability of this approximation. The BSE spectra of T14, as well as those of alite and belite, closely resemble the corresponding IPA curves, with only minor changes near the absorption

onset and small excitonic features. These similarities indicate that e-h interactions in some wide band gap phases have a relatively modest effect on the overall spectral shape. On this basis, a simplified description of the dielectric response using IPA spectra in the cases of C3A and ettringite can be considered a reasonable first approximation. The calculated electronic dielectric constants of ettringite are 2.24 in the x and y directions and 2.21 in the z direction. These values indicate a very small anisotropy of the electronic dielectric response.

Jennite is a calcium silicate hydrate whose optical spectrum reveals a pronounced excitonic feature at approximately 7 eV, with an exciton binding energy of approximately 1.07 eV. The calculated binding energies are overestimated due to the sparse k-meshes used in the calculations and real binding energies may be less than half as large. The excitonic transitions are the strongest along the y axis, with some low intensity contributions from the remaining directions. Despite the directional dependence of individual spectral features, the overall electronic polarizability of jennite is nearly isotropic. The calculated electronic dielectric constants are approximately 2.53, with only minor differences between the crystallographic directions.

Except from portlandite, all hydrated phases exhibit absorption peaks in the ATW region, as shown in Figure 4.13. The absorption bands of T14, T11, ettringite and jennite in the ATW region originate from the Si-O bond, as shown in Figure 4.10. The ionic dielectric constants of T14 are 4.91, 4.07 and 5.85 along the x, y and z polarization directions, while somewhat larger dielectric constants were found in T11, equal to 5.86, 5.77 and 5.29 for the x, y and z axes, respectively. The most anisotropic dielectric constants were found in portlandite, with 8.85 in the in-plane and 1.63 in the out-of-plane direction, which originates from its layered structure. In contrast, the isotropic dielectric constant of cubic C3AH equals to 5.66. The dielectric constants

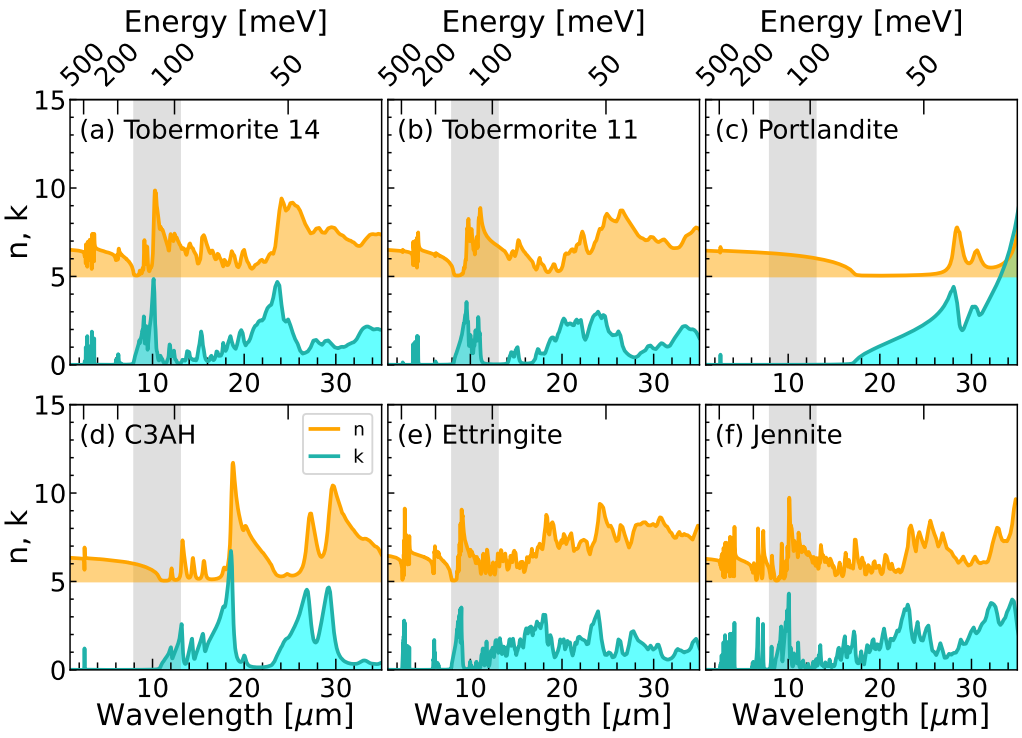

Figure 4.14: Calculated complex refractive indices of hydrated concrete phases. The shaded areas correspond to the IR atmospheric transparency window.

of ettringite are 5.69, 4.64 and 6.25, and the dielectric constants of jennite are 5.17, 5.66 and 7.80, along the x, y and z axis, respectively. The complex refractive indices of concrete phases in the IR range are plotted in Figure 4.14. A common feature of the hydrated phases is a series of peaks around 2.5 µm which are related to the O-H vibration modes.

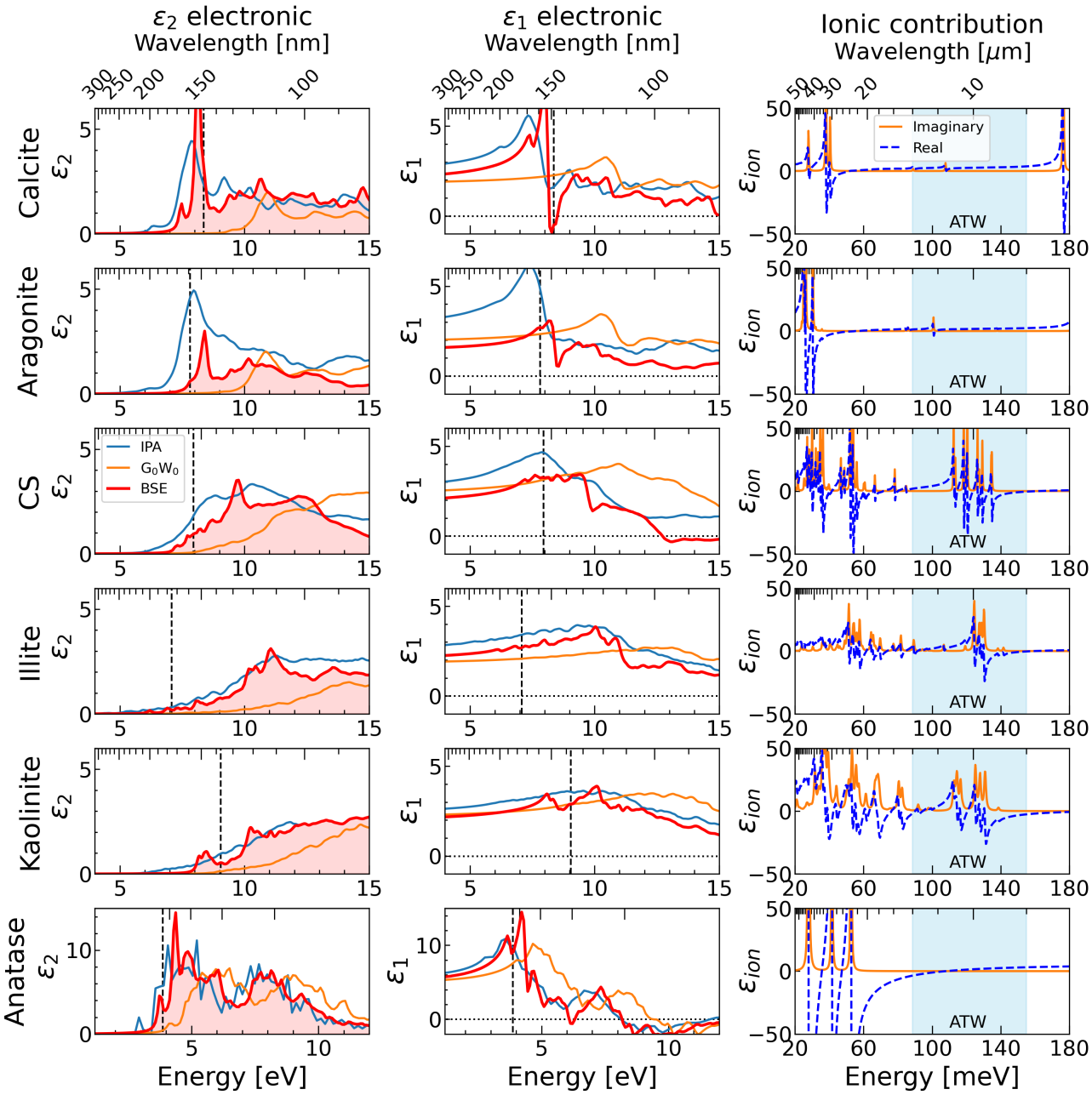

Figure 4.15: Calculated electronic and ionic dielectric functions of raw materials and concrete additives.

4.5 Raw materials and additives

The main raw material used in the production of cement is $CaCO_3$ in the form of limestone, which provides the primary source of CaO. Secondary input materials, most commonly clays and aluminosilicates, supply SiO_2, Al_2O_3, and other oxide building blocks required for the formation of clinker phases. The electronic and ionic dielectric functions of raw materials and some additives are summarized in Figure 4.15.

Both polymorphs of $CaCO_3$, calcite and aragonite, display large redistribution of spectral weights when comparing the GW and GW+BSE spectra. In calcite, the first high-intensity peak is clearly associated with a strongly bound exciton, which appears well below the quasiparticle band gap and dominates the absorption onset. On the other hand, the sharp peak observed in aragonite is positioned just above the band gap and requires a more detailed analysis.

Even though CS wollastonite and illite exhibit some spectral features below the GW band gap, they do not display high-intensity excitonic peaks comparable to those found in calcite or kaolinite. Especially in the case of illite, the IPA spectrum could serve as a reasonable approximation of the dielectric spectrum. Even though illite and kaolinite have similar layered crystal structures, the latter exhibits well separated excitonic peak. The broad exciton peak in kaolinite is composed of contributions in all three polarization directions.

The spectrum of anatase shows a well-defined exciton peak at the spectral onset, which is most pronounced in the x and y polarization directions. This anisotropy reflects the tetragonal crystal structure of anatase and the directional character of the Ti-O bonding network. The presence of a strong excitonic feature at the absorption edge is consistent with previous theoretical and experimental studies of TiO_2 polymorphs [143].

The electronic dielectric constants of calcite are 3.0 in the xy plane and 2.4 in the z direction, consistent with the layered arrangement of CO_3^{2-} units. A different structural arrangement of aragonite causes a distinct dielectric response. Its electronic dielectric constants are 2.54, 3.16, and 3.19 along the x, y, and z directions, respectively, with a more pronounced anisotropy and a generally higher polarizability along two of the crystallographic directions. In CS, the electronic dielectric constants are nearly isotropic, with values of approximately 2.77 along all principal directions. The dielectric constants of illite are 2.62, 2.61 and 2.67 along the x, y and z axes. These small differences indicate that the electronic contribution to the dielectric response is only weakly affected by the layered structure of illite, at least in the range of static electronic dielectric function. Kaolinite shows slightly lower values overall, with dielectric constants of 2.44, 2.55, and 2.46 along the x, y, and z directions. In contrast to the carbonates and silicates, anatase exhibits larger electronic dielectric constants, reaching 6.76 in the xy plane and 6.27 in the z direction. This enhanced polarizability is associated with the electronic structure of TiO_2, where the relatively small band gap and the presence of transition metal d states at the bottom of the conduction band, as shown in Figure 3.8, increase the oscillator strength of interband transitions.

Except from TiO_2, the materials described in this section exhibit absorption peaks in the ATW region, as shown in Figure 4.16. A direct comparison can be made between the calculated and measured spectra for calcite and anatase [144, 145]. The agreement in calcite is almost perfect, while the positions of the absorption peaks in TiO_2 agree very well with measurements.

In calcite, the ionic dielectric constants equal to 6.1 in the plane of the CO_3^{-2} groups and 5.7 in the out-of-plane direction, which indicates a relatively small anisotropy of the ionic dielectric response. In aragonite, the ionic dielectric constants are 4.74, 5.64, and 6.14 along the x, y,

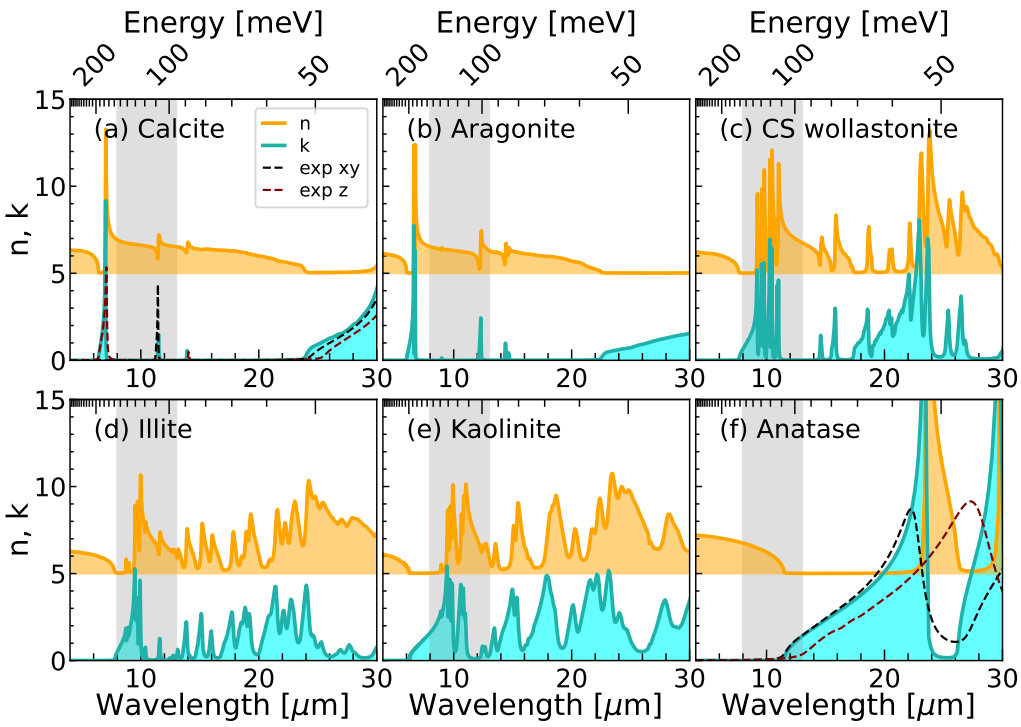

Figure 4.16: Calculated complex refractive indices of raw materials and concrete additives. The shaded area marks the IR atmospheric transparency window. The extinction coefficients of calcite and TiO_2 are compared with experimental measurements along different polarization directions [144, 145].

and z crystallographic axes, respectively. Comparing with calcite, aragonite shows a somewhat larger directional dependence, which can be attributed to its orthorhombic structure and a more complex arrangement of carbonate groups. For CS wollastonite, the ionic dielectric constants are 4.71, 4.81, and 4.40 along the x, y, and z directions, respectively. These values are similar, which indicates a small anisotropy response despite the chain-like silicate structure. The ionic dielectric constants of the clay minerals are somewhat larger and more anisotropic. In illite, the constants are 5.35, 7.19, and 6.18 along the x, y, and z axes, respectively, while in kaolinite they are 9.91, 5.95, and 7.59 along the same directions. A different behavior is observed in anatase, where the calculated ionic dielectric constants equal to 54.31 in the plane and 22.27 along the out-of-plane direction. These very large values reflect the strong lattice polarization typical of transition-metal oxides with highly polarizable Ti-O bonds and low-frequency optical phonon modes.

$CaCO_3$

Dielectric functions of both calcite and aragonite show high intensity peaks in the BSE spectra. First we compare the spectra calculated using IPA and G_0W_0 methods with those obtained using the BSE formalism, as shown in Figure 4.17. The optical anisotropy between the two polarization directions is found at all levels of theory. The spectral onset in both polymorphs is formed by the polarization along the xy-plane, with a negligible contribution from the out-of-plane direction. The IPA and G_0W_0 spectra exhibit similar features, with a shift of approximately 3 eV between

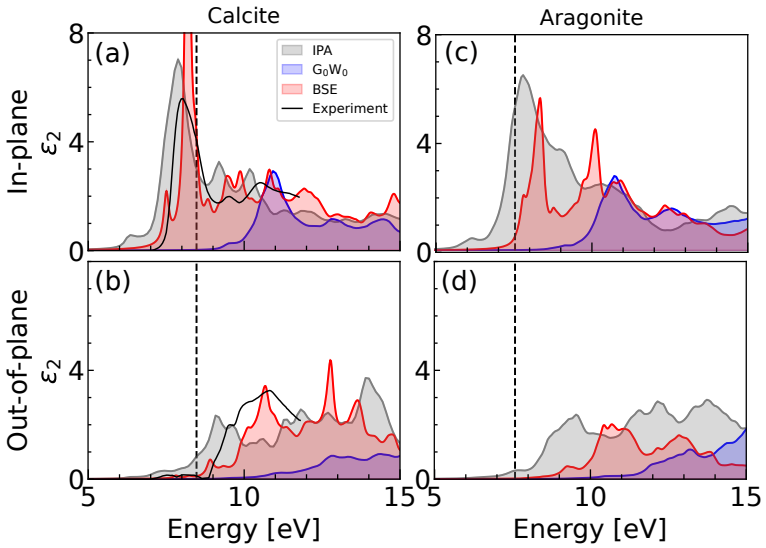

Figure 4.17: Imaginary dielectric function of (a–b) calcite and (c–d) aragonite calculated using SCAN (IPA), SCAN+G_0W_0 and BSE on top of SCAN+G_0W_0. The results for calcite are compared with experimental data [146]. The vertical dashed lines denote the indirect GW band gaps.

each other. In both minerals, the spectra begin with a low-intensity peak, followed by the main peak. In calcite, the prominent IPA and GW peaks arise from transitions to the two lowest conduction bands at the BZ edges, as shown in Figure 4.18.

The excitonic peaks are formed almost exclusively in the in-plane polarization direction. In calcite, besides the main excitonic peak at 8.2 eV, we report another lower intensity peak at 7.5

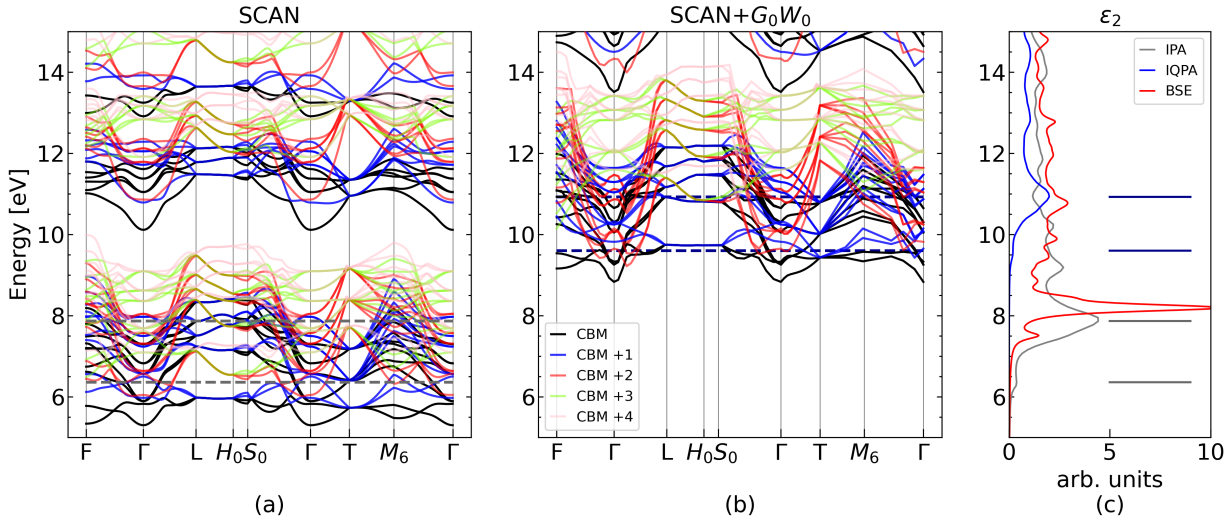

Figure 4.18: Joint band structure of calcite calculated using the (a) SCAN and (b) SCAN+G_0W_0 methods, compared with the (c) k-mesh averaged imaginary dielectric function calculated using BSE (red line), SCAN+G_0W_0 (blue line) and SCAN (grey line). Energies of the highlighted peaks are indicated by horizontal lines in the corresponding JBS diagrams.

eV, which marks the onset of the spectral profile. The available experimental data on the light absorption of calcite allows for comparison only up to 12 eV [146]. The experimental dielectric function is characterized by a dominant peak in the in-plane polarization direction, followed by two low-intensity peaks around 10 eV, in agreement with the BSE spectrum. The main experimental peak is broader and of lower intensity, which is likely due to finite temperature effects. Furthermore, thermal broadening may explain the absence of the small excitonic peak predicted by BSE. The positions and intensities of the spectral features in the out-of-plane polarization agree well with the experimental results. In aragonite, there is a small peak below the main peak in the in-plane polarization direction as well, though it is not fully separated from the spectrum.

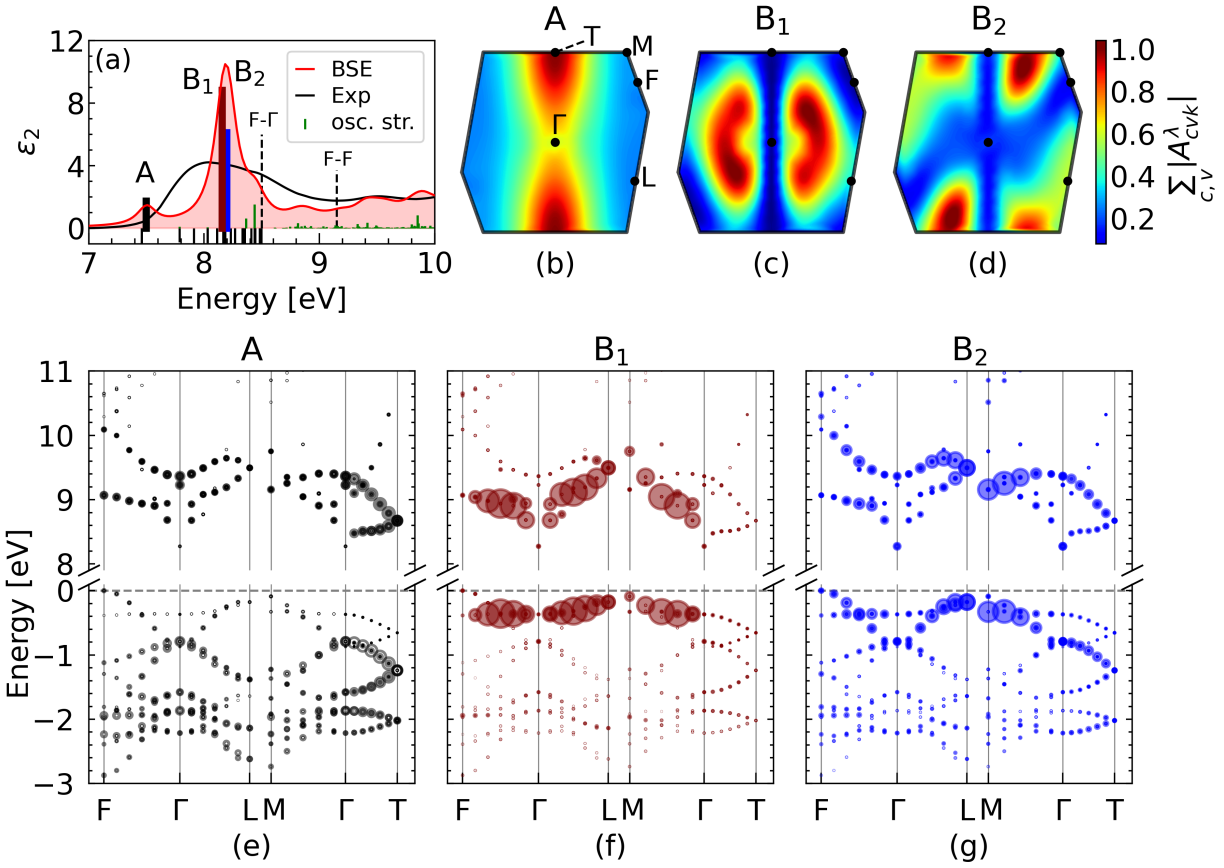

Figure 4.19: G_0W_0+BSE excitonic spectrum of calcite. (a) Dielectric function ϵ_2 calculated using k-mesh averaging (red line), with BSE oscillator strengths (green lines) and dark exciton energies (negative black lines), compared to the experiment [146]. (b) - (d) Amplitude of coupling coefficient $|X_\lambda^{cv\mathbf{k}}|$ summed over all bands projected onto (100) plane of the Brillouin zone, showing the reciprocal space distribution of excitons highlighted in the panel a. (e) - (g) Band structure segments with $|X_\lambda^{cv\mathbf{k}}|$ represented by the circle size, calculated on 12^3 k-mesh [54].

In order to understand the prominent BSE spectral features of calcite and aragonite, we analyzed the excitonic eigenstates with the highest oscillator strengths, as shown in Figure 4.19 and Figure 4.20. The spatial distribution and the character of excitons can be determined from the electron-hole coupling coefficient resolved in the k-space. Its amplitude, $|X_\lambda^{cv\mathbf{k}}|$, is represented by the size of the circles in Figure 4.19e–g and Figure 4.20b–d [54].

The exciton wavefunction of calcite is delocalized in k-space, with contribution from multiple valence and conduction bands, which explains the complicated convergence behaviour. We first focus on the peak A, shown in more detail in Figure 4.19e. The exciton comprises transitions from the non-bonding O p upper valence bands to the two lowest π^* conduction bands. The involved valence bands are primarily composed of O p_z states, and the conduction bands are made of the hybridized C-O p_z and Ca d orbitals. The topmost flat valence band with the O p_{xy} character has a negligible contribution to the formation of the exciton A. This exciton is delocalized across the entire Brillouin zone, with a large contribution along the $\Gamma-$T high symmetry path. This delocalization is evident from the reciprocal space distribution of $\sum_{cv} |X_\lambda^{cv\mathbf{k}}|$ in the (100) BZ cut, as shown in Figure 4.19b. The largest contribution to the exciton is observed in the z direction, with a peak at the T point [54].

In calcite, the main peak B is composed of two excitons with comparable optical strengths. The exciton B_1 stems mostly from a single pair of bands that form the band gap edges (see Figure 4.19f). The exciton develops between a hole in the non-bonding O p_{xy} valence band and an excited electron in the π^* band. In contrast to the exciton A, the exciton B_1 is delocalized in all k-space directions, except along the $\Gamma-$T direction. The exciton localization in Figure 4.19c shows a disperse character with the highest contribution from the k-points situated between the center and at the vertices of the BZ.

The exciton B_2 has a complementary character to the exciton B_1. It originates from the transitions between the two topmost valence bands and the second lowest conduction band. Analogously to the peak B_1, the contribution from the $\Gamma-$T path to the peak B_2 is reduced. The largest contribution to $|X_\lambda^{cv\mathbf{k}}|$ comes from the bands where the exciton B_1 has small amplitude, i.e., close to the BZ faces. The two peaks B_1 and B_2 taken together are responsible for excitations between the three uppermost valence and lowest conduction bands [54].

Both excitons A and B are highly delocalized across the first BZ, which implies a significant localization in real space. Furthermore, the diminishing exciton wavefunction of the peak B in the $\Gamma-$T direction, equivalent to the z direction, suggests a large anisotropy. The e-h pairs are mainly localized on the CO_3^{2-} structural units, and show a 2D-like in-plane behavior with minimal extension along the z-axis, perpendicular to the CO_3^{2-} planes [54].

The real space representation of the excitonic wavefunction has been reported with a hole centered on an oxygen atom [54]. In agreement with the previous analysis, the main excitons were found to be highly confined. The exciton A is localized exclusively on the CO_3^{2-} units with negligible in-plane spatial extent. In contrast, both excitons B_1 and B_2 involve Ca electrons and a certain degree of delocalization. Despite the larger delocalization of excitons B_1 and B_2, both are highly confined and involve mainly the nearest Ca atom and the CO_3^{2-} units around the hole. The exciton A is centered on a single CO_3^{2-} unit, which is typical of Frenkel excitons, while the excitons B have some contribution from the Ca atoms, which qualifies them as charge-transfer excitons.

In the case of calcite, the determination of the binding energy for an exciton delocalized in k-space is problematic. We calculated the binding energy as the difference between the BSE eigenvalue and the interband separation at the k-point with the largest contribution to the oscillator strength. The BSE binding energies of the excitons A and B (see Figure 4.19) are 1.65 eV and 1.05 eV, respectively. The excitons centered on the planar CO_3^{2-} units with large binding energies resemble the excitons in low-dimensional systems [147].

Similarly to calcite, the main peak in the dielectric function of aragonite was observed predominantly in the CO_3 plane, as shown in Figure 4.17c–d. The BSE dielectric function of

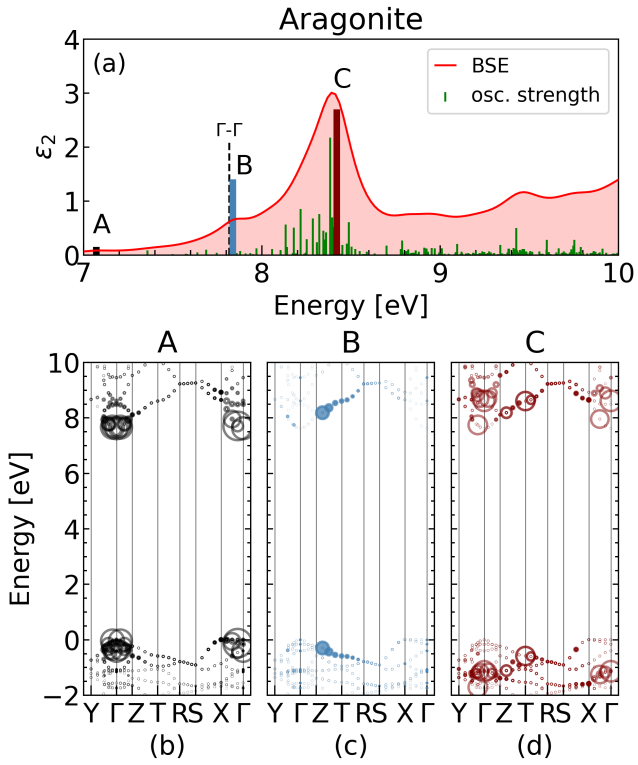

Figure 4.20: G_0W_0+BSE excitonic spectrum of aragonite. (a) Dielectric function ϵ_2 calculated using k-mesh averaging (red line), with BSE oscillator strengths (green bars). (b) - (d) Band structure with $|X_\lambda^{cv\mathbf{k}}|$ represented by the circle size, plotted for three excitons, calculated on a 8^3 k-mesh.

aragonite averaged over the three polarization directions is shown in Figure 4.20a. Even though the e-h interaction significantly modifies the optical spectrum of aragonite, there are no prominent peaks below the band gap energy in the BSE spectrum. This means that exciton peaks are not formed below the band gap energy. Lower intensity of excitonic features in aragonite might be related to the slightly aplanar arrangement of CO_3 units that are the main contributors to the excitonic effects in $CaCO_3$. In Figure 4.20, we defined the first bright exciton as the peak A and the two lowest BSE peaks as B and C.

The exciton A is located below the band gap energy, however, its low oscillator strength in not sufficient to form a distinct peak in the optical spectrum. It is the first Γ point exciton formed between the VBM and CBM. The exciton wavefunction, shown in Figure 4.20b, identifies a localized exciton with significant contribution in the Γ−X direction. The almost dark exciton A is strongly bound, with a binding energy of 0.75 eV. The low intensity of this excitonic feature might be attributed to limited overlap between the initial and final electronic states

The exciton B is located at the band gap energy and forms a low-intensity peak in the optical spectrum. Its position at the absorption onset suggests it is a band-edge exciton, arising from transitions between the highest valence-band states and the lowest conduction-band states. The exciton B originates from states located near the face of the first Brillouin zone, primarily along the region between the Z and T high-symmetry points, as shown in Figure 4.20c.

The main peak C is composed of various high oscillator strength excitations, the strongest

one of which is shown in Figure 4.20d. It is mostly a Γ-point exciton between the sixth topmost valence band and the third lowest conduction band, which explains the position of the peak above the band gap energy. The binding energy is equal to 0.66 eV.

The anisotropy of calcite is reflected in its dielectric constants. At low frequencies, the experimental ϵ_0 is equal to 8.64 for the xy plane and 8.23 along the z axis [148]. The electronic contribution, measured by far-infrared reflectance, yields $\epsilon_\infty = 2.63$ and 2.17 along the xy and z directions [148], which implies an almost isotropic ionic dielectric constant $\epsilon_\mathrm{I} \approx 6$. Our calculated values are in a good agreement with these reports. The the local field effects within the G_0W_0 approximation at the level of RPA bring the values of ϵ_∞ even closer to experimental values [54].

4.6 Outline

The results presented in this chapter highlight the need for accurate and sophisticated approaches when calculating the optical properties of cementitious materials and their constituent phases. The combined SCAN+G_0W_0+BSE approach significantly improves the predictive capability of first principles calculations and enables a parameter-free description of optical excitations, by avoiding empirical corrections such as the scissor operator.

A common observation across many of the studied materials is the presence of bound electron-hole pairs, or excitons, at or near the onset of optical absorption. These excitonic features, although sometimes of low intensity, play an important role in shaping the spectral profile and determining the effective optical gap. Their occurrence is closely related to the wide band gaps and moderate dielectric screening characteristic of cement phases, which favors the formation of excitons. The relatively low values of the electronic dielectric constants obtained for most calcium silicates, aluminates, and hydrates are consistent with their predominantly ionic bonding character and limited electronic polarizability, especially when compared with more covalently bonded semiconductors or transition-metal oxides.

Accurate knowledge of optical and dielectric properties is essential for emerging applications that extend beyond the traditional structural uses of cement-based materials. In particular, the ability to predict the optical response in the IR and UV–Vis is crucial for the design of materials for radiative cooling, thermal management, and photonic applications. The results obtained in this chapter provide a reliable basis for modeling macroscopic optical properties, including emissivity, reflectance, and absorption in heterogeneous systems. In subsequent chapters, the calculated IR and UV–Vis spectra will be used to investigate size-dependent optical effects and to predict the radiative behavior of both simple phases and complex cementitious composites.

Chapter 5

Radiative cooling in the bulk

The radiative cooling technology has the potential to reduce the energy consumption and running costs of buildings through the design of building materials with novel optical properties. For instance, the photonic concrete (PC) can reduce the running costs and reduce the CO_2 footprint [2]. PC is a promising candidate for daytime radiative cooling applications [2–5], that aims not only to reduce the large air-conditioning energy consumption, but also to mitigate the urban heat island effect [6]. PC capable of radiative cooling will be able to passively dissipate heat into space through the atmospheric transparency window (ATW) in the IR range of 8–13 µm [3–5]. The heat radiated in the ATW does not warm the atmosphere, which reduces the overall contribution of urban areas to the greenhouse effect.

This chapter focuses on the radiative properties of bulk cement and concrete phases, with particular emphasis on their thermal emission and absorption in the IR range. We introduce and describe the emissivity spectra obtained from heat-transfer models to quantify the thermally radiated power. Similarly, we evaluate the absorption of incoming solar radiation in the bulk limit. These models provide a consistent theoretical framework for linking intrinsic material properties, such as optical constants and phase composition, to macroscopic radiative performance.

By establishing the modeling approach, the chapter lays the foundation for a systematic investigation of the radiative properties of cement- and concrete-based materials. This analysis represents a crucial first step toward understanding how these widely used construction materials interact with solar and thermal IR radiation. In the following chapter, this framework is extended to account for size-dependent phenomena, which have an important effect on scattering, emissivity, reflectance and therefore the overall radiative behaviour.

5.1 Computational details

In this chapter, we calculated the Mie scattering using the summation order of 35, as defined in Equation 2.47 and Equation 2.48. The hemispherical emissivities were calculated using the Hapke model and Mie single-particle albedo. The atmospheric transmittance was assumed for the summer-time in Pamplona, Spain [18] and the temperature of materials was set to 300 K. The solar absorbance was estimated using the ASTM solar irradiation tables [149], with the net solar power of 1017.7 $\frac{W}{m^2}$.

5.2 Bulk emissivity

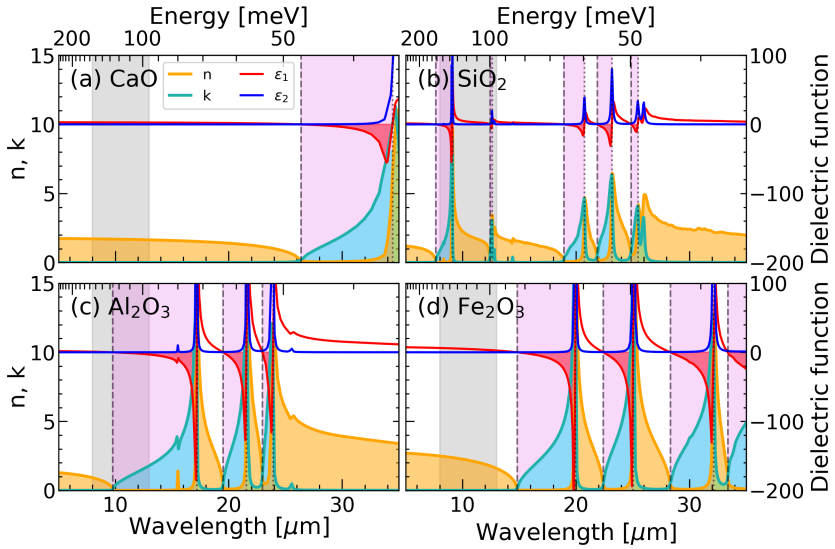

Figure 5.1: Complex refractive index and dielectric function of (a) CaO, (b) α-SiO_2, (c) α-Al_2O_3, and (d) α-Fe_2O_3. The ATW region is shown as grey and the Reststrahlen bands as violet areas. Dielectric functions were shifted above the refractive index curves for a better readability.

One of the leading parameters regarding the radiative cooling performance is emissivity, which can be expressed in terms of the complex refractive index within Hapke model. It is therefore useful to examine the relationship between the dielectric function, the refractive index, and emissivity. The refractive indices of simple cement-forming oxides are compared with their dielectric functions in Figure 5.1. In this figure, the Reststrahlen bands, spectral regions where the real part of the dielectric function ϵ_1 becomes negative, are highlighted as violet regions. The refractive index n approaches zero within the Reststrahlen bands, which is associated with high reflectance. Similarly, k values grow there and reach the peak values where the imaginary part of the dielectric function ϵ_2 has the highest values.

Emissivity is a dimensionless quantity that ranges between zero and one. A comparison of the refractive index and emissivity of simple cement-forming oxides (see Figure 5.2) reveals a clear correlation between the two. Specifically, emissivity is reduced in the Reststrahlen bands where the real part of the refractive index n is small. Reflectance dominates in Reststrahlen bands, which leads to a suppression of thermal emission. Conversely, emissivity increases with increasing refractive index, both within and outside of the Reststrahlen bands. Selective emissivity describes the ability of a material to exhibit high emission within the ATW and reflect radiation at other wavelengths. An ideal radiative cooling material would therefore combine Reststrahlen bands located outside the ATW region with high emissivity within it.

In this chapter, the bulk or single-crystal-like emissivities are calculated for large particles, which are described by the Mie single-scattering albedo. The bulk properties were obtained for a representative particle radius of 5000 µm. The resulting emissivity spectra are compared with the corresponding refractive indices data in Figure 5.2–Figure 5.5.

For radiative cooling applications, high emissivity within the atmospheric transparency window is essential. The presence of absorption bands within the ATW leads to reduced hemispher-

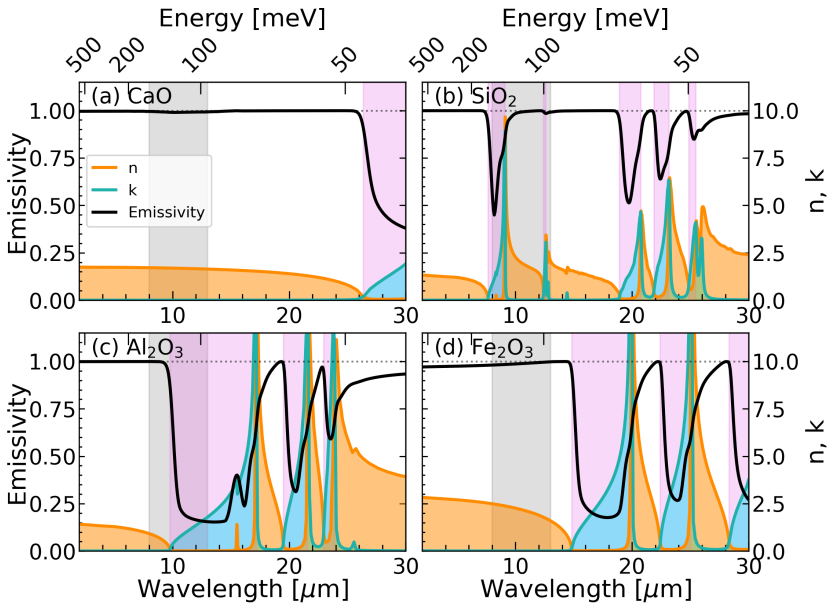

Figure 5.2: Hemispherical emissivity and complex refractive index of (a) CaO, (b) α-SiO_2, (c) α-Al_2O_3, and (d) α-Fe_2O_3. The ATW region is shown as grey and the Reststrahlen bands as violet areas.

ical emissivity of bulk materials, which negatively affects the cooling performance. Among the simple cement-forming oxides, shown in Figure 5.2, α-SiO_2 and α-Al_2O_3 exhibit significant absorbance within the ATW. In particular, α-SiO_2 shows absorption between approximately 8 and 14 µm, which originates from optically active phonons associated with various Si-O stretching modes [150, 151]. These vibrational modes give rise to multiple peaks in the imaginary part of the dielectric function ϵ_2 [152] and the extinction coefficient k spectrum, which are responsible for the corresponding emissivity minima. Similarly, the emissivity minimum observed in α-Al_2O_3 spans over the range of 13–17 µm and is associated to Al-O vibrational modes [153], which includes the ATW region. Because of these intrinsic vibrational properties, complex oxides that contain SiO_2 or Al_2O_3 as constituents also exhibit absorption bands in the ATW. In contrast, CaO and α-Fe_2O_3 have their dominant absorption bands at longer wavelengths outside of the ATW and their bulk hemispherical emissivity remains high there. As shown in Figure 5.2b, the only simple oxide that exhibits some selective emissivity within the ATW region is α-SiO_2, with two narrow Reststrahlen bands at the edges of the ATW region.

The emissivity spectra of the investigated cement phases are shown in Figure 5.3. All six cement structures exhibit relatively high emissivity over a large portion of the infrared spectrum, which indicates that these materials are generally efficient thermal emitters. At the same time, each cement phase displays narrow emissivity minima within the ATW. In the case of alite, this minimum does not significantly reduce the total radiated power, because it coincides with an atmospheric absorption band located just below 10 µm (compare Figure 5.3 with Figure 1.3 and Figure 5.6). Minima at other wavelengths within the ATW region affect the cooling properties more negatively. Out of the cement phases, C4AF has the highest emissivity in the ATW with only one shallow minimum. Compared to the simple oxides, the more complex crystal structures of cement phases give rise to a larger number of optically active phonon modes. Each of these modes contributes an absorption peak in the IR region, which in turn influences the spectral

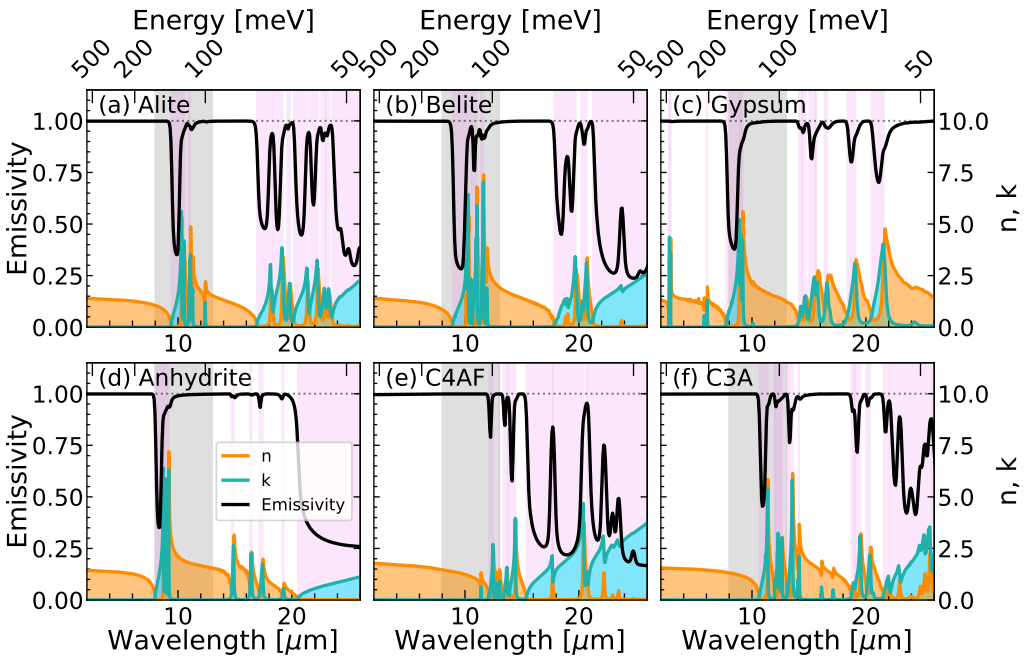

Figure 5.3: Hemispherical emissivity and complex refractive index of cement phases. The ATW region is shown as grey and the Reststrahlen bands as violet areas.

dependence of the refractive index and extinction coefficient. When multiple absorption peaks occur in close spectral proximity, their combined effect modifies the emissivity profile over a broader wavelength range. In particular, the presence of closely spaced phonon resonances reduces the width and depth of individual emissivity minima, which leads to a smoother emissivity spectrum. Among the studied cement phases, the spectral positions of the Reststrahlen bands are the closest to the ideal selective-emitter configuration in gypsum, where the ATW region is in between two high reflectance spectral regions.

The results for the studied concrete phases are shown in Figure 5.4. With exception of portlandite, the hydrated phases exhibit complex crystallographic structures that strongly influence their optical response in the infrared spectral range. As in the case of cement phases, this structural complexity leads to a dense distribution of vibrational modes, which reduces the width of individual spectral features. As a consequence, the corresponding emissivity minima are generally shallower and narrower than those observed in simpler oxides, which results in a more uniform and relatively high emissivity across a broad range of IR wavelengths. In contrast, portlandite has a simple crystal structure, which is reflected in the dielectric function characterized by only a few prominent vibrational resonances. Accordingly, its emissivity spectrum exhibits a single broad emissivity minimum located at wavelengths above 17 µm. Since this minimum lies outside the ATW region, it does not significantly affect radiative cooling performance in the single-crystal limit. The remaining concrete phases have emissivity minima that fall within the ATW region. These minima are in T11, T14 and jennite similar to the emissivity minimum found in α-SiO_2, both in terms of the spectral position and shape. In a similar way, the emissivity spectrum of ettringite partly resembles that of gypsum, which highlights the important role of phase composition and hydration products in determining the radiative properties of concrete composites. These similarities suggest that the IR optical behavior of hydrated calcium

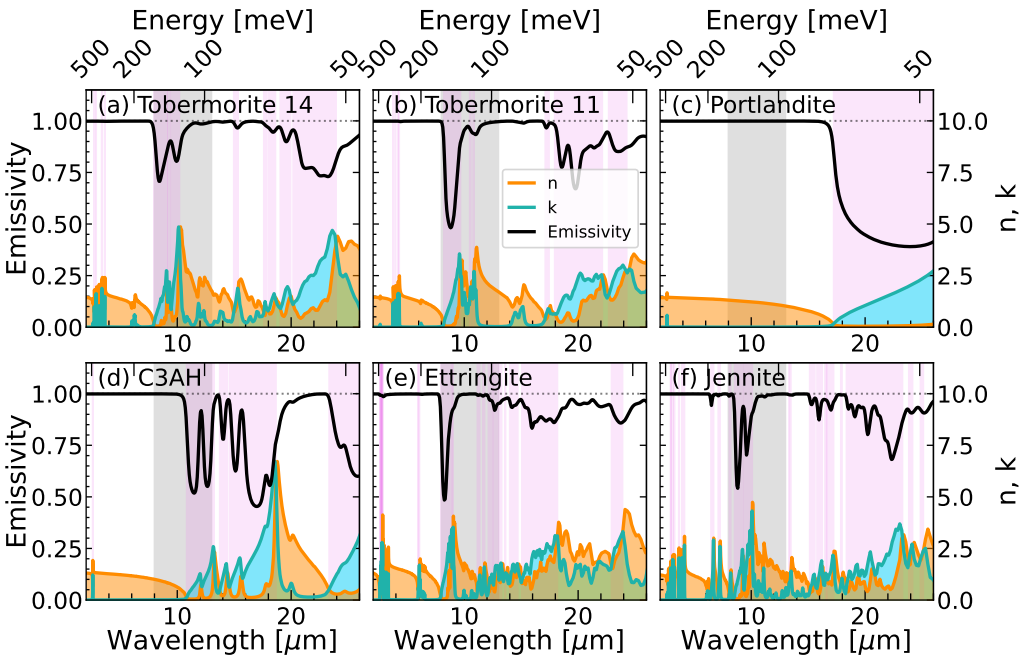

Figure 5.4: Hemispherical emissivity and complex refractive index of some hydrated concrete phases. The ATW region is shown as grey and the Reststrahlen bands as violet areas.

silicates and sulfates is largely governed by the vibrational modes of Si-O and SO_4 structural units, which produce characteristic Reststrahlen bands in comparable wavelength ranges. Based on the spectral distribution of the Reststrahlen bands, T11, T14, ettringite, and jennite exhibit a certain degree of selective emissivity, as their reflectance bands partially surround the ATW region.

The emissivity spectra of the raw materials and clays are shown in Figure 5.5. Both studied polymorphs of $CaCO_3$ exhibit high-intensity absorption peaks located just below the ATW. These absorption features correspond to narrow and deep emissivity minima, which reduce thermal emission in specific spectral intervals. In contrast, clays and CS display broader emissivity minima and multiple absorption peaks within the ATW region. This behavior arises from their more complex crystal structures, which give rise to numerous optically active vibrational modes associated with Si-O and Al-O bonding environments. Anatase, on the other hand, has a simpler crystal structure, which results in more widely separated absorption peaks and extended spectral regions where the refractive index remains low. These features give rise to a broad emissivity minimum that extends into the ATW region. A certain degree of selective emissivity was also observed in aragonite, CS wollastonite, illite, and kaolinite. Low emissivity, or equivalently high reflectance in the ATW above 10 µm is particularly unfavorable for radiative cooling performance. In this spectral region, the atmospheric transmittance is the highest, which means that thermal radiation emitted by a material can escape most efficiently into outer space through there. Suppressed emissivity in this wavelength range therefore reduces the overall radiative cooling potential, as it limits the thermal power that can be effectively dissipated.

Comparing to the simple cement-forming oxides, the spectral features of the complex phases are narrower and shallower. The smoother spectra may be beneficial for maintaining relatively high thermal emission over a wide spectral interval. Such characteristics are particularly relevant

for the macroscopic radiative properties of concrete, where multiple phases coexist and their individual spectral features are averaged in composite materials.

5.3 Net radiated powers

Radiative cooling occurs when the net radiated thermal power of a material exceeds the total incoming energy from solar irradiation, atmospheric thermal radiation, and non-radiative heat transfer processes such as conduction and convection. In order to isolate the radiative contribution, we first evaluate the balance between thermal emission and atmospheric absorption. In Figure 5.6a–b, two limiting cases are shown: a full black-body radiator and an ideal selective emitter, in thermal equilibrium with the atmosphere at 300 K. The temperature-dependent radiated power of a broadband emitter are approximated by Planck's black-body radiation law, defined in Equation 2.74. For such emitter, the total radiated power corresponds to the area under the black-body radiation curve. The atmospheric losses are calculated by multiplying the spectral radiance of the material by the atmospheric emissivity. Thermal radiation absorbed by a radiating object from the atmosphere in thermal equilibrium is shown in Figure 5.6a as the blue-shaded area.

Materials that emit strongly within the ATW release thermal energy into outer space through spectral region where atmospheric absorption is minimal. As shown by the red-shaded area in Figure 5.6, the emitted power within the ATW exceeds the absorbed atmospheric radiation in that region. The resulting imbalance between emitted and absorbed radiation leads to a net loss of energy, which leads to a temperature decrease below the ambient one. This energy difference

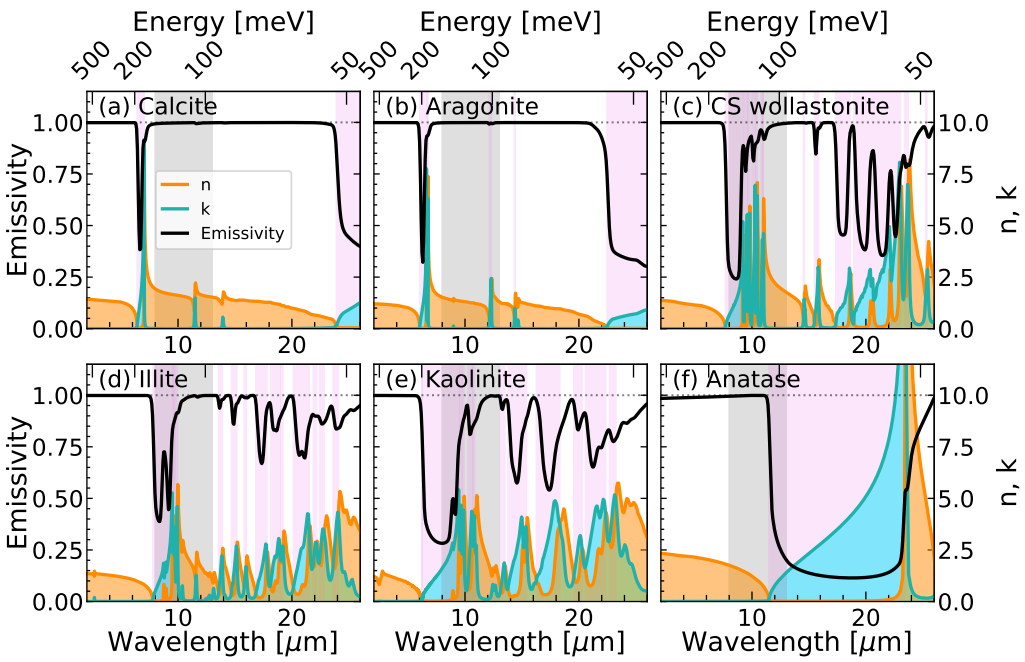

Figure 5.5: Hemispherical emissivity and complex refractive index of (a) calcite, (b) aragonite, (c) wollastonite, (d) illite, (e) kaolinite, and (f) anatase. The ATW region is shown by grey and Reststrahlen bands by violet areas.

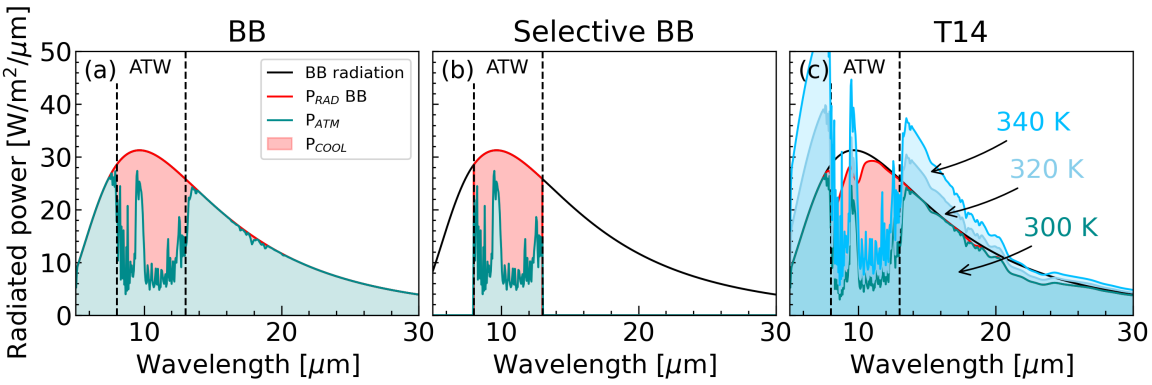

Figure 5.6: Radiated powers of (a) the black body radiator, (b) the perfect selective black-body radiator, and (c) tobermorite 14Å. The black curves are the black body radiation envelopes at 300 K, the red area shows the energy radiated by materials, and the blue area is the radiation absorbed from the atmosphere. For tobermorite 14Å the effect of the atmospheric temperature on the radiated power is included.

is the fundamental mechanism of radiative cooling.

The cooling performance is defined as the difference between the radiated and absorbed powers. Therefore, materials with selective emissivity within the ATW region have better radiative cooling performance, as demonstrated by the ideal case of a perfect selective radiator shown in Figure 5.6b. The ideal selective radiator does not absorb radiation outside of the ATW region, which significantly reduces atmospheric losses and increases its cooling capabilities at higher ambient temperatures, as shown in Figure 5.7. Since realistic materials absorb in a wide range of wavelengths, their radiated powers decrease quickly at higher atmospheric temperatures.

The radiated and absorbed powers of realistic materials are governed by their thermal emissivities, which determine how efficiently a material emits and absorbs thermal radiation. The radiated power of T14, shown in Figure 5.6c, is reduced in comparison with ideal black-body radiation due to the emissivity minimum at 8 µm, which is shown in Figure 5.4. The influence of the atmospheric temperature on radiative cooling performance of materials is illustrated on the example of T14. Because the emitted thermal radiation follows the shape of the black-body distribution, an increase in temperature shifts the atmospheric emission spectrum towards shorter wavelengths and increases its overall intensity, as shown in Figure 5.6c. As the ambient temperature rises, the overlap between the material emission and the atmospheric radiation becomes larger. Consequently, the power absorbed from the atmosphere increases and the net radiated power decreases. Eventually, the cooling potential vanishes when the power emitted by the material equals the power absorbed from the atmosphere. At this point, radiative equilibrium with the surroundings is reached and no further cooling below the ambient temperature is possible.

5.3.1 Atmospheric losses

The radiated powers of bulk materials in the single-crystal limit are shown in Figure 5.7 as a function of ambient temperature. The theoretical curves for black-body and the perfect selective radiator are shown as the full and dashed black lines, respectively. The dashed colour lines account for non-radiative losses, while solar losses were neglected. These results provide an

upper limit of the radiative cooling performance and describe the temperatude-dependence of the radiated powers.

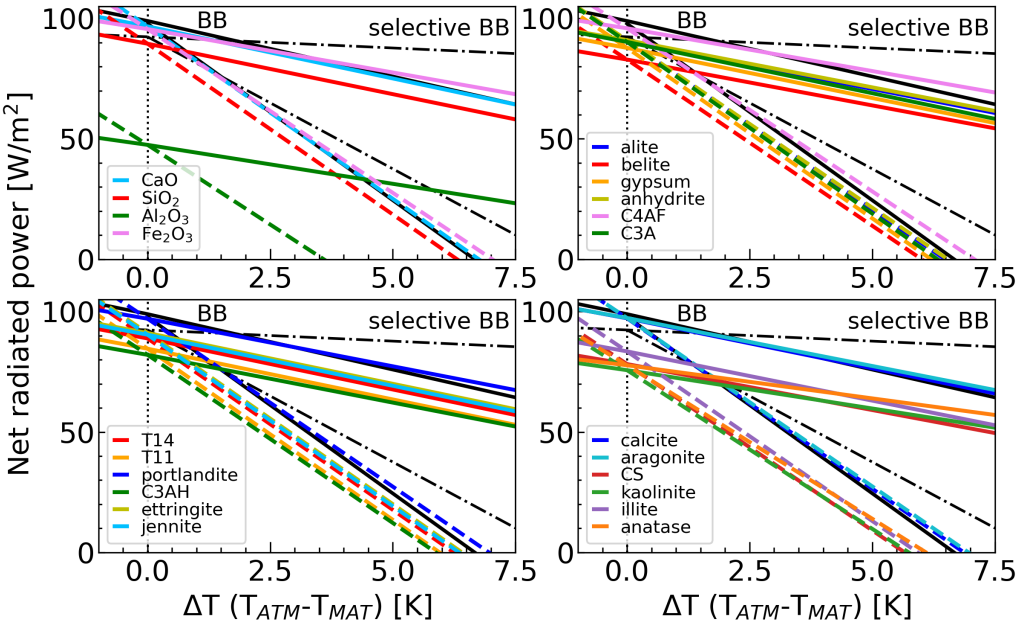

Figure 5.7: Net radiated power as a function of the temperature difference between material at 300 K and the atmosphere for cement-related materials. The full lines represent atmospheric losses and the dashed lines include non-radiative losses. The full black body radiator and selective black-body radiator in the ATW are plotted with solid and dash-dotted black lines.

As shown in Figure 5.7, most cement and concrete phases exhibit high net radiated powers at thermal equilibrium ($\Delta T = 0$), with several materials reaching values comparable to those of the black body. This trend indicates that many of the studied phases are efficient thermal emitters under ambient conditions. In contrast, a low net radiated power is observed for α-Al_2O_3, due to its deep emissivity minimum in the ATW spectral region. Similarly, clays, CS, and anatase show reduced radiated powers. On the other hand, high net radiated powers are obtained for CaO, iron oxides, portlandite, and $CaCO_3$. These materials benefit from their high thermal emissivity in the ATW region, related to the absence of strong absorption bands in this region.

The BB selective radiator exhibits slowly decreasing net radiated power, as shown by the dash-dotted lines in Figure 5.7. The slope of the net radiated power curves with respect to temperature can be therefore related to the selectivity of the thermal radiation within the ATW. The slope of the temperature-dependent radiated power curves is for most phases smaller than that of the black-body radiation. Notably, large crystals of C4AF, portlandite, $CaCO_3$ and anatase reach higher radiated powers than the black-body radiator at higher ambient temperatures. These materials exhibit emissivity minima outside of the ATW region, which reduces their atmospheric losses.

The net radiated power of a black-body emitter (solid black line in Figure 5.7) is higher than that of a perfect selective radiator (dashed black line in Figure 5.7) at temperatures below the equilibrium temperature. This regime corresponds to the region to the left of the vertical dotted line in Figure 5.7, where the temperature of the emitter exceeds that of the environment. Broadband emission across the entire infrared spectrum allows the black body to release more

thermal energy overall. Even though part of this radiation is reabsorbed by the atmosphere, it is possible to cool an object whose temperature is higher than that of its surroundings by emitting thermal radiation at any wavelength. For this reason, many real material phases can act as more efficient radiators than an ideal selective emitter at temperatures above ambient. Radiative performance in this range is particularly relevant for applications in which devices operate significantly above ambient temperature. One such example is the thermal management of photovoltaic modules, where efficient heat removal significantly improves the performance [17].

Figure 5.7 also provides information about the temperature-dependence of the radiated powers. The zero-crossing with the x-axis determines the highest temperature difference between the radiating material and the atmosphere. The radiated powers that include non-radiative losses are plotted by dashed lines. We assumed the coefficient of non-radiative losses, defined in Equation 2.76, equal to 10 $\frac{\mathrm{W}}{\mathrm{m^2K}}$, which is an intermediate value. Non-radiative losses are defined as a linear function of the temperature difference between material and the atmosphere, therefore they change the slope of the net radiated power curves. The cooling potential without considering the solar losses of the studied phases in the single-crystal limit is defined by the zero-crossings of the dashed lines in Figure 5.7. Neglecting solar losses is a equivalent of the night cooling. The largest cooling potential of around 7 K was found for hematite, C4AF. portlandite and $CaCO_3$. The lowest cooling temperature depends on location and the weather, since the non-radiative, atmospheric and solar losses strongly depend on the atmospheric conditions.

5.3.2 Solar losses

Solar losses are caused by the absorption of more energetic radiation in the UV, Vis, and NIR ranges, which is facilitated by the excitation of electrons. The absorption edge is given by the optical band gap. Solar losses are defined similarly to atmospheric losses, but instead of atmospheric transmissivity, the inputs are the solar spectral irradiation and the material response in the UV–Vis–NIR region, as defined in Equation 2.75. The electronic response, band gaps, and dielectric functions of cement and concrete phases were discussed in Chapters 1 and 2.

In order to estimate the solar losses, we use Beer-Lambert law in Equation 2.77. The solar powers absorbed by macroscopic particles with diameter of 4 cm subtracted from the radiated powers are shown in Figure 5.8. The green bars show the radiated powers reduced by the solar losses and the grey bars show the magnitude of the net radiated powers without solar losses, which represent the theoretical upper limit of the thermal radiated power. Materials for which solar loss exceeds radiated power are shown with red bars. In the case of the iron oxides the complete red bars are not shown, since they by far exceed the thermal radiated powers.

Most oxides are wide-bandgap insulators, therefore the absorbance of the solar radiation is minimal. The lowest solar losses were identified for $CaCO_3$ and portlandite with almost zero losses, followed by $CaSO_4$, α-Al_2O_3, belite, α-SiO_2, C3AH, CS and clays. In contrast, the smaller band gap of hematite and C4AF, calculated by SCAN+G_0W_0 to be 2.42 eV and 3.24 eV, results in absorption of the UV–Vis frequencies. Consequently, α-Fe_2O_3 strongly absorbs light and does not scatter UV–Vis efficiently, as shown in Ref. [154]. This completely diminishes the radiated thermal power of iron oxides. Similarly, CaO, alite and anatase have smaller band gaps and absorb some UV light. The absorption spectrum of C3A was calculated at the DFT level; therefore, the true bandgap is larger and the absorption in the UV range should be smaller. Solar losses in these materials can be significantly reduced by increasing reflectance, for instance

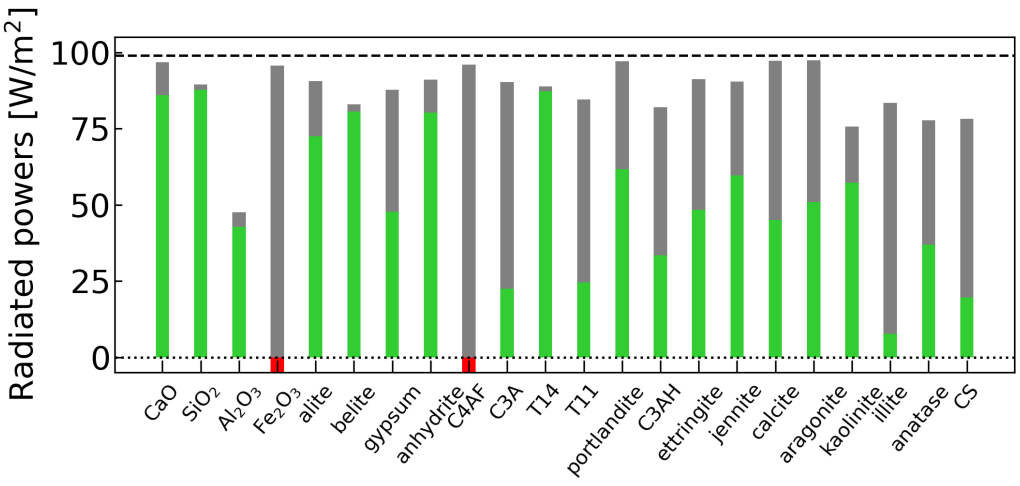

Figure 5.8: Radiated thermal powers of large crystals at 300 K in equilibrium with atmosphere are shown in grey, the radiated powers reduced by solar losses as green bars and red bars represent materials where the solar losses exceed the radiated powers. Dashed black line shows net radiated power of the black-body radiator.

by using smaller particles that effectively reflect solar radiation.

5.4 Outlook

The radiative properties of cement and concrete phases are governed by their thermal emissivities, which control the amount of emitted and absorbed thermal radiation. We analyzed the emissivity and radiative properties of perfect bulk crystals of cement and concrete phases. We evaluated the theoretical upper limit of the radiative cooling power and determined the solar absorption losses. Deviations from ideal black-body behavior, such as emissivity minima in specific spectral regions, can significantly reduce the radiated power of certain materials. The net radiative cooling power is also strongly temperature-dependent, as increasing temperature enhances atmospheric absorption and eventually suppresses cooling when emitted and absorbed powers balance out. The results demonstrate that both chemical composition and crystallographic complexity play a decisive role in determining the emissivity spectra of raw materials and additives used in cement and concrete.

The results presented in this chapter already provide clear indications of which materials are suitable for radiative cooling applications. In terms of radiated power, only alumina exhibits distinctly lower values compared with other oxides. More critically, the solar losses associated with iron-containing oxides are prohibitively high, which makes these materials unsuitable for efficient radiative cooling.

Building on the findings of this chapter, further analysis focuses on strategies to mitigate solar losses. One effective approach is to enhance light scattering in the UV–Vis spectral region to reducing solar absorption. In this context, the photonic properties of cement and concrete play a central role and form the cornerstone of photonic concrete development.

Chapter 6

Photonic properties of cement and concrete

A significant portion of the heat trapped in urban areas comes from the solar radiation absorption. Approximately 6% of the total solar energy falls within the UV range, 40% in the VIS range and 54% in the NIR range [166]. The reflection of solar radiation is essential to reduce the heating of buildings exposed to the sun. Because light scattering is maximized when particle sizes are comparable to the wavelength of incident radiation, we investigate the photonic properties of cement and concrete phases to identify those that reflect solar energy most efficiently. In parallel, we analyze the size dependence of emissivity to clarify how particle size influences radiative cooling performance

The size-dependent interaction of light with matter can be investigated using classical Mie theory [2, 62, 152], which provides a description of single particle scattering and absorption processes. This theory accounts for the reflection, refraction, and diffraction of light by well-separated spherical cement particles. In the context of radiative cooling, the objective is to identify materials that combine high emissivity within the ATW and strong reflectance of solar radiation. As the interparticle distance decreases, scattering behavior and related optical properties are modified by multiple-scattering effects. The emissivity of densely packed powders can be described using the Hapke multiple-scattering model [67, 69, 70, 155]. Together, Mie scattering and Hapke emissivity models provide a good starting framework for the design of PC-based radiative coolers.

This chapter examines the photonic properties of the main cement and concrete oxides over the sizes ranging from the nano- to micro-scale. We used the full dielectric functions with ionic and electronic contributions to compute the key photonic quantities, such as scattering efficiency, size-dependent emissivity, and spectral reflectance over a broad wavelength range. The results of this chapter are essential to understand and tailor the radiative properties of cement- and concrete-based components for environmental and energy-related applications.

6.1 Computational details

In this chapter, we calculated the Mie scattering using the summation order of 35, as defined in Equation 2.47 and Equation 2.48. The scattering anisotropy was in the emissivity calculation included via Equation 2.64. The Mie scattering order used in the calculation of the single-

particle albedo and Hapke-Hulst (HH) reflectance was set to 45. In order to avoid the ill-defined H-function and Hapke emissivity at albedo values approaching one, we truncated the albedo at $w = 0.999$. We use HH method instead of the Hapke model, which fails at large albedo values and can even predicts reflectance above unity. The atmospheric transmittance was assumed for the summer-time in Pamplona, Spain [18] and the temperature of materials was set to 300 K. The solar absorbance was estimated using the ASTM solar irradiation tables [149].

We performed scattering calculations using the MSTM code, which implements the multiple-sphere T-matrix method for clusters of spheres with arbitrary sizes, refractive indices, and spatial arrangements. The code solves Maxwell's equations rigorously by accounting for multiple-scattering interactions between spheres and provides access to orientation-averaged and fixed-orientation optical properties. The Mie order was set to 10 and the particle clusters contained 960 and 370 spheres for diameters of 0.5 and 1 microns and 43 particles for all remaining particle diameters. The number of spheres in a cluster was chosen such that the aggregates are larger than the wavelength of the scattered light and at least 20 microns in diameter. The spherical aggregates contained closely packed spherical particles.

6.2 Size dependent IR emissivity

Hapke theory approximates the multiple scattering processes in a qualitative way and can be used to describe the emissivity spectra of particulate materials. The size dependence of emissivity exhibits distinct trends across different spectral regions, governed by the values of the real and imaginary parts of the refractive index, n and k [71]. In the bulk limit, strong absorption bands characterized by large k values correspond to emissivity minima, known as class 1 behavior. In these regions, surface reflection at particle boundaries dominates, which allows little radiation to escape the material. Conversely, when $n > 1$ and k approaches zero, absorption is weak and volume transmission becomes dominant, which leads to high emissivity. This regime, referred to as class 3, typically occurs in spectral regions between absorption bands. Additionally, class 2 behavior is defined for intermediate values of k with $n > 1$ typical for weakly absorbing regions, while class 4 behavior corresponds to regions where both $k \approx 0$ and $n \approx 1$ [71].

Class 1 behavior is characterized by strong absorption and high internal reflection. For large particles, the thermal radiation generated within the interior of the material encounters only a limited number of internal interfaces before reaching the surface. As the particle size decreases, the number of internal reflections increases. Each internal interface contributes not only reflected but also emitted radiation, which enhances the probability that thermal energy escapes from the material. Consequently, the cumulative effect of multiple scattering events leads to an increase in emissivity. Within strong absorption bands, this mechanism becomes particularly strong, as emissivity increases with decreasing particle diameter [71].

In contrast, class 3 behavior is characterized by a reduction in emissivity for powders composed of smaller particles [71]. In this regime, the increased number of interfaces associated with decreasing particle size, together with $n > 1$, extends the optical path length within the material. Because absorption remains weak due to small but nonzero values of k, the longer optical paths increase absorption, which ultimately reduces emissivity.

The aforementioned behaviour is observed in Figure 6.1–Figure 6.5 for all oxides. The bulk emissivity, shown as black curves, is close to unity at most wavelengths except from the class 1 absorption bands. Emissivity within the absorption bands increases with decreasing particle

diameter, as indicated by the changing colours. The region of class 3 between the absorption bands shows the opposite behaviour and emissivity decreases there.

The emissivity spectrum of CaO is shown in Figure 6.1a. The bulk emissivity shows a deep minimum in the absorption band above 25 µm. Emissivity increases with decreasing particle size in the absorption band (class 1) and decreases in the region of the shallow minimum (class 3), where a wide emissivity minimum eventually forms. As a result, a peak appears between these two regions, which also known as the Christiansen feature [71] related to the class 4 behaviour, where n is close to unity and k is negligible. There is virtually no reflection at interfaces at the Christiansen frequency and radiation freely escapes the material regardless of the particle diameter. The Christiansen feature is material-dependent and has application in the spectroscopy, especially in the planetary research [156, 157]. The Christiansen peak can be found in other oxides below the first IR absorption band.

Silica is well known for its radiative cooling properties [4], which arise from being optically active within the ATW. The size-dependent emissivity of α-SiO_2 is shown in Figure 6.1b. Reduced particle sizes fill the emissivity minimum between 8 and 10 µm but also diminish the high-emissivity regions between 10 and 18 µm. The total radiated power within the ATW decreases accordingly to the relative magnitude of these emissivity changes in the ATW region. When the particle diameter decreases below 5 microns, a clear shift in the trend is observed as the single particles become highly emissive across the entire wavelength range. The emissivity spectra of α-SiO_2 enable a direct comparison between the calculations and experimental data [71, 156, 158]. The Hapke-Mie method successfully captures the size-dependent emissivity trends by predicting an increase in emissivity within the absorption bands and a corresponding decrease in the interband regions. The model predicts slightly deeper emissivity minima for both class 1 and class 3, which may be attributed to the underestimation of multiple scattering

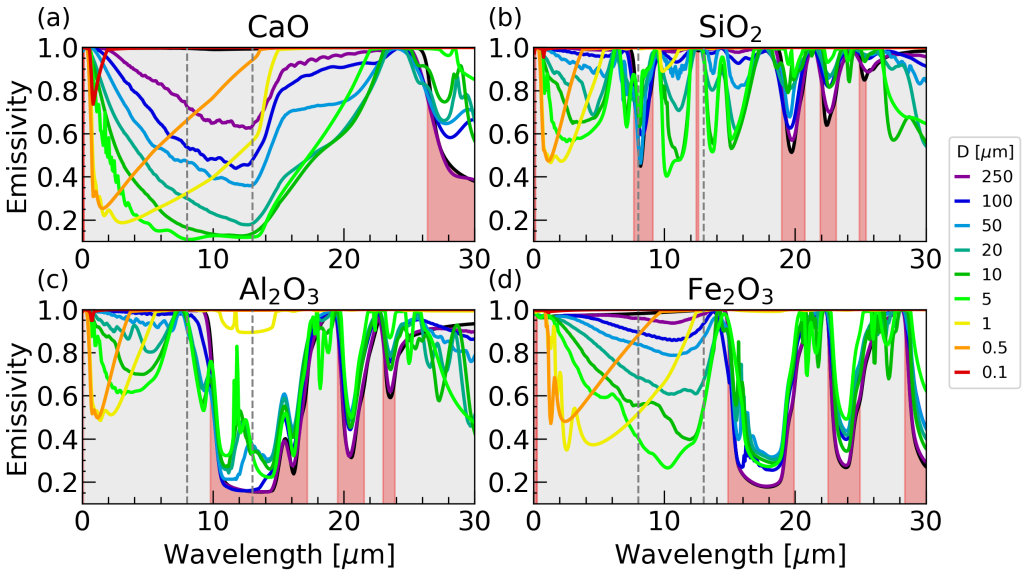

Figure 6.1: Size dependent Hapke-Mie emissivity of cement-forming oxides (a) CaO, (b) α-SiO_2, (c) α-Al_2O_3, and (d) α-Fe_2O_3, in air. The line colours represent different particle diameters, and the dashed lines correspond to the ATW. The high reflectance Reststrahlen bands are shown as red areas.

effects [71, 159] and to anisotropic scattering in realistic silica powders.

The emissivity spectra of α-Al_2O_3, shown in Figure 6.1c, are dominated by a broad and deep absorption band spanning through the 10–16 µm range, which significantly reduces the emitted power within the ATW. The Christiansen feature, located at 7.5 µm, is broader than in the case of silica. The particles with diameters below 5 microns become highly emissive across the IR range as they become much smaller than the wavelength of light. As the particle size decreases, the emissivity increases at all wavelengths. The emissivity measurements on particulate α-Al_2O_3 show good agreement with our results in terms of both spectral features and intensities [158, 160, 161]. Indeed, alumina nanoparticles have been reported to enhance emissivity and improve the radiative cooling performance of polymer films [158]. Our calculations support these findings and demonstrate the reliability of the theoretical approach.

The thermal emissivity of α-Fe_2O_3, shown in Figure 6.1d, is characterized by multiple broad and deep minima, which arise from several absorption bands. For α-Fe_2O_3, trends similar to those observed for the oxides discussed above can be identified. Similarly to CaO, hematite microparticles efficiently scatter thermal radiation with wavelengths below 15 µm, as the first absorption band is located at longer wavelengths than in α-SiO_2 or α-Al_2O_3. However, the corresponding emissivity minimum does not extend into the visible wavelength range, which implies low reflectance of solar radiation by hematite nanoparticles.

To quantify the effect of particle size on the radiated thermal power, we calculated the radiated powers for each particle size in the same way as in the previous chapter. In Figure 6.2, we present the net radiated powers for particle radii up to 200 microns in two different media: air and C-S-H, approximated by tobermorite 14 Å. The environment of concrete was simulated using a modification of Mie theory for absorbing media [64]. The dielectric properties of the C-S-H medium were approximated using the dielectric function of crystalline T14, which can be found in Chapter 2.

The net radiated powers of simple cement-forming oxides, obtained by integrating the radiated powers over the wavelengths in the range from 4.5 to 40 µm, are shown in Figure 6.2a. In this representation, the single-crystal limit discussed in the previous chapter corresponds to the particle diameters on the right side of each plot. For emitters in air, the highest radiated powers in the large single-crystal limit were obtained for CaO and α-Fe_2O_3. However, this behavior changes fast for smaller particles, as both minerals exhibit deep emissivity minima at diameters below 50 microns. In contrast, α-SiO_2 maintains high radiated powers over a wide range of particle sizes, with a shallow minimum at diameters of around 7 microns. For even smaller particles, the radiated power increases again, a trend that is common to all the studied materials in air. Conversely, the radiated powers in the absorbing T14 medium initially decrease with decreasing particle diameter and then remain nearly constant. Overall, silica particles exhibit the highest radiated powers in both environments, with the exception of large CaO and α-Fe_2O_3 particles with diameters over 500 microns.

The high radiated powers of sub-micron particles are a consequence of high emissivity, which is almost equal to unity at these sizes. The comparison between calculated emissivity spectra and experimental data for particulate samples shows excellent qualitative agreement. Nevertheless, the Hapke-Mie theory employed in this work exhibits certain limitations when confronted with experimental conditions. The Beer-Lambert law defines a linear dependence of the transmission on the particle diameter. Therefore, below a critical diameter, particles become semitransparent to most of the IR wavelengths, which is manifested by the increase of emissivity. The diameter at which single spheres become semitransparent is defined by the minima in Figure 6.2. The emis-

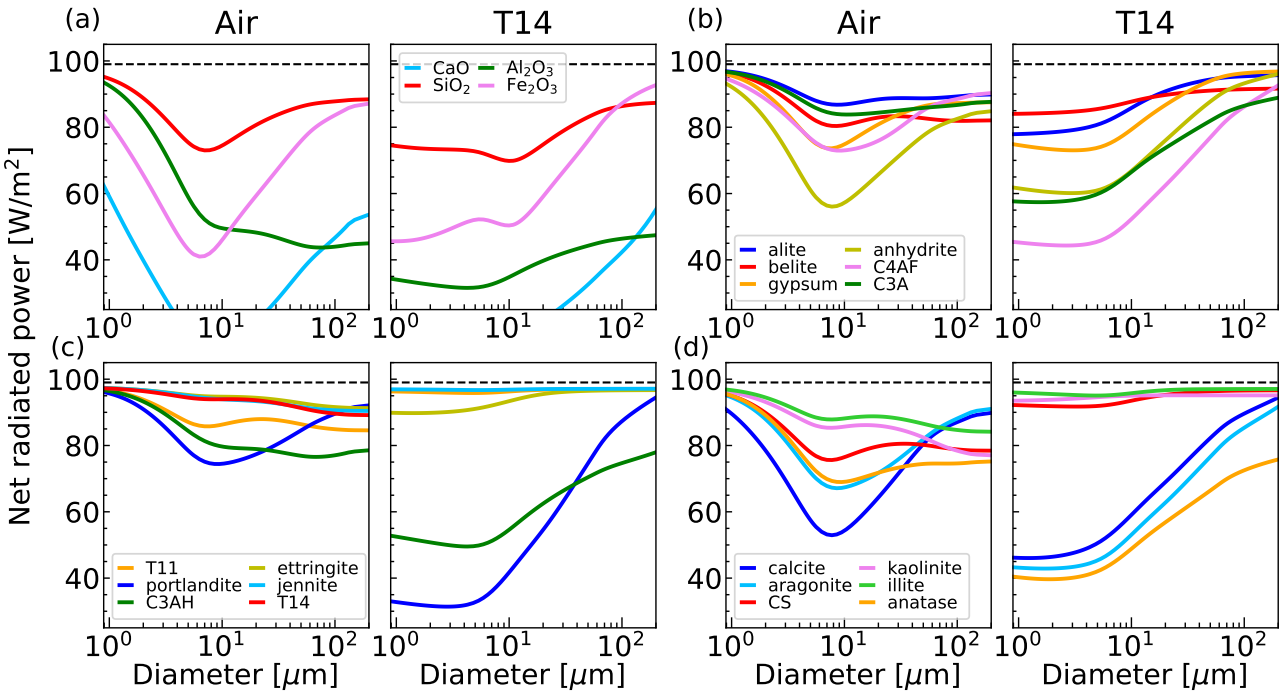

Figure 6.2: Sized-dependent net radiated powers of (a) simple cement-forming oxides, (b) cement phases, (c) concrete phases, and (d) raw materials, clays and additives in equlibrium with the atmosphere at 300 K in air (left) and C-S-H-like medium (right) approximated by T14. The horizontal dashed line represents the power radiated by the black-body.

sivities are obtained according to the Kirchhoff law $e = 1 - r$, with emissivity e and reflectance r, while transmittance was neglected. This approximation is valid for large samples and in spectral regions dominated by absorption bands and agrees well with indirect experimental techniques such as reflectance spectroscopy [129, 161]. However, the high emissivity of large particles in broad non-absorbing wavelength ranges is, in reality, largely influenced by transmittance. The spectral region below the first Christiansen feature corresponds to the non-absorbing interval between the UV–Vis and infrared absorption bands, where emissivity is dominated by transmittance. The reduction in emissivity observed for microparticles arises from enhanced scattering at these wavelengths, which separates two transparency limits: the non-dispersive single crystals and nanoparticles, that are too small to scatter infrared radiation effectively. The steep increase of emissivity for small particles is a consequence of using a single-sphere approximation. Real powders composed of particles with submicron diameters are not expected to increase the net radiated power, as in the case of using the single-particle Mie albedo, as shown later by the MSTM results.

The cement phases exhibit more complex emissivity spectra than the simple oxides, as shown in Figure 6.3. In all phases, the emissivities of small particles show a deep minimum at the wavelengths below the ATW, which is in the case of gypsum interrupted by the O-H absorption band just below 3 µm. Alite maintains high emissivity within the ATW even at smaller particle diameters with exception of the Reststrahlen band at 10 µm. In contrast, gypsum and anhydrite develop deep emissivity minima within the ATW, which reduces their radiative cooling performance. C4AF particles display a high emissivity in the 11–15 µm range, which does not lie fully

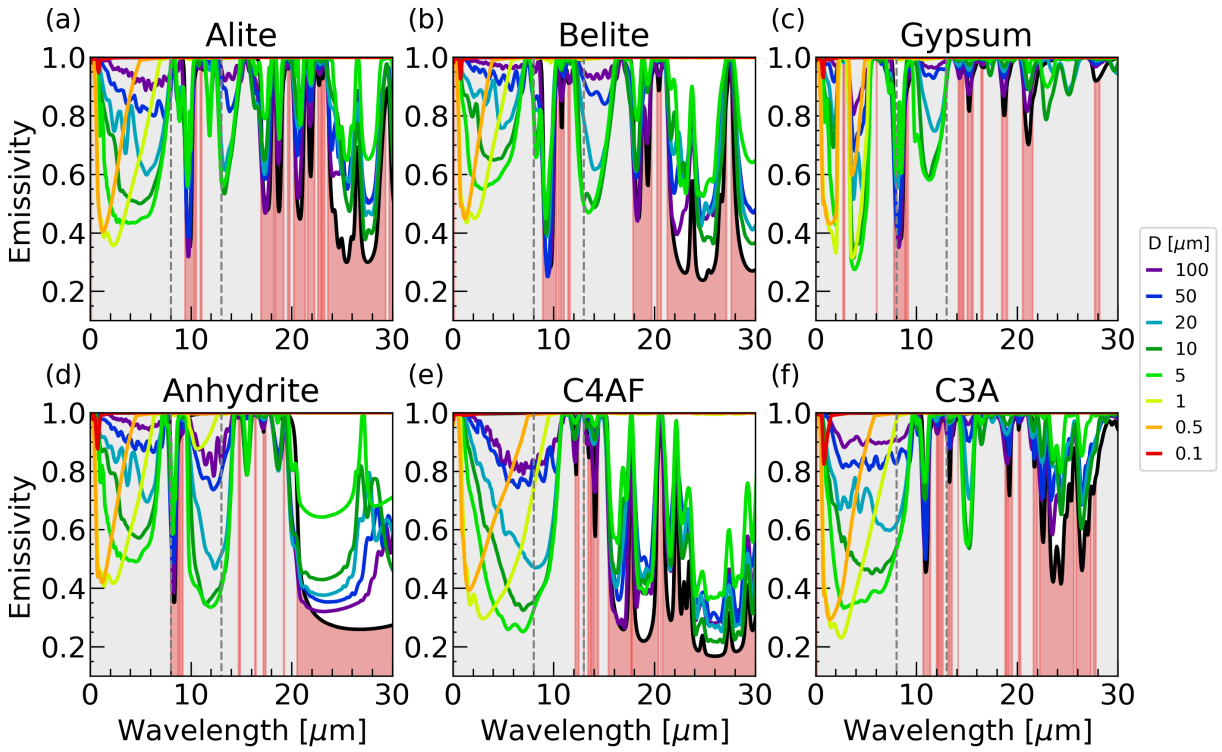

Figure 6.3: Size dependent Hapke-Mie emissivity of some cement phases in air. The line colours represent different particle diameters, and the dashed lines correspond to the ATW. The high reflectance Reststrahlen bands are shown as red areas.

within the ATW region. The size-dependent radiated powers of the cement phases are summarized in Figure 6.2b. In air, alite, β-belite, and C3A maintain high-intensity emissivity peaks within the ATW across all particle diameters. Consequently, decreasing the particle diameter has the smallest negative impact on the net radiated power of these phases. For particles in air, the largest decrease in radiated power is observed for anhydrite due to its deep emissivity minimum around 12 µm. The C-S-H-like medium has almost no effect on the radiative powers of alite, belite, gypsum and anhydrite, whereas the radiated powers of C3A and C4AF are reduced in this medium.

The emissivity spectra of concrete phases are shown in Figure 6.4. With exception of portlandite, the complex IR absorption spectra of hydrated phases reduce wide emissivity minima at wavelengths below the ATW. Such wide emissivity minima are observed in portlandite, as well as in most cement phases and simple oxides at wavelengths below the ATW range, or within it in the case of CaO and hematite. The highest emissivity within the ATW was found in ettringite, jennite, and T14.These three phases show high selective emissivity within the ATW region throughout all particle sizes. The size dependence of the net radiated powers of hydrated phases is shown in Figure 6.2c. For particles in air, the radiated powers of concrete phases remain high across all particle diameters. The largest decrease was observed in portlandite and C3AH, whereas T14, ettringite, and jennite maintain high radiated power without pronounced minima. The particles of T11, ettringite, and jennite embedded in a C-S-H-like medium exhibit an increase in their radiated powers. In contrast, portlandite and C3AH show a large reduction in net thermal radiated power in the C-S-H environment. This drop of the net radiated power

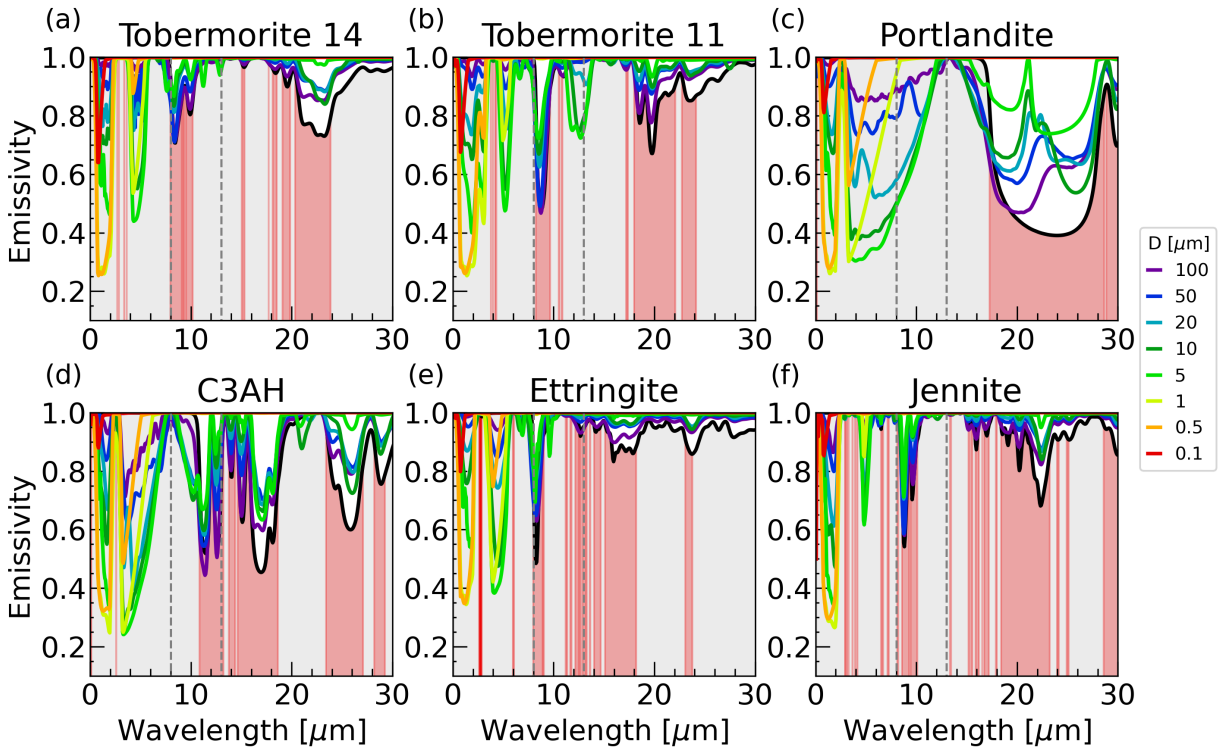

Figure 6.4: Size dependent Hapke-Mie emissivity of concrete phases in air. The colour lines represent different particle diameters, and the dashed lines correspond to the ATW. The high reflectance Reststrahlen bands are shown as red areas.

arises because the high-emissivity region of the Christiansen feature in portlandite and C3AH coincide with an absorption band of T14, which causes reabsorption and reduces net emission.

The size dependence of the emissivity spectra of $CaCO_3$, clays, anatase, and CS is shown in Figure 6.5. The emissivity of particulate calcite decreases significantly within the ATW region, similarly to CaO, anhydrite and other phases. Aragonite also exhibits a decrease in emissivity at smaller particle diameters, although it is less pronounced than in calcite, thanks to the emissivity peak around 9 µm. The emissivities of clays and CS remain high and largely independent of the particle size in the spectral region above 10 µm. The emissivity of anatase remains high at 11 µm due to the Christiansen feature located just below the first absorption band. These emissivity trends are reflected in the size-dependent radiated powers shown in Figure 6.2d. Calcite exhibits the largest reduction in the net radiated power at smaller particle sizes, whereas kaolinite and illite appear to benefit from reduced particle diameters, similarly to alumina and C3AH. The interaction with the T14 medium further diminishes the radiative cooling potential of $CaCO_3$ and anatase, while CS and clays emit more in the presence of the C-S-H-like medium.

The size dependence of the thermal radiative performance of the studied oxides, shown in Figure 6.2, indicates that certain materials are more sensitive to decreased particle sizes than others. Most of the materials emit less at smaller sizes, with exception of ettringite, jennite, T14 and clays, which appear to benefit from the reduced particle diameters. The poorest performance at small particle sizes in air was observed in CaO, α-Fe_2O_3, β-anhydrite, and calcite. The radiative properties of the studied oxides embedded in a C-S-H-like matrix deviate significantly from those in air. Notably, jennite, ettringite, illite, kaolinite, and CS are predicted to exhibit

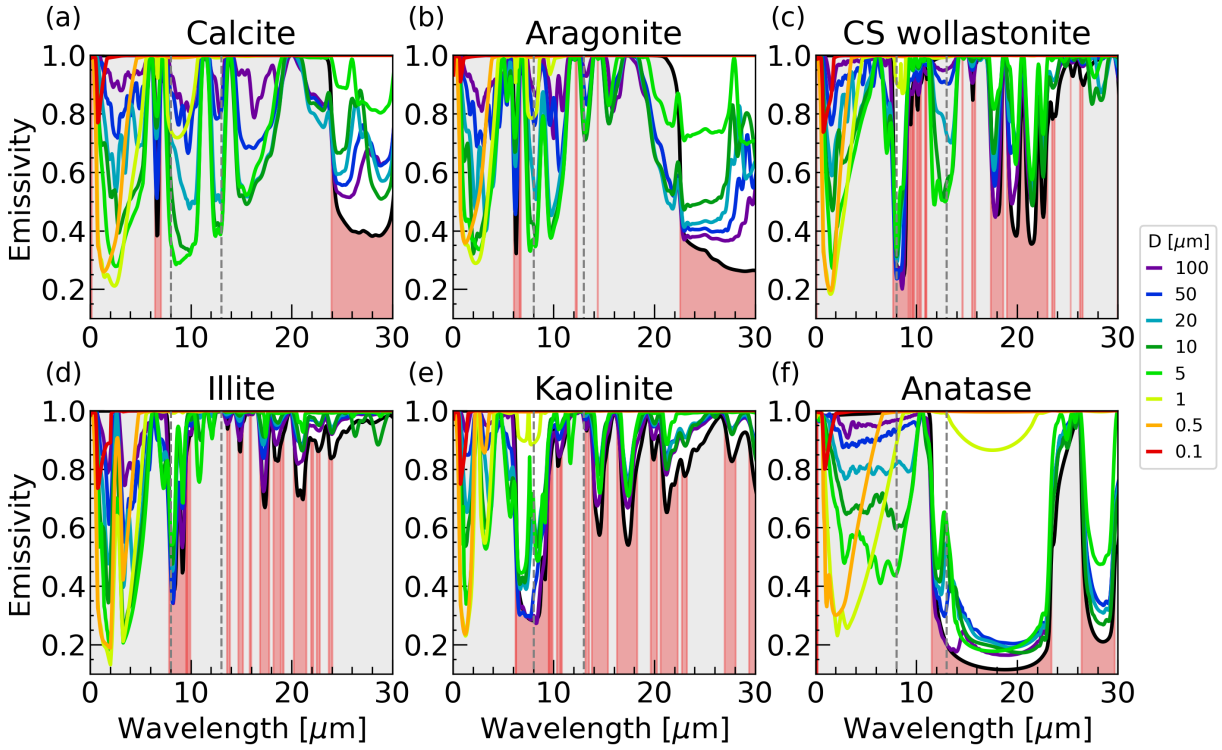

Figure 6.5: Size dependent Hapke-Mie emissivity of concrete phases in air. The colour lines represent different particle diameters, and the dashed lines correspond to the ATW. The high reflectance Reststrahlen bands are shown as red areas.

improved radiative performance in the concrete environment, making them promising candidates for the design of PC.

The radiated power of hematite particles in air decreases to nearly half of the bulk values, which further diminishes its suitability for radiative cooling applications, given its high absorption of solar radiation. In contrast, the second phase that contains Fe, C4AF, maintains high radiated power even at smaller particle sizes. Since the band gap of C4AF is bigger than that of hematite, it can potentially be a more suitable candidate for colored radiative cooling products, such as paints [162].

According to Kirchoff law, the sum of emissivity and reflectivity equals to one. Thus, IR regions with high emissivity are associated with low reflectance and a reduced scattering cross-section. These suppressed scattering regions are observed in all oxides at their material-specific Christiansen wavelengths, where the emissivity is high. While the height of the Christiansen emissivity peak remains nearly independent of the particle size, its width increases as the particle diameter decreases, which results in a broadening of the suppressed scattering region. The emissivity minimum in the thermal IR range is both deepest and widest in CaO, as shown in Figure 6.1a. This behavior arises from its relatively simple dielectric function and makes CaO particles particularly effective reflectors of thermal radiation. In general, the particles with diameters in the order of tens of microns reflect IR radiation most efficiently, as shown in the size-dependent emissivity spectra. Powders with a size distribution in this range can therefore act as effective reflectors of thermal radiation.

Experimental emissivity is strongly dependent on sample conditions. The isotropic scattering

approximation is applicable to randomly oriented small particles, large absorbing or irregular particles, rough surfaces, and closely packed powders. However, real samples may exhibit a combination of these characteristics and may therefore require more advanced approaches that account for anisotropic scattering lobes or enhanced backscattering [69, 70, 163–165]. The magnitude of emissivity changes in different spectral regions as a function of particle size can depend on the chosen scattering approximation. Deviations from experimental values may also arise from the use of the Mie single-particle albedo. Incorporating multiple-scattering effects would modify the size-dependent emissivities and, consequently, the net radiated powers. Nevertheless, the use of IMSA captures general trends that are robust and highly instructive for understanding radiative behaviour.

6.2.1 MSTM emissivity

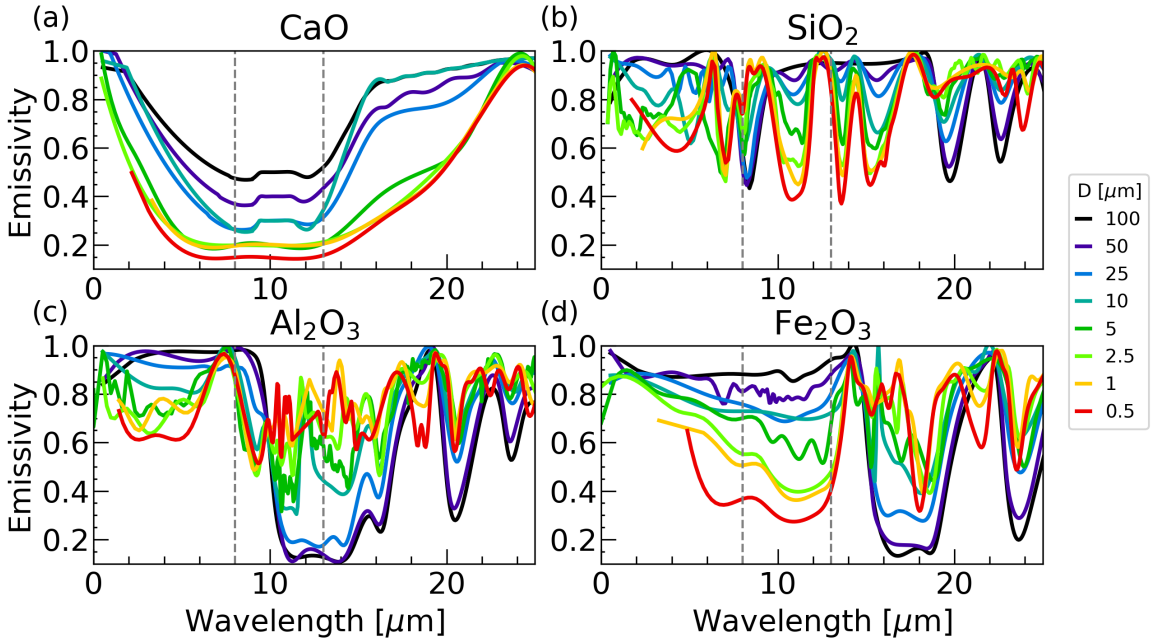

Figure 6.6: Size-dependent emissivity spectra calculated using Hapke model with multiple-scattering albedo computed using the MSTM method of (a) CaO, (b) α-SiO_2, (c) α-Al_2O_3, and (d) α-Fe_2O_3.

In order to evaluate if the use of the single-particle albedo is sufficient to describe multiple-scattering effects, we compare size-dependent emissivity calculated using albedo from Mie and MSTM methods. The T-matrix approach implemented in the MSTM method allows for the full many-body interaction with light and provides scattering efficiencies of large aggregates of spherical particles.

The size-dependent emissivity of simple cement-forming oxides is shown in Figure 6.6. The size-related changes of emissivity follow the same trends and are consistent between the two approaches. A comparison with Figure 6.1 shows that the two methods produce very similar results in terms of the positions, shapes, and intensities of the spectral features down to particle diameters of 5 microns. A discrepancy is observed for smaller particles, as the Mie single-particle albedo predicts an increase in emissivity up to unity at micron and sub-micron diameters,

whereas the use of the MSTM albedo does not predict such a rapid change in trends. The difference arises because single particles become transparent to wavelengths much larger than their diameter, which is not the case in aggregates and realistic assemblies of small particles. The radiated powers and radiative cooling performance of simple cement-forming oxides calculated using the multiple-scattering albedo are shown in Figure 6.15.

6.3 Size-dependent solar reflectance

Approximately 95% of the solar irradiance at the sea level consists of Vis and NIR light [166]. The thermal losses due to the absorption of solar radiation can therefore be mitigated by achieving high reflectance in this spectral range. We employed the HH method to calculate the hemispherical multiple-scattering reflectance based on the theoretical frequency-dependent refractive index. The reflectance was computed using the Mie single-scattering albedo for particles both in air and embedded in tobermorite 14Å.

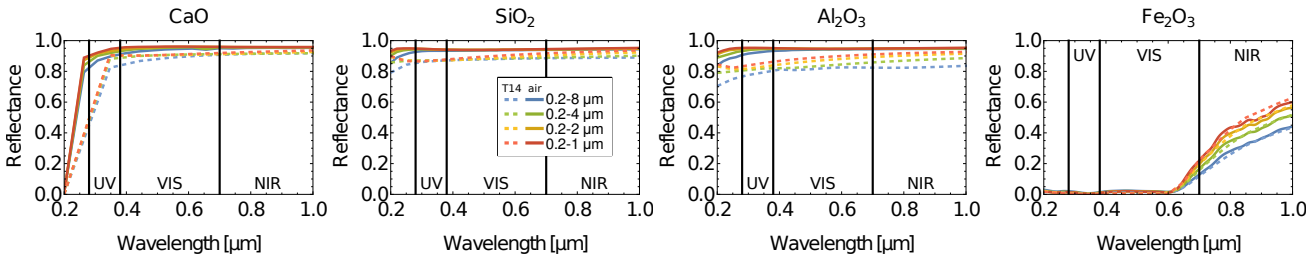

Figure 6.7: Size dependent averaged reflectance spectra of (a) CaO, (b) α-SiO_2, (c) α-Al_2O_3, and (d) α-Fe_2O_3. Each curve was averaged over particles with diameters in the ranges specified in the legend.

We calculated multiple-scattering reflectance for closely packed powders composed of spherical particles with diameters in the range of 0.1 to 10 microns, at wavelengths ranging from 0.2 to 10 µm. The solar reflectance curves averaged over different particle size ranges are summarized in Figure 6.7. The averages were calculated for particles with diameters larger than 200 nm and smaller than 1, 2, 4, and 8 microns, as distinguished by the colour of the corresponding curves. The reflectance in air is indicated by full lines whereas reflectance in the T14 C-S-H-like medium is shown by dashed lines. In air, the scattering of the UV–Vis radiation is most efficient for α-SiO_2 and α-Al_2O_3 particles. CaO scatters UV wavelengths less efficiently due to its smaller band gap, but it exhibits slightly highest reflectance in the NIR region. In contrast, α-Fe_2O_3 particles show very low reflectance in the UV–Vis range, with only a moderate increase in the NIR range. The influence of the C-S-H-like (T14) matrix is similar among the oxides. CaO and α-SiO_2 exhibit small decrease of reflectance when embedded in the T14 medium, and the reflectance of α-Al_2O_3 decreases more noticeably. In the plotted range, the reflectance of α-Fe_2O_3 is not affected by the T14 medium. The reflectance of α-Al_2O_3 in the solar range is reduced more due to similarities between the refractive indices of alumina and T14, which reduce the refractive-index contrast and consequently weaken scattering [167].

The reflectance of cement phases in the UV–Vis–NIR is shown in Figure 6.8 averaged over different particle sizes to simulate realistic powders size distribution. Apart from C4AF, all cement-phase nanoparticles exhibit strong reflectance of visible and NIR light in air, which

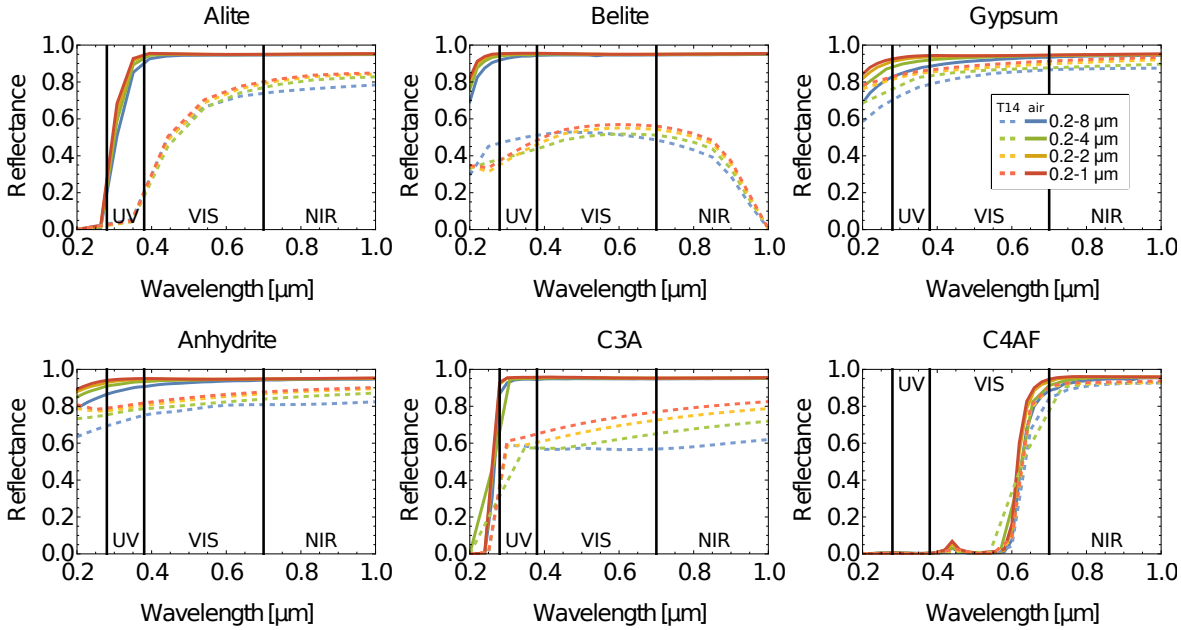

Figure 6.8: Size dependent averaged reflectance spectra of cement phases. Each curve was averaged for particles with diameters in the ranges specified by the legend.

indicates efficient scattering of solar radiation at these wavelengths. Unlike the other phases, C4AF has a relatively small band gap, which leads to significant absorption in the UV range. As a result, C4AF reflects only a small fraction of the incident solar radiation, similarly to α-Fe_2O_3. Likewise, alite particles reflect less in the UV region, which is related to its smaller band gap and weak excitonic peaks at the spectral onset. C3A shows comparable reflectance to β-belite, β-anhydrite and gypsum, although its reflectance in the UV range starts to decrease earlier. The reflectance of C3A was calculated using the IPA spectrum and the actual reflectance may therefore be somewhat different.

When embedded in the C-S-H-like T14 matrix, the reflectance of most cement phases decreases. This reduction arises from partial matching of refractive indices between the particles and the surrounding medium, as well as from absorption in the matrix itself, both of which reduce scattering efficiency. Gypsum and C4AF are the phases whose reflectance is least affected by the T14 matrix, and gypsum in particular maintains high UV–Vis reflectance in this concrete-like environment. This suggests that gypsum nanoparticles could be effective in minimizing solar absorption when incorporated into cementitious composites. The largest reduction in reflectance within the T14 matrix is observed for β-belite and C3A. The presence of absorbing surrounding medium introduces new features in reflectance, particularly in spectral regions close to the absorption bands of T14. Most cement phases exhibit a region of strongly suppressed reflectance just below 2.5 µm, where the refractive indices of the cement phases closely match that of the T14 matrix.

The size-averaged reflectance spectra of concrete particles in both air and the T14 matrix are shown in Figure 6.9. Overall, the hydrated phases exhibit high reflectance in air across the solar wavelengths thanks to large band gaps. Reflectance of T14 and portlandite decays faster in the UV range than in the case of other hydrates, but they maintain high values in the Vis and NIR ranges. When embedded in the T14 matrix, the reflectance of several phases decreases significantly. In particular, T11, portlandite, and C3AH show a pronounced reduction in UV–Vis

reflectance, which decreases scattering and increases solar losses. On the contrary, ettringite and jennite maintain high reflectance even in the T14 environment, which indicates that their optical properties are less affected by the concrete-like matrix. For jennite and ettringite in particular, the absorption bands occur at wavelengths similar to those of T14 within the considered spectral range, so the surrounding medium has a small influence on their optical response. Overall, the studied hydrated phases show potential for enhancing radiative cooling performance by reducing the solar absorption losses thanks to their high reflectance.

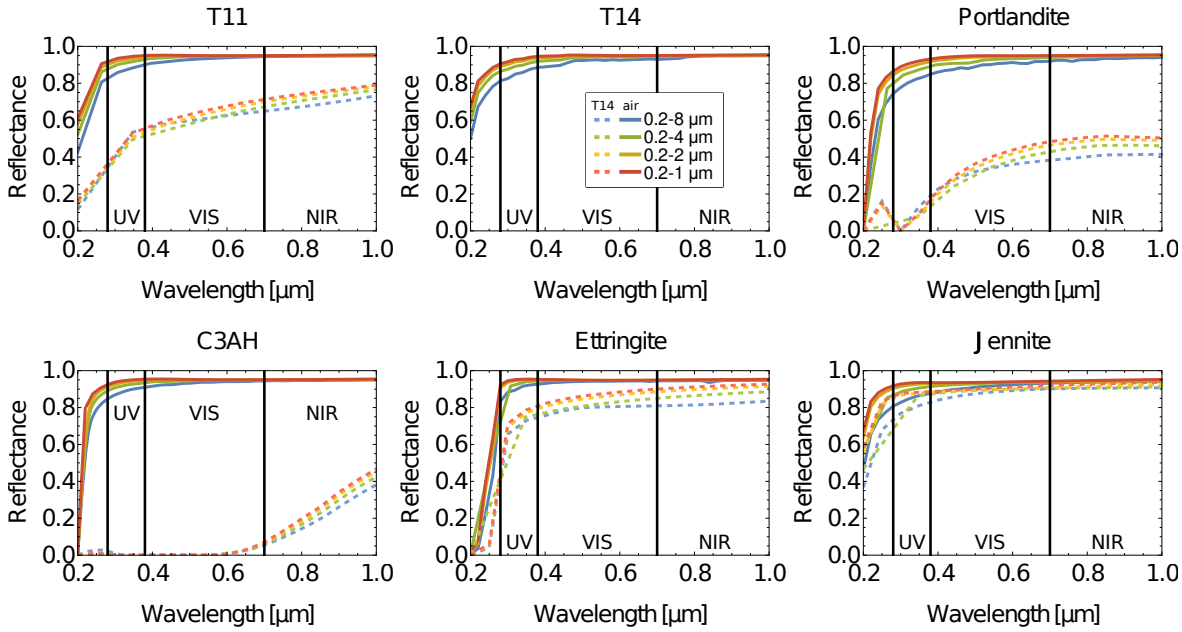

Figure 6.9: Size-dependent, averaged reflectance spectra of concrete phases. Each curve represents an average over particles with the diameters specified in the legend.

The averaged reflectance spectra of the various additives and raw materials in both air and the T14 matrix are shown in Figure 6.10. All examined phases exhibit relatively high reflectance across the UV–Vis spectral range, with the notable exception of anatase. TiO_2 reflects significantly less UV light due to its small band gap; however, it reflects strongly in the Vis and NIR ranges. Among the analyzed materials, CS shows the highest reflectance in air across the solar spectrum, which indicates its strong scattering properties and low absorption of solar irradiation. When incorporated into the T14 matrix, reflectance of calcite and clays decreases most significantly. In contrast, reflectance of anatase and CS are affected less, with relatively minor changes. The reflectance of visible light by most of the additives and raw materials considered here is high, which is important for minimizing solar absorption in radiative cooling applications.

The reflectance of powders in air in the range of wavelengths up to 10 µm is shown in Figure 6.11. The non-hydrated phases display high reflectance over larger range of wavelengths thanks to their simpler absorption spectra. The widest spectrum of wavelengths is reflected by CaO and TiO_2, followed by alite, β-belite and calcite, which reflect well wavelengths at least up to 7 µm. The materials with O-H bonds in their crystal structure, namely hydrated phases and clays, decrease their reflectance above 2.5 µm. The effects of the particle size distribution are compared in Figure 6.11a–d for average over diameters between 0.2 and 1 microns, and in

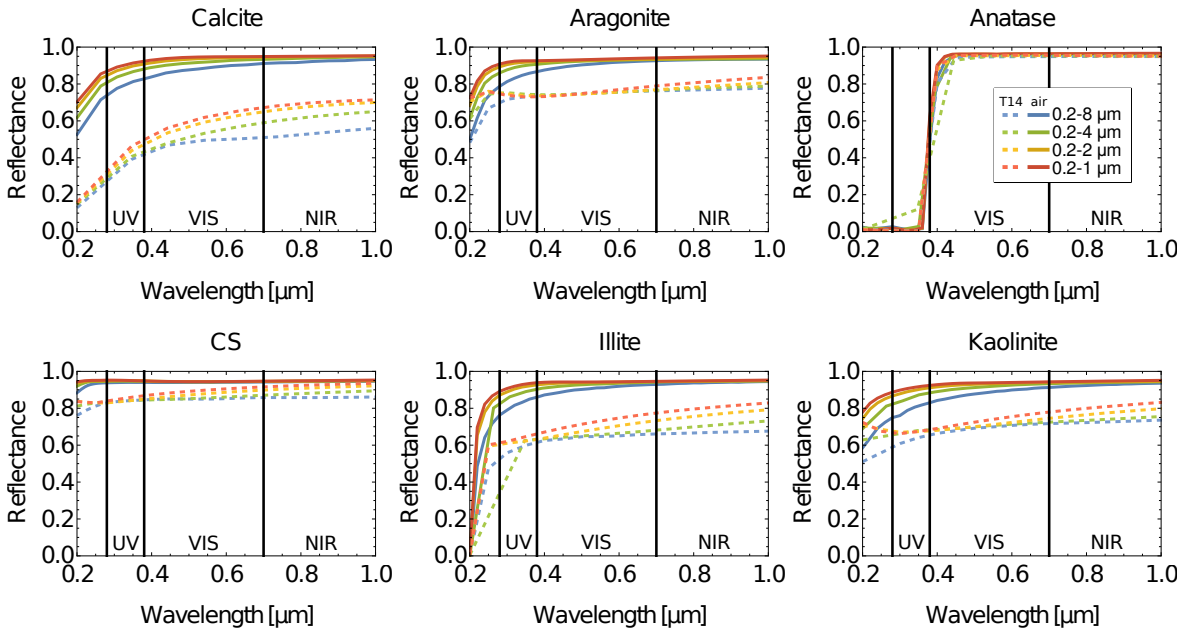

Figure 6.10: Size dependent averaged reflectance spectra of raw minerals, clays and additives. Each curve represents an average over particles with the diameters specified in the legend.

Figure 6.11e–h for average over 0.2 and 8 microns. Larger particles slightly reduce reflectance of short wavelengths and noticeably increase reflectance of NIR light, where new spectral features emerge. The reflectance in the solar range remains high even for the largest particles.

The use of nanoparticles with an appropriate size distribution can enhance scattering and reflectance, which could significantly lower the surface temperature. Therefore, we evaluate the

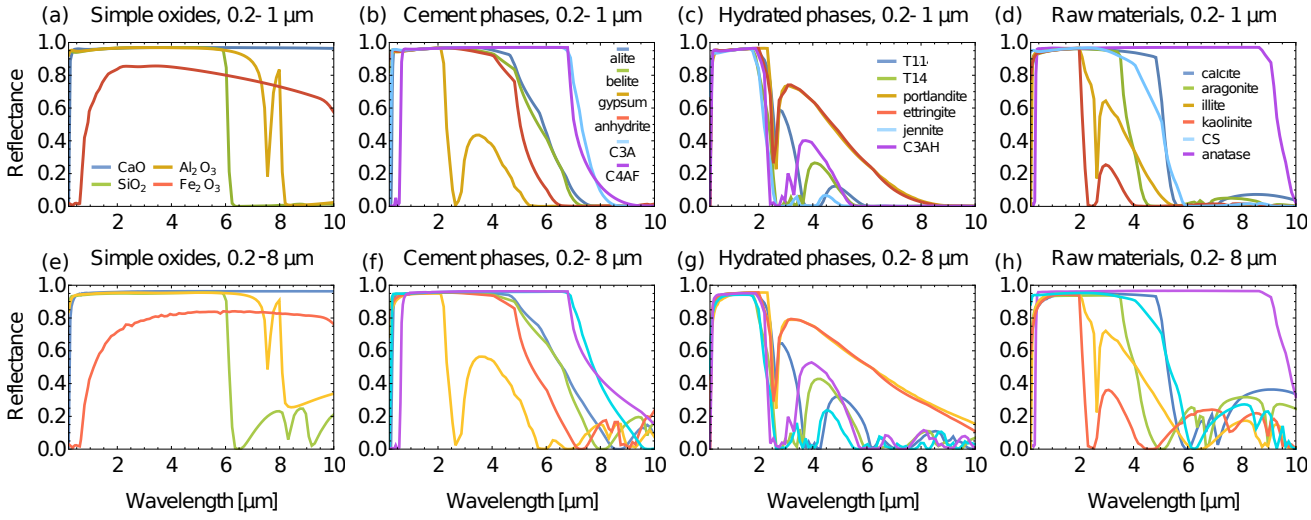

Figure 6.11: Reflectance in air shown at wavelengths up to 10 μm, averaged for particle diameters larger than 0.2 and smaller than (a–d) 1 micron, and (e–h) 8 microns.

average solar reflectance can using the expression

$$R_{sun} = \frac{\int_{0.28\mu m}^{2.5\mu m} R(\lambda) I_{sun}(\lambda) \mathrm{d}\lambda}{\int_{0.28\mu m}^{2.5\mu m} I_{sun}(\lambda) \mathrm{d}\lambda}, \tag{6.1}$$

where $R(\lambda)$ is the reflectance and I_{sun} the solar irradiance [168]. The integration limits were set to include most of the solar irradiated power in the UV–Vis–NIR spectral region.

The average solar reflectance R_{sun} of the studied phases is shown in Figure 6.12 as a function of particle diameter, where panels (a–d) represent the reflectance in air and panels (e–h) in the T14 matrix. Each particle diameter represents reflectance of a powder composed of particles with the same diameter. In air, the highest solar reflectance was obtained for CaO, CS, C3A, α-Al_2O_3, α-SiO_2, β-belite and alite. The reflectance of cement nanoparticles is high and similar across the phases, while gypsum exhibits slightly lower reflectance due to O-H absorption bands around 2.5 µm. Hydrated concrete phases also reflect well, among which ettringite, C3AH and T11 perform better. The best reflecting additives at nanometer diameter scale are CS, $CaCO_3$ and illite.

The reflectance of solar radiation decreases with increasing particle size. However, some materials have a reflectance maximum within the studied diameter range. For example the maxima of the hydrated phases and $CaCO_3$ are located at particle diameters of approximately 300–500 nm. The smallest decrease of the solar reflectance due to particle size was found in β-belite, C3A and CS. The simple oxides, except from hematite, are highly reflective and show a small decrease of R_{sol} for larger particles. Portlandite is the most reflecting material at the nanoscale but its reflectance reduces faster at larger particle sizes than in other hydrates. The solar reflectance of the additives for large particles decreases the least in CS and anatase. The largest reflectance reduction at large particle sizes was found in kaolinite, calcite and portlandite.

The reflectance in the T14 medium decreases for all cement related phase, as shown in Figure 6.12(e–h). The least affected phases are CaO, α-SiO_2, ettringite and anatase. On the other hand, the largest decrease was found for belite, portlandite, T11 and calcite. Among the

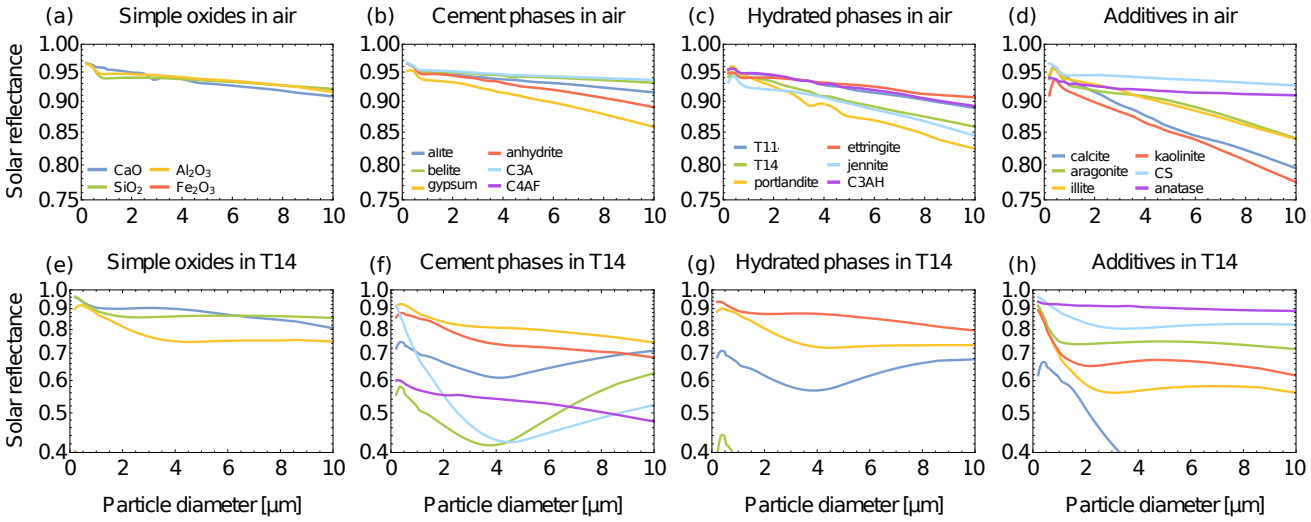

Figure 6.12: The average solar reflectance R_{sol} integrated between 0.2 and 2.5 µm of cementitious phases at different particle sizes, (a-d) in air and (e-h) in the T14 medium.

investigated phases, these materials are therefore particularly promising for PC applications, with high reflectance over a broad range of particle sizes.

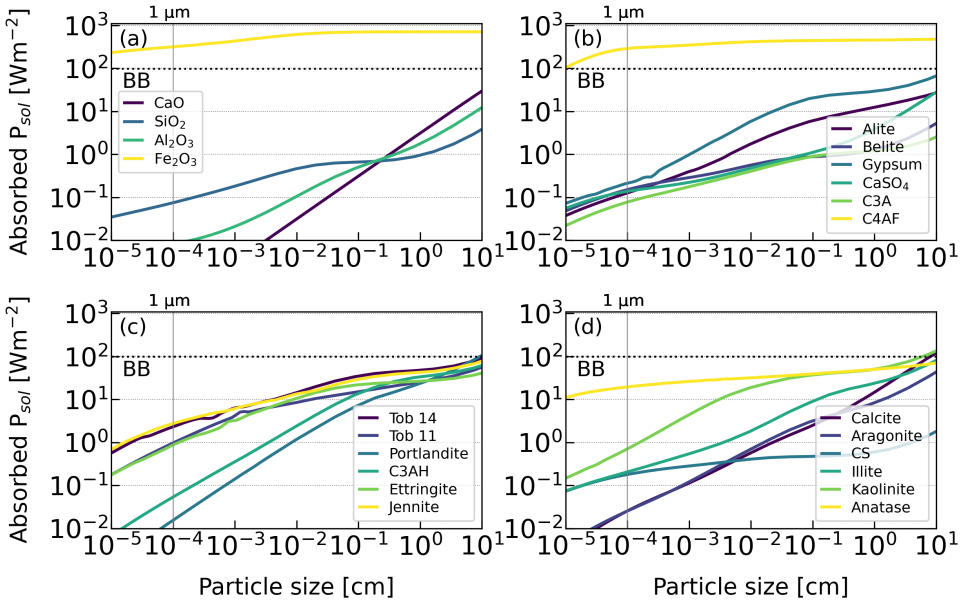

Figure 6.13: Solar absorbance by single particles as a function of diameter for (a) simple oxides, (b) cement phases, (c) hydrated phases, and (d) additives and raw materials.

We also calculated size-dependent absorbance of wavelengths up to 10 µm by single spheres of all studied materials, as shown in Figure 6.13. Absorbance was calculated using Beer-Lambert law and the internal reflections were taken into account as a sum of reflection and transmission events, which lead to a geometric series, as defined in Equation 2.78. There are two materials absorbing at all particle sizes – hematite and C4AF. The rest of materials absorb less than 100 Wm^{-2} at diameters below 10 cm. The least absorbing materials at large diameters are α-SiO_2, C3A and CS. Hydrated phases absorb more energy, therefore phases without O-H bonds, with exception of anatase that has higher k values, are practically unrestricted by the particle size. The absorbed power of most of the studied phases is lower than the radiated one up to diameters of tens of centimeters in the perfect crystal limit. Hydrated phases become absorbing faster, but diameters in the micrometer range have negligible absorbance. The thermal losses in these materials are therefore completely determined by the reflectance. The linear size-dependence of absorbance is typical for materials without strong absorption bands below 10 µm limit used for the integration. This is the best seen for CaO, which has the only IR absorption band at 30 µm. The non-linear dependences arise from the absorption bands and higher k values that increase the losses at bigger diameters.

6.4 Radiative cooling potential

In order to compare the potential of the studied materials for radiative cooling applications, we summarize the calculated radiated power, average solar reflectance, and solar losses in Figure 6.14. The green bars represent the lowest thermal radiated powers obtained with respect to particle size in air, as discussed in Figure 6.2. The grey bars correspond to the highest theoretical

radiated powers, following the analysis presented in Figure 5.8. The blue bars indicate the solar reflectance R_{sun}, defined in Figure 6.12, averaged over particle diameters up to 10 microns in air to mimic the random size distribution in realistic powders. Lastly, the red bars show the solar losses calculated using the averaged solar reflectance (blue bars). The powers in Figure 6.14 are normalized to the black-body radiation at 300 K for purposes of comparison between materials. The materials are arranged from left to right in order of decreasing radiative cooling capability, according the difference between the lowest thermal radiated power (green bars) and the solar loss (red bars).

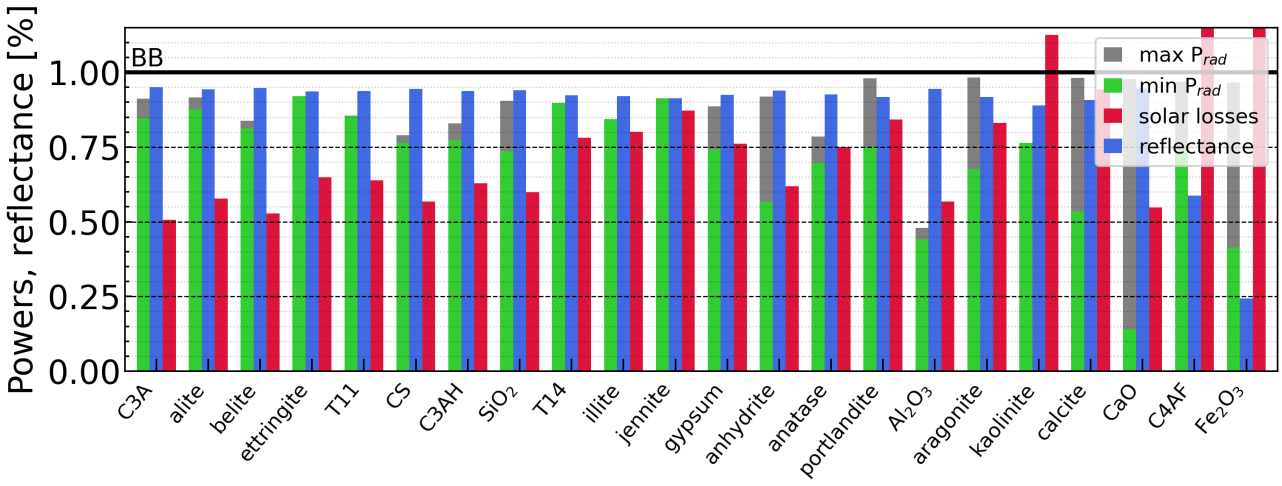

Figure 6.14: Radiative cooling of powders composed of cement-related materials. Green and grey bars are the lowest and highest material radiated powers, blue and red bars are average reflectances and solar losses of powders composed of particles with diameters in the range of 0.2–10 microns. Radiated abd absorbed powers are normalized to the black-body radiation.

According to the analysis shown in Figure 6.14, most of the studied phases are promising candidates for radiative cooling applications. There are eleven materials whose radiated powers are larger than solar losses in the used average reflectance setup, and are therefore capable of daytime radiative cooling. These materials are jennite, illite, T14, α-SiO_2, C3AH, CS, T11, ettringite, β-belite, alite and C3A. Their performance is good thanks to their high emissivity and low solar losses. The highest size-averaged reflectance was obtained for C3A, β-belite, CaO, CS, α-Al_2O_3 and α-SiO_2. The largest radiated power including solar losses were found for C3A, alite and β-belite. Favorable behavior arises from the combination of high thermal radiated power, high solar reflectance, and large electronic band gaps that limit solar absorption. Ettringite, jennite, T14, T11, and illite maintain comparable or even higher radiated power at smaller particle sizes, which shows that their cooling performance remains high in the micro- and nano-particle regimes. On the downside, the water molecules make hydrated phases absorbing in the NIR range, which reduces their radiative cooling performance. The phases without water or OH groups are therefore better suited for daytime radiative cooling.

Radiative cooling has previously been reported for materials such as α-SiO_2 and calcite, which are also included in the present study. As shown in Figure 6.14, calcite is located in the second half of the radiative cooling performance ranking. Our analysis identifies additional cement-related phases that are expected to perform even better than silica, which suggests that they could further enhance radiative cooling capacity.

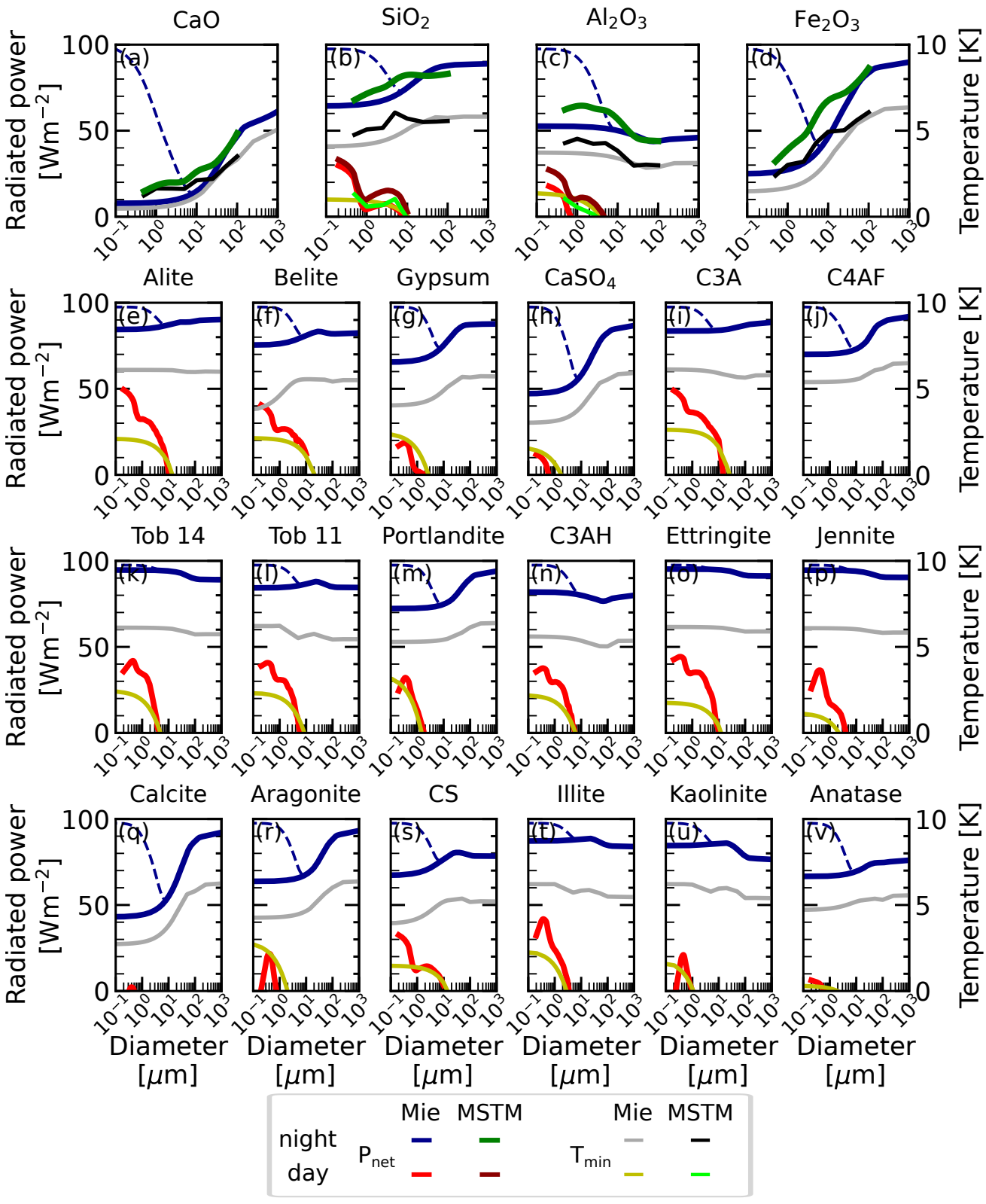

Figure 6.15: Radiated powers and potential cooling capacity of cement related phases. Net radiated powers at night (without solar losses) are shown in dark blue, daytime net radiated powers (including solar losses) in red, night powers calculated using the MSTM albedo in green and MSTM daytime powers in dark red. The minimum temperature that can be reached in atmosphere of 300 K at night is shown as grey (black for MSTM) during night and yellow (light green for MSTM) during day. Dashed blue lines are Mie single-scattering albedo powers, as eplained in the text.

In Figure 6.14, we show the radiative cooling performance of powders with an average size distribution. Since the size dependence of powder reflectance strongly affects solar losses, we plot the net radiative powers in Figure 6.15 as a function of particle diameter. Here, the radiated powers without solar loses are shown in dark blue and are denoted as radiance at night. The dashed dark blue lines correspond to the radiated powers shown in Figure 6.2, while the solid lines below 10 microns are extrapolated in order to mimic the behaviour of realistic powders. The steep increase in radiative power predicted using the Mie albedo arises from the limitations of this method, as shown in Figure 6.6. The radiative powers calculated using the MSTM multiple-scattering albedo, plotted as green curves in Figure 6.15, do not predict any rapid change of trends for the smallest particles. The daytime radiative powers, shown as red and dark red curves, were obtained by subtracting solar losses from the blue and green curves, corresponding to the Mie and MSTM albedos, respectively. Furthermore, we estimated the minimum temperature that each phase can reach during both nighttime and daytime conditions. These are shown in grey and yellow for the Mie albedo, and in black and dark yellow for the MSTM albedo, respectively. The minimum temperatures achievable through radiative cooling in an atmosphere at 300 K were estimated from the zero-crossings of the temperature-dependent net radiative powers shown in Figure 5.7. The cooling temperatures corresponding to the Mie albedo results were extrapolated for particle radii below 10 µm and should therefore be regarded as approximate. Non-radiative losses were included in the calculation of cooling temperatures according to Equation 2.76, assuming a conduction-convection coefficient of $h_c = 10\ \mathrm{Wm^{-2}K^{-1}}$.

Net radiative powers of simple cement-forming oxides calculated using the single-particle Mie albedo were compared with those obtained using the multiple-scattering MSTM albedo in Figure 6.15a–d. In all four cases, the results are in good agreement when the steep increase in the Mie radiative powers at the smallest particle diameters is neglected (solid dark blue lines). The agreement is good for both nighttime and daytime radiative powers. Similarly, the cooling temperatures calculated using the two methods compare well. This comparison shows that the Mie albedo can be used to predict the radiative properties of these materials, provided that the response for the smallest particles is appropriately extrapolated.

The analysis presented in Figure 6.15 shows that most materials exhibit positive daytime net radiative powers, shown by the red curves, and are therefore capable of passive daytime radiative cooling. The only exceptions are CaO, because of its small radiated power, and iron oxides, because of their large absorption. The highest daytime radiative powers, and therefore the best radiative cooling performance, were predicted for alite, C3A, ettringite, and illite. Powders of these materials composed of particles with diameters up to 10–20 μm still radiate more energy than they absorb. Other well-performing materials include β-belite, tobermorites, portlandite, C3AH, jennite, and wollastonite. Interestingly, α-Al_2O_3 powders with small particle diameters are also capable of radiative cooling due to their high reflectance and the filling of the emissivity minimum located in the atmospheric transparency window (ATW) region in the bulk material, as shown in Figure 6.6c and Figure 6.1. In contrast to the results shown in Figure 6.14, a larger number of phases are capable of daytime radiative cooling when composed of monodisperse particles.

We also analyzed the lowest temperatures to which the cement and concrete phases can cool under both daytime and nighttime conditions. The nighttime cooling ranges from 1 to 6 K within the plotted range and is, in most cases, more efficient for larger particles. The highest nighttime cooling capacities were found for iron oxides, aragonite, and clays. In contrast, daytime cooling is more efficient for smaller particle sizes, as indicated by the yellow curves in Figure 6.15. As

the MSTM results for the simple cement-forming oxides show, the cooling temperature curves closely follow the shape of the daytime net radiative powers. The cooling temperatures of some phases may be even higher than those predicted by the extrapolated temperature dependence. Overall, the daytime cooling potential reaches up to 3–4 K.

The results presented here were obtained for ideal crystalline structures. In practice, many phases present in concrete are partially or fully amorphous, such as C–S–H gel and silica. Amorphous materials generally exhibit broader and less well-defined ionic absorption peaks, and their band gaps may differ from those of their crystalline counterparts. Furthermore, additional experimental factors, including finite temperature, material purity, cracks, surface roughness, and particle shape, can significantly influence emissivity and reflectance.

6.5 Outlook

In this chapter, we analyzed the size-dependent emissivity of the investigated phases to identify materials suitable for radiative cooling applications. The highest net radiated powers were obtained for hydrated phases such as ettringite, jennite, tobermorite 14Å but also alite and C3A. Most of the studied phases maintain relatively high radiated power even at smaller particle sizes. In contrast, the lowest size-dependent net radiated powers were observed for CaO, α-Fe_2O_3, α-Al_2O_3, calcite, and β-anhydrite.Most of the cementitious phases reduce their thermal emissivity at smaller particle sizes, with exception of alumina, T14, C3AH, ettringite, jennite and clays.

The multiple-scattering albedo obtained using the MSTM method justifies the use of Mie theory for the calculation of emissivity down to particle diameters of 5 microns. The applicability of the single-particle albedo below this value is very limited.

Furthermore, we evaluated the solar reflectance of all phases. Our results show that wide-band-gap insulating materials generally exhibit high solar reflectance. The best performance was found for CS wollastonite, C3A, β-belite, α-Al_2O_3 and CaO. These materials effectively scatter incident solar radiation, particularly at sub-micron particle sizes. On the other hand, absorbing oxides of Fe have markedly lower reflectance.

A combination of high emissivity in the ATW region and solar reflectance are prerequisites for daytime radiative cooling, which can potentially achieve sub-ambient temperatures even under direct solar irradiation. Considering these factors together, powders of C3A, alite and β-belite are as the most promising candidates for daytime radiative cooling applications. The powders of ettringite, T14, C3AH and illite with specific particle size exhibit similarly high daytime radiative cooling. However, high reactivity with water makes the use of the clinker phases complicated. The hydrated products are therefore good materials for radiative cooling, regardless of their slightly increased solar losses due to OH groups.

The emissivity and reflectance of the studied phases embedded in the C-S-H-like T14 medium were also analyzed. Most phases exhibit reduced performance in a C-S-H-like environment, though CaO, α-SiO_2, gypsum ettringite, CS, anatase, jennite maintain high emissivity and reflectance when incorporated into a concrete-like matrix. These results demonstrate that the interaction between individual phases and the surrounding matrix strongly influences their optical behavior within the composite material.

Overall, our findings highlight the critical roles of particle composition, particle size, and the surrounding matrix in determining the optical properties of cement phases. This understanding is essential for optimizing the radiative cooling performance of concrete materials. Thus, cement

and concrete emerge as promising candidates for radiative cooling applications.

Conclusions

In this thesis we investigated the optical properties of common cement and concrete phases in order to evaluate their radiative cooling properties. The underlying optical constants were obtained from G_0W_0 and Bethe-Salpeter calculations in order to include many-body effects. Our results demonstrate that approaches beyond standard DFT are necessary to accurately predict the optical response of cement-based materials and achieve excellent agreement with available experimental data. The size-dependent phenomena were analyzed using Mie theory and Hapke model. The outcomes of this study provide a guidance for the development of photonic concretes capable of radiative cooling through the incorporation of nano- and micro-particles as cement additives.

A comparison of exchange-correlation functionals reveals that the SCAN functional performs better than the GGA functional in predicting both lattice parameters and DFT band gaps. Importantly, the SCAN+G_0W_0 approach yields electronic structures that are in better agreement with experimental data. These findings indicate that SCAN provides an efficient and reliable ground-state description for subsequent optical-property calculations, without the need for semi-empirical variables.

Our results emphasize the crucial role of electron-hole interactions in achieving accurate optical spectra, since these interactions account for exciton formation at the absorption onset. Several cement and concrete phases exhibit excitonic peaks below the quasiparticle band gap. More importantly, BSE redistributes and shifts the GW spectra, which is essential for obtaining optical spectra that can be quantitatively compared with experimental results.

The computed dielectric functions, which include both electronic and ionic contributions, provide reliable inputs for simulations of nanoparticle models in concrete composites with tailored optical responses. Radiative cooling relies on two fundamental requirements: selective emissivity in the atmospheric transparency window and high solar reflectance. Both properties can be modeled using Hapke model in combination with Mie theory. While all studied materials exhibit high emissivity in the bulk limit, certain phases maintain high emissivity even at small diameters. The highest emissivity of particulate materials was found in ettringite, jennite, tobermorite, alite and C3A. On the other hand, the lowest emissivity was obtained for CaO and hematite.

Arguably, solar reflectance is more critical for daytime radiative cooling than selective emissivity, since even minor solar absorption losses can significantly reduce cooling performance. Most wide-band gap materials exhibit high average solar reflectance. The highest values were found for unhydrated phases, namely CS wollastonite, CaO, α-Al_2O_3, alite, β-belite and C3A. Combining both emissivity and reflectance, the best materials for radiative cooling are C3A, alite ettringite, tobermorites and β-belite. The high reactivity of clinker phases with water makes their application difficult. Hydrated phases are more resistant to the humidity and offer an efficient alternative to the clinker phases.

Since concrete is a multi-phase composite, its solar reflectance can be tuned by controlling both the composition and particle size of the additives. Owing to the abundance and low cost of the constituent materials, this approach is highly scalable and compatible with existing production technologies. In this context, the addition of CaO, α-SiO_2, ettringite, anatase and other discussed nanoparticles appears particularly promising. These findings further demonstrate that interactions between individual phases and the surrounding matrix strongly influence the overall optical response of the composite. Properly accounting for such interactions is essential for predicting the performance of cementitious materials in practical applications, including coatings and structural concrete, where the embedding medium significantly affects reflectance.

This work provides atomic-level insights into the optical and radiative behavior of cementitious oxides, which are key components in emerging concrete-based photonic and energy-efficient technologies. We demonstrate that many cement-based materials are highly promising for daytime radiative cooling applications. The most suitable candidates were identified based on three key criteria: optical absorption onset (band gap), selective emissivity, and high solar reflectance. Calcium silicates, particularly their hydrated phases, exhibit outstanding performance. In contrast, Fe-containing materials show substantial solar absorption losses, which are detrimental for daytime radiative cooling. The thesis contributes to the advancement of materials design through predictive, multiscale modeling.

The results obtained in this work provide a solid foundation for future research. The highly accurate optical properties calculated here can be used in more advanced reflectance modeling approaches, including explicit multiple-scattering simulations and polycomponent powder models. The effective dielectric response of concrete composites can also be approximated using suitable averaging schemes based on the single-phase dielectric functions.

One of the broader goals of this thesis was to explore new high-tech applications of cement and concrete beyond their traditional mechanical roles. Future work will therefore focus on low-dimensional systems derived from selected cement phases. Their layered crystal structures and excitonic properties open up new possibilities for novel applications in photonics and energy-related technologies, which extend the functional scope of cementitious materials far beyond conventional construction uses.

List of publications

1. **J. Janovec**, L. Straka, A. Sozinov, O. Heczko, & M. Zelený, First-principles study of Zn-doping effects on phase stability and magnetic anisotropy of Ni-Mn-Ga alloys, Mater. Res. Express 7(2) (2020) 026101.

2. M. Zelený, M. Heczko, **J. Janovec**, D. Holec, L. Straka, & O. Heczko, The effect of local arrangement of excess Mn on phase stability in Ni–Mn–Ga martensite: an ab initio study. Shape. Mem. Superelast. 6(1) (2020) 35-44.

3. **J. Janovec**, M. Zelený, O. Heczko, & A. Ayuela, Localization versus delocalization of d-states within the Ni_2MnGa Heusler alloy, Sci. Rep. 12(1) (2022) 20577.

4. T. Leiner, N. Koutná, **J. Janovec**, M. Zelený, P. H. Mayrhofer, & D. Holec, On energetics of allotrope transformations in transition-metal diborides via plane-by-plane shearing. Vacuum 215 (2023) 112329.

5. R. O. Agbaoye, **J. Janovec**, A. Ayuela, & J. S. Dolado, Thermoelectric properties of the main species present in Portland cement pastes, Cem. Concr. Res. 183 (2024) 107587.

6. **J. Janovec**, J. S. Dolado, & A. Ayuela, Optical and excitonic properties of calcite $CaCO_3$, J. Mater. Chem. C 13(12) (2025) 6267-6276.

7. **J. Janovec**, R. O. Agbaoye, J. S. Dolado, & A. Ayuela, Optical properties of CaO, SiO_2, Al_2O_3 and Fe_2O_3 cementitious oxides, Mater. Des. 260 (2025) 114803.

8. J. Ryu, V. Krivenkov, A. Olejniczak, M. Arruabarrena, **J. Janovec**, S. E. Hadjadj, M. Ilyn, A. Leonardo, V. Martínez-Martínez, A. Ayuela, A. Y. Nikitin, & Y. Rakovich, Nickel doping unlocks ambient-condition photostability in individual cesium lead bromide perovskite quantum dots, Nano Lett. 25(47) (2025) 16630-16636.

9. **J. Janovec**, G. Goracci, J. S. Dolado, & A. Ayuela, Selective Optical Properties of Cement for Enhanced Radiative Cooling and Energy-Efficient Construction Materials, Energy Environ. Mater. (2026) e70210.

10. **J. Janovec**, R. O. Agbaoye, J. S. Dolado, & A. Ayuela, Size-dependent photonic and radiative properties of CaO, SiO_2, Al_2O_3 and Fe_2O_3 cementitious oxides, Cem. Concr. Res. 203 (2026) 108156.

11. Low dimensional cement based materials as a playground for investigation of exciton-polariton interaction (In preparation).

Appendices

Appendix A

Green's functions representation

In general, Green's functions are solutions to inhomogeneous differential equations with homogeneous boundary conditions and a Dirac delta function as the source term. They find wide use in acoustics, fluid dynamics, thermodynamics, radiative transfer, electromagnetism or quantum mechanics. The Green's function can be used to transform an inhomogeneous differential equation into an integral form as

$$\hat{O}f(x) = g(x), \tag{A.1}$$

$$f(x) = \int G(x, x')g(x')\,dx', \tag{A.2}$$

$$\hat{O}G(x, x') = \delta(x - x'), \tag{A.3}$$

where $\hat{O}$ is a linear differential operator, $g(x)$ is the inhomogenity source term and G(x,x') is the Green's function. The relations in Equation A.1–A.3 hold thanks to the property $f(x) = \int_{-\infty}^{\infty} \delta(x - x')f(x')dx'$ of the Dirac delta $\delta(x - x')$ [46, 169].

The Schrödinger equation is a linear homogeneous differential equation

$$\hat{H}\Psi(\mathbf{r}, t) - i\frac{\partial}{\partial t}\Psi(\mathbf{r}, t) = 0, \tag{A.4}$$

where the Hamiltonian operator consists of the kinetic energy $-\frac{1}{2}\nabla^2$ ($-\nabla^2\frac{\hbar^2}{2m}$ in the SI units) and the external or effective potential acting on electrons $V(\mathbf{r}, t)$. The equation can be reorganized as

$$\left[i\frac{\partial}{\partial t} + \nabla^2\frac{1}{2}\right]\Psi(\mathbf{r}, t) = V(\mathbf{r}, t)\Psi(\mathbf{r}, t), \tag{A.5}$$

with the right hand side representing the source term. Functions on both sides of the equation are the same, which calls for a self-consistent iterative approach. This complicated many-body problem can be simplified by considering a solution for a non-interacting system with the external potential added perturbatively. This is the philosophy of the many-body perturbation theory (MBPT) methods. Following Equation A.2, the wavefunction of a system of free electrons can be written as

$$\psi_0(\mathbf{r}, t) = \int G_0(\mathbf{r}, t, \mathbf{r}', t')\psi_0(\mathbf{r}', t')d\mathbf{r}', \tag{A.6}$$

where the non-interacting Green's function satisfies

$$\left[i\frac{\partial}{\partial t} + \nabla^2\frac{1}{2}\right]G_0(\mathbf{r}, t, \mathbf{r}', t') = \delta(\mathbf{r} - \mathbf{r}')\delta(t - t'). \tag{A.7}$$

In the noninteracting particle limit the two wavefunctions are equal, i.e., $\Psi(\mathbf{r},t) = \psi_0(\mathbf{r},t)$. The physical interpretation of Equation A.6 is the time evolution of ψ_0 from a given time and position, defined by $\mathbf{r}'$ and t', to another time and space point, defined by $\mathbf{r}$ and t. Due to this property, Green's functions are also called propagators.

Changes in the wavefunction caused by an external perturbing potential can be described using the Lippmann-Schwinger equation [45]. In this representation, the integral form of the Schrödinger equation can be written as

$$\Psi(\mathbf{r},t) = \psi_0(\mathbf{r},t) + \int_{-\infty}^{t}\int G_0(\mathbf{r},t;\mathbf{r}',t')V(\mathbf{r}',t')\Psi(\mathbf{r}',t')\,d\mathbf{r}'dt', \tag{A.8}$$

$$\Psi(\mathbf{r},t) = \psi_0(\mathbf{r},t) + \int_{-\infty}^{t}\int G(\mathbf{r},t;\mathbf{r}',t')V(\mathbf{r}',t')\psi_0(\mathbf{r}',t')\,d\mathbf{r}'dt'. \tag{A.9}$$

The wavefunction is thus expressed recursively in terms of its values at earlier times[1]. Iterative substitution generates a perturbative expansion known as the Born series, which describes the propagation of a particle undergoing successive scattering events due to the potential. By substituting $\Psi(\mathbf{r}',t')$ by a wavefunction at another space-time $(\mathbf{r}'',t'')$, we get

$$\Psi = \psi_0 + \int\int G_0 V\left[\psi_0 + \int\int G_0 V\Psi d\mathbf{r}''dt''\right]d\mathbf{r}'dt', \tag{A.10}$$

which is the first term in the Born scattering series. The Born series describes propagation of an electron and in the interacting picture each interaction is a scattering event due to the potential. The scattering events take place at successive times $t > t' > t''$ etc. By repeated substitution of Ψ one gets a simplified form

$$\Psi = \psi_0 + (1 + G_0V + G_0VG_0V + \dots)G_0V\psi_0 \tag{A.11}$$

$$= \psi_0 + (1 - G_0V)^{-1}G_0V\psi_0. \tag{A.12}$$

Equation A.11 was rewritten as a geometric series of operators using the expression $\sum_{i=1} a(x)^{i-1} = a(1-x)^{-1}$. From Equation A.12 and Equation A.9, Dyson equation writes

$$GV = (1 - G_0V)^{-1}G_0V, \tag{A.13}$$

$$G = G_0 + G_0VG, \tag{A.14}$$

which is the famous Dyson equation for Green's function [46]. In interacting systems, the full Green's function can be expressed in terms of the non-interacting one via the Dyson equation. In interacting many-body systems, the potential V is replaced by the self-energy operator Σ, which accounts for exchange and correlation effects beyond the noninteracting approximation.

Green's functions provide a description of propagation in space and time, which is closely related to the time-evolution operator U

$$\Psi(\mathbf{r},t) = \int \langle\mathbf{r}|U(t,t')|\mathbf{r}'\rangle\Psi(\mathbf{r}',t')\,d^3\mathbf{r}', \tag{A.15}$$

$$U(t,t') = e^{-iH(t-t')}, \tag{A.16}$$

[1]The form Equation A.8 can be motivated by using the set of equations $(E-H_0)\psi_0 = 0$ and $(E-H_0-V)\psi = 0$ for the wavefunctions, as well as $H_0G_0 = \delta$ and $(H_0 - V)G = \delta$, which lead to $G_0 = (E - H_0)^{-1}$ and $G = (E - H_0 - V)^{-1}$, i.e., G is the resolvent of H

for a time-independent Hamiltonian. The time-evolution operator defines the wavefunction at time t knowing it at some earlier time, giving $\Psi(t) = U(t,t')\Psi(t')$. The Equation A.15 uses the position representation $\Psi(\mathbf{r},t) = \langle \mathbf{r}|\Psi(t)\rangle$. Using this notation, the Green's function describes propagation forward in time, like

$$G(\mathbf{r},t,\mathbf{r}',t') = -i\theta(t-t')\,\langle \mathbf{r}|U(t,t')|\mathbf{r}'\rangle\,, \tag{A.17}$$

where θ is the Heaviside step function, which is equal to zero for negative and one for positive arguments. By inserting ths eigenstates of $\hat{H}$, following the closure relation $\sum_n |n\rangle\,\langle n| = 1$, we obtain

$$G(\mathbf{r},t,\mathbf{r}',t') = -\theta(t-t')\sum_n \langle \mathbf{r}|e^{-iH(t-t')}|n\rangle\,\langle n|\mathbf{r}'\rangle\,, \tag{A.18}$$

$$= -\theta(t-t')\sum_n \langle \mathbf{r}|n\rangle\,\langle n|\mathbf{r}'\rangle\,e^{-i\epsilon_n(t-t')}, \tag{A.19}$$

$$= -\theta(t-t')\sum_n \phi_n(\mathbf{r})\phi_n^*(\mathbf{r}')e^{-i\epsilon_n(t-t')}. \tag{A.20}$$

The action of eigenstates on H produces eigenvalues ϵ_n, and the basis in the position representation gives single particle orbitals $\phi_n(\mathbf{r})$. These can be obtained, for example, from the Kohn-Sham solution. After the Fourier transform from time to energy domain, the non-interacting Green's function writes

$$G_0(\mathbf{r},\mathbf{r}',\omega) = \sum_j \frac{\phi_j(\mathbf{r})\phi_j^*(\mathbf{r}')}{\omega - \epsilon_j \pm i\eta}, \tag{A.21}$$

where the $i\eta$ term ensures proper boundary conditions, guarantees causality by defining retarded or advanced Green's function and makes the Fourier transform well defined. It is important to note that the poles of the Green's function correspond to the single-particle eigenenergies.

Appendix B

GW formalism

B.1 Second quantization in GW

In the position representation, field operators can be defined as expansions over a complete set of single-particle wavefunctions ϕ_i, as

$$\hat{\psi}^\dagger(\mathbf{r}) = \sum_i \phi_i(\mathbf{r}) c_i^\dagger, \tag{B.1}$$

$$\hat{\psi}(\mathbf{r}) = \sum_i \phi_i(\mathbf{r}) c_i. \tag{B.2}$$

The field operators represent the addition or removal of a particle at position $\mathbf{r}$ from whatever single-particle state i weighted by their amplitudes at that position. The field operators are the sums of all the possible ways to add or remove a particle to the system at position $\mathbf{r}$ through any of the basis states ϕ_i.

The Green's function formalism can be naturally expressed in terms of field operators and the time-ordering operator [48]. The time-ordered one-particle Green's function is defined as

$$iG(\mathbf{r}, t, \mathbf{r}', t') = \langle \Psi_0^N | T[\hat{\psi}(\mathbf{r}, t)\hat{\psi}^\dagger(\mathbf{r}', t')] | \Psi_0^N \rangle \tag{B.3}$$

$$= \theta(t - t') \langle \Psi_0^N | \hat{\psi}(\mathbf{r}, t)\hat{\psi}^\dagger(\mathbf{r}', t') | \Psi_0^N \rangle - \theta(t' - t) \langle \Psi_0^N | \hat{\psi}^\dagger(\mathbf{r}, t)\hat{\psi}(\mathbf{r}', t') | \Psi_0^N \rangle , \tag{B.4}$$

where θ is a Heaviside step function, which is zero for negative and one for positive arguments and Ψ_0^N is the ground-state wavefunction. The first part of the one-body time-ordered Greens function in Equation B.4 for $t > t'$ describes the propagation of an electron from $\mathbf{r}'$ to $\mathbf{r}$, that was created at time t' and annihilated at time t. It gives the propagation amplitude for adding an electron at (r', t') and removing it at (r, t). Similarly, when $t < t'$, the second part in Equation B.4 can be interpreted as the propagator of a hole. In this way, the single-particle Green's function describes the propagation of particles and holes in an interacting environment and provides direct access to excited-state properties that are not directly available in ground-state methods such as DFT.

In order to obtain explicit dependence on the excitation energies, we introduce a complete sets of many-body eigenstates of the systems with N+1 and N-1 particles. Inserting the closure

relation $\sum_i |\Psi_i\rangle \langle\Psi_i| = 1$ in Equation B.4, we obtain

$$\begin{aligned} iG(\mathbf{r},t,\mathbf{r}',t') = \theta(t-t') \sum_n \langle\Psi_0^N|\hat{\psi}(\mathbf{r},t)|\Psi_n^{N+1}\rangle \langle\Psi_n^{N+1}|\hat{\psi}^\dagger(\mathbf{r}',t)|\Psi_0^N\rangle \\ - \theta(t'-t) \sum_n \langle\Psi_0^N|\psi^\dagger(\mathbf{r},t)|\Psi_n^{N-1}\rangle \langle\Psi_n^{N-1}|\hat{\psi}(\mathbf{r}',t)|\Psi_0^N\rangle \,, \end{aligned} \tag{B.5}$$

for all excited electronic states n. Using the time-independent field operators $\hat{\psi}(\mathbf{r},t) = e^{i\hat{H}t}\hat{\psi}(\mathbf{r})e^{-i\hat{H}t}$, we get

$$\begin{aligned} iG(\mathbf{r},t,\mathbf{r}',t') = \theta(t-t') \sum_n \langle\Psi_0^N|\hat{\psi}(\mathbf{r})|\Psi_n^{N+1}\rangle \langle\Psi_n^{N+1}|\hat{\psi}^\dagger(\mathbf{r}')|\Psi_0^N\rangle \, e^{-iE_n^{N+1}(t-t')} \\ - \theta(t'-t) \sum_n \langle\Psi_0^N|\psi^\dagger(\mathbf{r})|\Psi_n^{N-1}\rangle \langle\Psi_n^{N-1}|\hat{\psi}(\mathbf{r}')|\Psi_0^N\rangle \, e^{-iE_n^{N-1}(t-t')}, \end{aligned} \tag{B.6}$$

with the total energies $E^{N\pm1}$. The first term describes the propagation of an electron introduced to a system of N particles described by Ψ_0^N, with the resulting n-th excited system is described by Ψ_n^{N+1}. On the other hand, the second term describes a system without one electron, which corresponds to the direct photoemission experiment. The Fourier transform from the time domain to the energy domain gives the Lehmann representation of Green's function

$$G(\mathbf{r},\mathbf{r}',\omega) = \sum_n \frac{\psi_n^{N+1}(\mathbf{r})\psi_n^{*N+1}(\mathbf{r}')}{\omega - \epsilon_n^{N+1} + i\eta} + \sum_n \frac{\psi_n^{N-1}(\mathbf{r})\psi_n^{*N-1}(\mathbf{r}')}{\omega - \epsilon_n^{N-1} - i\eta}, \tag{B.7}$$

where $\psi_n^{N+1}(\mathbf{r}) = \langle\Psi_0^N|\hat{\psi}(\mathbf{r})|\Psi_n^{N+1}\rangle$ and the Heaviside step-function in the frequency domain has the form $\int \theta(t-t')e^{i\omega(t-t')-\eta|(t-t')|} = (\omega + i\eta)^{-1}$. The infinitesimal parameter η appears to use complex frequencies for good behaviour of Fourier transform. The Lehmann representation provides a direct link between the poles of the Green's function and the many-body excitation energies $\epsilon_n^{N+1} = E_n^{N+1} - E_0^N$ and $\epsilon_n^{N-1} = E_0^N - E_n^{N-1}$, where ϵ_0 is the the total energy of the ground state and $\epsilon_j^{N\pm1}$ is the total energy of the j-th excited state. The Lehmann representation therefore establishes a direct connection between the Green's function and measurable excitation spectra, such as those observed in photoemission and inverse photoemission experiments [47,48]. This representation is exact for interacting many-body systems and forms the foundation of many-body perturbation theory methods such as the GW approximation.

B.2 Equation of motion

The reformulation of the many-body problem in terms of Green's functions requires solving the equation of motion for the Green's function [45,48,49]. The time derivative of the time-ordered

Green's function gives

$$\begin{aligned} i\frac{\partial}{\partial t}G(\mathbf{r},t,\mathbf{r}',t') &= \frac{\partial}{\partial t}\left\langle \Psi_0^N|T[\hat{\psi}(\mathbf{r},t)\hat{\psi}^\dagger(\mathbf{r}',t)]|\Psi_0^N\right\rangle \\ &= \frac{\partial}{\partial t}\theta(t-t')\left\langle \Psi_0^N|\hat{\psi}(\mathbf{r},t)\hat{\psi}^\dagger(\mathbf{r}',t)|\Psi_0^N\right\rangle \\ &\quad + \theta(t-t')\left\langle \Psi_0^N|(\frac{\partial}{\partial t}\hat{\psi}(\mathbf{r},t))\hat{\psi}^\dagger(\mathbf{r}',t)|\Psi_0^N\right\rangle \\ &\quad + \frac{\partial}{\partial t}\theta(t'-t)\left\langle \Psi_0^N|\psi^\dagger(\mathbf{r},t)\hat{\psi}(\mathbf{r}',t)|\Psi_0^N\right\rangle \\ &\quad - \theta(t'-t)\left\langle \Psi_0^N|\psi^\dagger(\mathbf{r},t)(\frac{\partial}{\partial t}\hat{\psi}(\mathbf{r}',t))|\Psi_0^N\right\rangle \\ &= \delta(t-t')\delta(\mathbf{r}-\mathbf{r}') - i\left\langle \Psi_0^N|T[i(\frac{\partial}{\partial t}\hat{\psi}(\mathbf{r},t))\hat{\psi}^\dagger(\mathbf{r}',t)]|\Psi_0^N\right\rangle. \end{aligned} \tag{B.8}$$

Using the Heisenberg equation of motion for the field operator, the time derivative is defined as

$$i\frac{\partial}{\partial t}\hat{\psi}(\mathbf{r},t) = [\hat{\psi}(\mathbf{r},t),\hat{H}] = h_0\hat{(\mathbf{r})}\hat{\psi}(\mathbf{r},t) + \int v_c(\mathbf{r},\mathbf{r}')\hat{\psi}^\dagger(\mathbf{r}',t)\hat{\psi}(\mathbf{r}',t)\hat{\psi}(\mathbf{r},t)d\mathbf{r}' \tag{B.9}$$

where v_c is the instantaneous Coulomb interaction and h_0 is a one-particle non-interacting Hamiltonian. Substituting into the equation of motion gives

$$\begin{aligned} i\frac{\partial}{\partial t}G(\mathbf{r},t,\mathbf{r}',t') &= \delta(t-t')\delta(\mathbf{r}-\mathbf{r}') + i\hat{h_0}\left\langle \Psi_0^N|T[\hat{\psi}(\mathbf{r},t)\hat{\psi}^\dagger(\mathbf{r}',t)]|\Psi_0^N\right\rangle \\ &\quad - \int v_c(\mathbf{r},\mathbf{r}'')\left\langle \Psi_0^N|T[\hat{\psi}^\dagger(\mathbf{r}'',t)\hat{\psi}(\mathbf{r}'',t)\hat{\psi}(\mathbf{r},t)\hat{\psi}^\dagger(\mathbf{r}',t')]|\Psi_0^N\right\rangle dr'' \\ &= \delta(t-t')\delta(\mathbf{r}-\mathbf{r}') + i\hat{h_0}G(\mathbf{r},t,\mathbf{r}',t') - i\int v_c(\mathbf{r},\mathbf{r}'')G(\mathbf{r},t,\mathbf{r}'',t,\mathbf{r}'',t^+,\mathbf{r}',t') \end{aligned} \tag{B.10}$$

with $t > t'$. The equation of motion of single Green's functions leads to a higher order, two-body Green's function. The time variation of the two-body function leads to a three-body problem and so on. This property is called hierarchy of Green's function, which cannot be solved exactly.

The equation containing two-body interactions can be solved using perturbation theory. To truncate this hierarchy, one introduces a fictitious external potential U and considers the functional derivative of the Green's function with respect to U. Using the notation $(\mathbf{r},t) = 1$, we can define the variation of a single particle Green's function with respect to an external perturbation as

$$\frac{\partial G(1,2)}{\partial U(3)} = -G(1,3;2,3^+) + G(1,2)G(3,3^+) \tag{B.11}$$

here 3^+ represents an infinitesimally larger time. The potential U is a mathematical tool used to remove the two-body term and is set to zero after the calculation. Inserting Equation B.11 in Equation B.10 and using Equation A.7 yields

$$\begin{aligned} \left[i\frac{\partial}{\partial t} - \hat{h_0}\right]G(1,2) + i\int v_c(1,3)G(3,3^+)G(1,2)d3 \\ - i\int v_c(1^+,3)\frac{\partial G(1,2)}{\partial U(3)}d3 = \delta(1,2). \end{aligned} \tag{B.12}$$

Since $-iG(3,3^+) = n(3)$, which is the electron density, the second term in Equation B.12 describes the action of the Hartree operator on the Green's function, written as $V_H G(1,2)$. The third term contains interactions beyond V_H, i.e. the exchange-correlation effects. The equation of motion of the one-particle Green's function can be written as

$$\left[i\frac{\partial}{\partial t} - \hat{h_0}(\mathbf{r}) - V_H(1)\right] G(1,2) - \int \Sigma(1,3)G(3,2)d3 = \delta(1,2), \tag{B.13}$$

introducing the self-energy operator Σ that collects remaining interactions beyond the Hartree term. Hence the exchange-correlation interactions are described by a non-local and frequency dependent self-energy. The Equation B.13 is a self-contained equation that can be expressed in terms of the Dyson equation $G = G_0 + G_0\Sigma G$.

By comparing Equation B.13 and Equation B.12, the self-energy [50] can be expressed as

$$\Sigma(1,2) = i\int\int v_c(1^+,3)\frac{\partial G(1,4)}{\partial U(3)}G^{-1}(4,2)d3d4, \tag{B.14}$$

$$\Sigma(1,2) = i\int\int v_c(1^+,3)G(1,4)\frac{\partial G^{-1}(4,2)}{\partial U(3)}d3d4. \tag{B.15}$$

Defining the total electrostatic potential as $V = U + V_H$, the self-energy can be written as

$$\begin{aligned}\Sigma(1,2) &= i\int v_c(1^+,3)G(1,4)\frac{\partial G^{-1}(4,2)}{\partial V(5)}\frac{\partial V(5)}{\partial U(3)}d3d4d5 \\ &= i\int W(1^+,3)G(1,4)\Gamma(4,2;3)d3d4,\end{aligned} \tag{B.16}$$

where Γ is the three body operator called irreducible vertex function and W is the screened Coulomb interaction. Here W is screened via the dielectric function

$$\epsilon^{-1}(1,2) = \frac{\partial V(1)}{\partial U(2)} = \frac{\partial(U(1)+V_H(1))}{\partial U(2)} = \delta(1,2) + \int v_c(1,3)\chi(3,2), \tag{B.17}$$

using $V_H(1) = \int v_c(1,2)n(2)d2$. The reducible polarizability χ is defined as the response of the density to the action of an external potential

$$\begin{aligned}\chi(1,2) = \frac{\partial n(1)}{\partial U(2)} &= -i\int\frac{\partial G(1,1^+)}{\partial U(2)}d2 = -i\int\frac{\partial G(1,1^+)}{\partial V(3)}\frac{\partial V(3)}{\partial U(2)}d3 \\ &= P(1,2) + \int P(1,3)v_c(3,4)\chi(4,2)d3d4\end{aligned} \tag{B.18}$$

These relations can be in the matrix representation concluded as $\epsilon^{-1} = 1 + v_c\chi = (1 - v_cP)^{-1}$ and $\chi = P + Pv_c\chi$. The irreducible polarizability is defined as the variation of the density due to the total potential, therefore

$$\begin{aligned}P(1,2) = \frac{\partial n}{\partial V} = \frac{\partial G(1,2)}{\partial V(3)} &= \int G(1,4)\frac{\partial G^{-1}(4,5)}{\partial V(3)}G(5,2)d4d5 \\ &= -1\int G(1,3)G(4,1)\Gamma(3,4;2)d3d4,\end{aligned} \tag{B.19}$$

by setting $1^+ = 2$, using the chain rule $\frac{\partial G(1,2)}{\partial V(3)} = -\int G(1,4)\frac{\partial G^{-1}(4,5)}{\partial V(3)}G(5,2)d4d5$ and the definition of the vertex function from Equation B.16. Hence the screened Coulomb interaction can be expressed as

$$\begin{aligned} W(1,2) &= \int \epsilon^{-1}(1,3)v_c(3,2)d3 = v_c(1,2) + \int v_c(1,3)\chi(4,2)v_c(4,3)d3d4 \\ &= v_c(1,2) + \int v_c(1,3)P(3,4)W(4,2)d3d4 \end{aligned} \tag{B.20}$$

Here W and ϵ^{-1} are time (or frequency) dependent quantities.

B.3 GW approximation

Within the GW method, the self-energy is approximated as $\Sigma = GW$. This simple form is obtained by setting the vertex function to unity. The screened Coulomb interaction W describes the bare Coulomb interaction modified by the response of the electronic system. When an electron or hole is added to a material, the surrounding charge density rearranges. The screened interaction is weaker relative to the bare Coulomb potential. The screened particles are in the GW method called quasiparticles.

In practical GW calculations, the starting point is usually a non-interacting Green's function G_0, constructed from eigenvalues and eigenfunctions obtained from a mean-field theory such as Kohn–Sham DFT. In frequency representation, this Green's function can be written schematically as a sum over all occupied and unoccupied single-particle state, as

$$G_0(\mathbf{r_1}, \mathbf{r_2}, \omega) = \sum_n \frac{\phi_n^{KS*}(\mathbf{r_1})\phi_n^{KS}(\mathbf{r_2})}{\omega - \epsilon_n \pm i\eta}, \tag{B.21}$$

with poles at the mean-field eigenvalues and a small imaginary part $\pm\eta$, which ensures the proper boundary conditions. Similarly the polarizability can be approximated as a product of G_0, which is called the random phase approximation (RPA). The free particle irreducible polarizability becomes P_0=-iG_0G_0=χ_0. Following Equation B.20, the screened interaction W then becomes $W_0 = v_c + v_c\chi_0 v_c = v_c + v_c P_0 W_0$ and the self-energy writes $\Sigma = iG_0W_0$. These Hedin relations depend on each other in a self-consistent loop. In practice, the GW calculation can stop after performing a single circle, which is called a single-shot GW or G_0W_0 method. After the first cycle one can update G, W or both and continue the calculation, which leads to a self-consistent GW method.

Quasiparticle energies are obtained by solving an effective eigenvalue problem in which the exchange–correlation potential is replaced by the non-local, energy-dependent self-energy operator. Starting from the Dyson equation and the Lehmann representation, the quasiparticle equation can be written as

$$(\hat{h_0}(\mathbf{r}) - V_H(\mathbf{r}))\phi_n(\mathbf{r}) + \int \Sigma(\mathbf{r}, \mathbf{r'}, \omega = \epsilon_n)\phi_n(\mathbf{r'}) = \epsilon_n\phi_n(\mathbf{r}). \tag{B.22}$$

Since the self-energy depends explicitly on the energy, which is itself the eigenvalue of the equation, Eq. (B.22) is non-linear and must be solved self-consistently in principle. In practice,

the quasiparticle energy is often evaluated perturbatively with respect to a DFT reference system, which leads to

$$\omega = \epsilon_n^{KS} + \langle \phi_n(\mathbf{r}) | \Sigma(\mathbf{r}, \mathbf{r}', \omega) - V_{xc}^{KS}(\mathbf{r}) | \phi_n(\mathbf{r}) \rangle \,, \tag{B.23}$$

where V_{xc}^{KS} is the xc potential at the DFT level. Because the self-energy is frequency dependent, this equation may have multiple solutions. The physically relevant quasiparticle solution corresponds to the pole of the Green's function with the largest spectral weight. A common approximation is to linearize the self-energy around the Kohn–Sham eigenvalue using a first-order Taylor expansion

$$\Sigma_{nn}(\mathbf{r}, \mathbf{r}', \omega) \approx \Sigma_{nn}(\mathbf{r}, \mathbf{r}', \epsilon_n^{KS}) + \left. \frac{\partial \Sigma_{nn}(\mathbf{r}, \mathbf{r}', \omega)}{\partial \omega} \right|_{\omega = \epsilon_n^{KS}} (\omega - \epsilon_n^{KS}). \tag{B.24}$$

This leads to the definition of the renormalization factor defined as

$$Z_n = \left[1 - \mathrm{Re} \left(\left. \frac{\partial \Sigma(\mathbf{r}, \mathbf{r}', \omega)}{\partial \omega} \right|_{\omega = \epsilon_n^{KS}} \right) \right]^{-1}. \tag{B.25}$$

The renormalization factor Z_n measures how strongly an electron behaves like a well-defined quasiparticle in an interacting system. It corresponds to the spectral weight of the quasiparticle pole and takes values between 0 and 1. A quasiparticle peak with large Z_n carries most of the spectral weight, whereas satellite features have smaller weights. Since Z_n depends on the derivative of the self-energy, it is close to unity when the self-energy varies slowly with energy and its imaginary part is small near the quasiparticle energy. Within the linearized approximation, the GW quasiparticle energies are finally given by

$$\epsilon^{GW} = \epsilon_n^{KS} + Z_n \mathrm{Re}[\langle \phi_n(\mathbf{r}) | \Sigma_{nn}(\mathbf{r}, \mathbf{r}', \epsilon_n^{KS}) - V_{xc}^{KS}(\mathbf{r}) | \phi_n(\mathbf{r}) \rangle]. \tag{B.26}$$

Appendix C

Bethe-Salpeter equation

Neutral excitations, such as electron-hole pairs, require description of the propagation of two correlated particles by the two-particle Green's function, which can be obtained formally from the functional derivative of the one-particle Green's function with respect to an external perturbation, as shown in Equation B.11. The two-particle correlation function can be defined as

$$L(1,2;3,4) = -\frac{\partial G(1,2)}{\partial U(3,4)} = -G(1,5)\frac{\partial G^{-1}(5,6)}{\partial U(3,4)}G(6,2) \tag{C.1}$$

using the chain rule. The Dyson equation for the G can be written in a compact form as $G = G_0 + G_0 \Sigma G$. Dividing by G and G_0, one gets $G^{-1} = G_0^{-1} - \Sigma$. If the external perturbation U is included in the single-particle Hamiltonian, this may be written schematically as $= G_0^{-1} - U - \Sigma$. Therefore Equation C.1 can be rewritten as

$$L(1,2;3,4) = -G(1,5)\frac{\partial [G_0^{-1}(5,6) - U(5,6) - \Sigma(5,6)]}{\partial U(3,4)}G(6,2) \tag{C.2}$$

since G_0 is independent of U and $\frac{\partial U(5,6)}{\partial U(3,4)} = \delta(5,3)\delta(6,4)$. Equation C.2 becomes

$$\begin{aligned} L(1,2;3,4) &= G(1,3)G(4,2) + G(1,5)G(6,2)\frac{\partial \Sigma(5,6)}{\partial U(3,4)} \\ &= L_0(1,2,3,4) + L_0(1,2,5,6)\frac{\partial \Sigma(5,6)}{\partial G(7,8)}\frac{\partial G(7,8)}{\partial U(3,4)} \\ &= L_0(1,2,3,4) + L_0(1,2,5,6)\Xi(5,6,7,8)L(7,8,3,4), \end{aligned} \tag{C.3}$$

which is the Bethe–Salpeter equation (BSE) [47, 49, 52, 170].

Within the GW approximation, the BSE kernel is commonly separated into two contributions. One arises from the Hartree term and gives the bare Coulomb interaction, while the exchange-correlation part yields another contribution involving the screened interaction W. Using the GW solution to define the self-energy, the four point Hartree-exchange-correlation kernel is given by

$$\Xi(5,6,7,8) = \frac{\partial \Sigma(5,6)}{\partial G(7,8)} = \frac{\partial V_H(5)\delta(5,6)}{\partial G(7,8)} + \frac{\partial \Sigma_{xc}(5,6)}{\partial G(7,8)}, \tag{C.4}$$

where the first term equals to v_c and the second to W. In the standard approximation, this leads to an effective electron-hole interaction kernel of the form $\Xi = v_c - W$. Hence, the BSE can be

written as

$$L(1,2,3,4) = L_0(1,2,3,4) + L_0(1,2,5,6)[v_c(5,7)\delta(5,6)\delta(7,8) - W(5,6)\delta(5,7)\delta(6,8)]L(7,8,3,4). \tag{C.5}$$

Here v_c produces a repulsive electron-hole dipole-dipole interaction, which corresponds to the exchange term. The screened interaction W provides an attractive direct interaction responsible for exciton formation.

In practice, L_0 is expressed in terms of the non-interacting Green's functions, i.e. $L_0 = -iG_0G_0$, the GW eigenvalues are used instead of the KS single-particle energies in Equation B.21, and the screened interaction W is considered in a static approximation, evaluated at $\omega = 0$, which simplifies the BSE kernel.

In a basis of single-particle transitions between valence and conduction states, the Bethe–Salpeter equation becomes an effective eigenvalue problem

$$H^{BSE}X_\lambda = E_\lambda X_\lambda \tag{C.6}$$

where E_λ and X_λ are excitonic eigenvalues and eigenfunctions. In the transition space, this equation can be written in the matrix notation as

$$\begin{pmatrix} A & B \\ B^* & A^* \end{pmatrix} \begin{pmatrix} X_\lambda \\ Y_\lambda \end{pmatrix} = E_\lambda \begin{pmatrix} 1 & 0 \\ 0 & -1 \end{pmatrix} \begin{pmatrix} X_\lambda \\ Y_\lambda \end{pmatrix}. \tag{C.7}$$

The kernel matrix elements are in practice expressed in the single-electron basis. The matrices A are called resonant while B contains coupling between resonant and anti-resonant transitions. The matrix A is defined as

$$\begin{aligned} A^{v,v'}_{c,c'} &= (\epsilon_v - \epsilon_c)\delta_{vv'}\delta_{cc'} + \langle cv'|v_c|vc'\rangle - \langle cv'|W|c'v\rangle \\ &= (\epsilon_v - \epsilon_c)\delta_{vv'}\delta_{cc'} + \int \phi^*_c(\mathbf{r_1})\phi^*_{v'}(\mathbf{r_2})v_c(\mathbf{r_1}-\mathbf{r_2})\phi_v(\mathbf{r_1})\phi_{c'}(\mathbf{r_2})d\mathbf{r_1}d\mathbf{r_2} \\ &\quad - \int \phi^*_c(\mathbf{r_1})\phi^*_{v'}(\mathbf{r_2})W(\mathbf{r_1},\mathbf{r_2})\phi_{c'}(\mathbf{r_1})\phi_v(\mathbf{r_2})d\mathbf{r_1}d\mathbf{r_2}. \end{aligned} \tag{C.8}$$

The bare Coulomb interaction defines the dipolar interaction between cv at $\mathbf{r_1}$ and $c'v'$ at $\mathbf{r_2}$, while W mediates the direct charge interaction between a hole at $\mathbf{r_1}$ and an electron at $\mathbf{r_1}$. The matrix elements of B are defined as

$$B^{v,v'}_{c,c'} = \langle vv'|v_c|cc'\rangle - \langle vv'|W|cc'\rangle. \tag{C.9}$$

The matrix A describes the resonant and anti-resonant transitions between the unoccupied conduction c, c' and occupied valence v, v' states. It describes the creation and recombination of interacting electron-hole pairs or excitons. The matrices B describe coupling between excitation and de-excitation terms. The matrices A contain dominant terms and are related to absorption processes, therefore the B matrices are usually neglected. This approximation is known as the Tamm-Dancoff approximation (TDA), which makes the Hamiltonian become Hermitian and the eigenvalue equation can be simplified to

$$AX_\lambda = E_\lambda X_\lambda \tag{C.10}$$

The use of a static screened interaction and the TDA leads to real exciton energies and neglects lifetime effects, since finite lifetimes originate from the imaginary part of the self-energy and from dynamical screening, neither of which is fully included in this approximation.

Appendix D

Ionic dielectric response

The energy of a system with atomic positions slightly displaced from the equilibrium can be expressed as a Taylor expansion around the ground-state configuration, which writes

$$E(\mathbf{R}) = E(\mathbf{R_0}) + \sum_{I\alpha} \frac{\partial E(\mathbf{R_0})}{\partial u_{I\alpha}} u_{I\alpha} + \frac{1}{2} \sum_{I\alpha J\beta} \frac{\partial^2 E(\mathbf{R_0})}{\partial u_{I\alpha} \partial u_{J\beta}} u_{I\alpha} u_{J\beta} + O(u^3), \tag{D.1}$$

where the indices I and J run over nuclei, and α and β define the Cartesian directions of displacements. Expansion truncated after the third term gives the the harmonic approximation of phonons. The second term corresponds to the force on a displaced atom and vanishes at equilibrium. Equation D.1 can be rewritten as

$$E(\mathbf{R}) = E(\mathbf{R_0}) - \frac{1}{2} \sum_{I\alpha J\beta} \frac{\partial^2 E_{I\alpha}(\mathbf{R_0})}{\partial u_{J\beta}} u_{I\alpha} u_{J\beta} = E(\mathbf{R_0}) + \frac{1}{2} \sum_{I\alpha J\beta} \Phi_{I\alpha J\beta} u_{I\alpha} u_{J\beta}, \tag{D.2}$$

where Φ is the matrix of second order force constants. The equation of motion becomes

$$F_I = M_I a_I, \tag{D.3}$$

$$-\frac{\partial E(\mathbf{R})}{\partial u_{I\alpha}} = M_I \frac{d^2 u_{I\alpha}}{dt^2}, \tag{D.4}$$

$$-\sum_{J\beta} \Phi_{I\alpha J\beta} u_{J\beta} = M_I \frac{d^2 u_{I\alpha}}{dt^2}. \tag{D.5}$$

In periodic systems, the atomic displacement can be expressed as a plane wave propagating with wavevector q as $u_{I\alpha}(t) = \eta_{I\alpha\nu} e^{i\mathbf{q}\mathbf{R_I}} e^{-i\omega_\nu t}$, where ν is the phonon mode and $\eta_{\alpha\nu}$ is the polarization direction vector along a Cartesian coordinate α. Substituting this expression into the equation of motion in Equation D.5 gives

$$-\sum_{J\beta} \Phi_{I\alpha J\beta} \eta_{J\beta\nu} e^{i\mathbf{q}\mathbf{R_J}} e^{-i\omega_\nu t} = -M_I \omega_\nu^2 \eta_{I\alpha\nu} e^{i\mathbf{q}\mathbf{R_I}} e^{-i\omega_\nu t}, \tag{D.6}$$

$$\sum_{J\beta} \Phi_{I\alpha J\beta} \eta_{J\beta\nu} e^{-i\mathbf{q}(\mathbf{R_I}-\mathbf{R_J})} = M_I \omega_\nu^2 \eta_{I\alpha\nu}. \tag{D.7}$$

This is a generalized eigenvalue problem because of the presence of the mass matrix on the right hand side. In order to get an eigenvalue equation we redefine the eigenvectors using the square

root of mass as $u_{I\alpha}(t) = \frac{1}{\sqrt{M_I}}\gamma_{I\alpha\nu}e^{i\mathbf{qR_I}}e^{-i\omega_\nu t}$. We then obtain a standard Hermitian eigenvalue problem, which writes

$$\sum_{J\beta} D_{I\alpha J\beta}(\mathbf{q})\gamma_{J\beta\nu}(\mathbf{q}) = \omega_\nu^2\gamma_{I\alpha\nu}(\mathbf{q}) \tag{D.8}$$

$$D_{I\alpha J\beta}(\mathbf{q}) = \frac{1}{\sqrt{M_I M_J}}\Phi_{I\alpha J\beta}e^{i\mathbf{q}(\mathbf{R_J}-\mathbf{R_I})}, \tag{D.9}$$

where $D_{I\alpha J\beta}(\mathbf{q})$ is the so called dynamical matrix in the harmonic approximation. Solving this eigenvalue problem yields phonon frequencies and eigendisplacements.

The ionic contribution to the dielectric function can be written as

$$\epsilon_{\alpha\beta}(\omega) = \frac{1}{\Omega}\sum_\nu \frac{S_{\alpha\beta\nu}}{\omega_\nu^2 - (\omega + i\eta)^2}, \tag{D.10}$$

where the oscillator strength $S_{\alpha\beta\nu}$ is defined as

$$S_{\alpha\beta\nu} = \sum_{Ie} Z^*_{I\alpha e}\gamma_{Ie\nu}(\mathbf{q}=0)\sum_{Je} Z^*_{J\beta e}\gamma_{Je\nu}(\mathbf{q}=0). \tag{D.11}$$

Here Z^* is the Born effective charge and e is the polarization direction. The dielectric function is evaluated at the Γ point since only zone-center optical phonons couple to a homogeneous electric field due to near-zero momentum of photons.

Appendix E

GW convergence

The GW convergence behaviour for the studied cement, concrete and related phases is shown in Figure E.1. The G_0W_0 bandgaps reported in this thesis were obtained by interpolating to an infinite number of empty bands. Most systems show a nearly linear decrease over the sampled range, which suggests smooth convergence with respect to the number of empty bands (NBANDS). Tobermorite has the steepest slope among the shown fits, while C4AF and Anatase have much flatter slopes, meaning their band gaps change less with NBANDS. Moreover, the GW band gap of portlandite basically does not vary with NBANDS. It can be realized from the convergence plots that the dependence on the energy cutoff is significantly smaller than the dependence on the empty bands. In most materials with large computational cells the dependence on the cutoff energy is even negligible.

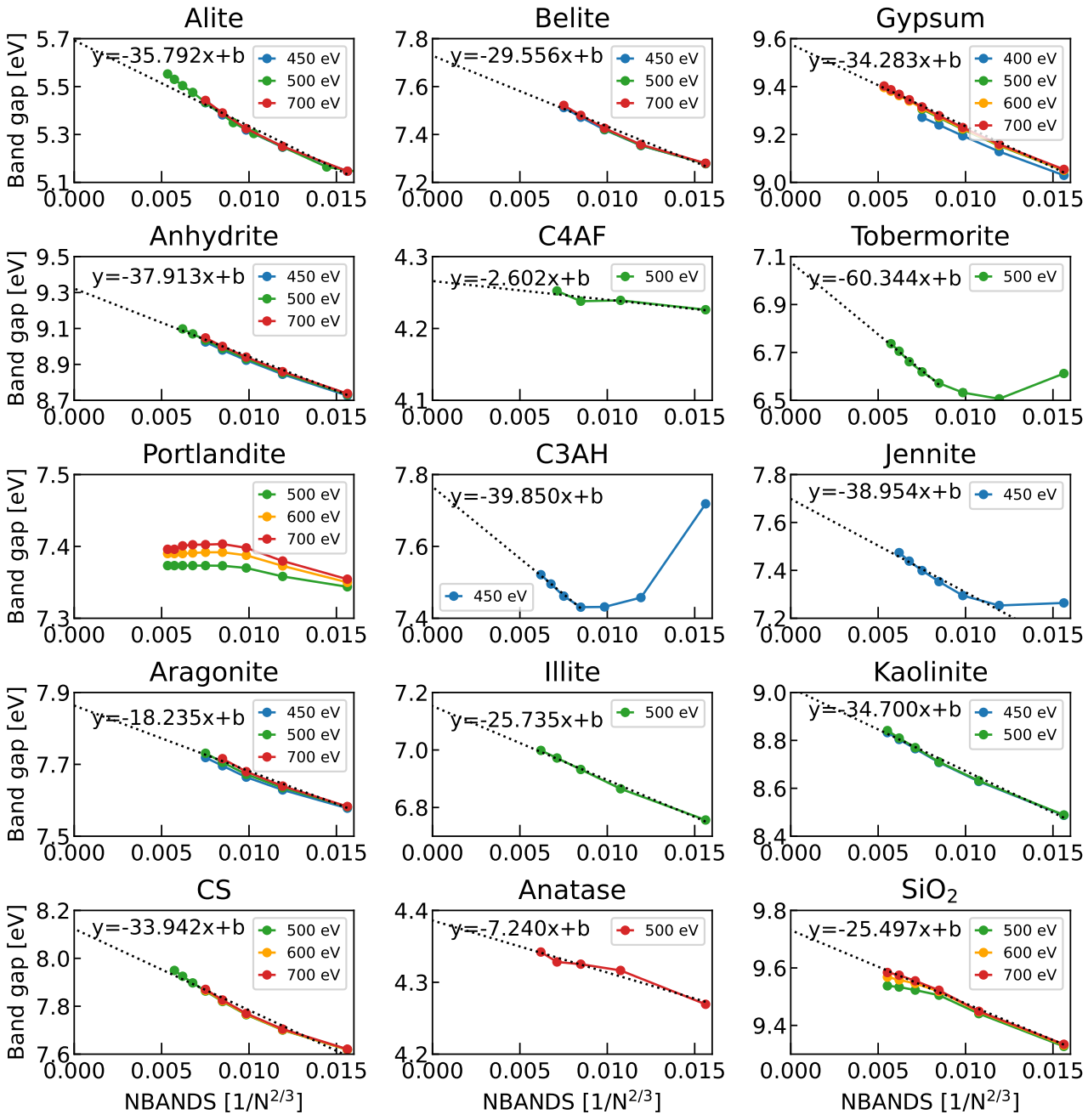

Figure E.1: Convergence of the G_0W_0 bandgap as a function of the number of unoccupied bands at different cut-off energies.

Bibliography

[1] U. N. E. Programme, Global Status Report for Buildings and Construction 2024/2025: Not Just Another Brick in the Wall–The Solutions Exist. Scaling Them Will Build on Progress and Cut Emissions Fast, Paris: United Nations Environment Programme (2025).

[2] J. S. Dolado, G. Goracci, S. Arrese-Igor, A. Ayuela, A. Torres, I. Liberal, M. Beruete, J. J. Gaitero, M. Cagnoni, F. Cappelluti, Radiative Cooling Properties of Portlandite and Tobermorite: Two Cementitious Minerals of Great Relevance in Concrete Science and Technology, ACS Appl. Opt. Mater. 2 (6) (2023) 1000–1009.

[3] A. P. Raman, M. A. Anoma, L. Zhu, E. Rephaeli, S. Fan, Passive radiative cooling below ambient air temperature under direct sunlight, Nature 515 (7528) (2014) 540–544.

[4] M. M. Hossain, M. Gu, Radiative cooling: principles, progress, and potentials, Adv. Sci. 3 (7) (2016) 1500360.

[5] D. Zhao, A. Aili, Y. Zhai, S. Xu, G. Tan, X. Yin, R. Yang, Radiative sky cooling: Fundamental principles, materials, and applications, Appl. Phys. Rev. 6 (2) (2019) 021306.

[6] G. Goracci, E. Saeed, M. B. Ogundiran, A. Iturrospe, A. Arbe, C. Aymonier, J. S. Dolado, Cool concrete incorporating carbonated Periwinkle Shell: a sustainable solution for mitigating urban heat island effects, ACS Sustain. Chem. Eng. 12 (5) (2024) 1911–1917.

[7] J. Ballester, M. Quijal-Zamorano, R. F. Méndez Turrubiates, F. Pegenaute, F. R. Herrmann, J. M. Robine, X. Basagaña, C. Tonne, J. M. Antó, H. Achebak, Heat-related mortality in Europe during the summer of 2022, Nat. Med. 29 (7) (2023) 1857–1866.

[8] V. D. Bruggeman, Berechnung verschiedener physikalischer Konstanten von heterogenen Substanzen. I. Dielektrizitätskonstanten und Leitfähigkeiten der Mischkörper aus isotropen Substanzen, Ann. Phys. 416 (7) (1935) 636–664.

[9] H. F. Taylor, et al., Cement Chemistry, Vol. 2, Thomas Telford London, 1997.

[10] S. Mindess, F. Young, D. Darwin, Concrete, Vol. 2, American Concrete Institute United States, 2003.

[11] J. Taylor, I. Hinczak, C. Matulis, Rietveld full-profile quantification of Portland cement clinker: The importance of including a full crystallography of the major phase polymorphs, Powder Diffr. 15 (1) (2000) 7–18.

[12] M. Bishop, S. G. Bott, A. R. Barron, A new mechanism for cement hydration inhibition: solid-state chemistry of calcium nitrilotris (methylene) triphosphonate, Chem. Mater. 15 (16) (2003) 3074–3088.

[13] Kinetics of Cement Hydration, https://www.globusogs.com/kinetics-of-cement-hydration/.

[14] J. Newman, B. S. Choo, Advanced concrete technology 3: processes, Elsevier, 2003.

[15] Atmospheric window, https://en.wikipedia.org/wiki/Atmospheric_window.

[16] G. Lu, W. She, X. Tong, W. Zuo, Y. Zhang, Radiative cooling potential of cementitious composites: Physical and chemical origins, Cem. Concr. Compos. 119 (2021) 104004.

[17] M. Cagnoni, A. Tibaldi, J. S. Dolado, F. Cappelluti, Cementitious materials as promising radiative coolers for solar cells, Iscience 25 (11) (2022) 105320.

[18] A. E. Torres-García, R. O. Agbaoye, L. Carlosena, G. Goracci, C. Lezaun, J. S. Dolado, M. Beruete, Towards cooling concrete: Evaluation of cement and cement composites under realistic climatic conditions, Appl. Therm. Eng. (2025) 125531.

[19] J. S. Dolado, G. Goracci, G. Moutaoukil, R. O. Agbaoye, M. Beruete, A. E. Torres-García, L. Carlosena, A. Prabhu, J. A. Ibáñez, N. Adams, et al., A Modern Roman-Inspired Concrete with Daytime Radiative Cooling Capacity, Adv. Sci. 12 (47) (2025) e11691.

[20] H. Fujiwara, R. W. Collins, Spectroscopic ellipsometry for photovoltaics, Vol. 1, Springer, 2018.

[21] Dielectric spectroscopy, https://webposta.ehu.eus/imp/dynamic.php?page=mailbox#mbox:SU5CT1g.

[22] S. Dhar, Excitons in Semiconductors, Springer, 2025.

[23] H. Manzano, J. S. Dolado, A. Ayuela, Structural, mechanical, and reactivity properties of tricalcium aluminate using first-principles calculations, J. Am. Ceram. Soc. 92 (4) (2009) 897–902.

[24] N. L. Mai, N.-H. Hoang, H. T. Do, M. Pilz, T. T. Trinh, Elastic and thermodynamic properties of the major clinker phases of portland cement: Insights from first principles calculations, Constr. Build. Mater. 287 (2021) 122873.

[25] J. Fu, S. Kamali-Bernard, F. Bernard, M. Cornen, Comparison of mechanical properties of CSH and portlandite between nano-indentation experiments and a modeling approach using various simulation techniques, Compos. B: Eng. 151 (2018) 127–138.

[26] R. O. Agbaoye, J. Janovec, A. Ayuela, J. S. Dolado, Thermoelectric properties of the main species present in portland cement pastes, Cem. Concr. Res. 183 (2024) 107587.

[27] C. Qi, L. Liu, J. He, Q. Chen, L.-J. Yu, P. Liu, Understanding cement hydration of cemented paste backfill: DFT study of water adsorption on tricalcium silicate (111) surface, Minerals 9 (4) (2019) 202.

[28] J. Jiang, H. Wang, J. Lin, Z. Liu, L. Li, Y. Li, Z. Li, L. Lu, Y. Li, Z. Lu, Accelerating mechanism of cement hydration by hydroxyl free radicals: new perspectives from photoexcited nano-TiO_2, Compos. B: Eng. 301 (2025) 112524.

[29] R. Dupuis, J. S. Dolado, J. Surga, A. Ayuela, Doping as a way to protect silicate chains in calcium silicate hydrates, ACS Sustain. Chem. Eng. 6 (11) (2018) 15015–15021.

[30] P. Rejmak, J. S. Dolado, M. A. Aranda, A. Ayuela, First-principles calculations on polymorphs of dicalcium silicate—Belite, a main component of Portland cement, J. Phys. Chem. C 123 (11) (2019) 6768–6777.

[31] R. Zhao, H. Liu, G. Fan, X. Guan, J. Zhu, Unraveling the doping preference of zinc ions in sulfoaluminate cement clinker minerals: A study combining experiments and DFT calculations, Compos. B: Eng. 242 (2022) 110072.

[32] A. Ayuela, J. S. Dolado, I. Campillo, Y. De Miguel, E. Erkizia, D. Sánchez-Portal, A. Rubio, A. Porro, P. M. Echenique, Silicate chain formation in the nanostructure of cement-based materials, J. Chem. Phys. 127 (16) (2007).

[33] H. Manzano, A. Ayuela, J. Dolado, On the formation of cementitious C–S–H nanoparticles, J. Comput. Aided Mater. Des. 14 (2007) 45–51.

[34] M. Izadifar, J. S. Dolado, P. Thissen, A. Ayuela, Interactions between reduced graphene oxide with monomers of (calcium) silicate hydrates: A first-principles study, Nanomaterials 11 (9) (2021) 2248.

[35] M. Izadifar, J. S. Dolado, P. Thissen, N. Ukrainczyk, E. Koenders, A. Ayuela, Theoretical elastic constants of tobermorite enhanced with reduced graphene oxide through hydroxyl vs epoxy functionalization: a first-principles study, J. Phys. Chem. C 127 (36) (2023) 18117–18126.

[36] R. M. Martin, Electronic structure: basic theory and practical methods, Cambridge university press, 2020.

[37] E. Engel, Density functional theory, Springer, 2011.

[38] P. Hohenberg, W. Kohn, Inhomogeneous electron gas, Phys. Rev. 136 (3B) (1964) B864.

[39] W. Kohn, L. J. Sham, Self-consistent equations including exchange and correlation effects, Phys. Rev. 140 (4A) (1965) A1133.

[40] J. P. Perdew, K. Burke, M. Ernzerhof, Generalized gradient approximation made simple, Phys. Rev. Lett. 77 (18) (1996) 3865.

[41] C. J. Cramer, Essentials of computational chemistry: theories and models, John Wiley & Sons, 2013.

[42] J. Sun, A. Ruzsinszky, J. P. Perdew, Strongly constrained and appropriately normed semilocal density functional, Phys. Rev. Lett. 115 (3) (2015) 036402.

[43] P. E. Blöchl, Projector augmented-wave method, Phys. Rev. B 50 (24) (1994) 17953.

[44] S. Yip, Handbook of materials modeling, Springer Science & Business Media, 2007.

[45] E. K. Gross, E. Runge, Many-particle theory, Adam Hilger, 1986.

[46] I. Lindgren, J. Morrison, Atomic many-body theory, Vol. 3, Springer Science & Business Media, 2012.

[47] R. M. Martin, L. Reining, D. M. Ceperley, Interacting electrons, Cambridge University Press, 2016.

[48] C. Friedrich, A. Schindlmayr, Many-body perturbation theory: The GW approximation, NIC Series 31 (2006) 335.

[49] G. Strinati, Application of the Green's functions method to the study of the optical properties of semiconductors, Riv. Nuovo Cim. 11 (12) (1988) 1–86.

[50] L. G. Molinari, A derivation of hedin's equations (2017).

[51] L. Hedin, New method for calculating the one-particle Green's function with application to the electron-gas problem, Phys. Rev. 139 (3A) (1965) A796.

[52] G. Onida, L. Reining, A. Rubio, Electronic excitations: density-functional versus many-body Green's-function approaches, Rev. Mod. Phys. 74 (2) (2002) 601.

[53] P.-F. Loos, P. Romaniello, J. Berger, Green functions and self-consistency: insights from the spherium model, J. Chem. Theory Comput. 14 (6) (2018) 3071–3082.

[54] J. Janovec, J. S. Dolado, A. Ayuela, Optical and excitonic properties of calcite $CaCO_3$, J. Mater. Chem. C 13 (2025) 6267–6276.

[55] Y. Peter, M. Cardona, Fundamentals of semiconductors: physics and materials properties, Springer Science & Business Media, 2010.

[56] S. L. Adler, Quantum theory of the dielectric constant in real solids, Phys, Rev. 126 (2) (1962) 413.

[57] N. Wiser, Dielectric constant with local field effects included, Phys. Rev. 129 (1) (1963) 62.

[58] M. Gajdoš, K. Hummer, G. Kresse, J. Furthmüller, F. Bechstedt, Linear optical properties in the projector-augmented wave methodology, Phys. Rev. B 73 (4) (2006) 045112.

[59] F. Fuchs, C. Rödl, A. Schleife, F. Bechstedt, Efficient $O(N^2)$ approach to solve the Bethe-Salpeter equation for excitonic bound states, Phys. Rev. B 78 (8) (2008) 085103.

[60] X. Gonze, C. Lee, Dynamical matrices, Born effective charges, dielectric permittivity tensors, and interatomic force constants from density-functional perturbation theory, Phys. Rev. B 55 (16) (1997) 10355.

[61] Y. Le Page, P. Saxe, Symmetry-general least-squares extraction of elastic data for strained materials from $ab-initio$ calculations of stress, Phys. Rev. B 65 (10) (2002) 104104.

[62] H. C. van de Hulst, Light scattering by small particles, Courier Corporation, 1981.

[63] W. Hergert, T. Wriedt, The Mie theory: basics and applications, Vol. 169, Springer, 2012.

[64] Q. Fu, W. Sun, Mie theory for light scattering by a spherical particle in an absorbing medium, Appl. Opt. 40 (9) (2001) 1354–1361.

[65] D. W. Mackowski, M. I. Mishchenko, A multiple sphere T-matrix Fortran code for use on parallel computer clusters, Journal of Quantitative Spectroscopy and Radiative Transfer 112 (13) (2011) 2182–2192.

[66] A multiple sphere T-matrix FORTRN code for use on parallel computer clusters, https://github.com/cheaps10/mstm-scan/blob/master/mstm-manual-2013-v3.0.pdf.

[67] B. Hapke, Bidirectional reflectance spectroscopy: 1. theory, J. Geophys. Res. Solid Earth 86 (B4) (1981) 3039–3054.

[68] B. Hapke, A model of radiative and conductive energy transfer in planetary regoliths, J. Geophys. Res. Planets 101 (E7) (1996) 16817–16831.

[69] B. Hapke, Bidirectional reflectance spectroscopy: 5. The coherent backscatter opposition effect and anisotropic scattering, Icarus 157 (2) (2002) 523–534.

[70] B. Hapke, Theory of reflectance and emittance spectroscopy, Cambridge university press, 2012.

[71] J. Moersch, P. R. Christensen, Thermal emission from particulate surfaces: A comparison of scattering models with measured spectra, J. Geophys. Res. Planets 100 (E4) (1995) 7465–7477.

[72] A. E. Wald, Modeling thermal infrared (2–14 μm) reflectance spectra of frost and snow, J. Geophys. Res. Solid Earth 99 (B12) (1994) 24241–24250.

[73] S. Chandrasekhar, Radiative transfer, Dover Publ, 1960.

[74] L. G. Sokoletsky, A. A. Kokhanovsky, F. Shen, Comparative analysis of radiative transfer approaches for calculation of diffuse reflectance of plane-parallel light-scattering layers, Appl. Opt. 52 (35) (2013) 8471–8483.

[75] A. A. Kokhanovsky, L. G. Sokoletsky, Reflection of light from semi-infinite absorbing turbid media. Part 1: Spherical albedo, Color Res. Appl. 31 (6) (2006) 491–497.

[76] H. Van de Hulst, The spherical albedo of a planet covered with a homogeneous cloud layer, Astron. Astrophys. 35 (1974) 209–214.

[77] G. Kresse, J. Hafner, Ab initio molecular dynamics for liquid metals, Phys. Rev. B 47 (1) (1993) 558.

[78] G. Kresse, D. Joubert, From ultrasoft pseudopotentials to the projector augmented-wave method, Phys. Rev. B 59 (3) (1999) 1758.

[79] M. Shishkin, G. Kresse, Implementation and performance of the frequency-dependent GW method within the PAW framework, Phys. Rev. B 74 (2006) 035101.

[80] D. K. Smith, H. Leider, Low-temperature thermal expansion of LiH, MgO and CaO, J. Appl. Crystallogr. 1 (4) (1968) 246–249.

[81] M. Lucht, M. Lerche, H.-C. Wille, Y. V. Shvyd'Ko, H. Rüter, E. Gerdau, P. Becker, Precise measurement of the lattice parameters of α-Al_2O_3 in the temperature range 4.5–250 K using the Mössbauer wavelength standard, J. Appl. Crystallogr. 36 (4) (2003) 1075–1081.

[82] R. Ratnawulan, A. Fauzi, A. Hayati, Characterization of silica sand due to the influence of calcination temperature, IOP Conf. Ser. Mater. Sci. Eng. 335 (1) (2018) 012008.

[83] J. Janovec, R. O. Agbaoye, J. S. Dolado, A. Ayuela, Optical properties of CaO, SiO_2, Al_2O_3 and Fe_2O_3 cementitious oxides, Mater. Des. 260 (2025) 114803.

[84] A. Hill, F. Jiao, P. Bruce, A. Harrison, W. Kockelmann, C. Ritter, Neutron diffraction study of mesoporous and bulk hematite, α-Fe_2O_3, Chem. Mater. 20 (15) (2008) 4891–4899.

[85] R. C. Whited, W. C. Walker, Exciton and interband spectra of crystalline CaO, Phys. Rev. 188 (3) (1969) 1380.

[86] J. Janine, L. Cotton, Photoconductibilite de l'oxyde de calcium, Compt. Rend. Hebd. Séances Acad. Sci. 246 (10) (1958) 1536.

[87] V. I. Neeley, J. C. Kemp, Optical absorption in CaO single crystals, J. Phys. Chem. Solids 24 (11) (1963) 1301–1304.

[88] R. C. Whited, C. J. Flaten, W. C. Walker, Exciton thermoreflectance of MgO and CaO, Solid State Commun. 13 (11) (1973) 1903–1905.

[89] Y. Kaneko, T. Koda, New developments in IIa–VIb (alkaline-earth chalcogenide) binary semiconductors, J. Cryst. Growth 86 (1-4) (1988) 72–78.

[90] A. Riefer, F. Fuchs, C. Rödl, A. Schleife, F. Bechstedt, R. Goldhahn, Interplay of excitonic effects and van Hove singularities in optical spectra: CaO and AlN polymorphs, Phys. Rev. B 84 (7) (2011) 075218.

[91] L. Garvie, P. Rez, J. Alvarez, P. Buseck, Interband transitions of crystalline and amorphous SiO_2: An electron energy-loss spectroscopy (EELS) study of the low-loss region, Solid State Commun. 106 (5) (1998) 303–307.

[92] H. Peng, D. O. Scanlon, V. Stevanovic, J. Vidal, G. W. Watson, S. Lany, Convergence of density and hybrid functional defect calculations for compound semiconductors, Phys. Rev. B 88 (11) (2013) 115201.

[93] R. H. French, D. J. Jones, S. Loughin, Interband Electronic Structure of α-alumina up to 2167 K, J. Am. Ceram. Soc. 77 (2) (1994) 412–422.

[94] S. Piccinin, The band structure and optical absorption of hematite (α-Fe_2O_3): a first-principles GW-BSE study, Phys. Chem. Chem. Phys. 21 (6) (2019) 2957–2967.

[95] R. Zimmermann, P. Steiner, R. Claessen, F. Reinert, S. Hüfner, P. Blaha, P. Dufek, Electronic structure of 3d-transition-metal oxides: on-site Coulomb repulsion versus covalency, J. Phys.: Condens. Matter 11 (7) (1999) 1657.

[96] E. K. Chang, M. Rohlfing, S. G. Louie, Excitons and optical properties of α-quartz, Phys. Rev. Lett. 85 (12) (2000) 2613.

[97] L. Martin-Samos, G. Bussi, A. Ruini, E. Molinari, M. Caldas, SiO_2 in density functional theory and beyond, Phys. Status Solidi B 248 (5) (2011) 1061–1066.

[98] F. Tran, J. Stelzl, P. Blaha, Rungs 1 to 4 of DFT Jacob's ladder: Extensive test on the lattice constant, bulk modulus, and cohesive energy of solids, J. Chem. Phys. 144 (20) (2016).

[99] M. Innocenzi, R. Swimm, M. Bass, R. French, A. Villaverde, M. Kokta, Room-temperature optical absorption in undoped α-Al_2O_3, J. Appl. Phys. 67 (12) (1990) 7542–7546.

[100] Z. D. Pozun, G. Henkelman, Hybrid density functional theory band structure engineering in hematite, J. Chem. Phys. 134 (22) (2011).

[101] E. Krén, B. Molnàr, E. Svàb, E. Zsoldos, Neutron diffraction study of the (1-x)αFe_2O_3 - xAl_2O_3 system, Solid State Commun. 15 (10) (1974) 1707–1710.

[102] S. Kim, Y. Lee, J. Plank, J. Moon, Fundamental discrepancy of chemical reactivity of tricalcium oxy silicate (alite), dicalcium silicate (belite), and their polymorphs: A density functional theory study, Int. J. Concr. Struct. Mater. 16 (1) (2022) 46.

[103] L. Gracia, A. Beltran, D. Errandonea, J. Andres, $CaSO_4$ and its pressure-induced phase transitions. A density functional theory study, Inorg. Chem. 51 (3) (2012) 1751–1759.

[104] P. Comodi, S. Nazzareni, P. F. Zanazzi, S. Speziale, High-pressure behavior of gypsum: A single-crystal X-ray study, Am. Miner. 93 (10) (2008) 1530–1537.

[105] J. Janovec, G. Goracci, J. Dolado, A. Ayuela, Selective optical properties of cement for enhanced radiative cooling and energy-efficient construction materials, Energy Environ. Mater. (2026) e70210.

[106] T. Fukami, S. Tahara, K. Nakasone, C. Yasuda, Synthesis, crystal structure, and thermal properties of $CaSO_4 \cdot 2H_2O$ single crystals, Int. J. Chem. 15 (2) (2015) 12–20.

[107] T.-L. Li, P.-L. Lee, Structural evolution of gypsum under high pressure: single-crystal X-ray experiments revisited, Phys. Chem. Miner. 45 (2018) 895–906.

[108] F. Beaugnon, S. Quiligotti, S. Chevreux, G. Wallez, On the monoclinic distortion of β-anhydrite $CaSO_4$, Solid State Sci. 108 (2020) 106399.

[109] A. Colville, S. Geller, The crystal structure of brownmillerite, Ca_2FeAlO_5, Struct. Sci. 27 (12) (1971) 2311–2315.

[110] A. Cuesta, I. Santacruz, S. Sanfélix, F. Fauth, M. Aranda, A. De la Torre, Hydration of C4AF in the presence of other phases: a synchrotron X-ray powder diffraction study, Constr. Build. Mater. 101 (2015) 818–827.

[111] D. Henderson, H. Gutowsky, A nuclear magnetic resonance determination of the hydrogen positions in $Ca(OH)_2$, Am. Mineral. 47 (11-12) (1962) 1231–1251.

[112] Thecrystal structure of the 11A natural tobermorite.

[113] E. Bonaccorsi, S. Merlino, A. R. Kampf, The crystal structure of Tobermorite 14 Å (plombierite), a C–S–H phase, J. Am. Ceram. Soc. 88 (3) (2005) 505–512.

[114] C. Phrompet, C. Sriwong, S. Maensiri, P. Chindaprasirt, C. Ruttanapun, Optical and dielectric properties of nano-sized tricalcium aluminate hexahydrate (C3AH6) cement, Constr. Build. Mater. 179 (2018) 57–65.

[115] G. D. Gatta, U. Hålenius, F. Bosi, L. Cañadillas-Delgado, M. T. Fernandez-Diaz, Minerals in cement chemistry: A single-crystal neutron diffraction study of ettringite, $Ca_6Al_2(SO_4)_3(OH)_{12}{\cdot}27H_2O$, Ame. Mineral. 104 (1) (2019) 73–78.

[116] E. Bonaccorsi, S. Merlino, H. Taylor, The crystal structure of jennite, $Ca_9Si_6O_{18}(OH)_6{\cdot}8H_2O$, Cem. Concr. Res. 34 (9) (2004) 1481–1488.

[117] K. K. Rao, S. N. Naidu, K. S. Murthy, Precision lattice parameters and thermal expansion of calcite, J. Phys. Chem. Solids 29 (2) (1968) 245–248.

[118] S. M. Antao, I. Hassan, The orthorhombic structure of $CaCO_3$, $SrCO_3$, $PbCO_3$ and $BaCO_3$: Linear structural trends, Can. Mineral. 47 (5) (2009) 1245–1255.

[119] M. Rezaee, S. M. M. Khoie, K. H. Liu, The role of brookite in mechanical activation of anatase-to-rutile transformation of nanocrystalline TiO_2: An XRD and Raman spectroscopy investigation, Cryst. Eng. Comm. 13 (16) (2011) 5055–5061.

[120] D. Bish, R. Von Dreele, Rietveld refinement of non-hydrogen atomic positions in kaolinite, Clays Clay Miner. 37 (4) (1989) 289–296.

[121] V. A. Drits, B. B. Zviagina, D. K. McCarty, A. L. Salyn, Factors responsible for crystal-chemical variations in the solid solutions from illite to aluminoceladonite and from glauconite to celadonite, Am. Mineral. 95 (2-3) (2010) 348–361.

[122] Y. Ohashi, Polysynthetically-twinned structures of enstatite and wollastonite, Phys. Chem. Miner. 10 (5) (1984) 217–229.

[123] S. M. Antao, I. Hassan, W. H. Mulder, P. L. Lee, B. H. Toby, In situ study of the orientational disorder in calcite, Phys. Chem. Miner. 36 (3) (2009) 159–169.

[124] L. Guimarães, A. N. Enyashin, J. Frenzel, T. Heine, H. A. Duarte, G. Seifert, Imogolite nanotubes: stability, electronic, and mechanical properties, Acs Nano 1 (4) (2007) 362–368.

[125] T. Sander, E. Maggio, G. Kresse, Beyond the Tamm-Dancoff approximation for extended systems using exact diagonalization, Phys. Rev. B 92 (4) (2015) 045209.

[126] J. H. Skone, M. Govoni, G. Galli, Nonempirical range-separated hybrid functionals for solids and molecules, Phys. Rev. B 93 (23) (2016) 235106.

[127] H. Philipp, Optical transitions in crystalline and fused quartz, Solid State Commun. 4 (1) (1966) 73–75.

[128] R. H. French, H. Müllejans, D. J. Jones, Optical properties of aluminum oxide: determined from vacuum ultraviolet and electron energy-loss spectroscopies, J. Am. Ceram. Soc. 81 (10) (1998) 2549–2557.

[129] M. R. Querry, Optical constants, US Army Armament, Munitions & Chemical Command, Chemical Research & Development Center, 1985.

[130] E. Kane, Coulomb effects at saddle-type critical points, Phys. Rev. 180 (3) (1969) 852.

[131] B. Velický, J. Sak, Excitonic effects in the interband absorption of semiconductors, Phys. Status Solidi B 16 (1) (1966) 147–157.

[132] H. Lawler, J. Rehr, F. Vila, S. D. Dalosto, E. L. Shirley, Z. H. Levine, Optical to UV spectra and birefringence of SiO_2 and TiO_2 first-principles calculations with excitonic effects, Phys. Rev. B 78 (20) (2008) 205108.

[133] A. Marinopoulos, M. Grüning, Local-field and excitonic effects in the optical response of α-alumina, Phys. Rev. B 83 (19) (2011) 195129.

[134] M. L. Urquiza, M. Gatti, F. Sottile, Pseudopotential Bethe-Salpeter calculations for shallow-core x-ray absorption near-edge structures: Excitonic effects in α-Al_2O_3, Phys. Rev. B 107 (20) (2023) 205148.

[135] Y. Ma, P. Johnson, N. Wassdahl, J. Guo, P. Skytt, J. Nordgren, S. Kevan, J.-E. Rubensson, T. Böske, W. Eberhardt, Electronic structures of α-Fe_2O_3 and Fe_3O_4 from O K-edge absorption and emission spectroscopyP, Phys. Rev. B 48 (4) (1993) 2109.

[136] B. Gilbert, C. Frandsen, E. Maxey, D. Sherman, Band-gap measurements of bulk and nanoscale hematite by soft X-ray spectroscopy, Phys. Rev. B 79 (3) (2009) 035108.

[137] A. Hofmeister, E. Keppel, A. Speck, Absorption and reflection infrared spectra of MgO and other diatomic compounds, Mon. Not. R. Astron. Soc. 345 (1) (2003) 16–38.

[138] W. Spitzer, D. Kleinman, Infrared lattice bands of quartz, Phys. Rev. 121 (5) (1961) 1324.

[139] R. King-Smith, D. Vanderbilt, Theory of polarization of crystalline solids, Phys. Rev. B 47 (3) (1993) 1651.

[140] H. Bilz, W. Kress, Phonon dispersion relations in insulators, Vol. 10, Springer Science & Business Media, 2012.

[141] M. R. Querry, Optical constants of minerals and other materials from the millimeter to the ultraviolet, US Army Armament, Munitions & Chemical Command, Chemical Research & Development Center, 1987.

[142] A. Pishtshev, S. Z. Karazhanov, M. Klopov, Excitons in $Mg(OH)_2$ and $Ca(OH)_2$ from $ab-initio$ calculations, Solid State Commun. 193 (2014) 11–15.

[143] E. Baldini, L. Chiodo, A. Dominguez, M. Palummo, S. Moser, M. Yazdi-Rizi, G. Auböck, B. P. Mallett, H. Berger, A. Magrez, et al., Strongly bound excitons in anatase TiO_2 single crystals and nanoparticles, Nat. Commun. 8 (1) (2017) 13.

[144] T. Posch, A. Baier, H. Mutschke, T. Henning, Carbonates in space: the challenge of low-temperature data, Astrophys. J. 668 (2) (2007) 993.

[145] S. Zeidler, T. Posch, H. Mutschke, H. Richter, O. Wehrhan, Near-infrared absorption properties of oxygen-rich stardust analogs-the influence of coloring metal ions, Astron. Astrophys. 526 (2011) A68.

[146] S.-i. Kondo, H. Yamashita, K. Nakamura, Optical properties of calcite in the vacuum ultraviolet, J. Phys. Soc. Jpn. 34 (3) (1973) 711–714.

[147] P. Cudazzo, L. Sponza, C. Giorgetti, L. Reining, F. Sottile, M. Gatti, Exciton band structure in two-dimensional materials, Phys. Rev. Lett. 116 (6) (2016) 066803.

[148] L. Long, M. Querry, R. J. Bell, R. W. Alexander, Optical properties of calcite and gypsum in crystalline and powdered form in the infrared and far-infrared, Infrared Phys. 34 (2) (1993) 191–201.

[149] ASTM, Standard tables for reference solar spectral irradiances: direct normal and hemispherical on 37 tilted surface, G173 (ASTM) (2007).

[150] E. R. Lippincott, A. Van Valkenburg, C. E. Weir, E. N. Bunting, et al., Infrared studies on polymorphs of silicon dioxide and germanium dioxide, J. Res. Natl. Bur. Stand. 61 (1) (1958) 61–70.

[151] D. L. Ou, A. B. Seddon, Near-and mid-infrared spectroscopy of sol-gel derived ormosils: vinyl and phenyl silicates, J. Non-Cryst. Solids 210 (2-3) (1997) 187–203.

[152] J. M. Pérez-Escudero, A. E. Torres-García, C. Lezaun, A. Caggiano, I. Peralta, J. S. Dolado, M. Beruete, I. Liberal, Suppressed-scattering spectral windows for radiative cooling applications, Opt. Express 31 (4) (2023) 6314–6326.

[153] P. Li, M. Lei, W. Tang, Raman and photoluminescence properties of α-Al_2O_3 microcones with hierarchical and repetitive superstructure, Mater. Lett. 64 (2) (2010) 161–163.

[154] I. N. Sokolik, O. B. Toon, Incorporation of mineralogical composition into models of the radiative properties of mineral aerosol from uv to ir wavelengths, J. Geophys. Res. Atmos. 104 (D8) (1999) 9423–9444.

[155] B. Hapke, Bidirectional reflectance spectroscopy: 4. The extinction coefficient and the opposition effect, Icarus 67 (2) (1986) 264–280.

[156] K. Shirley, T. Glotch, Particle size effects on mid-infrared spectra of lunar analog minerals in a simulated lunar environment, J. Geophys. Res. Planets 124 (4) (2019) 970–988.

[157] P. G. Lucey, B. Greenhagen, K. Donaldson Hanna, N. Bowles, A. Flom, D. A. Paige, Christiansen feature map from the lunar reconnaissance orbiter diviner lunar radiometer experiment: Improved corrections and derived mineralogy, J. Geophys. Res. Planets 126 (6) (2021) e2020JE006777.

[158] J. Wu, T. Ma, X. Du, S. Liu, Z. Sui, X. Xia, Novel passive radiation cooling materials with high emissivity discovered by FDTD method, Energies 16 (4) (2023) 1832.

[159] B. G. Henderson, B. M. Jakosky, C. E. Randall, A Monte Carlo model of polarized thermal emission from particulate planetary surfaces, Icarus 99 (1) (1992) 51–62.

[160] A. Picon, A. Alvarez-Gila, J. A. Arteche, G. A. López, A. Vicente, A probabilistic model and capturing device for remote simultaneous estimation of spectral emissivity and temperature of hot emissive materials, IEEE Access 9 (2021) 100513–100529.

[161] O. Rozenbaum, D. D. S. Meneses, Y. Auger, S. Chermanne, P. Echegut, A spectroscopic method to measure the spectral emissivity of semi-transparent materials up to high temperature, Rev. Sci. Instrum. 70 (10) (1999) 4020–4025.

[162] Y. Peng, J.-C. Lai, X. Xiao, W. Jin, J. Zhou, Y. Yang, X. Gao, J. Tang, L. Fan, S. Fan, et al., Colorful low-emissivity paints for space heating and cooling energy savings, Proc. Natl. Acad. Sci. 120 (34) (2023) e2300856120.

[163] F. M. Howari, G. Acbas, Y. Nazzal, F. AlAydaroos, Hapke-based computational method to enable unmixing of hyperspectral data of common salts, Chem. Cent. J. 12 (2018) 1–15.

[164] M. K. Shepard, P. Helfenstein, A test of the Hapke photometric model, J. Geophys. Res. Planets 112 (E3) (2007).

[165] M. Wu, J. Wang, Q. Wang, K. Zhou, Z. Zhang, X. Ma, W. Chen, Retrieval of Particle Size of Natural Granite From Multiangular Bidirectional Reflectance Spectra Using the Hapke Model, IEEE Trans. Geosci. Remote Sens. 59 (8) (2020) 6537–6548.

[166] G. E. Thomas, K. Stamnes, Radiative transfer in the atmosphere and ocean, Cambridge University Press, 2002.

[167] J. Janovec, R. O. Agbaoye, J. S. Dolado, A. Ayuela, Size-dependent photonic and radiative properties of CaO, SiO_2, Al_2O_3 and Fe_2O_3 cementitious oxides, Cement and Concrete Research 203 (2026) 108156.

[168] C. A. Gueymard, The sun's total and spectral irradiance for solar energy applications and solar radiation models, Sol. Energy 76 (4) (2004) 423–453.

[169] M. M. Odashima, B. G. Prado, E. Vernek, Pedagogical introduction to equilibrium Green's functions: condensed-matter examples with numerical implementations, Rev. Bras. Ensino Fís. 39 (2016).

[170] M. Rohlfing, S. G. Louie, Electron-hole excitations in semiconductors and insulators, Phys. Rev. Lett. 81 (11) (1998) 2312.